

The site-specific kinetics of OH radicals with esters

Niamh Cyrilene Keegan Robertson

Submitted in accordance with the requirements for the degree of
Doctor of Philosophy

The University of Leeds
School of Chemistry

May 2025

I confirm that the work submitted is my own, except where work which has formed part of jointly authored publications has been included. My contribution and the other authors to this work has been explicitly indicated below. I confirm that appropriate credit has been given within the thesis where reference has been made to the work of others.

The work in Chapter 3 appears in the publication:

Temperature-Dependent, Site-Specific Rate Coefficients for the Reaction of OH (OD) with Methyl Formate Isotopologues via Experimental and Theoretical Studies.

Niamh C. K. Robertson, Lavinia Onel, Mark A. Blitz, Robin Shannon, Daniel Stone, Paul W. Seakins, Struan H. Robertson, Christian Kühn, Tobias M. Pazdera and Matthias Olzmann, *J. Phys. Chem. A*. 2024, 128, 25, 5028 – 5040.

The experimental kinetics of methyl formate ($\text{CH}_3\text{OC}(\text{O})\text{H}$) + OH/OD from the Leeds group were primarily determined by Lavinia Onel. The experimental kinetics of OH/OD with isotopologues $\text{CH}_3\text{OC}(\text{O})\text{D}$, $\text{CD}_3\text{OC}(\text{O})\text{H}$ and $\text{CH}_3\text{OC}(\text{O})\text{D}$ were determined by me (Niamh C. K. Robertson) and Mark A. Blitz. Robin Shannon led the *ab initio* calculations and development of MESMER, with input from Struan H. Robertson. Paul W. Seakins led the supervision of the project with contributions from Daniel Stone, one of my PhD supervisors. Experiments from the Karlsruher Institut für Technologie (KIT) were conducted by Christian Kühn with supervision by Matthias Olzmann. Tobias M. Pazdera performed *ab initio* calculations which did not make it into the publication but may have informed interpretation of the experimental data by KIT.

This copy has been supplied on the understanding that it is copyright material and that no quotation from the thesis may be published without proper acknowledgement.

The right of Niamh Cyrilene Keegan Robertson to be identified as Author of this work has been asserted by her in accordance with the Copyright, Designs and Patents Act 1988.

Acknowledgements

I would like to express my immense appreciation to my supervisors, Paul Seakins and Daniel Stone. Thank you for the opportunity to join your research groups and for all your guidance and mentorship. I have really enjoyed the past three to four years and am incredibly grateful for the freedom I had to explore my interests and learn from you both.

I would also like to thank everyone else I have learnt from. Mark Blitz, thank you for your teaching, technical support, and constructive criticism. Particularly, for your contribution to the work in Chapters 3 and 4, which was a joint effort. Thank you to Robin Shannon for introducing me to computational chemistry, for the calculation in Chapters 3 and 4 and for your time and patience. I would also like to thank Lavinia Onel for her contributions to the kinetics of methyl and ethyl formate. Thank you to Owen Dudman for his contributions to determining the overall kinetics of tertbutyl formate. I also thank Ludovico Einaudi for helping me write this thesis. I recommend everyone listen to his work when they need a focused Experience. A big thank you goes to the friends I have made during the PhD, particularly for making conference trips so enjoyable.

On a personal note, I would like to thank Indi and Hugo, and the Spencer family for their support, and Hamish for the cuddles and distractions throughout. Thank you to my grandad, Niall, for encouraging me into science and my parents for instilling within me a feeling that I can achieve anything I set my mind to.

To my number 1 gal pal and fellow STEM Queen, thank you for keeping me sane. I am so grateful you are my sister - my built-in best friend. Thank you for inspiring me and always making me laugh.

To Josh, thank you for being my biggest supporter. Your endless encouragement and care have kept me going during the writing of this thesis. Thank you for always listening and talking through my problems, even when they involve methyl formate, again.

Abstract

This work uses laser flash photolysis coupled with laser induced fluorescence to experimentally determine the overall and site-specific kinetics of a series of formates. The total kinetics for OH and OD + methyl formate and its deuterated isotopomers ($\text{CH}_3\text{OC}(\text{O})\text{H}$, $\text{CH}_3\text{OC}(\text{O})\text{D}$, $\text{CD}_3\text{OC}(\text{O})\text{H}$ and $\text{CD}_3\text{OC}(\text{O})\text{D}$) have been determined between 298 and 573 K and are outlined in Chapter 3. The kinetics of OH + methyl formate determined in this work are in excellent agreement with literature studies at 298 K and bridge the gap between the work of Le Calve et al. (253 – 372 K) and Lam et al. (876 – 1371 K). The KIE indicates similar branching ratios from both the methyl and formate reaction sites, which are determined to be coupled, with a coupling factor of 2.38 at 298 K.

The experimental site-specific kinetics of OH + methyl formate ($\text{CH}_3\text{OC}(\text{O})\text{H}$) and $\text{CH}_3\text{OC}(\text{O})\text{D}$ are outlined in Chapter 4. The rates of thermal decomposition of the $\text{CH}_3\text{OC}(\text{O})$ radical formed following formate abstraction have also been determined, and decomposition is demonstrated to dominate over oxygen addition above ~ 423 K. The rate coefficients for $\text{CH}_3\text{OC}(\text{O}) + \text{O}_2$ and $\text{CH}_2\text{OC}(\text{O})\text{H} + \text{O}_2$ are investigated in the low-pressure regime between 8 and 84 Torr, and 298 and 573 K. Experiments indicate the ether-centred radicals react with oxygen faster than carbonyl-centred radicals, in agreement with literature trends. The site-specific kinetics for hydrogen abstraction reactions of the OH radical with methyl formate are determined from Stern-Volmer intercepts, utilising the decomposition of $\text{CH}_3\text{OC}(\text{O})$ to determine the branching ratio for methyl abstraction. The site-specific kinetics are also determined from the internal isomerisation of thermalised RO_2 radicals, which form a carbon-centred radical (QOOH) that promptly decomposes to regenerate OH. There is good agreement between the OH yields determined from both methods. The experimental site-specific kinetics are also compared with MESMER calculated rate coefficients determined by Dr Robin Shannon.

Chapter 5 outlines the overall and site-specific kinetics of isopropyl formate. This work demonstrates that the current temperature-dependent kinetics of OH radicals with isopropyl formate by Zhang et al. likely underestimate the overall rate

coefficient due to interference from OH regeneration. At 298 K, the site-specific kinetics for formate abstraction have been determined in good agreement with Pimentel et al. Above 400 K, decomposition of the $(\text{CH}_3)_2\text{CHOC}(\text{O})$ radical prevents OH regeneration following formate abstraction. Thanks to *ab initio* calculations at the M062X/6-31+G** level of theory, OH regeneration above 400 K is attributed to tertiary abstraction, providing the site-specific kinetics for tertiary abstraction by OH radicals between 400 and 573 K. The *ab initio* calculations also indicate the acceleration in the overall rate coefficient below room temperature is due to tertiary abstraction, which has a negative energy barrier. Above approximately 400 K, abstraction at the tertiary site is experimentally determined to decrease, coinciding with an increase in the rate coefficient, largely attributed to increasing formate abstraction.

The experimental site-specific kinetics of methyl formate (Chapters 3 and 4), isopropyl formate (Chapter 5), ethyl formate (determined by Dr Lavinia Onel, Appendix E), tertbutyl formate (Appendix E) and n-butyl formate (Appendix E) are combined in Chapter 6 and discussed in terms of wider trends in ester reactivity. The coupling between reaction sites in methyl formate is also demonstrated for the other formates and higher esters. Experimental site-specific kinetics are implemented into an updated structure activity relationship (SAR). The overall and site-specific kinetics of n-butyl formate are reserved from SAR development and used to test the updated SAR. The updated SAR improves upon the current SAR prediction of overall and site-specific ester kinetics. Consequently, the atmospheric chemistry of esters can be better represented within atmospheric chemical models. However, this work also highlights issues with the current SAR approach, namely the inability to predict hydrogen-bonding interactions, which influence reactivity in the esters and other oxygenated molecules. Alternative SAR approaches and suggestions for future work are proposed.

Contents

Acknowledgements.....	3
Abstract.....	4
Contents.....	6
Chapter 1 Introduction	29
1.1. Introduction	29
1.2. What is Atmospheric Chemistry and why is it important?.....	30
1.3. Esters as a sustainable petrochemical alternative	31
1.4. Sources of esters and volatile organic compounds (VOCs)	31
1.4.1. Direct emissions of esters	32
1.4.2. <i>In situ</i> formation of esters in the atmosphere	33
1.5. VOC Oxidation.....	34
1.5.1. Sources of atmospheric oxidants	35
1.5.2. VOC oxidation under high NO _x conditions	36
1.5.3. VOC Oxidation under low NO _x conditions.....	38
1.6. Highly Oxidised Molecules	39
1.6.1. Autoxidation	40
1.7. Secondary Organic Aerosols	42
1.8. Multiphase chemistry	43
1.9. Air Quality & Climate.....	44
1.9.1. Tropospheric ozone formation.....	46
1.10. An Introduction to Structure Activity Relationships (SARs)	47
1.10.1. Group Additivity SARs.....	50
1.11. Atmospheric modelling.....	52
1.12. Thesis outline	54
Chapter 2 Chemical kinetics theory and experimental methods.....	57
2. Reaction Kinetics.....	57
2.1. Temperature-dependent reaction kinetics	58
2.2. Transition state theory (TST).....	60
2.3. Pressure-dependent reactions	61
2.4. Rice Ramsperger Kassel Marcus (RRKM) statistical rate theory	62
2.5. Theoretical methods implemented in this work	63
2.6. The kinetic isotope effect	64
2.7. Overview of the experimental set-up.....	65
2.8. Flash Photolysis	66
2.9. Nd:YAG lasers	67
2.10. Dye lasers	67
2.11. Laser induced fluorescence (LIF) of OH/OD	68
2.12. UV absorption spectroscopy	70
2.13. Experimental procedures used in this work	70
2.13.1. Preparing dilute mixtures of esters	70
2.13.2. Ester flow corrections.....	71
2.13.3. Temperature calibrations	72
Chapter 3 The kinetics of OH/OD + methyl formate and its deuterated isotopomers	74
3. Introduction	74
3.1. Literature studies of OH + methyl formate kinetics	75
3.2. Experimental.....	77
3.2.1. Experimental set-up	77
3.2.2. Analysis of OH/OD traces	78
3.3. Kinetics of OH/OD with methyl formate	80
3.4. Theoretical calculations to explain the temperature dependence of OH + methyl formate	84
3.4.1. Theoretical methods.....	84

3.4.2.	Potential energy surface for the reaction of OH + methyl formate	87
3.5.	OH kinetics of the deuterated isotopomers: OH + CH ₃ OC(O)D, CD ₃ OC(O)H and CD ₃ OC(O)D	90
3.6.	Extracting site-specific information from deuterated kinetics	93
3.7.	Experiments by the Olzmann group at the Karlsruhe Institute of Technology to determine the kinetics of OH + isotopomers of methyl formate	97
3.8.	Results of the Theoretical Calculations by Dr Robin Shannon	99
3.9.	Atmospheric impacts	102
3.10.	Conclusions	104
Chapter 4 Branching ratios for OH abstraction from methyl formate via yield studies of OH and OD from deuterated isotopomers		106
4.	Introduction	106
4.1.1.	Experimental Methods	110
4.1.2.	Data analysis	111
4.1.3.	OD signal calibration	114
4.2.	Initial temperature-dependent rate coefficients for CH ₃ OC(O) and CH ₂ OC(O)D + O ₂ in the low-pressure (well-skipping) region	116
4.2.1.	R + O ₂ kinetics	116
4.2.2.	Evidence for R decomposition	118
4.3.	Experimental yields from the OH and Cl initiated oxidation of CH ₃ OC(O)H + O ₂	120
4.4.	Experimental yields from the OH and Cl initiated oxidation of CH ₃ OC(O)D + O ₂	128
4.5.	OH/OD yields from the thermalised RO ₂ isotopomers	135
4.6.	Atmospheric Implications	137
4.7.	Conclusions	139
Chapter 5 The site-specific kinetics of OH + isopropyl formate		141
5.	Introduction	141
5.1.	Literature studies of isopropyl formate kinetics	142
5.2.	Experimental	147
5.2.1.	Synthesis of isopropyl formate isotopomers	147
5.2.2.	Low temperature reaction cell and UV absorption measurements	150
5.2.3.	Computational calculations	152
5.3.	Temperature dependent kinetics of OH/OD with isopropyl formate	152
5.4.	Yields of OH from the reaction of OH + isopropyl formate	158
5.4.1.	Pressure dependence of OH + isopropyl formate at low temperatures	159
5.4.2.	OH yields as a function of pressure and oxygen at 298 K	160
5.4.3.	OH yields as a function of added oxygen and pressure between 393 and 523 K	162
5.4.4.	Yields of OH from thermalised RO ₂ species at high pressures	168
5.5.	Kinetics of OH/OD with deuterated isopropyl formate, (CH ₃) ₂ CHOC(O)D	173
5.5.1.	OH + (CH ₃) ₂ CHOC(O)D	173
5.5.2.	OD + (CH ₃) ₂ CHOC(O)D	176
5.6.	Yields of OD from OH and OD-initiated oxidation of (CH ₃) ₂ CHOC(O)D	178
5.7.	Atmospheric impacts	180
5.8.	Conclusions	181
Chapter 6 An updated ester Structure Activity Relationship		183
6.	Introduction	183
6.1.	Comparing ester reactivity with other oxygenated molecules	184
6.1.1.	Alcohol and ether reactivity	184
6.1.2.	Aldehyde and ketone reactivity	187
6.1.3.	Ester reactivity	189
6.1.4.	Site-specific kinetics of formates	190
6.1.5.	Influences of adjacent R groups in higher esters	192
6.1.6.	The dominant site of reactivity in the esters	195
6.2.	Challenges in predicting ester kinetics	197
6.3.	Methods for SAR Development	198
6.3.1.	General group additivity methods	198
6.3.2.	The history of ester SARs	199

6.3.3.	Differences between methods in the present work and the literature	201
6.3.4.	Experimental kinetics implemented in the present work.....	204
6.3.5.	Site-specific kinetics for the formate SAR	207
6.4.	SAR Results.....	211
6.5.	EsterSAR1.0 and EsterSAR2.0	214
6.5.1.	EsterSAR1.1 and EsterSAR2.1	217
6.6.	Testing the updated formate SAR on the kinetics of n-butyl formate.....	218
6.6.1.	Overall kinetics of n-butyl formate.....	218
6.6.2.	Site-specific kinetics of n-butyl formate	220
6.7.	Implications of this work	222
6.8.	Alternative SAR Approaches	224
6.8.1.	Topological Indices.....	224
6.8.2.	Machine Learning.....	226
6.9.	Conclusions	227
6.10.	Future Works	228
Chapter 7 Conclusions and future works		231
Appendix A Equation derivations.....		234
A.1.	Stern-Volmer Analysis.....	234
A.2.	Simple growth and decay derivation	236
Appendix B Supplementary Cl-initiated reactions		239
B.1	(COCl) ₂ as a precursor to Cl	239
B.2	OH LIF Signal Quenching by Oxygen and Methyl Formate.....	241
B.2.3	Branching ratio for the reaction of Cl + (CH ₃) ₃ COOH	245
Appendix C Chapter 4 supplementary Information.....		249
Appendix D Chapter 5 supplementary information.....		258
Appendix E The overall and site-specific kinetics of ethyl formate, tertbutyl formate and n-butyl formate		265
References		278

List of Figures

Figure 1.1 – The atmospheric oxidation of methyl formate. Depending on the initial reaction site, the atmospheric impact is very different.....	29
Figure 1.2 – Molecular structure of an ester. When $R_2 = H$, the ester is a formate.....	31
Figure 1.3 – Molecular structure of texanol, a coalescent in latex paints [1].....	32
Figure 1.4 – The atmospheric oxidation of dimethyl ether produces methyl formate as the dominant product [2]. Hydrogen abstraction by the OH radical adjacent the ether functionality (the dominant reaction site) typically leads to the formation of esters, as exemplified by the oxidation mechanism of dimethyl ether.....	33
Figure 1.5 – The tropospheric ROx (OH, HO ₂ and RO ₂) cycle. Reproduced from Liu et al. [3].....	36
Figure 1.6 – The alpha-ester rearrangement is an example of a unique alkoxy reaction of a functionalised molecule. With increasing R size of the ester, this reaction dominates leading to the formation of an organic acid [4].....	37
Figure 1.7 - The approximate partitioning of HOMs and Peroxy Radical Isomerisation Products (PRIP) by their volatilities. Reproduced from Bianchi et al.....	40
Figure 1.8 – General autoxidation scheme. Reproduced from Crounse et al. [5].....	41
Figure 1.9 – Overview of the interactions between air quality and climate change. Reproduced from von Scheidemesser et al. [6].....	44
Figure 1.10 – An area proportional Venn diagram demonstrating the overlap between our knowledge of the total rate coefficients for gas phase organic compounds and the species formed in the atmospheric oxidation of α -pinene, predicted by the automatic mechanism generator GECKO-A. “Known unknowns” refers to species whose rate coefficients have not been experimentally determined, however the species is predicted to form following α -pinene oxidation. “Unknown unknowns” refers to the species unknown to form in the atmosphere, for example through unknown pathways not currently considered in mechanism generators such as GECKO-A. The figure is adapted from McGillen et al. [7].....	48

Figure 1.11 – Qualitative energy barriers for the reactions of OH radicals with methane (purple) and methanol (blue). The alcohol functional group in methanol reduces the energy barrier for hydrogen abstraction by OH.....	51
Figure 2.1 – Potential energy surface for an example reaction with an energy barrier between reactant and products.....	59
Figure 2.2 – Potential energy surface for an example simple OH abstraction reaction of an organic compound, RH, with an activation barrier.....	60
Figure 2.3 – Overview of the experimental set-up.....	66
Figure 2.4 – Laser induced fluorescence of OH $A^2\Sigma^+(v'=0) \rightarrow X^2\Pi(v''=0)$. On-resonance fluorescence is shown in blue, where OH is excited at 308 nm to $A^2\Sigma^+(v'=0)$. Off-resonance fluorescence is shown in purple, where OH is excited at 282 nm to $A^2\Sigma^+(v'=1)$ and monitored at 308 nm from $A^2\Sigma^+(v'=0)$, due to vibrational energy transfer (VET) with another molecule e.g., the bath gas. Radiative energy transfer (RET) is illustrated in green, whereby collisional energy transfer occurs between different rovibrational states.....	69
Figure 2.5 – Bimolecular plot for the reaction of OH radicals with H₂ at 294 K, 1190 sccm flow rate and 120 Torr of argon. The intercept is $(18.7 \pm 2.3) \text{ s}^{-1}$ due to diffusion. The slope is equal to $(6.32 \pm 0.18) \times 10^{-15} \text{ cm}^3 \text{ molecule}^{-1} \text{ s}^{-1}$.....	73
Figure 2.6 – The left figure shows the calibrated temperature plotted against the temperature measured with the thermocouple (thermocouple temperature). The right figure shows the deviation between the calibrated and measured temperature (ΔT) against the thermocouple temperature.....	73
Figure 3.1 – Literature temperature-dependent studies of OH + methyl formate. Le Calvé et al. [8] is shown in black (squares), Lam et al. [9] is in blue (circles) and Jiménez et al. [10] is in purple (triangles). Arrhenius temperature-dependent fits to each data set are shown as solid lines and extrapolated to the full temperature range. Inset A shows a zoomed in view between $0 - 1.3 \times 10^{-11} \text{ cm}^3 \text{ molecule}^{-1} \text{ s}^{-1}$ and $0 - 1400 \text{ K}$. Inset B shows a zoomed in view between $200 - 500 \text{ K}$ and $0 - 5 \times 10^{-13} \text{ cm}^3 \text{ molecule}^{-1} \text{ s}^{-1}$.....	75

Figure 3.2 – The atmospheric fate of methyl formate. Solid arrows are determined by Wallington et al. [11] and dashed arrows represent additional reaction pathways determined by Good et al. [12].....76

Figure 3.3 – Example bimolecular plot for the reaction of OH + CD₃OC(O)H at 393 K. The slope/bimolecular rate coefficient is equal to $(2.34 \pm 0.08) \times 10^{-13} \text{ cm}^3 \text{ molecule}^{-1} \text{ s}^{-1}$, determined over $(1.11 - 8.48) \times 10^{15} \text{ molecule cm}^3$. Although there, the uncertainties in k' are smaller than the size of the symbols79

Figure 3.4 – Simplified scheme for the reaction of OH with methyl formate, where OH is regenerated in the presence of oxygen via oxygen addition to form a peroxy radical, RO₂, which undergoes internal isomerisation followed by decomposition to OH.....80

Figure 3.5 – Temperature-dependent kinetics of OH (black squares) and OD (blue circles) + methyl formate between 296 – 588 K.....81

Figure 3.6 – The temperature dependence of OH + methyl formate determined in this work (black squares) and the literature. The dark blue solid line represents the temperature-dependent fit to the Le Calvé et al. [8] dataset (253 – 372 K). The light blue solid line represents the temperature dependence of the Lam et al. [9] data (876 – 1371 K). Both Le Calvé et al. [8] and Lam et al. [9] temperature-dependent fits have been extrapolated to 200 – 1400 K. The black solid line is a temperature-dependent fit to the rate coefficients determined in this work, Le Calvé et al. [8] and Lam et al. [9]. The left figure shows the overall kinetics between 200 and 600 K and the right figure shows the overall kinetics over an extended temperature range between 200 and 1400 K.....82

Figure 3.7 – The secondary KIE ($k_{\text{OD}}/k_{\text{OH}}$) for the reactions of OH/OD + methyl formate. The solid line is calculated from the temperature-dependent fits of k_{OH} and k_{OD} , whereas the individual black squares represent experimental values where the rate coefficients for OH and OD have been obtained at the same temperature.....83

Figure 3.8 – Potential energy surface for formate (blue) and methyl (purple) abstraction by OH. Calculated by Dr Robin Shannon at the CCSD(T)-F12/aug-cc-pVTZ//M06-2X/6-31+G** level of theory, with higher-level “AN10-like” calculations for the energies of the transition state barriers.....88

Figure 3.9 – Lowest energy transition states for OH abstraction from methyl formate. Abstraction at the methyl site has two transition states – a low-energy transition state

(A) and a high-energy transition state (B) presented in Figure 3.17. Abstraction from the formate site has one transition state, shown on the right.....89

Figure 3.10 – Rate coefficients for the reactions of OH + CH₃OC(O)H (black squares), CH₃OC(O)D (blue circles), CD₃OC(O)H (purple triangles) and CH₃OC(O)D (green diamonds)..... 90

Figure 3.11 – The primary KIE calculated by dividing the rate coefficient, $k_{\text{OH} + \text{MF}}$, with the rate coefficient for each isotopomer. $k_{\text{OH} + \text{MF}}/k_{\text{OH} + \text{dMF}}$ is shown in blue, $k_{\text{OH} + \text{MF}}/k_{\text{OH} + \text{d3MF}}$ is shown in purple, and $k_{\text{OH} + \text{MF}}/k_{\text{OH} + \text{d4MF}}$ is shown in green. The solid lines are calculated from the non-Arrhenius temperature-dependent fits to the experimental data.....91

Figure 3.12 – BDEs (C-H) for the major abstraction site in a series of organic molecules alongside their KIEs presented in Table 3.2.....93

Figure 3.13 – The sum of rate coefficients $k(\text{CH}_3\text{OC(O)H})$ and $k(\text{CD}_3\text{OC(O)D})$ are shown in black squares, whilst the sum of rate coefficients $k(\text{CH}_3\text{OC(O)D})$ and $k(\text{CD}_3\text{OC(O)H})$ are shown in blue. Both pairs of rate coefficients are within error of each other, indicating the reaction sites are independent of a common coupling factor that applies.....94

Figure 3.14 – The coupling factor between the methyl (CH₃) and formate (H) reaction sites within methyl formate, determined via E3.18 and E3.20.....95

Figure 3.15 – A comparison of rate coefficients for the reactions of OH with CH₃OC(O)H (top left), CH₃OC(O)D (top right), CD₃OC(O)H (bottom left) and CD₃OC(O)D (bottom right) determined in this work (black squares) and by KIT (blue circles).....98

Figure 3.16 – Experimental rate coefficients determined in the present work (filled-in symbols) and by KIT (hollowed symbols) alongside theoretically calculated rate coefficients. Solid lines represent calculated rate coefficients from fitted barriers whilst dashed lines represent calculated rate coefficients from *ab initio* calculations. The top panel is OH-initiated reactions whilst the bottom panel is OD-initiated reactions.....100

Figure 3.17 – High energy conformer for methyl abstraction accessed via rotation of two torsional coordinates.....102

Figure 3.18 – Abstraction ratios from the methyl site in methyl formate as a function of temperature (200 – 1000 K). Reproduced from Robertson et al. [13]......104

Figure 4.1 – The OH + CH₃OC(O)H reaction scheme under experimental conditions 298 – 523 K and 2 – 150 Torr in the presence of the bath gas (Ar) and oxygen (0 – 1.6 × 10¹⁶ molecule cm⁻³). Above ~ 420 K, the CH₃OC(O) radical undergoes thermal decomposition preventing its addition reaction with O₂ to form the peroxy radical. Peroxy radicals can undergo collisional stabilisation or chemically activated internal isomerisation followed by decomposition to OH. Above ~ 540 K the stabilised peroxy radicals have enough thermal energy to undergo internal isomerisation followed by decomposition to OH. The other products of decomposition, HCHO and CO₂, are proposed based on the structure of the peroxy radicals......107

Figure 4.2 – Schematic potential energy surface for the regeneration of OH following the general reaction of R + O₂......107

Figure 4.3 – Reaction scheme for OH + CH₃OC(O)D in the presence of oxygen. Abstraction at the methyl site leads to the regeneration of OD (blue) whilst abstraction from the formate site leads to the regeneration of OH (purple)......108

Figure 4.4 – Corresponding OH (black) and OD (blue) traces from the OH-initiated oxidation of 4.24 × 10¹⁵ molecule cm⁻³ CH₃OC(O)D in the presence of 2.09 × 10¹⁶ molecule cm⁻³ of oxygen at 2.8 Torr and 373 K......109

Figure 4.5 – Biexponential decay following the OH-initiated oxidation of 1.87 × 10¹⁵ molecule cm⁻³ methyl formate at 90 Torr and 515 K......111

Figure 4.6 – Simplified reaction scheme for methyl formate + OH. k_d is loss of OH via diffusion and its reaction with H₂O₂, k_{MF} is the rate coefficient for reaction of OH with methyl formate, k_R is the rate coefficient for R + O₂, k_{Regen} is the rate coefficient for isomerisation of RO₂^{*} to recycle OH and k_{Stab} is the rate coefficient for collisional stabilisation of RO₂^{*}......112

Figure 4.7 – OH yields as a function of pressure from the OH-initiated reaction of CH₃OC(O)H in argon. Yields in black are calculated via E3 whilst yields in blue are calculated with E1. The inset at 298 K shows good agreement between the two methods whilst the main figure at 423 K, shows a discrepancy between the yields calculated via the two methods. The discrepancy is due to the thermal decomposition of CH₃OC(O).

In the presence of oxygen larger yields of OH are observed due to the reaction of $\text{CH}_3\text{OC(O)} + \text{oxygen}$ regenerating OH.....113

Figure 4.8 – Simplified reaction scheme for the growth and decay of OD from the OH-initiated oxidation of $\text{CH}_3\text{OC(O)D}$. k_D represents diffusional loss.....113

Figure 4.9 – Example spectra of OH and OD at 20 Torr and 298 K show a 1:1 relationship between the OH and OD signal. The OH and OD lines chosen in this work are shown with arrows and correspond to the $\text{A}^2\Sigma^+ (v'=0) \leftarrow \text{X}^2\Pi_i (v''=0)$ transition with rotational assignments $\text{R}_1(1)$ and $\text{Q}_1(1)$, respectively.....115

Figure 4.10 – OH (black) and OD (blue) spectra under vacuum between 307.1 – 307.4 nm at 300 K, as predicted by LIFBASE [14]. The OH and OD lines chosen in this work are shown with arrows and correspond to the $\text{A}^2\Sigma^+ (v'=0) \leftarrow \text{X}^2\Pi_i (v''=0)$ transition with rotational assignments $\text{R}_1(1)$ and $\text{Q}_1(1)$, respectively.....115

Figure 4.11 – Reaction schematic used to derive the equation to fit the traces of OH and OD globally to determine k_R and k_D116

Figure 4.12 – Temperature-dependent rate coefficients for the reactions of R radicals $\text{CH}_3\text{OC(O)}$ (black squares) and $\text{CH}_2\text{OC(O)D}$ (blue circles) with O_2 determined between 8 and 9 Torr.....117

Figure 4.13 – Bimolecular rate coefficients for $\text{CH}_3\text{OC(O)} + \text{O}_2$ (left) and $\text{CH}_2\text{OC(O)D} + \text{O}_2$ (right) determined from the global analysis of respective OH and OD traces as a function of pressure and temperature.....118

Figure 4.14 – Bimolecular plots for $\text{CH}_3\text{OC(O)}$ (black squares) and $\text{CH}_2\text{OC(O)D}$ (blue circles) + O_2 at 423 K (left) and 298 K (right). Both bimolecular plots were determined at 14 Torr.....119

Figure 4.15 – Decomposition rates of $\text{CH}_3\text{OC(O)}$ as determined from this work (black squares) and experiments by Dr Lavinia Onel under lower oxygen additions ($\sim 1 \times 10^{13} - 1 \times 10^{15} \text{ molecule cm}^{-3}$).....120

Figure 4.16 – Stern-Volmer plots of the reciprocal OH yield following the OH-initiated oxidation of $\text{CH}_3\text{OC(O)H}$ in argon at 298, 353 and 448 K. The shaded regions illustrate the 95% confidence limits.....122

Figure 4.17 – Stern-Volmer plots of the reciprocal OH yield following the Cl-initiated oxidation of $\text{CH}_3\text{OC(O)H}$ in argon between 298 and 453 K. The shaded regions illustrate the 95% confidence limits.....122

Figure 4.18 – Stern-Volmer parameters from the OH (black squares) and Cl-initiated (blue circles) oxidation of $\text{CH}_3\text{OC(O)H}$. The main figure has a y-axis limit of $1 \times 10^{-17} \text{ cm}^3 \text{ molecule}^{-1}$. The inset shows all of the data, with a y-axis limit of $4.5 \times 10^{-17} \text{ cm}^3 \text{ molecule}^{-1}$. Rather than having physical meaning, the linear lines provide a qualitative representation of the general trend as a function of temperature.....123

Figure 4.19 – Temperature-dependent Stern-Volmer intercepts from OH and Cl-initiated oxidation of $\text{CH}_3\text{OC(O)H}$124

Figure 4.20 – Stern-Volmer plot at 423 K (left) and 473 K (right) from the OH-initiated oxidation of $\text{CH}_3\text{OC(O)H}$. OH yields extracted from biexponential traces (E1, black squares) observed in the absence of added oxygen are lower than OH yields in the presence of added oxygen (E3, blue circles). When oxygen is added, $\text{CH}_3\text{OC(O)}$ decomposition is intercepted by the $\text{CH}_3\text{OC(O)} + \text{O}_2$ reaction, resulting in higher yields of OH.....125

Figure 4.21 – Stern-Volmer plots at 498 K (left) and 523 K (right) in blue. Yields from biexponential decays in the absence of added oxygen represent OH yields from the thermalised RO_2 ($\text{OOCH}_2\text{OC(O)H}$) and are shown in black.....127

Figure 4.22 – Experimental branching ratios for methyl abstraction discussed above (black) alongside MESMER predicted values (blue).....128

Figure 4.23 – Comparisons of Stern-Volmer parameters from the OH and Cl-initiated oxidation of $\text{CH}_3\text{OC(O)D}$. OD yields representing methyl abstraction are shown on the left and OH yields representing formate abstraction are shown on the right.....129

Figure 4.24 – Comparison of Stern-Volmer parameters following methyl and formate abstraction. Comparisons following Cl-initiated oxidation are shown on the left, and the right shows comparisons from OH-initiated oxidation.....130

Figure 4.25 –Yield sums of the reciprocal Stern-Volmer intercepts for OH and OD yields from the OH (black squares) and Cl-initiated (blue circles) oxidation of $\text{CH}_3\text{OC(O)D}$..132

Figure 4.26 – OH (black squares) and OD (blue circles) yields following the reaction of Cl + CH₃OC(O)D as a function of added oxygen are quantitative at 423 K (left) and qualitative at 398 K (right).....	134
Figure 4.27 – Branching ratios for the OH-initiated oxidation of CH₃OC(O)D. The ratios are calculated from the reciprocal of their respective OH / OD Stern-Volmer intercepts.....	134
Figure 4.28 – Branching ratios for methyl abstraction from the different isotopomers of methyl formate.....	136
Figure 4.29 – High temperature branching ratios for methyl abstraction from isotopomers CH₃OC(O)H (top left), CH₃OC(O)D (top right), CD₃OC(O)H (bottom left) and CD₃OC(O)D (bottom right) compared with MESMER predicted values using <i>ab initio</i> and fitted barriers.....	137
Figure 4.30 – Experimental branching ratios (black squares) for OH-initiated oxidation at the methyl site in methyl formate, CH₃OC(O)H. MESMER predicted branching ratios are shown in blue and purple alongside the Jenkin et al. [15] SAR predictions.....	138
Figure 5.1 – Literature rate coefficients for the reaction of OH + isopropyl formate alongside the Eurochamp recommended temperature dependence [16].....	143
Figure 5.2 – Oxidation of isopropyl formate following formate abstraction. Oxidation products are iPOPAN and acetone. Based on the experimental studies of Pimentel et al. [17] at 700 Torr and 298 K.....	145
Figure 5.3 - Oxidation of isopropyl formate following CH₃/methyl site abstraction. Oxidation products are formaldehyde, formic acid and acetic formic anhydride. Based on the experimental studies of Pimentel et al. [17] at 700 Torr and 298 K.....	145
Figure 5.4 – Oxidation of isopropyl formate following CH/tertiary site abstraction. Oxidation products are acetone and acetic formic anhydride. Based on the experimental studies of Pimentel et al. [17] at 700 Torr and 298 K.....	146
Figure 5.5 – Esterification reaction between formic acid and isopropyl alcohol, forming isopropyl formate and water.....	148
Figure 5.6 – The reaction mechanism for the Fischer esterification reaction between formic acid and isopropyl alcohol, catalysed by sulphuric acid [18].....	148

Figure 5.7 – Reflux set up for the synthesis of isopropyl formate.....	149
Figure 5.8 – Experimental setup to determine gas-phase kinetics of OH/OD + ester...151	151
Figure 5.9 – Rate coefficients for the reactions of OH and OD + isopropyl formate determined in this work between 230 – 575 K and 110 – 120 Torr Ar shown alongside literature studies for OH + isopropyl formate. The inset shows a focused view between 290 – 300 K at OH + isopropyl formate determined in this work and the literature. Solid lines represent non-Arrhenius temperature-dependent fits.....	153
Figure 5.10 – Generic potential energy surface for a hydrogen abstraction reaction leading to the production of OH.....	153
Figure 5.11 – Potential energy surface for the initial hydrogen abstraction of OH + isopropyl formate from the formate reactive site (blue), the tertiary site (purple) and the methyl site (green)....	155
Figure 5.12 – Transition state structures for hydrogen abstraction from isopropyl formate by OH at the tertiary, formate and methyl sites from left to right.....	155
Figure 5.13 – The secondary KIE, k_{OD}/k_{OH}. Individual points on the graph are experimentally measured values of k_{OD}/k_{OH} and the fitted line is k_{OD}/k_{OH} calculated from the temperature-dependent fits shown in Figure 5.9.....	158
Figure 5.14 – Rate coefficients determined at 232 K (top) and corresponding yields of OH (bottom) as a function of pressure in the absence of any added oxygen.....	160
Figure 5.15 – Yields of OH as a function of pressure. The left figure shows OH yields whilst the right figure shows the reciprocal of the OH yield, i.e., the Stern-Volmer plot. Yields above 90 Torr, shown in red, have been excluded from the Stern-Volmer slope as these come from a thermalised RO_2. The Stern-Volmer slope shown on the right is equal to 0.073 ± 0.012 with an intercept of 1.30 ± 0.68.....	161
Figure 5.16 – Yields of OH at 12 (black squares) and 24 (blue circles) Torr as a function of added oxygen at 298 K. Yields have been calculated from the difference in the pseudo-first order rate coefficient in the absence and presence of oxygen (E2).....	162
Figure 5.17 – Yields as a function of added oxygen at 393 K and 113 Torr.....	163
Figure 5.18 – Yields as a function of added oxygen at 413 K and 120 Torr.....	164

Figure 5.19 – Yields of OH calculated via different methods at 423 K. Yields at this temperature are independent of added oxygen.....165

Figure 5.20 – Stern-Volmer plots at 423 K with an instrumental fit (left) and unweighted fit (right). The instrumental fit has a slope equal to 0.028 ± 0.005 and an intercept equal to 1.59 ± 0.22 . The unweighted fit has a slope equal to 0.039 ± 0.004 and an intercept equal to 1.55 ± 0.57166

Figure 5.21 - Yields as a function of added oxygen at 473 K and 120 Torr. Yields are independent of added oxygen and can be attributed to abstraction at the tertiary and methyl reaction sites. The radical formed following formate abstraction, $(\text{CH}_3)_2\text{CHOC}(\text{O})\cdot$, thermally decomposes preventing OH regeneration.....166

Figure 5.22 – Yields of OH following the reaction of OH with isopropyl formate calculated via different methods at 523 K.....168

Figure 5.23 – Yields of OH from OH + isopropyl formate obtained by fitting biexponential decays above 120 Torr.....169

Figure 5.24 – Temperature-dependent kinetics for the reactions of OH + $(\text{CH}_3)_2\text{CHOC}(\text{O})\text{H}$ (black squares) fitted with the expression $((2.13 \pm 1.53) \times 10^{-15}) \times \exp((2117 \pm 212)/T) \times (T/300)^{(5.89 \pm 0.61)} \text{ cm}^3 \text{ molecule}^{-1} \text{ s}^{-1}$ and $(\text{CH}_3)_2\text{CHOC}(\text{O})\text{D}$ (blue circles) fitted with the expression $((9.24 \pm 2.45) \times 10^{-15}) \times \exp((1636 \pm 79)/T) \times (T/300)^{(4.39 \pm 0.23)} \text{ cm}^3 \text{ molecule}^{-1} \text{ s}^{-1}$174

Figure 5.25 – The k_{OH} KIE ($\text{ROC}(\text{O})\text{H}/\text{ROC}(\text{O})\text{D}$) for $\text{R} = \text{CH}_3$ (methyl formate) shown in black squares and $\text{R} = (\text{CH}_3)_2\text{CH}$ (isopropyl formate) shown in blue circles. The KIE is calculated from experimental values of $k_{\text{OD}}/k_{\text{OH}}$ for a given temperature and the temperature-dependent fits of k_{OD} and k_{OH} , which are shown as solid lines.....174

Figure 5.26 – Temperature-dependent kinetics for the reactions of OD + $(\text{CH}_3)_2\text{CHOC}(\text{O})\text{H}$ (black squares) fitted with the expression $((5.25 \pm 1.74) \times 10^{-15}) \times \exp((1926 \pm 97)/T) \times (T/300)^{(4.91 \pm 0.28)} \text{ cm}^3 \text{ molecule}^{-1} \text{ s}^{-1}$ and $(\text{CH}_3)_2\text{CHOC}(\text{O})\text{D}$ (blue circles) fitted with the expression $((1.80 \pm 0.56) \times 10^{-15}) \times \exp((2120 \pm 91)/T) \times (T/300)^{(5.83 \pm 0.27)} \text{ cm}^3 \text{ molecule}^{-1} \text{ s}^{-1}$. Kinetics were determined between 80 and 127 Torr of argon.....176

Figure 5.27 – The k_{OD} KIE ($\text{ROC}(\text{O})\text{H}/\text{ROC}(\text{O})\text{D}$) for $\text{R} = \text{CH}_3$ (methyl formate) shown in black squares and $\text{R} = (\text{CH}_3)_2\text{CH}$ (isopropyl formate) shown in blue circles. The KIE is

calculated from experimental values of k_{OD}/k_{OH} for a given temperature and the temperature-dependent fits of k_{OD} and k_{OH} , which are shown as solid lines.....177

Figure 5.28 – The secondary KIE for $(CH_3)_2CHOC(O)H$ (black squares) and $(CH_3)_2CHOC(O)D$ (blue circles). The KIE is calculated from experimental values of k_{OD}/k_{OH} for a given temperature and the temperature-dependent fits of k_{OD} and k_{OH} , which are shown as solid lines.....178

Figure 5.29 – Yields of OH from the OH and OD-initiated oxidation of $(CH_3)_2CHOC(O)H$ (black squares) and yields of OD from the OH and OD-initiated oxidation of $(CH_3)_2CHOC(O)D$ (blue circles) as a function of temperature.....179

Figure 5.30 – Branching ratios for tertiary abstraction from isopropyl formate experimentally determined in this work between 393 and 573 K (black squares), by Pimentel et al. at 298 K (blue circle), and SAR predictions by Jenkin et al. [15] (solid green line).....181

Figure 6.1 – Rate coefficients for the reactions of OH + linear alkanes, alcohols and ethers, as recommended by Eurochamp [16]. Rate coefficients are plotted as a function of the number of CH_2 groups. Ether rate coefficients with two CH_2 groups are from diethyl ether and methoxy propane.....185

Figure 6.2 – Rate coefficients for each additional CH_2 group (k_{CH_2}) in the reactions of OH + linear alkanes, alcohols (ROH) and ethers (ROR), plotted as a function of the number of CH_2 groups. Additional points for ethers with two CH_2 groups are from diethyl ether and methoxy propane186

Figure 6.3 – Rate coefficients for the reactions of OH + linear alkanes, aldehydes and ketones as recommended by Eurochamp [16]. Rate coefficients are plotted as a function of the number of CH_2 groups.....188

Figure 6.4 – Rate coefficients for each additional CH_2 group (k_{CH_2}) in the reactions of OH + linear alkanes, aldehydes ($RC(O)H$) and ketones ($RC(O)R$), plotted as a function of the number of CH_2 groups.....188

Figure 6.5 – Rate coefficients for the reactions of OH + linear alkanes, formates ($ROC(O)H$), acetates ($ROC(O)CH_3$) and propanoates ($ROC(O)CH_2CH_3$) as recommended by Eurochamp [16] and this work. Rate coefficients are plotted as a function of the number of CH_2 groups.....189

Figure 6.6 – Resonance structures of a formate (ROC(O)H).....	190
Figure 6.7 – Experimentally determined rate coefficients for formate abstraction at 298 K.....	191
Figure 6.8 – Experimentally determined rate coefficients for formate abstraction at 423 K. Although presented here, the Jenkin et al. [15] SAR is trained up to 400 K.....	192
Figure 6.9 – Rate coefficients for each additional CH₂ group (<i>k</i>CH₂) in the reactions of OH + linear alkanes, formates (ROC(O)H), acetates (ROC(O)CH₃) and propanoates (ROC(O)CH₂CH₃), plotted as a function of the number of CH₂ groups.....	194
Figure 6.10 – The structure of methyl pivalate.....	196
Figure 6.11 – The atmospheric oxidation of methyl formate as determined by Wallington et al. [11]. Products following oxidation at the formate site are circled in blue whilst products from methyl abstraction are circled in purple.....	197
Figure 6.12 – Temperature-dependent data for the reactions of OH + formates. Each formate is represented with a different colour. Solid lines are the temperature-dependent recommendations of Calvert et al., which are used to train the Jenkin et al. [15] SAR. The temperature-dependent rate coefficients used in this work are shown above as dashed lines and are based on Eurochamp recommendations, with a few modifications to include overall kinetics in this work. The rate coefficients for methyl formate are updated to include kinetics outlined in Chapter 3. Ethyl formate kinetics are adapted to include the work of Dr Lavinia Onel (Appendix E), rate coefficients for isopropyl formate are adapted to include the kinetics outlined in Chapter 5 and tertbutyl formate kinetics are adapted to include the kinetics in Appendix E.....	205
Figure 6.13 - The site-specific kinetics of methyl formate implemented in the SAR, as determined experimentally in the present work (Chapter 4) and theoretically by Dr Robin Shannon (labelled MESMER, based on isotopomer studies).....	208
Figure 6.14 – The site-specific kinetics of ethyl formate implemented in the SAR, as determined experimentally by Dr Lavinia Onel.....	209
Figure 6.15 – The site-specific kinetics of isopropyl formate implemented in the SAR, as determined in this work and by Pimentel et al.....	210

Figure 6.16 – The site-specific kinetics of tertbutyl formate implemented in the SAR, as determined in this work.....	211
Figure 6.17 – Formate temperature-dependent kinetics determined experimentally (black squares) and via different SAR calculations.....	213
Figure 6.18 – Branching ratios for each formate included in the SAR. Experimental branching ratios are shown in black and SAR calculated branching ratios are shown in blue (EsterSAR1.0) and purple (EsterSAR2.0).....	214
Figure 6.19 – Branching ratios for each formate included in the SAR. Experimental branching ratios are shown in black and SAR calculated branching ratios are shown in blue (EsterSAR1.1) and purple (EsterSAR2.1). Both SARs incorporate secondary substituent factors.....	215
Figure 6.20 – Rate coefficients at 298 K for OH radical reactions with alkyl groups (R) (purple) and formates (blue). Rate coefficients for alkyl groups are calculated by subtracting k_{CH_3} from RCH_3, with k_{CH_3} calculated from $k_{CH_3CH_3}/2$.....	216
Figure 6.21 – Temperature-dependent rate coefficients for the reaction of OH + n-butyl formate determined in this work (black squares and solid black line), the literature (Le Calve et al. [8] (blue circles) and Wallington et al. [19] (burgundy triangles)), the Eurochamp [16] recommended temperature dependence (blue line), Jenkin et al. [15] SAR predictions (green line) and the EsterSAR2.1 predictions updated in this work (purple line).....	219
Figure 6.22 – SAR calculated rate coefficients for OH + n-butyl formate from this work (EsterSAR2.1) and Jenkin et al. [15] are plotted against experimental rate coefficients for OH + n-butyl formate calculated from the temperature-dependent fit to this work. The left figure shows rate coefficients between 200 and 600 K, whilst the right figure shows rate coefficients between 232 and 613 K.....	220
Figure 6.23 – OH yields determined in this work (black squares) following the OH-initiated oxidation of n-butyl formate at 120 Torr in the absence of added oxygen. Branching ratios for abstraction from the reaction site alpha to the ether oxygen calculated by Zaras et al. [20] are shown as blue circles.....	221
Figure 6.24 – The structure of n-butyl formate with each carbon numbered, C₁ starts at the formate carbon.....	221

Figure 6.25 – Branching ratios for OH abstraction adjacent to the ether group in n-butyl formate. Branching ratios calculated by Zaras et al. [20] are shown as blue circles, this works SAR EsterSAR2.1 is shown in purple and the Jenkin et al. [15] SAR is shown in green.....222

Figure 6.26 – Example correlations between physical quantities and a topological index, the Zagreb index. The left figure presents the transition state energies for hydrogen abstraction from the formate site (black squares), alpha to the ether group (blue circles) and beta to the ether group (purple triangles) calculated at the M062X/6-31+G** level of theory. The right figure shows the experimental rate coefficients for formate abstraction in methyl formate, isopropyl formate and tertbutyl formate.....225

Figure B.1 - Stern-Volmer plots from the Cl-initiated oxidation of methyl formate at 300 K following the analysis of OH traces via two methods; excluding (black) and including (blue) the secondary production of Cl from COCl. The inset shows an example OH trace fit with the two equations.....240

Figure B.2 – An example plot to calculate the quenching factor at 45 Torr and 448 K....242

Figure B.3 – Quenching factors of OH by oxygen as a function of temperature.....243

Figure B.4 – An example plot where the quenching factor of OH and OD by CH₃OC(O)H was calculated at 47 Torr and 573 K. There is good agreement between OH and OD indicating a global calibration factor can be used for both LIF signals.....244

Figure B.5 – Quenching factors of OH by CH₃OC(O)H, CH₃OC(O)D and CD₃OC(O)H as a function of temperature.....244

Figure B.6 – Example OH decay in the presence of 9.37×10^{13} molecule cm⁻³ of (COCl)₂, 2.36×10^{16} molecule cm⁻³ of tBuOOH and 3.93×10^{17} molecule cm⁻³ of argon.....246

Figure B.7 – Temperature dependent branching ratios for methyl abstraction from the Cl-initiated oxidation of tBuOOH.....248

Figure C.1 – Bimolecular plot for $k(\text{CH}_3\text{OC(O)} + \text{O}_2)$ at 398 K. Individual points on the bimolecular plot are determined from individual analysis of OH decays, whose data are shown in Figure C2. The intercept is $10,031 \pm 1786 \text{ s}^{-1}$, approximately equivalent to the rate of CH₃OC(O) decomposition. The slope is $(1.18 \pm 0.21) \times 10^{-12} \text{ cm}^3 \text{ molecule}^{-1} \text{ s}^{-1}$,

the bimolecular rate coefficient for $k(\text{CH}_3\text{OC}(\text{O}) + \text{O}_2)$ at 398 K. Global fits are shown in Figure C.2.....249

Figure C.2 – Each trace of OH following the reaction of $\text{Cl} + \text{CH}_3\text{OC}(\text{O})\text{D}$ has been fit globally at 398 K to determine the bimolecular rate coefficient for $k(\text{CH}_3\text{OC}(\text{O}) + \text{O}_2)$, equal to $(1.18 \pm 0.29) \times 10^{-12} \text{ cm}^3 \text{ molecule}^{-1} \text{ s}^{-1}$, in excellent agreement with the individual analysis presented in Figure C.1.....250

Figure C.3 – OH and OD decays measured at 298 K. The solid blue line through the OD decay is an analytically derived scheme for EC.1 – EC.2. The cyan dashed line is the MATLAB numerically integrated equivalent.....251

Figure C.4 – The analytical scheme is shown with the blue solid line, the MATLAB equivalent scheme is shown in the cyan dashed line, the MATLAB scheme accounting for production of the excited peroxy radical is shown in the pink dotted line and the MATLAB scheme accounting for OD to regenerate RO_2^* is shown in solid orange.....252

Figure C.5 – OH and OD yields following the Cl-initiated oxidation of $\text{CH}_3\text{OC}(\text{O})\text{D}$. The yield sum is less than 1, which is likely due to a systematic underrepresentation of OD yields.....253

Figure C.6 - Limited experiments determined the overall kinetics of $\text{Cl} + \text{CH}_3\text{OC}(\text{O})\text{D}$, at 294, 423 and 473 K. The fitted line is an Arrhenius temperature-dependent fit:

$$k(\text{Cl} + \text{CH}_3\text{OC}(\text{O})\text{D}) = \left((3.53 \pm 0.51) \times 10^{-11} \right) \times \exp \left(\frac{8098 \pm 522}{RT} \right) \dots\dots\dots 254$$

Figure C.7 – MESMER predicted OH yields are shown in orange circles alongside the experimental OH yields (cyan squares) presented in Chapter 4.....255

Figure C.8 – OH yields following the OH-initiated oxidation of $\text{CH}_3\text{OC}(\text{O})\text{D}$, representing the competition between the internal isomerisation and collisional stabilisation of the $\text{CH}_3\text{OC}(\text{O})\text{OO}^*$ peroxy radical formed following formate abstraction. MESMER predicted OH yields are shown in orange circles alongside the experimental OH yields (cyan squares) presented in Chapter 4.....256

Figure C.9 – OD yields following the OH-initiated oxidation of $\text{CH}_3\text{OC}(\text{O})\text{D}$, representing the competition between the internal isomerisation and collisional stabilisation of the $\text{CH}_3\text{OC}(\text{O})\text{OO}^*$ peroxy radical formed following methyl abstraction. MESMER predicted OD yields are shown in orange circles alongside the experimental OH yields (cyan

squares) presented in Chapter 4. The y-axis is labelled incorrectly and should say 1/(OD yield).....257

Figure D.1 – HNMR for isopropyl formate (CH₃)₂CHOC(O)H purchased from Sigma Aldrich.....258

Figure D.2 – HNMR for isopropyl formate (CH₃)₂CHOC(O)H synthesised in this work, as outlined in Chapter 5.....259

Figure D.3 – HNMR for deuterated isopropyl formate (CH₃)₂CHOC(O)D synthesised in this work, as outlined in Chapter 5. Comparisons of Figures D2 and D3 illustrate the formate hydrogen peak at 7.92 and 7.94 is not present in the deuterated sample shown in this Figure, indicating full deuteration of the formate site.....259

Figure D.4 - OD decay at 433 K, 127 Torr and (CH₃)₂CHOC(O)D = 1.48 × 10¹⁵ molecules cm⁻³.....261

Figure D.5 - OD decay at 433 K, 127 Torr and (CH₃)₂CHOC(O)D = 1.90 × 10¹⁴ molecules cm⁻³.....262

Figure D.6 – Bimolecular plot for the reactions of OH (black squares) and OD (blue circles) with (CH₃)₂CHOC(O)D at 433 K and 127 Torr. Shading represents the 95% confidence limits.....263

Figure D.7 - OD decay at 473 K, 120 Torr and (CH₃)₂CHOC(O)D = 3.84 × 10¹⁴ molecules cm⁻³.....264

Figure E.1 – The overall kinetics of OH + ethyl formate, determined by Dr Lavinia Onel (black squares), alongside literature studies and the recommendation by Eurochamp (purple solid line). The black solid line is a non-Arrhenius temperature-dependent fit to the data shown in the Figure and is used in SAR development in Chapter 6.....265

Figure E.2 – The overall kinetics of tertbutyl formate determined in this work (in collaboration with Dr Lavinia Onel and master's student Owen Dudman). The temperature-dependence has been updated to a non-Arrhenius equation (solid black line) fitting the data shown in the Figure and is used in SAR development in Chapter 6.266

Figure E.3 – OH yields following the OH-initiated oxidation of tertbutyl formate determined as a function of added oxygen at 453 K and 5, (black squares), 20 (blue squares).....24

circles), 30 (purple triangles) and 40 (green triangles) Torr. OH yields are independent of added oxygen, indicating $(\text{CH}_3)_3\text{COC}(\text{O})$ thermally decomposes at this temperature and cannot be captured by reaction with oxygen.....267

Figure E.4 – Branching ratios for methyl abstraction following OH + tertbutyl formate. As there are only two reaction sites in tertbutyl formate, when $(\text{CH}_3)_3\text{COC}(\text{O})$ thermally decomposes, OH yields can be attributed to methyl abstraction. At 420 and 450 K, branching ratios are determined from the Stern-Volmer intercept. Other branching ratios come from the thermalised RO_2 above 120 Torr.....268

Figure E.5 – Transition state structures for OH + tertbutyl formate have been determined at the M062X/6-31+G** level of theory. The left figure shows the transition state for formate abstraction which has a transition state energy of 1.71 kJ mol^{-1} . The transition state for methyl abstraction has two conformers with energies 8.86 kJ mol^{-1} and $-1.45 \text{ kJ mol}^{-1}$. The higher energy conformer is shown on the right hand side in this Figure. Hydrogen bond interactions are illustrated via dashed lines.....268

Figure E.6 – This work determined the temperature dependence of OH + n-butyl formate between 232 and 605 K. Shown here in black squares alongside literature values and the Eurochamp recommendation, used in SAR development in Chapter 6..269

Figure E.7 – OH and OD-initiated reactions of n-butyl formate determined in this work between 232 and 605 K. Solid lines represent non-Arrhenius temperature-dependent fits.....270

Figure E.8 – The positive secondary KIE ($k_{\text{OH}}/k_{\text{OD}}$) indicates OH/OD is partaking in the transition state.....271

Figure E.9 – Transition state for the internal isomerisation of $\text{CH}_3\text{CH}_2\text{CH}_2\text{CH}(\text{OO})\text{OC}(\text{O})\text{H}$, obtained at the M062X/6-31+G** level of theory.....272

List of Tables

Table 1.1 – Substituent factors for a range of functionalities from Kwok and Atkinson [21] and Jenkin et al. [15].....	52
Table 2.1 – Gas correction factors for various esters calculated via E2.19.....	72
Table 3.1 – Room temperature rate coefficients in the literature and this work for OH + methyl formate.....	81
Table 3.2 – The KIE for OH + methyl formate and other organic molecules.....	92
Table 3.3 – Barrier heights (<i>ab initio</i> calculated) for each isotopomer of methyl formate.....	101
Table 3.4 – Branching ratios for the reaction of OH + CH₃OC(O)H calculated by MESMER for methyl and formate abstraction.....	101
Table 4.1 – Barrier heights for the internal isomerisation of RO₂ radicals to QOOH following OH-initiated oxidation of CH₃OC(O)H at the methyl and formate abstraction sites. <i>ab initio</i> and fitted barriers determined in this work are compared with the work of Yang et al. [22].....	131
Table 5.1 – Hydrogen bond and hydrogen bond interaction distances in the transition states for abstraction from the formate, tertiary and methyl sites in isopropyl formate.....	157
Table 5.2 - Barriers for internal isomerisation of the thermalised RO₂ radicals formed following abstraction from the formate, methyl and tertiary sites in isopropyl formate..	170
Table 5.3 - Barriers for internal isomerisation of the thermalised RO₂ radicals formed following abstraction from the methyl and formate sites in methyl formate.....	171
Table 5.4 – Branching ratios for tertiary abstraction as a function of temperature calculated from the yield average of OH yields for a given temperature. OH yields were determined from biexponential decays in the absence of added oxygen above 120 Torr.....	173

Table 6.1 – Calculated rate coefficients at 298 K for each CH₂ group (k_{CH_2}) in a range of esters (R₁OC(O)R₂).....	194
Table 6.2 – Fixed SAR parameters from Jenkin et al. [15] used in the updated ester SARs.....	199
Table 6.3 – Comparison of ester SAR parameters used by Kwok and Atkinson [21], Le Calve et al. [8] and Jenkin et al. [15], demonstrating how ester SARs have evolved over time.....	200
Table 6.4 – Temperature range and parameters implemented in each SAR.....	203
Table 6.5 – Summary of the experimental temperature-dependent data used in the present work to update the formate SAR. The temperature dependence of each rate coefficient is visualised in Figure 6.12.....	206
Table 6.6 – Site-specific kinetics for OH + methyl formate implemented in the SAR.....	207
Table 6.7 – Site-specific kinetics for OH + ethyl formate implemented in the SAR.....	209
Table 6.8 – Site-specific kinetics for OH + isopropyl formate implemented in the SAR.....	210
Table 6.9 – Site-specific kinetics for OH + tertbutyl formate implemented in the SAR.....	211
Table 6.10 – Sum of the squared residuals (SSR) for each SAR in the present work.....	212
Table 6.11 – Substituent factor $F(-OC(O)H)$ values for different SARs.....	217
Table B.1 – Oxygen quenching factors of OH.....	242
Table B.2 – Branching ratios for the reaction of Cl with (CH₃)₃COOH. At 294 K the average is 0.18 ± 0.03 and at 423 K 0.32 ± 0.06, errors are at the 1 σ level.....	247
Table E.1 – Transition state structures for the reaction of OH with n-butyl formate, following abstraction from each reactive site labelled C₁ – C₅, beginning at the formate site. Only the lowest energy conformers are presented.....	272
Table E.2 – Transition state structures for the internal isomerisation of RO₂ radicals to QOOH, following abstraction at each reaction site.....	274

List of Abbreviations

VOC	Volatile Organic Compound
NMVOC	Non-Methane Volatile Organic Compound
VCP	Volatile Chemical Product
SAR	Structure Activity Relationship
MCM	Master Chemical Mechanism
TST	Transition State Theory
LIF	Laser Induced Fluorescence
KIE	Kinetic Isotope Effect
MFCs	MultiFunctional Compounds
MESMER	Master Equation Solver for Multi-Energy Well Reactions
PES	Potential Energy Surface
BDE	Bond Dissociation Energy
RRKM	Rice Ramsperger Kassel Marcus
DFT	Density Functional Theory
QOOH	Hydroperoxy Alkyl Radical
HOMs	Highly Oxidised Molecules
SOA	Secondary Organic Aerosol
PAN	Peroxyacyl nitrates
NMR	Nuclear Magnetic Resonance
GIE	Geometric Isotope Effect

Chapter 1 Introduction

1.1. Introduction

Esters (ROC(O)R) are a class of organic compounds released directly into the atmosphere from their use as biodiesels, sustainable solvents and from volatile chemical products (VCPs). Esters are also formed *in situ* following the atmospheric oxidation of ethers and in peroxy radical recombination reactions. The dominant atmospheric loss process for esters is the reaction with the OH radical. Depending on the initial site of attack, esters have very different atmospheric impacts. For example, the reaction of OH with methyl formate ($\text{CH}_3\text{OC(O)H}$) can proceed via reaction at the methyl (Figure 1.1, purple) or formate (Figure 1.1, blue) site. Hydrogen abstraction by OH at the formate site leads to carcinogenic formaldehyde (HCHO), whilst abstraction at the methyl site leads to formic acid (HC(O)OH) and formic acid anhydride (HC(O)OC(O)H). Organic acids such as formic acid contribute to the acidity of clouds and rainwater and the formation of aerosols, consequently impacting the climate. Organic acids and aldehydes (formaldehyde) have very different atmospheric impacts. As ester emissions are likely to increase, it is important to determine the overall and site-specific kinetics of esters to understand their atmospheric fate.

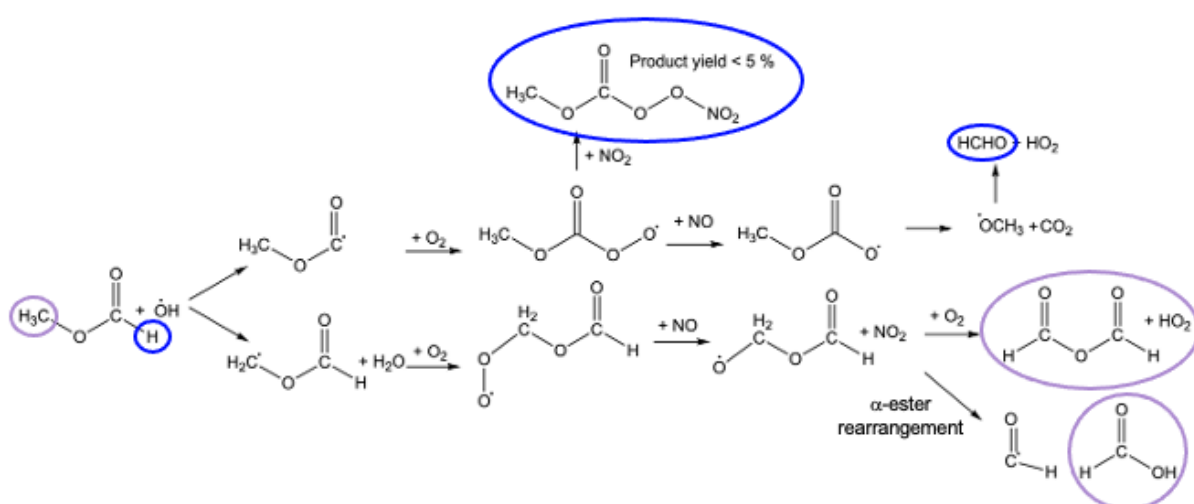


Figure 1.1 – The atmospheric oxidation of methyl formate. Depending on the initial reaction site, the atmospheric impact is very different.

Despite their increasing importance, there are not many site-specific kinetics available in the literature for the reactions of OH radicals with esters. Consequently, the atmospheric impact of increasing ester emissions is highly uncertain. This work experimentally determines the site-specific kinetics of formate esters and improves our understanding of ester reactivity.

1.2. What is atmospheric chemistry and why is it important?

The Earth's atmosphere is a layer of gas between 0 and ~ 1000 km described by five characteristic layers: the troposphere (0 – 12 km), stratosphere (12 – 50 km), mesosphere (50 – 80 km), thermosphere (80 – 1000 km) and the exosphere (above 1000 km). Atmospheric chemistry aims to understand how molecules are chemically transformed and influence the atmosphere. In an elegant symbiotic relationship, the atmosphere sustains life on Earth. Oxygen released from photosynthesis is converted into ozone via R1.1 – R1.2, creating the stratospheric ozone layer. Absorbing at 200 – 300 nm, the stratospheric ozone layer shields the atmosphere below from UV radiation, facilitating life on land [23].



The density of the atmosphere also creates a habitable pressure of ~ 760 Torr at sea-level. The fragility of life on Earth caused by changes in the atmosphere has been exemplified since the industrial revolution. In 1856, Eunice Newton Foote discovered the greenhouse effect [24]. Molecules such as CO₂ absorb infrared radiation emitted from the surface of the Earth and re-emit it back to Earth increasing the surface temperature. Since 1850 annual CO₂ emissions have increased from 196.85 million tonnes to 37,790 million tonnes (37.79 billion tonnes) in 2023 [25]. Increased surface temperatures have led to droughts which affect the ability to grow food, increases in disease, species losses, the acidification of the ocean as it absorbs excess CO₂ and many other impacts. The increase in CO₂ emissions is driven by anthropogenic activity, primarily the burning of fossil fuels. Replacing fossil fuel-derived products with sustainable alternatives is a key requirement to reduce greenhouse gas emissions.

1.3. Esters as a sustainable petrochemical alternative

Esters (Figure 1.2) are a sustainable alternative to many fossil fuel products as they can be made from organic waste [26]. Whilst esters such as fatty acid methyl esters (FAMES) can already be made from organic waste, such as the transesterification of oils and fats, catalysts are required to increase the efficiency, selectivity and cost-effectiveness required for widespread industry use [27]. The development of microbial cell factories (engineered microorganisms) is a promising technology for the processing of renewable biomass into esters [28, 29]. The most significant challenge in developing candidates for metabolic engineering is the selectivity of host strains for the target chemical [30]. However, technological breakthroughs in bioengineering, such as CRISPR (Clustered Regularly Interspaced Short Palindromic Repeats), are making the development of microbial cell factories more efficient [31]. Consequently, as converting biomass into esters becomes easier, the use of esters as sustainable chemicals may increase.

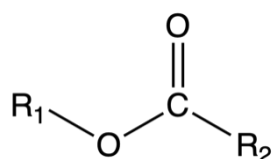


Figure 1.2 – Molecular structure of an ester. When R₂ = H, the ester is a formate.

1.4. Sources of esters and volatile organic compounds (VOCs)

Esters are a category of volatile organic compound (VOC), named non-methane VOCs (NMVOCs). VOCs are carbon-based compounds released into the atmosphere from anthropogenic and biogenic sources. Characterised by their high volatility, VOCs evaporate at typical room temperatures and atmospheric pressures. VOCs released from anthropogenic sources are released directly from human activity, including, but not limited to, combustion (from transport and fossil fuel power plants), solvent usage, industrial processes and consumer products. Due to the damaging health effects of VOCs such as benzene and 1,3-butadiene, the UK imposed specific concentration limits [32]. With increased policies targeting vehicular emissions, fossil fuel usage is no longer the largest source of anthropogenic VOCs in the UK, Los Angeles, and Paris. Instead, solvent usage is the largest VOC emitter [32, 33]. NMVOC emissions from solvent use contributed ~40%

of UK emissions in 2022 [34]. Despite policies aiming to reduce society's reliance on fossil fuels, the demand for petrochemical products is increasing. Emissions from VCPs (pesticides, coatings, cleaning products, personal care products, etc.) contribute to half of the fossil fuel VOC emissions in industrialised cities [35]. In the UK, emissions from solvents specifically used in consumer products, e.g. aerosols, detergents and fragrances, have increased and contribute nearly ~25% of UK NMVOC emissions [34].

1.4.1. Direct emissions of esters

Esters are released directly into the atmosphere from anthropogenic sources. The use of esters as solvents, flavourings and fragrances means they can be found in a wide range of VCPs, ranging from hand soap to paint. However, emissions from VCPs are difficult to constrain due to a lack of measurements of VOCs in consumer products [35]. In speciated inventories of VCPs such as McDonald et al. [35], methyl acetate, ethyl acetate, vinyl acetate, propyl acetate, isopropyl acetate, n-butyl acetate and isobutyl acetate, are specified esters. However, the ester functionality is also present in multifunctional compounds such as texanol (Figure 1.3). Fundamental studies to understand how the ester functionality impacts reactivity are important in determining the atmospheric impacts of esters, and the atmospheric fate of multifunctional compounds containing an ester functional group.

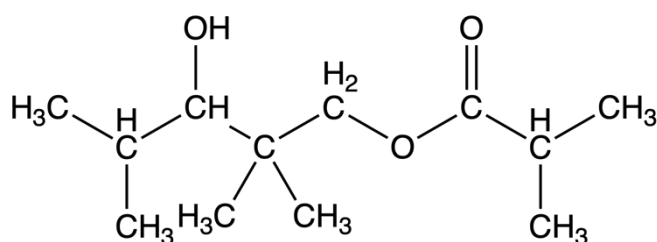


Figure 1.3 – Molecular structure of texanol, a coalescent in latex paints [1].

Esters are also used as fuel additives and biodiesels, releasing long chain esters such as methyl stearate ($\text{CH}_3(\text{CH}_2)_{16}\text{C}(\text{O})\text{OCH}_3$) into the atmosphere. Methyl formate has also been proposed as an efficient hydrogen carrier [36]. Consequently, esters may play a role in green energy production. The global emission of esters in

2022 was estimated to be 1,312 Gg in the EDGARv8.1 dataset [37]. Comparatively, the 2022 estimated global emissions of alcohols and ethers are 11,757 Gg and 1,171 Gg, respectively. EDGAR estimates speciated emissions by functional group from activity data, emission factors and abatement measures.

1.4.2. *In situ* formation of esters in the atmosphere

Esters are also formed *in situ* in the atmosphere following the atmospheric oxidation of ethers. For example, methyl formate is formed with a $(90 \pm 8)\%$ yield following the Cl-initiated oxidation of dimethyl ether [38]. The production of esters following the atmospheric oxidation of ethers is illustrated in Figure 1.4. Multifunctional esters are also formed following the atmospheric oxidation of multifunctional ethers, such as glycol ethers [39].

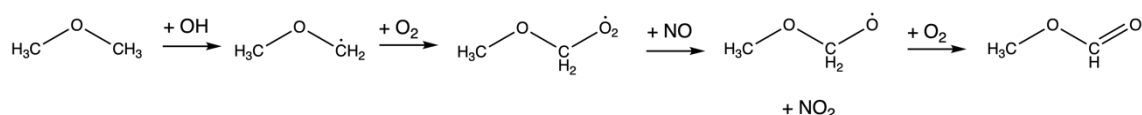


Figure 1.4 – The atmospheric oxidation of dimethyl ether produces methyl formate as the dominant product [2]. Hydrogen abstraction by the OH radical adjacent the ether functionality (the dominant reaction site) typically leads to the formation of esters, as exemplified by the oxidation mechanism of dimethyl ether.

Another *in situ* source of esters into the atmosphere is via peroxy radical recombination reactions ($\text{RO}_2 + \text{RO}_2$). It was previously thought that the only accretion products from RO_2 reactions were peroxides, ROOR . However, Peräkylä et al. [40] found a reaction channel for an α -pinene derived complex ($\text{C}_{10}\text{H}_{15}\text{O}_2\text{O}-\text{OC}_{10}\text{H}_{15}\text{O}_2$) where one of the alkoxy radicals underwent rapid β -scission producing an ester accretion product, $\text{C}_{19}\text{H}_{28}\text{O}_5$. Further work by Franzon et al. [41] determined endocyclic β -scissions are most competitive, leading to ester and ether products with the same mass as ROOR . Due to having the same mass, previous field experiments with mass spectrometry were not able to resolve the structure.

1.5. VOC oxidation

Once released into the atmosphere, VOCs can undergo a series of chemical transformations typically initiated by radical oxidation. VOCs can also undergo photo-induced oxidation and deposition. Esters are primarily oxidised in the atmosphere by OH. Oxidation occurs at multiple reactive sites within the VOC. Depending on the VOCs structure, the reaction mechanism differs. For saturated VOCs that contain no C=C double bonds, OH-initiated oxidation proceeds via hydrogen abstraction. OH abstracts a hydrogen atom from C-H bonds to form water (H₂O) and a carbon centred radical (R1.3).



The rate of a reaction can be described by the concentration of reactants and the rate coefficient. The rate coefficient is a proportionality constant relating the rate of a reaction with the concentration of species involved. The overall rate coefficient (*k*) for the reaction of esters with OH can be considered as the sum of the site-specific rate coefficients, which represent the reaction at each reactive site within a molecule. The overall rate coefficient for the smallest ester, methyl formate (CH₃OC(O)H), can be described as the sum of hydrogen abstraction at the methyl and formate sites (E1.1).

$$k(\text{OH} + \text{CH}_3\text{OC(O)H}) = k(\text{CH}_3\text{OC(O)}) + k(\text{OC(O)H}) \quad \text{E1.1}$$

From the overall rate coefficient, the atmospheric lifetime (τ) of a molecule can be calculated (E1.2). Atmospheric lifetimes are determined by the rate of a reaction and the concentration of OH. This work uses an average OH concentration of $\sim 1 \times 10^6$ molecule cm⁻³ to calculate atmospheric lifetimes of esters.

$$\tau = \frac{1}{k[\text{OH}]} \quad \text{E1.2}$$

Understanding a molecules atmospheric lifetime is a key tool in atmospheric chemistry as it contributes to understanding a molecules atmospheric fate. From the lifetime, the distance a molecule might travel before being oxidised can be calculated. Understanding where/when a molecule may be oxidised is important for predicting atmospheric conditions, products formed and health/climate impacts.

For example, the global warming potential of greenhouse gases such as methane (CH₄) are determined from their atmospheric lifetimes and their radiative potentials.

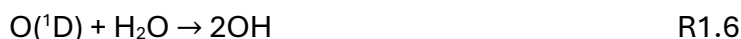
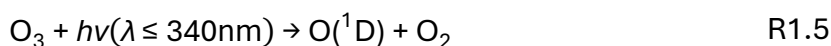
1.5.1. Sources of atmospheric oxidants

The dominant atmospheric oxidant is the hydroxyl radical, OH. However, oxidation can also be initiated by other species such as halogens (Cl, Br etc.), NO₃, O₃ and HO₂. Often described as the ‘detergent of the atmosphere’, OH controls most tropospheric oxidation through the removal and cycling of almost all trace gases: CH₄, CO, O₃ and NO_x, and has a mixing ratio around ~ 0.04 pptv and a concentration of ~ 1 × 10⁶ molecule cm⁻³ [42, 43]. This control makes the atmospheric lifetimes of VOCs largely dependent on the concentration of OH and the rate coefficient for the reaction of OH with that VOC [43].



$$\text{Reaction rate} = k[\text{OH}][\text{VOC}] \quad \text{E1.3}$$

OH is primarily formed when ozone is photolysed at wavelengths less than, or equal to, ~ 340 nm. This produces an excited oxygen atom, O(¹D) which, in competition with collisional relaxation to O(³P), reacts with water vapour, producing OH [44].



Nicely et al. [44] found that 33% of tropospheric OH is formed via this primary pathway (R1.5 – R1.6) and the remainder is due to reactions that recycle OH. The regeneration of atmospheric oxidants, such as OH, plays a key role in sustaining the oxidising capacity of the atmosphere and is often the dominant source of OH. Figure 1.5 illustrates the importance the cyclic role HO_x (HO_x = HO₂ + OH) plays in VOC oxidation.

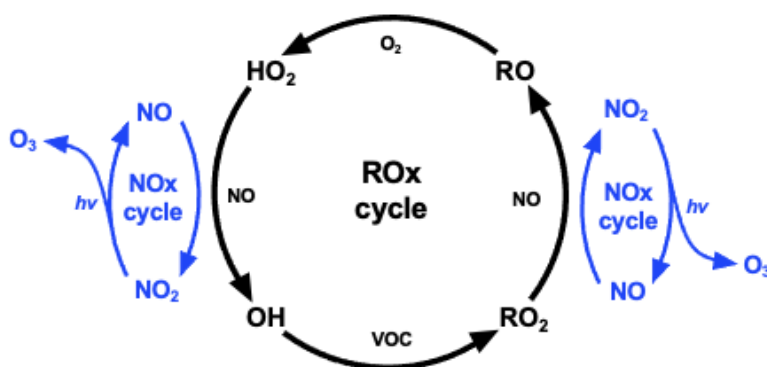


Figure 1.5 – The tropospheric ROx (OH, HO₂ and RO₂) cycle. Reproduced from Liu et al. [3].

1.5.2. VOC oxidation under high NOx conditions

Following initial hydrogen abstraction by OH, a radical (R) is formed alongside H₂O (R1.6). R subsequently reacts with oxygen to form a peroxy radical, RO₂ (R1.7).

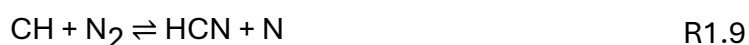


Formation of the peroxy radical represents a key branching point in the mechanism. Depending on the atmospheric conditions, multiple subsequent reactions can occur that will dictate the atmospheric fate of a molecule. VOC oxidation is often characterised by “low NOx” and “high NOx” environments, which influence the peroxy radical fate.

The largest source of NOx is combustion for road transport; NOx is produced thermally or promptly. Thermal production occurs when oxygen atoms are produced at high combustion temperatures and subsequently react with nitrogen to give a net reaction, R1.8.



However, prompt formation is the most likely source of NOx from combustion due to its rapid nature. When hydrocarbon radicals react with nitrogen in the air, they are oxidised via a sequence of reactions R1.9 – R1.11, producing NO.





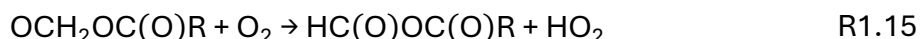
Under high NO_x conditions, RO₂ bimolecular reactions are dominated by their reaction with NO, producing the resultant alkoxy radical, RO (R1.12).



Whilst RO reactions with oxygen are common, the formation of RO represents a significant branching point in the reaction. Typical RO reactions include isomerisation, unimolecular decomposition or reactions with O₂. The branching ratios for RO reactions are critically determined by the structure of RO as well as atmospheric conditions [45, 46]. Hydrogen abstraction by oxygen at another C-H reaction site within the alkoxy radical leads to HO₂, further increasing the oxidising capacity of the atmosphere. For example, the alkoxy radical formed following formate abstraction from methyl formate is CH₃OC(O)O. CH₃OC(O)O decomposes into CH₃O, another alkoxy radical, and CO₂ (R1.13). The reaction of CH₃O with oxygen leads to carcinogenic formaldehyde (HCHO) and HO₂.



Alternatively, the alkoxy radical formed following methyl abstraction from methyl formate is OCH₂OC(O)H. Oxygen addition to OCH₂OC(O)H leads to the formation of an acid anhydride (R1.15). However, due to the ester functionality, the alkoxy radical can also undergo an alpha-ester rearrangement reaction (R1.16) [47].



Illustrated in Figure 1.6, the alpha-ester rearrangement leads to the formation of an organic acid. Experimental studies have shown alpha-ester rearrangement dominates over oxygen addition with increasing size of the adjacent R group [4].

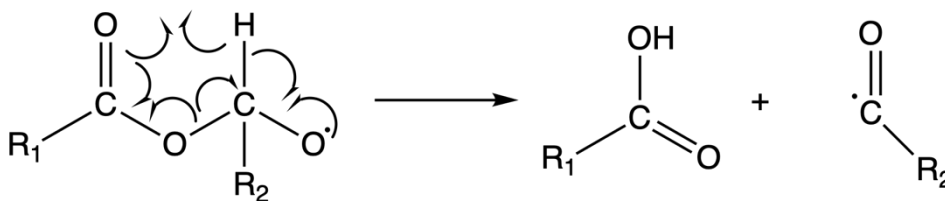


Figure 1.6 – The alpha-ester rearrangement is an example of a unique alkoxy reaction of a functionalised molecule. With increasing R size of the ester, this reaction dominates leading to the formation of an organic acid [4].

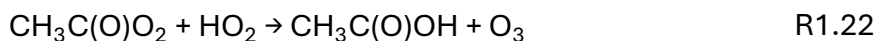
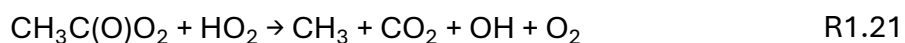
1.5.3. VOC oxidation under low NOx conditions

Low NOx conditions have long been thought to arise where anthropogenic activity is low. However, there are some exceptions where low NOx conditions occur in areas of high anthropogenic activity and high NOx conditions occur in areas of low anthropogenic activity. For example, a study in Beijing discovered VOC oxidation occurring via typically low NOx pathways, due to high afternoon concentrations of ozone suppressing NO formation [48]. Beijing has a dense and growing population so understanding how these reactions impact air quality is increasingly important.

Most prevalent in low NOx conditions are reactions of RO₂ with another peroxy radical. This can be with itself, HO₂, or another RO₂ (R'O₂). Peroxy radicals can also react with OH [49]. Depending on the functionalisation of the peroxy radical, other pathways such as bimolecular reactions are possible. For reactions with HO₂, there are several product channels reported.



Formation of a stable hydroperoxide (ROOH) (R1.17) is the principal reaction, particularly for smaller hydrocarbons such as propane [5, 50]. This was confirmed by Iyer et al. [51] who studied a range of monoterpene derived RO₂ molecules from both OH and O₃ oxidation pathways. They determined the formation of an alkoxy radical (RO) via R1.18, was only feasible for some isomers of RO₂ formed from O₃ oxidation. However, the presence of alkoxy radicals (RO) has been associated with surprisingly high OH concentrations in low NOx environments and it has been postulated that R1.18 contributes to this discrepancy. A comprehensive study by Winiberg et al. [52] on the acetyl peroxy radical (CH₃C(O)O₂) + HO₂ found ratios of R1.20 = 0.37 ± 0.1, R1.21 = 0.51 ± 0.12, and R1.22 = 0.12 ± 0.04.

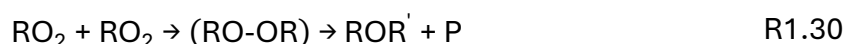


Clearly, R1.18 is more important than initially thought. Functionalisation often results in unexpected chemical pathways. For $\text{CH}_3\text{C}(\text{O})\text{O}_2$, this leads to the production of another radical (RO) and the recycling of OH (R1.21), further increasing the atmosphere's oxidising capacity.

Both cross and self-reactions of the RO_2 radical also have multiple reaction pathways with their dominance highly dependent on both the reactant and product formed. Their general schemes are R1.23 – R1.26 and R1.27 – R1.29, respectively [50].



Studies by Franzon et al. [41] and Peräkylä et al. [40] identified another reaction pathway for peroxy radicals, whereby one of the alkoxy radicals ($\text{RO--O}_2\text{--OR}$) undergoes rapid β -scission producing an ester or ether accretion product (R1.30).



For the α -pinene derived ROOR complex, $\text{C}_{10}\text{H}_{15}\text{O}_2\text{O--OC}_{10}\text{H}_{15}\text{O}_2$, $\text{C}_{19}\text{H}_{28}\text{O}_5$ is the ester accretion product (ROR') and CH_2O is the fragmentation product (P). Isomerisation reactions are also more likely to occur in low NO_x conditions and autoxidation (Section 1.6.1) of multifunctional compounds (MFCs) is highly likely (27). These reactions may lead to further oxidation and the formation of highly oxidised molecules therefore contributing to Secondary Organic Aerosol (SOA) formation.

1.6. Highly Oxidised Molecules

The reactions of RO_2 molecules outlined above leads to an increase in the carbon backbone and increased ratios of O:C atoms. As oxygenated functional groups add to the original RO_2 molecule, autoxidation rates (internal isomerisation and oxygen addition) increase leading to the formation of Highly Oxidised Molecules

(HOMs). HOMs were first discovered at night time in the Finnish Boreal Forest as negative ions (35). Chamber studies later identified these as ozonolysis induced α -pinene oxidation products (36). Their discovery filled a substantial discrepancy between laboratory and field measured OH loss rates, attributed to both the initial and subsequent product reactions with OH. Since their discovery, the term HOMs has had varying definitions, the most common being their classification as Extremely Low Volatility Organic Compounds (ELVOCs) with high O:C ratios (37). Bianchi et al. (38) have since defined HOMs by three strict criteria. ‘HOMs’ must be formed via autoxidation, under atmospheric conditions and contain six or more oxygen atoms. Bianchi has explicitly defined the required number of oxygen atoms so that molecules such as $C_2H_4O_2$ with a high O/C ratio are not defined as HOMs. Figure 1.7 is an illustrative example partitioning HOMs and their parent compounds, peroxy radical isomerisation products, by their approximate volatilities. As Figure 1.7 demonstrates, whilst HOMs primarily fall into ELVOCs, they are no longer defined as such and can also be LVOC and in some cases, Semi Volatile Organic Compounds (SVOC).

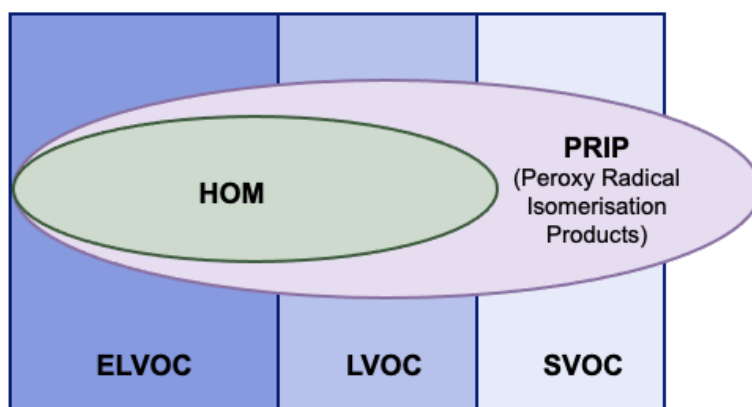


Figure 1.7 - The approximate partitioning of HOMs and Peroxy Radical Isomerisation Products (PRIP) by their volatilities. Reproduced from Bianchi et al. (38).

1.6.1. Autoxidation

Autoxidation is a sequential mechanism involving an internal isomerisation, hydrogen shift and oxygen addition. Under combustion conditions, where temperatures are greater than 500 K, oxidation is typically initiated by O_2 and autoxidation has a higher degree of repetition, forming a higher molecular weight

RO₂. Under atmospheric conditions, competing bimolecular reactions can terminate autoxidation, excluding the production of RO radicals, which can also undergo oxygen addition. The degree of repetition, and thus degree of oxidation, is dependent on the reaction conditions (temperature and pressure), concentration of competing species (such as NO) and the specific RO₂ structure [53]. Factors that lower the energy barrier to hydrogen shifts increase autoxidation and hence HOM formation. Activating substituents, such as OH, can aid isomerisation by forming hydrogen bonds that stabilise transition states. Further stabilisation of the radical products through hydrogen bonds can also make reverse reactions less likely. Furthermore, hydrogen bond interactions can weaken adjacent C-H bonds, increasing their likelihood of abstraction [54]. Through these effects, a molecule containing activating substituents is more likely to form HOMs. However, Wang et al. [53] highlighted the role alkanes play in HOMs and SOA formation via RO and RO₂ autoxidation pathways. Even for molecules with fewer substituents, autoxidation is a key formation mechanism of HOMs in the atmosphere. Figure 1.8 demonstrates the OH-initiated autoxidation mechanism of a ketone [5].

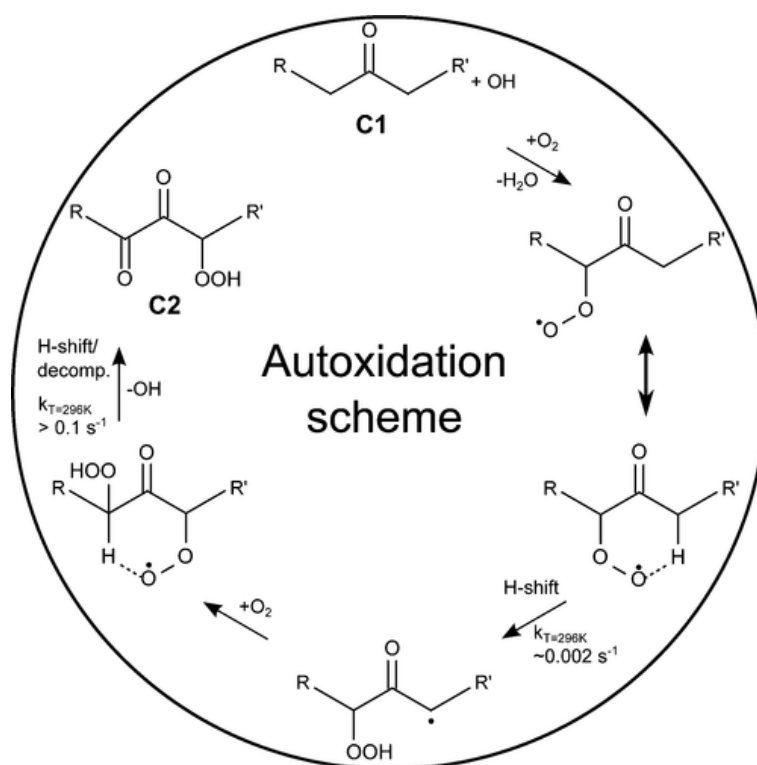


Figure 1.8 – General autoxidation scheme. Reproduced from Crounse et al. [5].

1.7. Secondary Organic Aerosols

The formation of SOA occurs via the atmospheric oxidation of organic matter and is intimately interlinked with volatility. Reactions leading to low volatility products are more likely to lead to SOA formation. Hydrogen bonding between polar functional groups such as alcohols (OH), formates (OC(O)H), esters (OC(O)R) and nitrates (ONO₂) decreases their volatilities. MFC volatilities are further reduced due to the retention of their carbon backbone. Condensation into the particle phase represents a new classification of reactions that also have a fundamental impact on the evolution and growth of SOA. Also pertinent to the description of SOA formation is the role of multi-generational chemistry, whereby the evolution of MFCs, and other organics, can influence SOA formation over many generations of oxidation reactions. As side products and their reactions increase with increasing functionality, mechanisms of SOA formation become increasingly harder to characterise [55].

The role of oxygenated VOCs in SOA formation is highly uncertain. Li et al. [56] studied SOA formation in the presence of NO_x from a range of oxygenated VOCs classed with intermediate volatilities, including molecules containing the ester functionality: dipropylene glycol methyl ether acetate (DPGMEA), dimethyl glutarate, texanol, glyceryl triacetate and methyl palmitate. Intermediate volatility compounds are exempt from many regulations as their evaporation into the atmosphere is thought of as insignificant. However, Li et al. [56] found over half of the studied VOCs lost more than 95% of their mass within one month. Of the esters studied, DPGMEA produced the highest mass concentrations of SOA, with delayed SOA formation indicating multi-generation processes. In the presence of H₂O₂, SOA formation increased from all VOCs. Li et al. [56] also measured SOA formation from a range of generic VCPs, observing SOA formation increased. Li et al. [56] postulate additive effects are due to increased sorptive partitioning. Implementing the Li et al. [56] results in a kinetic model, Sasidharan et al. [57] note SOA yields increase linearly with carbon number and estimate oxygenated VOCs are responsible for 25 – 40% of SOA formation from VCPs.

1.8. Multiphase chemistry

VOCs can exist in the gas, aqueous and particle phases. The larger O:C ratios in oxygenated molecules increases their solvation by water due to hydrogen bonding between H₂O and oxygen atoms within the oxygenated molecule. The solubility of a VOC can be expressed as an equilibrium between the gas and aqueous phases (E1.4).



Equilibrium between the gas and aqueous phase can be described by the Henry's law solubility constant (E1.5). H_s^{CP} describes the VOC concentration in the aqueous phase as proportional to the partial pressure of the VOC [58].

$$H_s^{\text{CP}} = \frac{\text{Concentration / M}}{\text{Pressure / atm}} \quad \text{E1.5}$$

Henry's law constants of very soluble gases are around $10^5 - 10^6 \text{ M atm}^{-1}$, whilst very insoluble gases have constants $\sim 10^{-3} - 10^{-4} \text{ M atm}^{-1}$. The Henry's law constants of esters such as methyl formate and ethyl acetate are 4.3 and 6.7 M atm^{-1} . Consequently, partitioning into the aqueous phase is not a dominant loss process for the esters. Organic acids such as formic acid and acetic acid have Henry's law constants of 5.3×10^3 and $6.2 \times 10^3 \text{ M atm}^{-1}$, respectively. Therefore, organic acids are readily solvated by water. Once solvated, organic acids can dissociate into H^+ and RC(O)O^- (R1.31), leading to the formation of acid rain [59].



An interesting study by Emmeline Longnecker [60], looked at the composition of surface films on glass sheets placed inside a university classroom at the University of Colorado Boulder. Surface films were formed from particles from outdoor air and VOCs from indoor and outdoor air. Functional group analysis on the composition of the surface films determined the ester functional group dominated in both day and night experiments. Quoted examples of speciated esters include phthalide, an ester used in food flavouring, and EGDMA, a diester used in plastics and resins. Other examples of molecules found included several organic acids (xylonic acid, sebacic acid and succinic acid), which the presentation speciated as esters. Although uncertainties remain on the contribution of organic

acids and esters, these initial results suggest esters partake in multiphase chemistry and are likely prevalent in indoor air.

1.9. Air quality & climate

Although air quality and climate are often considered two separate issues, as Figure 1.9 demonstrates, they are intrinsically linked. Aerosols impact human health and the climate via direct and indirect effects. Scattering and absorption of radiation are direct effects whilst their influence on cloud properties contributes an indirect effect [61]. SOA contributes to the formation of particulate matter which has negative health impacts, discussed below. Consequently, there is a large interest in understanding the formation, size and number distribution of particles in the atmosphere. One of the dominant oxidation products of esters are organic acids. Due to their high O:C ratios and solubility, organic acids contribute to the formation of SOA. Furthermore, organic acids influence the hygroscopicity of aerosols, impacting their climate effects [62]. Large uncertainties remain as to the impact of organic acids on aerosol hygroscopicity and the climate impacts of aerosols.

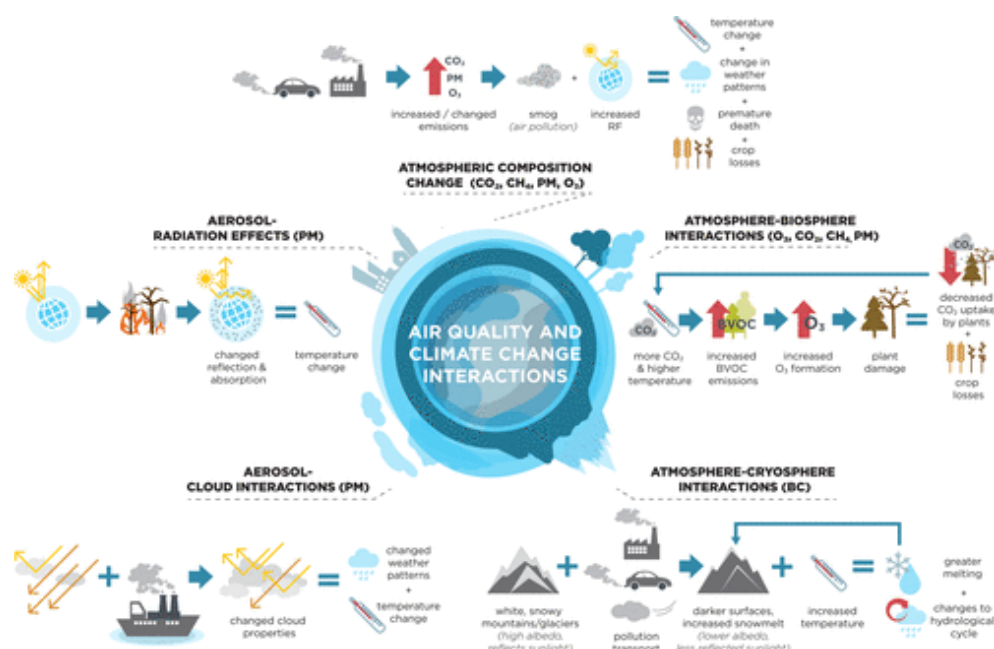


Figure 1.9 – Overview of the interactions between air quality and climate change. Reproduced from von Scheidemesser et al. [6].

Air pollution is defined by the World Health Organisation (WHO) as the “contamination of the indoor or outdoor environment by any chemical, physical or biological agent that modifies the natural characteristics of the atmosphere”. The Air Quality Index (AQI) for a specific location is given by the highest concentration of the pollutants NO_2 , SO_2 , O_3 , $\text{PM}_{2.5}$ and PM_{10} , where PM_x is particulate matter $< x \mu\text{m}$ in diameter. WHO guidelines target the same pollutants as the AQI and carbon monoxide (CO). PM is harmful to human health as inhalation can lead to damaging health problems ranging from neurodegenerative diseases to respiratory problems. The smaller the particles, the more serious the health implications – PM_{10} can get into airways such as the throat, $\text{PM}_{2.5}$ into the lungs, PM_1 into our blood vessels and ultrafine particles $< 0.1 \mu\text{m}$ can get into the blood stream leading to increased inflammation and risk for stroke, Parkinson’s and neurodevelopmental disorders [63].

VOCs have a significant impact on air quality and can contribute to the production of NO_2 , O_3 and particulate matter. VOCs can also have negative impacts on human health. Formaldehyde is carcinogenic and can irritate the nose, eyes and throat and exacerbate respiratory conditions such as bronchitis and asthma. Peroxyacyl nitrates (PANs) have the formula $\text{RC(O)OON}^+(\text{O})\text{O}^-$ and are a class of VOC that are very toxic as they can bind to DNA leading to mutations that can cause skin cancer and damage vegetation. PANs can also irritate the eyes and respiratory tract.

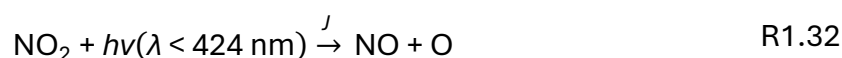
The health impacts of poor air quality are not trivial. Lelieveld et al. [64] estimated global excess mortality from all air pollution sources was between 10.41 and 7.11 million per year. According to the WHO, 99% of the global population breathes air that contains high levels of pollutants, exceeding WHO guideline limits. Poor air quality also comes with an economic cost. In 2022 the World Bank estimated the global cost of poor air quality was \$8.1 trillion US dollars, equivalent to 6.1% of global GDP. Tackling poor air quality has proven health and economic benefits. For example, the Bradford (UK) Clean Air Plan, which included a clean air zone, led to a $11.5 \mu\text{g}/\text{m}^3$ reduction in NO_2 concentrations alongside a decrease in

the number of respiratory and cardiovascular visits, saving the national health service (NHS) an estimated £30,743 per month [65].

As poor air quality from fossil fuels is reduced through the introduction of policies such as clean air zones, poor air quality from oxygenated VOCs is increasing. Indoor air quality is also a major issue as humans typically spend 90% of their time indoors. Sources of indoor air quality include VCPs such as cleaning products, perfumes, etc., cooking emissions and emissions from furniture and clothing. As esters are used as solvents, fragrances and flavourings they are likely to be found in indoor air, as evidenced in the study by Longnecker et al. [60].

1.9.1. Tropospheric ozone formation

One of the major health impacts of VOC oxidation is the formation of tropospheric ozone. Alongside the ROx cycle, Figure 1.5 illustrated the NOx cycle and the role VOCs play in ozone and NOx formation. Under high NOx conditions, the relationship between NO₂ and NO is controlled by reactions R1.32 – R1.35.



With increasing concentrations of NO₂, relative to NO, tropospheric ozone increases. Peroxy radical reactions with NO lead to increasing concentrations of NO₂, relative to NO, and hence increasing concentrations of tropospheric ozone. When NOx concentrations are elevated above ~ 1000 ppt, removal of NO₂ to form nitric acid, HNO₃ dominates the reactions of NO₂. This also leads to a reduction in OH. Consequently, increases in VOC concentrations recycle OH and lead to increases in ozone formation.



1.10. An introduction to Structure Activity Relationships (SARs)

Our knowledge of atmospheric chemistry is small. Although many molecules are present in the atmosphere, the overall kinetics of only a small subset have been measured experimentally. Figure 1.10 illustrates the largest dataset of gas-phase organic molecules in an area proportional Venn diagram with the number of oxidation products produced following the atmospheric oxidation of α -pinene, predicted by the automatic mechanism generator GECKO-A [16]. GECKO-A stands for Generator for Explicit Chemistry and Kinetics of Organics in the Atmosphere, and is an algorithm that predicts possible reaction pathways for a primary molecule (e.g., α -pinene) [66]. GECKO-A follows all reaction intermediates to CO or CO₂ production. The oxidation products of α -pinene contribute a small proportion of our known unknowns. However, the unknown unknowns are likely much larger. This illustrative example, borrowed from McGillen et al. [16], highlights the small proportion of experimentally determined rate coefficients for molecules known to exist in the atmosphere. Due to the large number of gas-phase organic molecules in the atmosphere, it would be impossible to experimentally determine the kinetics of each molecule. Therefore, there is a clear predictive requirement to model and predict atmospheric oxidation mechanisms.

Structure activity relationships (SARs) predict reaction kinetics based on the structure of a molecule. There are many ways to parameterise molecular structure. Consequently, there are many ways to predict reaction kinetics. Vereecken et al. [67] identified four categories of input variables that SARs are built upon:

- The molecular graph
- Molecular properties
- Topological indices
- Quantum chemical data

Unknown unknowns

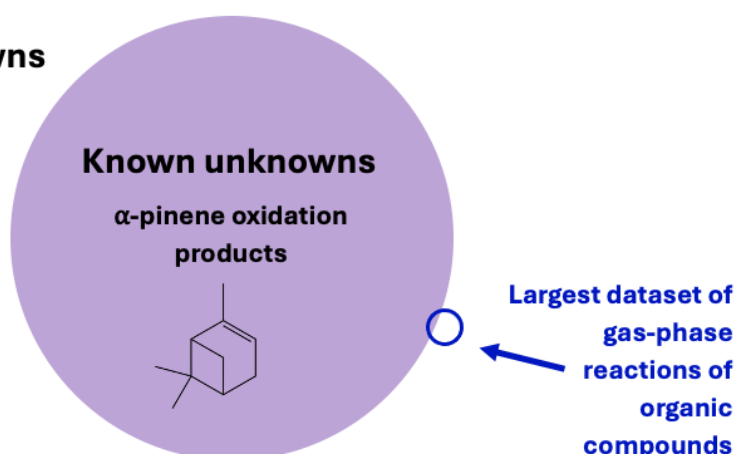


Figure 1.10 – An area proportional Venn diagram demonstrating the overlap between our knowledge of the total rate coefficients for gas phase organic compounds and the species formed in the atmospheric oxidation of α -pinene, predicted by the automatic mechanism generator GECKO-A. “Known unknowns” refers to species whose rate coefficients have not been experimentally determined, however the species is predicted to form following α -pinene oxidation. “Unknown unknowns” refers to the species unknown to form in the atmosphere, for example through unknown pathways not currently considered in mechanism generators such as GECKO-A. The figure is adapted from McGillen et al. [7].

The molecular graph describes the chemical structure of a molecule, with atoms as nodes and bonds as edges. Chemical graph theory is an adaptation of graph theory to characterise molecular structure. However, graph theory gets its name from the “graphical notation” used to describe chemical structure [68]. In graph theory, graphs are anything with nodes connected by edges. For example, a social network is a type of graph with users as nodes and connections between users, the edges. Graph neural networks, a type of machine learning model, are based on graph theory and are used today in reaction mechanism generators (RMGs). RMGs describe molecules as nodes and the reactions between molecules as edges. This application is not dissimilar to the origin of chemical graphs, which were first used by William Cullen in 1758 to illustrate chemical interactions occurring between molecules [68].

Chemical graph theory encompasses both group additivity and topological indices. Group additivity refers to properties determined from the sum of each

component part. For example, the total rate coefficient can be expressed as the sum of the site-specific rate coefficients. Topological indices are mathematical descriptions of chemical structure. The first topological index was the Wiener Index, calculated by summing the lengths of the shortest paths between all non-hydrogen atoms. One key benefit of topological indices is their reduction of multiple parameters – making SAR development easier. Although topological indices are derived from the molecular graph, Vereecken et al. [67], class topological indices as a distinct group. One reason to emphasise their difference is topological indices are a different interpretation of the molecular graph than group additivity. When referring to SARs based on the molecular graph, Vereecken et al. [67] refer to group additivity SARs. Group additivity SARs are the most widely used in atmospheric chemistry and will be the primary focus of SARs in this thesis. Historically, group additivity has also been used to predict physicochemical properties. However, physicochemical properties are typically molecular by nature.

SARs based on molecular properties such as ionisation potentials, dipoles and electron affinities are problematic as the resultant SAR is not site-specific. Another failing is their applicability to different reaction mechanisms. One property may describe a particular reaction well e.g., OH addition to double bonds yet fail for other reaction mechanisms. Furthermore, properties are often unavailable for MFCs.

Quantum chemical data utilises properties derived from the wavefunction such as HOMO/LUMO energies and atomic charge. Utilisation of the wavefunction is an advantage as molecular properties are incorporated into the SAR more directly. However, as Vereecken et al. [67] point out, a large number of species and hence data are required to develop these SARs which may hinder their adoption. Vereecken et al. [67] place ease of use at the highest importance, thus recommend SARs based on group additivity.

1.10.1. Group additivity SARs

Pioneering works by Atkinson [21, 69] are responsible for the SARs of OH reactions with organic molecules under atmospheric conditions. In an extensive review, Atkinson proposed the first estimations of OH rate constants for hydrogen abstraction reactions from alkanes, carbonyls, alkyl nitrates and the OH addition to alkene, alkyne and aromatic rings [69]. As the reactions in this thesis are primarily hydrogen abstraction reactions by OH, this work will also focus on SARs predicting rate coefficients for OH abstraction reactions. Atkinson derived the general equations E1.6 – E1.8 to predict the rate coefficients of hydrogen abstraction reactions. $F(X)$, $F(Y)$ and $F(Z)$ are the substituent factors to multiply the rate coefficient by, where X, Y and Z are the substituents and k_{prim} , k_{sec} and k_{tert} are the rate coefficients for each CH_3 , CH_2 and CH groups [70].

$$k(\text{CH}_3\text{-X}) = k_{\text{Prim}}F(X) \quad \text{E1.6}$$

$$k(\text{Y-CH}_2\text{-X}) = k_{\text{Sec}}F(X)F(Y) \quad \text{E1.7}$$

$$k(\text{X-CH(Z)-Y}) = k_{\text{Tert}}F(X)F(Y)F(Z) \quad \text{E1.8}$$

As these equations demonstrate, SARs are inherently site-specific. The overall rate coefficient is the sum of each site-specific rate coefficient. Furthermore, where additional reaction mechanisms occur, the overall rate coefficient is the sum of each. For example, a molecule that has a double bond and suitable hydrogens for abstractions has a k_{total} :

$$k_{\text{total}} = k(\text{H-atom abstraction}) + k(\text{OH addition to C=C})$$

The primary, secondary and tertiary rate coefficients used in SARs originate from kinetic studies of deuterated isotopomers. Deuterated studies of methane and ethane experimentally determine k_{Primary} , which was then used to determine $k_{\text{Secondary}}$ in deuterated studies of propane. These studies are outlined in detail in Chapter 2 which describes the Kinetic Isotope Effect (KIE). Because deuterated studies probe site-specific reactivity, they are a complementary technique used alongside SAR development to advance our understanding of ester reactivity, with a focus on site-specific kinetics.

Substituent factors ($F(X)$) represent the change in activation energy due to added functionality. Figure 1.11 qualitatively demonstrates the reduction in activation energy for methanol (blue) compared with methane (purple). Addition of the alcohol group lowers the activation energy and consequently, the rate coefficient for $k(\text{OH} + \text{CH}_3\text{OH})$ is faster than $k(\text{OH} + \text{CH}_4)$. The SARs of Atkinson et al. [69] use an Arrhenius temperature dependence for both k_{Primary} , $k_{\text{Secondary}}$ and k_{Tertiary} . The substituent factor also utilises an Arrhenius temperature dependence, however, the activation energy is replaced by the change in energy due to the functionality. Equations E1.9 and E1.10 are the temperature dependent SAR expressions for $k(\text{OH} + \text{CH}_4)$ and $k(\text{OH} + \text{CH}_3\text{OH})$, respectively.

$$k(\text{H}-\text{CH}_3) = A \times \exp \frac{E}{RT} \quad \text{E1.9}$$

$$k(\text{H}-\text{CH}_2\text{OH}) = \left(A \times \exp \frac{E}{RT} \right) \times \left(\exp \frac{\Delta E}{RT} \right) \quad \text{E1.10}$$

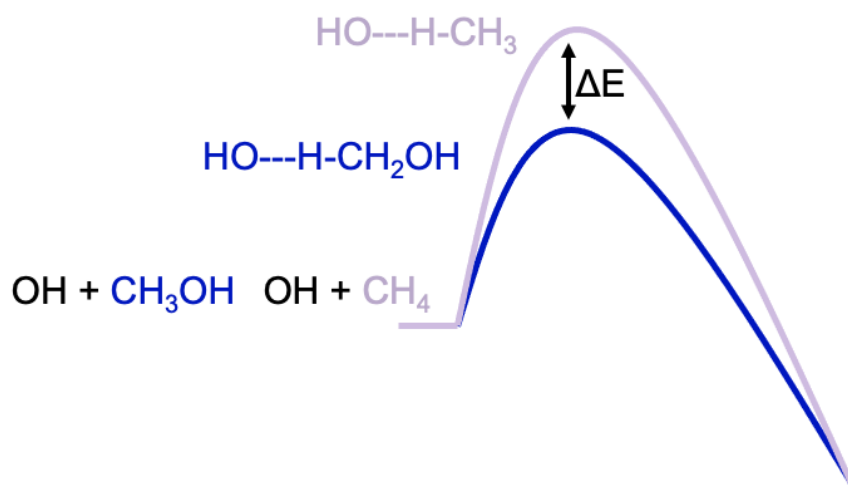


Figure 1.11 – Qualitative energy barriers for the reactions of OH radicals with methane (purple) and methanol (blue). The alcohol functional group in methanol reduces the energy barrier for hydrogen abstraction by OH.

A benefit of the group additivity SAR approach is the physical meaning. E represents the activation energy and ΔE the change in activation energy due to the added functionality. However, molecules that deviate from an Arrhenius temperature dependence, for example oxygenated molecules such as esters, are not as well represented by SARs. Temperature-dependent fits to molecules that exhibit both a negative and positive temperature dependence are empirical. This is due to the incorporation of the parameter n which has no fundamental meaning.

Consequently, SARs which are built upon the Arrhenius form also struggle to capture both the negative and positive temperature dependence in overall rate coefficients. Whilst the range of the temperature curvature varies between oxygenates, this is true for a wide range of oxygenated molecules and is discussed further in Chapter 6.

Table 1.1 – Substituent factors for a range of functionalities from Kwok and Atkinson [21] and Jenkin et al. [15].

Functionality	Kwok & Atkinson	Jenkin et al.
R-OH		3.6
R-O-R	8.4	3.5
R-C(O)-R	0.75	1.0
CH ₂ C(O)-	3.9	3.4
R-OC(O)-R	1.6	2.2
R-OC(O)H	N/A	0.85

1.11. Atmospheric modelling

Atmospheric modelling is described as one of the three pillars of atmospheric chemistry, alongside field measurements and laboratory studies [71]. Due to a growing concern over climate change, tropospheric models of atmospheric chemistry began development in the 1980s. Their predictive capabilities have important applications such as weather forecasting, predicting potential climate scenarios and analysing effective air pollution policies through exposure and health effect modelling. Simulations of atmospheric conditions test our understanding of the atmosphere and aid discovery. Testing our knowledge in this way is how many advancements in the field have originated. One key example of this is OH reactivity. OH reactivity (R1.37, where X_i is a VOC species) combines all OH loss rates [72].

$$\text{Total OH reactivity} = \sum k_{X_i+\text{OH}}[X_i] \quad \text{R1.37}$$

Comparisons of calculated and measured OH reactivity have uncovered large discrepancies in our understanding of OH and VOC chemistry/reactions. Sinha et al. [72] found between (25 – 75)% of OH reactants were missing from calculations in a Boreal forest which they attributed to an accumulation of low VOC concentrations undetectable by the measurement technique proton transfer mass spectrometer (PTR-MS). Large fractions of OH reactivity remain unaccounted, particularly in remote regions such as the Boreal forest. However, OH reactivity comparisons have been used successfully to evaluate the mechanism of isoprene oxidation [73].

The Master Chemical Mechanism (MCM) was first developed by Jenkin et al. [74] for use in any area where a detailed mechanism of chemistry was required. Today the MCM provides information on a wide range of VOC classifications from alcohols and esters to monoterpenes and sesquiterpenes. Mechanisms are based upon individual protocols for each class of compound using experimental rate coefficients and where no experimental data is available, SARs. One of the advantages of the MCM is the detailed nature of the chemical mechanisms. However, due to the computational cost of implementing such a detailed mechanism into three-dimensional climate models, simplified reaction mechanisms are often used. These are developed and tested against explicit mechanisms such as the MCM. As it is not clear within the MCM which rates are estimated and which are based on experimental data, this approach may extrapolate errors in our understanding of atmospheric chemistry into larger models such as GEOS-Chem.

GEOS-Chem is a global 3D tropospheric chemistry model that implements meteorology from the Goddard Earth Observing System (GEOS) [75]. Where possible, GEOS-Chem implements experimental data evaluations such as those from IUPAC and JPL. However, where no experimental data exists, GEOS-Chem refers to the MCM [76]. GEOS-Chem represents a limited number of oxygenated VOCs and does not currently include esters. Plans to include esters follow the typical pattern whereby the smallest molecule (in this case methyl formate) is treated explicitly, and the other esters (C_3+) are lumped and represented

collectively. For C_3+ esters, this will be via the kinetics of ethyl acetate. One of the barriers to incorporating esters into GEOS-Chem is the uncertainty in their emissions.

1.12. Thesis outline

The overall aim of this thesis is to experimentally determine the site-specific kinetics of esters and contribute towards an improved understanding of ester reactivity and their atmospheric impacts. As outlined in this first chapter, there are many sources of esters into the atmosphere, and their emissions are likely to increase on the path to net zero. Whilst studies determining the overall rate coefficient for OH radicals with esters are important to calculate the overall lifetime, without site-specific studies, the ratio of products formed, and hence atmospheric impact, is unknown. This is particularly important for esters, which have very different climate and health impacts depending on the initial reaction site. Despite their increasing importance, there are few site-specific literature studies for the kinetics of OH radicals with esters.

Following an overview of theoretical and experimental methods, in Chapter 2, this work begins by investigating the kinetics of the smallest ester, methyl formate. The site-specific kinetics of OH radicals with methyl formate have not been determined as a function of temperature. Chapter 3 aims to determine methyl formate's site-specific kinetics by measuring the overall rate coefficients for isotopomers $CH_3OC(O)H$, $CH_3OC(O)D$, $CD_3OC(O)H$ and $CD_3OC(O)D$. The reaction sites within methyl formate are determined to be coupled, meaning that deuteration at one site impacts the site-specific kinetics at another. Coupled reaction sites prevent the experimental determination of site-specific kinetics from the overall kinetics of the deuterated isotopomers. Nonetheless, theoretical calculations by Dr Robin Shannon calculate the site-specific kinetics of methyl formate and its deuterated isotopomers.

Chapter 4 aims to experimentally determine the site-specific kinetics of methyl formate. Following hydrogen abstraction, the radicals generated, $CH_3OC(O)$ and $CH_2OC(O)H$, react with oxygen to form peroxy radicals. At low pressure, excited

peroxy radicals, RO_2^* , can undergo chemically activated internal isomerisation reactions to a carbon-centred radical, QOOH , followed by prompt decomposition to OH . Alternatively, RO_2^* radicals undergo collisional stabilisation to the thermalised peroxy radical, RO_2 . This work determined the Stern-Volmer slopes, which describe the ratio of RO_2^* isomerisation and stabilisation. At high temperatures, the $\text{CH}_3\text{OC(O)}$ radical, formed following formate abstraction, undergoes thermal decomposition. Consequently, a reduction in the regeneration of OH is observed and attributed to formate abstraction. The site-specific kinetics are experimentally determined from Stern-Volmer intercepts. This work characterises the Stern-Volmer slopes and intercepts of $\text{CH}_3\text{OC(O)H}$ and $\text{CH}_3\text{OC(O)D}$. Furthermore, above ~ 500 K the thermalised peroxy radicals, RO_2 , have enough energy to overcome the energy barrier to internal isomerisation and decomposition to OH . Yields of OH above 500 K from high pressure OH decays provide further experimental determination of the site-specific kinetics of methyl formate.

To expand our understanding of ester reactivity beyond the smallest ester, this work also determines the site-specific kinetics of isopropyl formate ($((\text{CH}_3)_2\text{CHOC(O)H})$) with the OH radical. Combining the techniques outlined in Chapters 3 and 4, Chapter 5 determines the overall kinetics of $\text{OH/OD} + ((\text{CH}_3)_2\text{CHOC(O)H})$ and $((\text{CH}_3)_2\text{CHOC(O)D})$. Chapter 5 determines site-specific kinetics from Stern-Volmer intercepts at high temperatures where $(\text{CH}_3)_2\text{CHOC(O)}$ undergoes thermal decomposition and from OH regeneration following the internal isomerisation and decomposition of thermalised peroxy radicals. The experimental OH yields are attributed to tertiary abstraction following characterisation of the potential energy surface at the M062X/6-31+G^{**} level of theory.

Chapter 6 combines the experimental site-specific kinetics of methyl formate (Chapters 3 and 4) and isopropyl formate (Chapter 5) alongside the experimental site-specific kinetics of ethyl formate (determined by Dr Lavinia Onel), tertbutyl formate (overall kinetics were also determined by Dr Lavinia Onel and Owen Dudman) and n-butyl formate. Comparing the site-specific kinetics of the formates clearly indicates that formate abstraction is dependent on the adjacent R

group. Chapter 6 provides an overview of ester reactivity and critically evaluates whether group additivity SARs are adequate to predict the site-specific kinetics of oxygenated molecules such as esters. An updated group additivity SAR is presented, which leads to significant improvements in formate reactivity over current SARs. Finally, alternative SAR approaches and suggestions for future work are proposed.

Chapter 2 Chemical kinetics theory and experimental methods

2. Reaction kinetics

Reaction kinetics describes the rate of a reaction. For a unimolecular reaction (R2.1), the change in the concentration of reactant, [A], with respect to time, t , is described by E2.1, where k_{Uni} is the unimolecular rate coefficient.



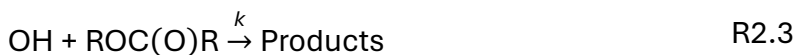
$$\frac{d[A]}{dt} = -k_{\text{Uni}}[A] \quad \text{E2.1}$$

The unimolecular reaction, R2.1, is a first order reaction, with the order of a reaction calculated from the exponents of the reactants. For a bimolecular reaction (R2.2), the change in reactant A is described by E2.2 and the reaction is second order.



$$\frac{d[A]}{dt} = -k_{\text{Bi}}[A][B] \quad \text{E2.2}$$

Where this work determines bimolecular rate coefficients, pseudo-first order conditions are utilised. Pseudo-first order conditions occur when the concentration of one reactant is in excess such that its concentration remains effectively constant during the reaction. For the reactions of OH radicals with esters (R2.3), this work uses pseudo-first order conditions with the ester in excess, approximately 2 – 3 orders of magnitude above the concentration of OH. Ester concentrations are approximately $(1 - 10) \times 10^{15}$ molecule cm^{-3} whilst OH concentrations are approximately 1×10^{12} molecule cm^{-3} .



$$\text{Reaction rate} = -\frac{d[\text{OH}]}{dt} = k[\text{OH}][\text{ROC(O)R}] \quad \text{E2.4}$$

$$k' = k[\text{ROC(O)R}] \quad \text{E2.5}$$

$$-\frac{d[\text{OH}]}{dt} = k'[\text{OH}] \quad \text{E2.6}$$

Under pseudo-first order conditions the reaction rate can be described by the pseudo-first order rate coefficient, k' outlined in E2.4 – E2.6. Integrating E2.6 produces E2.7 which describes the concentration of OH as a function of time.

$$[\text{OH}] = [\text{OH}]_0 \times \exp(-k't) \quad \text{E2.7}$$

OH decay traces can be fit with a single exponential decay (E2.7) to extract the pseudo-first order rate coefficient for a given concentration of ester. Determining the pseudo-first order rate coefficient for multiple concentrations of an ester allows the bimolecular rate coefficient to be determined via a plot of E2.5.

2.1. Temperature-dependent reaction kinetics

Interactions between two molecules, A and B, can be described by the potential energy surface (PES). As the distance between A and B varies, their interactions can be attractive and repulsive, with attractive interactions lowering the energy and repulsive interactions increasing the energy. As polyatomic systems have many coordinates ($3N-6$), that are hard to visualise simultaneously, the PES typically follows the reaction coordinate which connects the reactants and products via the minimum energy path.

The Arrhenius equation (E2.8) was developed by Svante Arrhenius in 1889, who observed the rate coefficient for a range of reactions increased as a function of temperature and followed the relationship outlined in E2.8 [77].

$$k = A \times \exp\left(\frac{-E_a}{RT}\right) \quad \text{E2.8}$$

The Arrhenius parameter, A , is the pre-exponential factor, E_a is the activation energy (the difference between the maximum on the PES and the reactants), R is the gas constant ($\text{J K}^{-1} \text{mol}^{-1}$) and T is temperature (K). A plot of $\ln(k)$ against $1/T$ is linear with an intercept equal to A and a slope equal to E_a (E2.9).

$$\ln k = \ln A - \frac{E_a}{RT} \quad \text{E2.9}$$

Figure 2.1 demonstrates a PES for a reaction with an energy barrier that follows the Arrhenius equation. At X^\ddagger the electron clouds of each reactant molecule repel each other producing a high energy state. Furthermore, during a reaction, bonds are typically broken, and new bonds are formed. The energy required to break a bond intuitively explains the reason for an energy barrier such as the one shown in Figure 2.1. As the temperature increases, more thermal energy is available to the reactants and proportionally more molecules have enough energy to overcome the energy barrier. Therefore, the rate coefficient increases as a function of temperature.

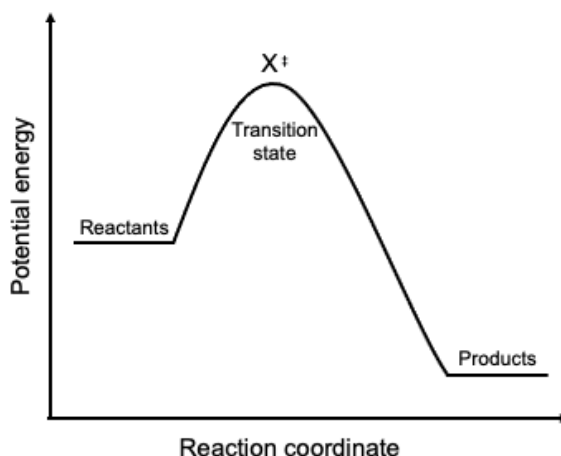


Figure 2.1 – Potential energy surface for an example reaction with an energy barrier between reactant and products.

Although the Arrhenius equation (E2.8) can accurately describe the temperature dependence of rate coefficients with an energy barrier such as the one shown in Figure 2.1, many reactions outlined in this thesis involve more complex PESs. A notable difference is the presence of pre- and post-reaction complexes due to favourable hydrogen bonding interactions between the OH radical and the ester molecule. For methyl formate with positive energy barriers to hydrogen abstraction at the methyl and formate sites, the presence of the pre-reaction complex leads to an acceleration in the reaction rate at low temperatures. However, acceleration occurs below 200 K at temperatures outside the tropospheric range (200 – 340 K), the focus of this thesis.

Larger esters than methyl formate (e.g., ethyl formate, isopropyl formate and n-butyl formate) have negative activation energies for hydrogen abstraction by OH at the reaction site adjacent to the ether group of the ester functionality (alpha-ester abstraction) (Chapters 5 and 6). As the temperature decreases the overall rate coefficient accelerates. In contrast, the Arrhenius equation predicts the rate coefficient decreases with decreasing temperature due to the presence of an energy barrier. As other reaction sites still have positive energy barriers, the likelihood of abstraction at their reaction sites increases with temperature creating a “U-shaped” plot that cannot be described by the Arrhenius equation. Consequently, the Arrhenius equation is modified to include an empirical parameter, n (E2.10). This

modified Arrhenius equation is used throughout the thesis to parameterise the temperature dependence of the overall rate coefficients for OH radicals with esters determined in this work.

$$A \times \exp\left(\frac{-E_a}{RT}\right) \times \left(\frac{T}{300}\right)^n \quad \text{E2.10}$$

2.2. Transition state theory (TST)

Transition state theory (TST) was developed by Eyring after collision theory was determined to be inadequate. Collision theory is not discussed here. TST describes the transition state as the highest energy point on the PES of the minimum energy reaction path. At the transition state, the reactants are depicted as an activated complex, shown as $[\text{HO} \cdots \text{HR}]^\ddagger$ in Figure 2.2 or X^\ddagger in Figure 2.1. TST also assumes the reaction is a two-stage process where the first step is the formation of the transition state and the second is the decomposition to products. Once reactants have passed over the transition state, it is assumed the products cannot cross back to reactants via the transition state. Figure 2.2 illustrates a hydrogen abstraction reaction where the OH radical abstracts a hydrogen from the representative organic compound, RH. As OH approaches RH, the HO-H distance decreases (bond being formed) and the R-H distance increases (bond breaking). The energy difference between the reactants (OH and RH) and the transition state ($[\text{HO} \cdots \text{HR}]^\ddagger$) is represented in the Arrhenius equation, outlined above, as the activation energy.

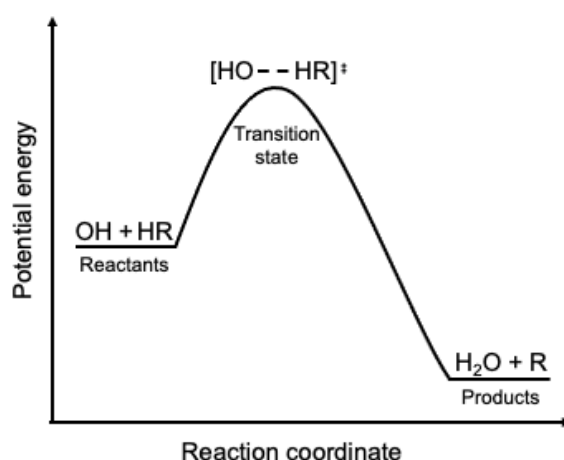


Figure 2.2 – Potential energy surface for an example simple OH abstraction reaction of an organic compound, RH, with an activation barrier.

Chemical equilibrium between the reactants and the TS is an important assumption of TST. The equilibrium constant is represented via E2.11.

$$K^\ddagger = \frac{[\text{HO}\cdots\text{HR}]^\ddagger}{[\text{OH}][\text{HR}]} \quad \text{E2.11}$$

The rate of the reaction is determined from the decomposition rate of the activated transition state, denoted k^\ddagger . Substituting the reaction rate defined in E2.4 gives E2.12.

$$\text{Reaction rate} = k^\ddagger K^\ddagger [\text{OH}][\text{HR}] \quad \text{E2.12}$$

According to statistical thermodynamics, the equilibrium constant can be expressed via E2.13.

$$K^\ddagger = \frac{Q^\ddagger}{Q_{\text{OH}} Q_{\text{RH}}} \times \exp\left(\frac{-E_0}{RT}\right) \quad \text{E2.13}$$

where E_0 is the energy difference between the energy of the transition states and the reactants, relative to the energy of atoms in the gaseous state at 0 K. Q describes the partition function of molecules OH (Q_{OH}), RH (Q_{RH}) and the transition state (Q^\ddagger) per unit volume ($Q = q/V$). The partition function, q , describes the sum of all allowed quantum microstates, or energy levels, weighted by their probabilities and is defined by E2.14.

$$q = \sum_{i=0}^{\infty} g_i \times \exp\left(\frac{-\varepsilon_i}{k_B T}\right) \quad \text{E2.14}$$

The Boltzmann law (E2.15) describes how molecules are distributed by energy with n_i the number of molecules in the i^{th} energy level and g_i is the degeneracy of the energy level ε_i (number of states with ε_i). Boltzmann predicts higher energy states become increasingly populated with temperature.

$$n_i \propto g_i \times \exp\left(\frac{-\varepsilon_i}{k_B T}\right) \quad \text{E2.15}$$

2.3. Pressure-dependent reactions

Unimolecular decomposition and association reactions exhibit similar pressure-dependent behaviour that can be rationalised via the Lindemann-Hinshelwood mechanism. The association reaction between A and B (R2.4) produces an activated complex, AB^* , with a high degree of internal excitation. The activated complex, AB^* is short lived and can either be stabilised by collisions with

a third body, M (R2.6) or dissociate back to reactants (R2.5). Whilst reactions R2.4 – R2.6 describe an association reaction, for example $R + O_2$, they can also be thought of as the reverse of a unimolecular decomposition reaction (e.g. $ROC(O) \rightarrow R + CO_2$). The reactions can also describe unimolecular isomerisation reactions where B is a third body required to transfer energy for the isomerisation ($AB^* \rightarrow AB$) to occur.



At high pressure, k_M is larger than $-k_A$. The rate determining step is formation of AB^* (k_A) and the overall rate coefficient for the reaction is independent of pressure. However, at low pressures, k_M is the rate determining step and the overall rate coefficient is directly proportional to pressure. At high pressures, AB^* is essentially in a steady state creating a Boltzmann distribution of energy. At the high-pressure limit, the overall rate coefficient can be described as a function of temperature by the Arrhenius equation for $k(T)$. Alternatively, the rate coefficient can be described as a function of energy, providing a range of microcanonical $k(E)$ values. A benefit of expressing the rate coefficient as a function of energy rather than temperature is non-Boltzmann distributions are now defined. Describing the overall rate coefficient with $k(E)$ is also able to predict the acceleration in the overall rate coefficient with decreasing temperature for reactions with a negative activation energy.

2.4. Rice Ramsperger Kassel Marcus (RRKM) statistical rate theory

RRKM can be considered a microcanonical version of TST, describing how energy is distributed among the internal degrees of freedom of a molecule. Drawing on the Lindemann-Hinshelwood mechanism, RRKM considers an energised molecule A^* and the transition state, before product formation. This enables RRKM to retain the linear dependence of the overall rate coefficient at low pressures and the pressure-independence observed at high pressures. In the intermediate/ falloff regime, RRKM shows a deviation from experiments which is a focus of improving theoretical descriptions [78].

In RRKM, each vibrational and rotational degrees of freedom are considered individually. The frequencies and energies of a molecule are calculated via *ab initio* methods and used as the input for RRKM calculations. The RRKM rate coefficient for a specific energy ($k(E)$) is calculated via E2.16, where $W(E^\ddagger)$ is the sum of the vibrational and rotational states in the transition state and $\rho(E^\ddagger)$ is the density of states of the excited AB^* . The density of states, $\rho(E^\ddagger)$, is calculated from the real frequencies rather than assuming each frequency is the same and very small.

$$k(E^*) = \frac{W(E^\ddagger)}{h\rho(E^*)} = \frac{\sum_0^{E^\ddagger} P(E^\ddagger)}{h\rho(E^*)} \quad \text{E2.16}$$

2.5. Theoretical methods implemented in this work

Throughout this thesis, computational chemistry is used to complement experimental measurements. In Chapters 3 and 4, the master equation solver, MESMER [79], is used to calculate the rate coefficients for the reaction of OH with methyl formate and its deuterated isotopomers. This work was primarily done by Dr Robin Shannon. However, *ab initio* calculations at the M062X/6-31+G** level of theory are used to characterise the potential energy surfaces of isopropyl formate and n-butyl formate. The energies and transition states of the R radicals formed following hydrogen abstraction by OH at different reaction sites within the respective formates are calculated and subsequent reactions with O_2 to form RO_2 and the internal isomerisation of RO_2 to QOOH species are also calculated.

Ab initio calculations aim to solve the Schrodinger equation, which depicts particles as wave functions and describes the probability of finding a particle at a particular position in space and time. Kohn-Sham Density Functional Theory (DFT) aims to solve the Schrodinger equation for one electron and combines many one-electron wavefunctions to obtain an approximate wavefunction of all electrons. Different levels of theory provide frequencies and energies with varying degrees of accuracy at different computational costs [80].

This work utilises Gaussian 09 [81] for the *ab initio* calculations. M062X is a Minnesota hybrid meta exchange-correlation functional developed by Zhao and Truhlar [82], and provides good performance for thermochemistry, kinetics and non-

covalent interactions. Given the reaction branching ratios determined in this work are influenced by hydrogen bonding interactions, M026X offers a good balance between accuracy and computational cost. 6-31+G** refers to the basis set, specifying how molecular orbitals are represented. 6-31 indicates a split-valance basis, the + sign indicates diffuse functions for heavy atoms and ** indicates polarisation functions on heavy and hydrogen atoms.

Input geometries are specified to Gaussian, which then varies the nuclear coordinates for the molecule until a stationary point is found. The PESs presented in this work represent the sum of the electronic and zero-point energy, relative to the reactants.

2.6. The Kinetic Isotope Effect (KIE)

Deuterium is an isotope of hydrogen with 1 neutron giving it a heavier mass than hydrogen. The larger reduced mass (of carbon and deuterium) lowers the zero point energy of the C-D bond compared with the C-H bond, making abstraction by OH slower as more energy is required for the analogous reaction. Deuterated isotopomers are variations of a molecule where hydrogen is replaced with deuterium. For example, there are four available deuterated isotopomers of methyl formate, $\text{CH}_3\text{OC(O)H}$, $\text{CH}_3\text{OC(O)D}$, $\text{CD}_3\text{OC(O)H}$ and $\text{CD}_3\text{OC(O)D}$. Determining the kinetics of deuterated isotopomers is a technique widely utilised in the literature to determine site-specific kinetics. To extract quantitative information on a reaction's branching ratio from isotopic studies depends on several assumptions:

1. Deuteration of one reactive site does not influence the site-specific kinetics at any other reactive sites.
2. The magnitude of the KIE is the same at each reaction site.

Evidence for assumption 1 comes from the work of Tully et al. [83] who determined the OH kinetics of CH_3CH_3 , CH_3CD_3 and CD_3CD_3 between ~ 293 (292.5) and 705 K. The overall rate coefficients of OH + ethane isotopomers can be written as the sum of the site-specific rate coefficients:

$$k(\text{CH}_3\text{CH}_3) = 2k(\text{CH}_3) \quad \text{E2.17}$$

$$k(\text{CH}_3\text{CD}_3) = k(\text{CH}_3) + k(\text{CD}_3) \quad \text{E2.18}$$

$$k(\text{CD}_3\text{CD}_3) = 2k(\text{CD}_3) \quad \text{E2.19}$$

The experimentally measured values of $\text{OH} + \text{CH}_3\text{CD}_3$ were consistently within error, as a function of temperature, of the calculated value for $\text{OH} + \text{CH}_3\text{CD}_3$ using the site-specific rate coefficients, determined from $\text{OH} + \text{CH}_3\text{CH}_3$ and $\text{OH} + \text{CD}_3\text{CD}_3$. The agreement between the experimental and calculated rate coefficient, suggests each site-specific rate coefficient is independent of another site.

The experimental value for k_{CH_3} determined from ethane isotopomers was used to determine $k_{\text{CH}_2} / k_{\text{Secondary}}$ in the study of $\text{OH} + \text{propane } \text{CH}_3\text{CH}_2\text{CH}_3$, and its deuterated isotopomers:

$$\begin{aligned} k(\text{CH}_3\text{CH}_2\text{CH}_3) &= 2k(\text{CH}_3) + k(\text{CH}_2) \\ k(\text{CH}_3\text{CD}_2\text{CH}_3) &= 2k(\text{CH}_3) + k(\text{CD}_2) \\ k(\text{CH}_3\text{CH}_2\text{CD}_3) &= k(\text{CH}_3) + k(\text{CH}_2) + k(\text{CD}_3) \\ k(\text{CH}_3\text{CD}_2\text{CD}_3) &= k(\text{CH}_3) + k(\text{CD}_2) + k(\text{CD}_3) \\ k(\text{CD}_3\text{CH}_2\text{CD}_3) &= 2k(\text{CD}_3) + k(\text{CH}_2) \\ k(\text{CD}_3\text{CD}_2\text{CD}_3) &= 2k(\text{CD}_3) + k(\text{CD}_2) \\ k(\text{CH}_3\text{CH}_2\text{CH}_3) + k(\text{CD}_3\text{CD}_2\text{CD}_3) &= k(\text{CH}_3\text{CD}_2\text{CH}_3) + k(\text{CD}_3\text{CH}_2\text{CD}_3) \\ &= k(\text{CH}_3\text{CH}_2\text{CD}_3) + k(\text{CD}_3\text{CD}_2\text{CH}_3) \end{aligned}$$

Droege and Tully [84] state the overall rate coefficient can be expressed as the sum of the site-specific rate coefficients at each reactive site, by experimentally determining the rate coefficients $k(\text{CH}_3\text{CH}_2\text{CH}_3) + k(\text{CD}_3\text{CD}_2\text{CD}_3)$ are equal to $k(\text{CH}_3\text{CH}_2\text{CH}_3) + k(\text{CD}_3\text{CH}_2\text{CD}_3)$ and $k(\text{CH}_3\text{CH}_2\text{CD}_3) + k(\text{CD}_3\text{CD}_2\text{CH}_3)$. They also state that each reaction site is independent of deuteration at any other reaction sites. This work has also applied the KIE to determine the site-specific kinetics of methyl formate and its deuterated isotopomers.

2.7. Overview of the experimental set-up

There are many experimental methods to determine the rate coefficient for a reaction. Methods typically measure the concentration of one of the reactants as a function of time to extract the rate coefficient for a given temperature and pressure. Kinetics in this work are absolute, meaning they are determined independently of other reactions. The most common, complementary technique is relative rate experiments which determine rate coefficients relative to another molecule.

Usually, the unknown rate coefficient is compared against several molecules whose rate coefficients are known. The unknown rate coefficient is calculated from the known rate coefficient and the relative rate.

This work experimentally determines the overall rate coefficients for the reactions of OH with esters via laser flash photolysis coupled with laser induced fluorescence (LIF) of OH/OD. The fluorescence of OH/OD is proportional to the concentration and measured as a function of time between ~ 0 and $25\ \mu\text{s}$ by varying the time delay between the photolysis (reaction-initiating) and fluorescence (reaction-monitoring) lasers. A schematic of the general experimental set-up is illustrated in Figure 2.3. The constituent parts of the set-up are described in more detail below.

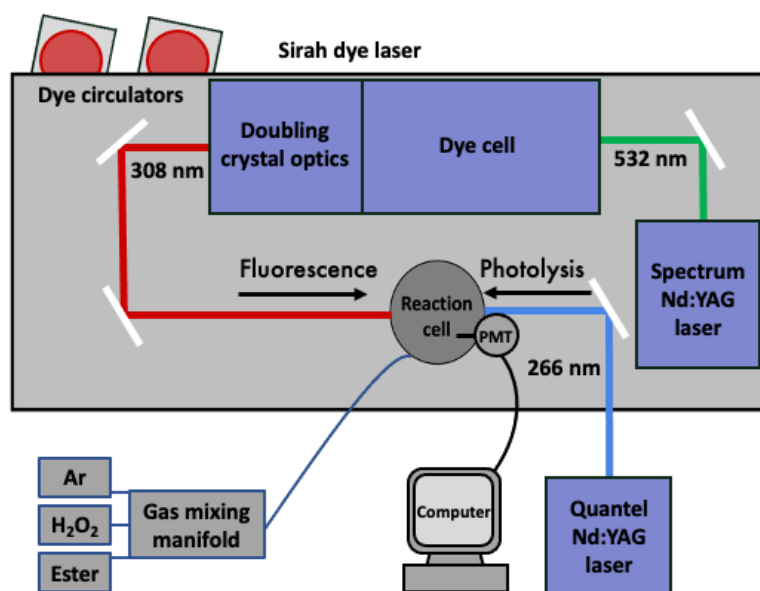


Figure 2.3 – Overview of the experimental set-up.

2.8. Flash Photolysis

Norrish and Porter received the 1967 Nobel Prize in Chemistry for developing flash photolysis. The technique uses a pulse of high-intensity light to initiate a reaction by generating a radical, e.g., OH or Cl. The main advantage of this technique is the ability to pre-mix reactants and optimise experimental conditions (e.g., pressure and temperature) before initiating the reaction. In 1940, when Norrish and Porter developed this technique, they used flash lamps to initiate reactions. The

timescale of the reaction that can be studied is determined by the light source and was several milliseconds when the technique was first developed. Due to the development of high-powered lasers, reactions can now be studied on timescales of nanoseconds or less. This work measures reactions over microseconds. Another advantage of modern lasers is their high specificity. Whilst flash lamps have a broad output, lasers can be tuned to specific wavelengths, ensuring the desired species is photolysed.

2.9. Nd:YAG lasers

This work uses the fourth harmonic of a Nd:YAG laser by Quantel (Q-smart 850 at 10 Hz) to photolyse the radical precursor (e.g., H_2O_2) at 266 nm. Nd:YAG stands for neodymium-doped (Nd) yttrium aluminium garnet (YAG). Neodymium ions (Nd^{3+}) are hosted within the YAG crystal, influencing their energy levels. The crystal is located as a rod within the laser, and a flashlamp provides the initial excitation of the Nd^{3+} ions. The YAG crystal enables the forbidden transition $^4\text{F}_{3/2} \rightarrow ^4\text{I}_{11/2}$ to occur, and after stimulated emission by the flashlamp, the laser outputs at 1064 nm. The laser output is frequency doubled, and the fourth output at 266 nm and 10 Hz is used in this work.

A telescope is used to increase the diameter of the laser beam. Increasing the diameter of the laser beam reduces the diffusion of gases outside the laser beam. The output of the Quantel Nd:YAG laser is ~ 50 mJ/pulse and the initial diameter of the beam is 8 mm. The beam is diverging and reaches ~ 2 cm by the time it enters the reaction cell. Thus, the laser fluence per pulse is ~ 16 mJ cm^{-2} .

2.10. Dye lasers

Dye lasers use organic dyes as their lasing medium. The changeability of the dye laser, and hence the broad wavelengths of tuneable light, is a key advantage of a dye laser. This work uses the Rhodamine 6G dye blended with Pyromethane 580. The conjugated structures of dyes enable absorption over a broad wavelength range. The dye in this work tunes the 532 nm frequency-doubled output from an Nd:YAG laser to ~ 616 nm before it is frequency doubled to ~ 308 nm. Frequency doubling occurs via crystals which lack inversion symmetry, known as nonlinearity.

Due to the crystals nonlinearity, the input wave oscillates at twice the frequency within the crystal, and consequently, the output is frequency doubled. The correct orientation of the crystal is important. Furthermore, the refractive index is sensitive to temperature, and controlled by a heated cell. The exact wavelengths used throughout this thesis are 307.290 nm for OH and 307.248 nm for OD. Wavelengths were chosen for their 1:1 relationship, outlined in more detail in Chapter 4.

2.11. Laser induced fluorescence (LIF) of OH/OD

LIF exploits specific energy transitions within a molecule. LIF of OH/OD exploits the ground electronic state ($X^2\Pi$) and the first excited state ($A^2\Sigma^+$), approximately 4 eV apart [85]. Used in conjunction with laser flash photolysis, the fluorescence of OH can be monitored at varying times throughout a reaction. This work initially used off-resonance fluorescence for the kinetics of OH and OD radicals with undeuterated methyl formate, $\text{CH}_3\text{OC(O)H}$ (Chapter 3). Off-resonance fluorescence is illustrated in Figure 2.4 in purple and occurs when OH radicals are excited at 282 nm to the first vibrational state of the excited electronic state ($A^2\Sigma^+ (v'=1)$). Vibrational energy transfer (VET) transfers vibrational energy from the excited OH via collision with another molecule, such as the bath gas, M. VET leads to a reduction in the vibrational energy to the ground vibrational state, $A^2\Sigma^+ (v'=0)$. Fluorescence is observed at ~ 308 nm $A^2\Sigma^+ (v'=0) \rightarrow X^2\Pi (v''=0)$. This work primarily uses on-resonance fluorescence (Figure 2.4, blue) where the OH radical is excited to and from the same energetic state at ~ 308 nm. VET is a similar mechanism to signal quenching. However, quenching leads to a reduction in the electronic state, preventing fluorescence and leading to a reduction in the OH signal.

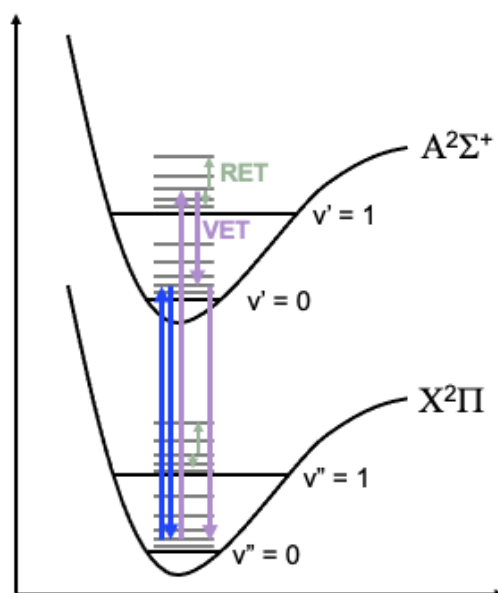


Figure 2.4 – Laser induced fluorescence of OH $A^2\Sigma^+(v'=0) \rightarrow X^2\Pi_i(v''=0)$. On-resonance fluorescence is shown in blue, where OH is excited at 308 nm to $A^2\Sigma^+(v'=0)$. Off-resonance fluorescence is shown in purple, where OH is excited at 282 nm to $A^2\Sigma^+(v'=1)$ and monitored at 308 nm from $A^2\Sigma^+(v'=0)$, due to vibrational energy transfer (VET) with another molecule e.g., the bath gas. Radiative energy transfer (RET) is illustrated in green, whereby collisional energy transfer occurs between different rovibrational states.

One disadvantage of on-resonance fluorescence is that the fluorescence signal cannot be separated from scattered laser radiation. However, scattered laser light can be removed from experimental traces of OH by gating the fluorescence signal. Gating is where the imaging sensor only opens its “gate” after a specified time delay. This work alters the time delay/gate to remove the initial scattered laser light. A photomultiplier tube (PMT) is used to detect the photons from OH off-resonance fluorescence. PMTs absorb a photon onto a photosensitive cathode that subsequently releases an electron. The electron is multiplied along a series of electrodes, multiplying the fluorescence signal by up to 10^8 [86]. For on-resonance fluorescence, a channel photomultiplier (CPM) is used. CPMs have a photocathode on the surface of the entrance channel. Photons enter the CPM and the cathode releases electrons into a curved semiconductive channel. Each time electrons hit the channel walls, multiple electrons are emitted, amplifying the fluorescence signal by over 10^7 [87].

2.12. UV absorption spectroscopy

UV absorption spectroscopy is a technique often used to directly measure the concentration of reactants or products. This work uses UV absorption of isopropyl formate and tertbutyl formate to ensure the esters are reliably being delivered to the reaction cell. UV absorption measures the absorbance of molecules and relates absorbance to concentration according to the Beer-Lambert law (E2.20), where A is absorbance, σ is absorption cross-section in cm^2 , c is the number density concentration in cm^{-3} and L is the optical path length in cm.

$$A = \sigma c L \quad \text{E2.20}$$

The absorbance is calculated from the intensity of light, at wavelength λ , in the absence (I_0) of ester and in the presence of ester (I) (E2.21).

$$A = \ln \left(\frac{I_0(\lambda)}{I(\lambda)} \right) \quad \text{E2.21}$$

UV absorption can also be used to follow a reaction by monitoring the intensity of light over the reaction timescale. By monitoring different wavelengths, the concentration of multiple reactant and product species can be determined. Details of the UV absorption apparatus used in this work are outlined in Chapter 5.

2.13. Experimental procedures used in this work

2.13.1. Preparing dilute mixtures of esters

Concentrations of ester were premixed with argon in a glass cylindrical bulb. Preparing reactant mixtures in advance meant the concentration of ester being delivered to the cell was well known. The concentration of ester within the bulb was typically (2 – 3)%. First, the ester was transferred to a clean glass finger before being attached to the vacuum line. Then, the glass finger was immersed in liquid nitrogen. The low temperature of liquid nitrogen meant the thermal energy of the ester solution was transferred to the liquid nitrogen, resulting in the ester solution freezing. Once the ester solution was frozen, the liquid nitrogen was removed and the tap to the vacuum line was opened. As the ester solution came back to room temperature and began melting, bubbles could be seen evaporating from the liquid. These are attributed to oxygen, which has a higher vapour pressure than the ester, so will off-gas first. The process was typically repeated three times whenever the

ester solution was exposed to ambient air. The primary motivation was to eliminate background oxygen present in the system.

2.13.2. Ester flow corrections

This work delivered gases to the reaction cell via calibrated mass flow controllers. Mass flow controllers regulate gas flows by measuring the temperature change required to maintain a constant temperature. The change in temperature is related to the ability of the gas to absorb heat - the specific heat capacity, C_p , of the gas. The mass flow controllers used in this work are typically calibrated with argon. Gas correction factors (GCFs) are applied to account for the concentration of ester when delivering the diluted mixture of ester and argon to the reaction cell via the calibrated mass flow controllers. Applying GCFs are important in accurately measuring the flow of ester and hence ester concentration. GCFs are calculated relative to nitrogen via E2.22, where 0.311 is the heat capacity of nitrogen multiplied by the density of nitrogen, 0.88 is a molecular structure correction factor for polyatomic gases, C_p is the heat capacity of the ester in cal/g and ρ is the density of the ester in g/l.

$$\text{GCF} = \frac{0.311 \times 0.88}{C_p \times \rho} \quad \text{E2.22}$$

The ester/argon flow correction is subsequently calculated via E2.23, where the argon GCF is 1.4.

$$\frac{[\text{Ester}] \times 100}{\text{GCF}} + \frac{100 - ([\text{Ester}] \times 100)}{\text{Argon GCF}} \quad \text{E2.23}$$

E2.23 has been experimentally verified by measuring the flow of an ester and argon diluted mixture with a flow meter. Table 2.1 presents the gas flow corrections for a series of esters. Typically, as the size of the ester increases, its ability to store heat increases due to an increase in the number of degrees of freedom. Therefore, the GCF is lower (inversely proportional to heat capacity) and the correction to the ester/argon flow increases.

Table 2.1 – Gas correction factors for various esters calculated via E2.19.

Ester	Gas correction factor
methyl formate	0.398
ethyl formate	0.270
isopropyl formate	0.222
tertbutyl formate	0.176
n-butyl formate	0.198
methyl acetate	0.298
ethyl acetate	0.227
tertbutyl acetate	0.190

2.13.3. Temperature calibrations

Calibrations of the temperature within the reaction cell have been determined via bimolecular plots of $\text{H}_2 + \text{OH}$ in argon between 294 and 574 K and flow rates of 1180 and 1280 sccm at approximately 120 Torr. The ranges of flow rate, temperature and pressure cover the typical experimental conditions of overall rate coefficients determined in this work. The rate coefficient for $\text{H}_2 + \text{OH}$ is well known. Using the experimental pseudo-first order rate coefficients, the temperature is varied to fit the slope of the pseudo-first order rate coefficients to the bimolecular rate coefficient for $\text{H}_2 + \text{OH}$, determined by Tully and Ravishankara [88]. An example bimolecular plot of $\text{OH} + \text{H}_2$ is shown in Figure 2.5 at 294 K.

Figure 2.6 illustrates the temperature calibrations determined in this work. As the temperature increases, the thermocouple appears to measure a lower temperature than the bimolecular rate coefficient of $\text{OH} + \text{H}_2$ suggests. However, the deviation in temperature is also observed in both directions between 390 and 470 K. Therefore, the error in the temperature is likely $\pm \sim 30$ K.

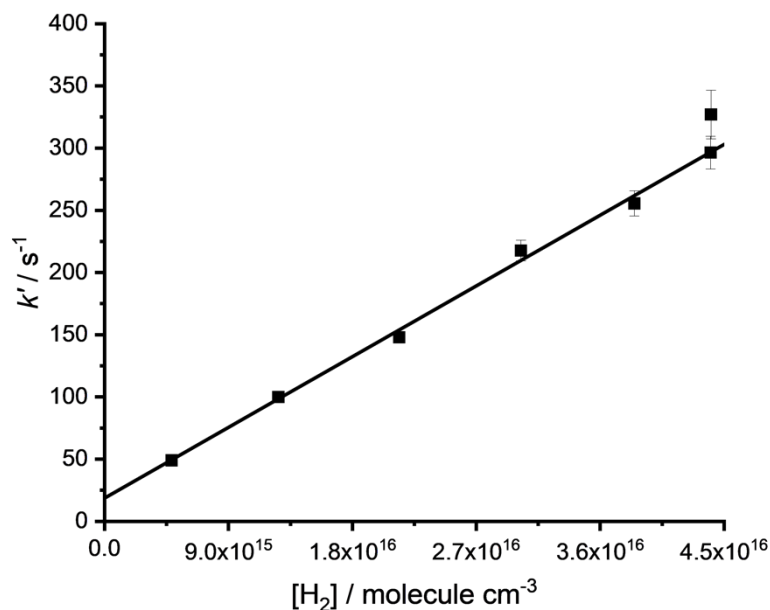


Figure 2.5 – Bimolecular plot for the reaction of OH radicals with H₂ at 294 K, 1190 sccm flow rate and 120 Torr of argon. The intercept is $(18.7 \pm 2.3) \text{ s}^{-1}$ due to diffusion. The slope is equal to $(6.32 \pm 0.18) \times 10^{-15} \text{ cm}^3 \text{ molecule}^{-1} \text{ s}^{-1}$.

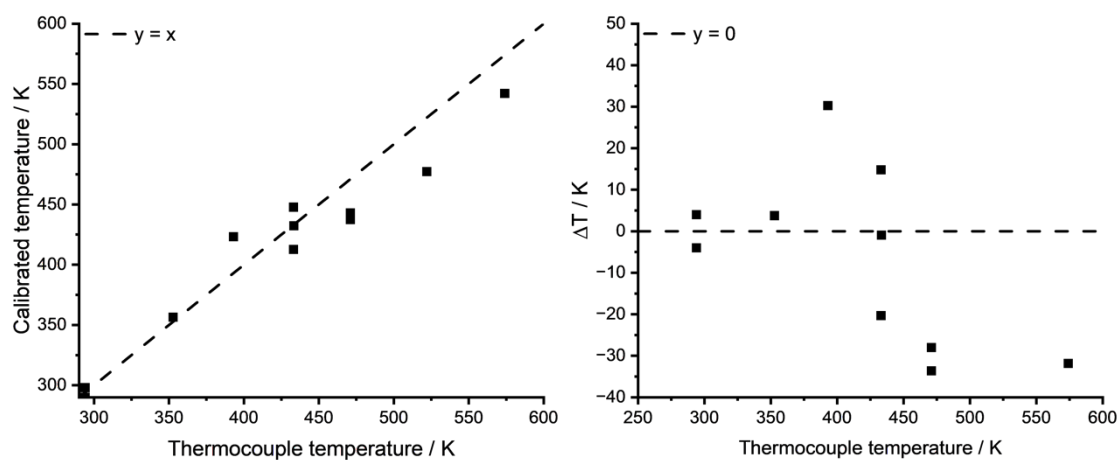


Figure 2.6 – The left figure shows the calibrated temperature plotted against the temperature measured with the thermocouple (thermocouple temperature). The right figure shows the deviation between the calibrated and measured temperature (ΔT) against the thermocouple temperature.

Chapter 3 The kinetics of OH/OD + methyl formate and its deuterated isotopomers

3. Introduction

Methyl formate, $\text{CH}_3\text{OC(O)H}$, is the simplest ester and can be used as a proxy to understand ester reactivity. The applications of methyl formate oxidation span a wide temperature range. Methyl formate has been detected in interstellar clouds and the interstellar medium [89]. Methyl formate has recently been proposed as a hydrogen carrier. Due to the intermittency of renewable energy (wind, solar or hydro power), chemical fuels are used as liquid organic hydrogen carriers to store “green hydrogen”. Methyl formate is an attractive industrial alternative to methanol, ammonia (both of which are toxic and flammable), and formic acid (which is corrosive), as it is non-toxic and easy to handle (non-corrosive). Methyl formate can also be produced sustainably from the hydrogenation of CO_2 in the presence of methanol. Additionally, the dehydrogenation of methyl formate is kinetically and thermodynamically favoured over formic acid and methanol, meaning it produces hydrogen significantly faster with a larger yield [36].

Methyl formate's plethora of applications results in its release into the atmosphere where it will react with the dominant atmospheric oxidant, OH. Previous temperature-dependent studies of OH + methyl formate are presented in Figure 3.1. Methyl formate is also formed *in situ* following the atmospheric oxidation of dimethyl ether (DME) by Cl with a yield of $(90 \pm 8)\%$ relative to DME loss [38]. DME is a biodiesel target and fuel antiknock agent [90]. Oxygenated molecules such as ethers and esters (e.g., fatty acid methyl esters, FAMES) are proposed biodiesels as they have higher O:C ratios than traditional diesel which is composed of hydrocarbons. Higher O:C ratios lead to more complete combustion, decrease a fuel's tendency to form soot, and decrease emissions of CO and the thermal production of NO_x. As FAMES are not fossil derived fuels, they do not release sulphur oxides ($\text{SO}_2 + \text{SO}_3 = \text{SO}_x$), consequently decreasing the formation of particulate matter. Therefore, understanding methyl formate oxidation has attracted attention from both atmospheric and combustion studies.

3.1. Literature studies of OH + methyl formate kinetics

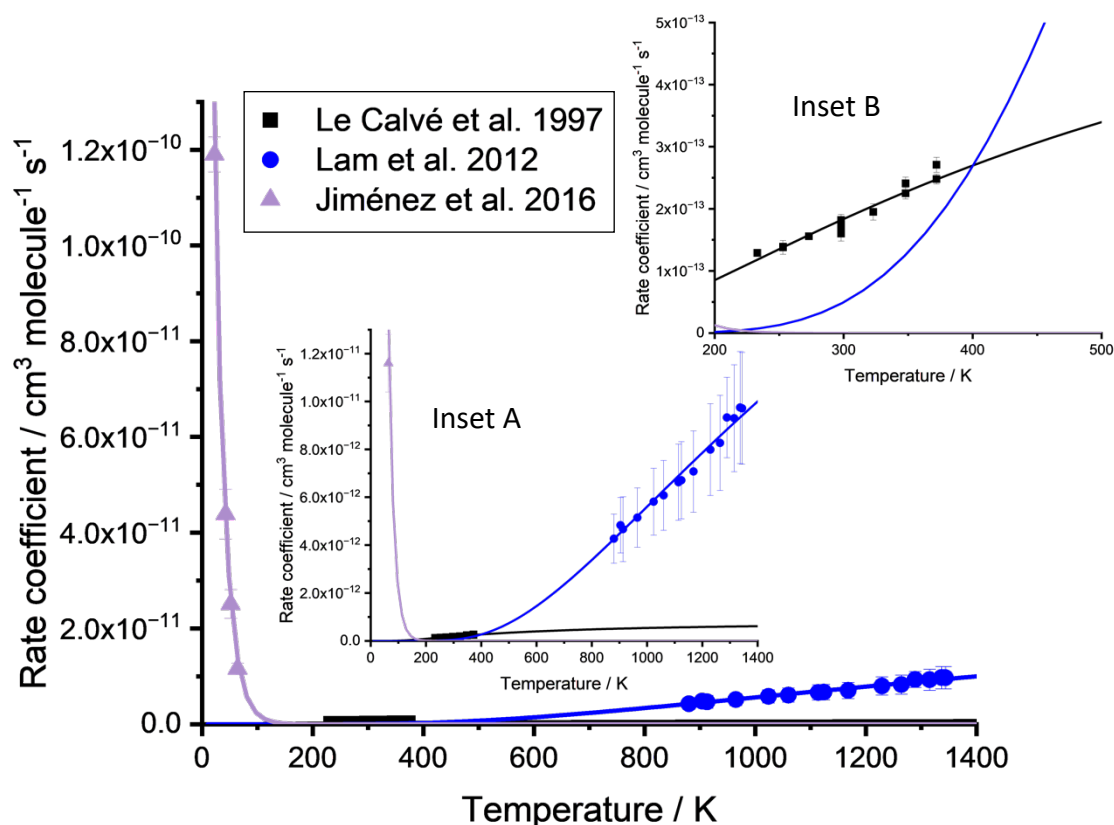


Figure 3.1 – Literature temperature-dependent studies of OH + methyl formate. Le Calvé et al. [8] is shown in black (squares), Lam et al. [9] is in blue (circles) and Jiménez et al. [10] is in purple (triangles). Arrhenius temperature-dependent fits to each data set are shown as solid lines and extrapolated to the full temperature range. Inset A shows a zoomed in view between $0 - 1.3 \times 10^{-11} \text{ cm}^3 \text{ molecule}^{-1} \text{ s}^{-1}$ and $0 - 1400 \text{ K}$. Inset B shows a zoomed in view between $200 - 500 \text{ K}$ and $0 - 5 \times 10^{-13} \text{ cm}^3 \text{ molecule}^{-1} \text{ s}^{-1}$.

Le Calvé et al. [8] studied the temperature dependence of OH + methyl formate between 253 and 372 K via pulsed laser photolysis coupled with laser induced fluorescence. The temperature dependence has also been determined between 876 and 1371 K by Lam et al. [9] via shock tube experiments with UV absorption of OH. Jiménez et al. [10] also determined the temperature dependence between 22 and 64 K, showing an acceleration in the rate coefficient at low temperatures. Figure 3.1 illustrates the temperature dependence of OH + methyl formate by Le Calvé et al. [8], Lam et al. [9], and Jiménez et al. [10]. Extrapolation of each temperature dependent Arrhenius fit (shown as solid lines) over the full temperature range leads to poor agreement between the studies. This is highlighted

in insets A and B via zoomed in views and leaves a critical gap in our knowledge, particularly between 372 and 876 K where low temperature combustion occurs.

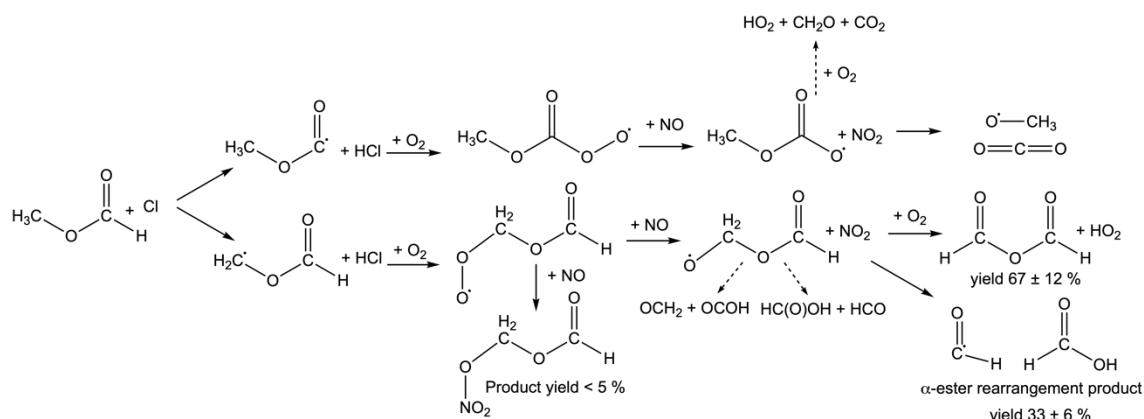


Figure 3.2 – The atmospheric fate of methyl formate. Solid arrows are determined by Wallington et al. [11] and dashed arrows represent additional reaction pathways determined by Good et al. [12].

Determining the site-specific kinetics of methyl formate is critical to understanding its atmospheric impact. Although the present work focuses on atmospheric chemistry, the site-specific kinetics of methyl formate are also relevant to combustion. Wallington et al. [11] quantified the site-specific kinetics of Cl-initiated oxidation of methyl formate in an atmospheric chamber at 700 Torr. Following hydrogen abstraction, the alkyl radicals reacted with Cl_2 to produce $\text{HC(O)OCH}_2\text{Cl}$ or ClC(O)OCH_3 . Product yields were monitored with FTIR spectroscopy and a branching ratio of $(55 \pm 7)\%$ for abstraction at the formate site and $(45 \pm 7)\%$ at the methyl site was determined. The reaction was followed further to determine the atmospheric fate of the radicals, as shown in Figure 3.2. Under atmospheric conditions, abstraction from the methyl site leads to formic acid and formic acid anhydride, whilst abstraction from the formate site leads to CO_2 and carcinogenic formaldehyde. The atmospheric fate of formic acid anhydride is decomposition to formic acid. Measured concentrations of formic acid in the atmosphere are currently underpredicted by models which utilise known production and loss pathways [91]. Therefore, there is significant interest in the formation of formic acid. Organic acids such as formic acid contribute to the acidity of clouds and rainwater and the formation of aerosols. Therefore, depending on the initial site of abstraction, methyl formate has quite different atmospheric impacts.

The site-specific kinetics of methyl formate with the dominant atmospheric oxidant OH, have been studied theoretically. Theoretical investigations by Good et al. [92] at the second-order Møller-Plesset (UMP2) level with the 6-31G(d) basis set indicate that 86% of the reaction occurs at the formate site. Their *ab initio* calculated rate coefficient at 298 K is $1.85 \times 10^{-13} \text{ cm}^3 \text{ molecule}^{-1} \text{ s}^{-1}$, whilst their experimental rate coefficient, determined via discharge flow with resonance fluorescence, is $(1.77 \pm 0.28) \times 10^{-13} \text{ cm}^3 \text{ molecule}^{-1} \text{ s}^{-1}$, in good agreement with other room temperature literature studies. This work aims to experimentally determine the site-specific kinetics of OH + methyl formate via temperature-dependent studies of methyl formate and its deuterated isotopomers – CH₃OC(O)H, CH₃OC(O)D, CD₃OC(O)H and CD₃OC(O)D between 294 and 573 K.

3.2. Experimental

3.2.1. Experimental set-up

This work used laser flash photolysis with laser induced fluorescence of OH/OD to determine the kinetics of OH/OD + methyl formate and its deuterated isotopomers. Hydrogen peroxide (H₂O₂, Sigma-Aldrich, 50% wt in H₂O) and tertbutyl peroxide (tBuOOH, (CH₃)₃COOH) were used as OH precursors. Precursors were deuterated by adding D₂O (Sigma-Aldrich 99.9 atom %D), making D₂O₂ and (CH₃)₃COOD. H₂O₂ was delivered via a pressurised bubbler flowing argon over H₂O₂, with the flow rate controlled manually by a valve. tBuOOH was delivered via a calibrated mass flow controller. Methyl formate isotopomers (CH₃OC(O)H (Sigma-Aldrich, 99%), CH₃OC(O)D (Sigma-Aldrich, 99%), CD₃OC(O)H (Sigma-Aldrich, 99%) and CD₃OC(O)D (QMX Laboratories, 99%)) were purified via several freeze-thaw pump cycles and stored as diluted mixtures in glass bulbs prepared with argon. Methyl formate was delivered via calibrated mass flow controllers, with a flow correction to account for the concentration of methyl formate within each gas bulb. All gases were passed into a mixing manifold before entering the reaction cell. Pressures within the reaction cell were controlled by a rotary vane pump and monitored via a capacitance manometer. Experiments in this chapter were conducted between 5 and 97 Torr.

A schematic of the experimental set-up is shown in Chapter 2, Figure 2.3. The temperature within the reaction cell was controlled by a ceramic oven and monitored with a calibrated thermocouple close to the reaction zone. The fourth harmonic of a pulsed Nd:YAG laser (Quantel Q-smart 850 at 10 Hz) photolysed OH/OD precursors at 266 nm. OH/OD radicals were excited by a Nd:YAG pumped dye laser at 282 (Spectra-Physics, Quanta-Ray, PDL-3, Rhodamine 6G blended with Pyromethane 580 dye) ($A^2\Sigma^+(\nu = 1) \leftarrow X^2\Pi(\nu = 0)$) or 308 nm ($A^2\Sigma^+(\nu = 0) \leftarrow X^2\Pi(\nu = 0)$) (Sirah, Cobra Stretch, DCM special dye). Fluorescence was detected at ~308 nm (OH detection at 307.290 nm and OD detection at 307.248 nm) through an interference filter (Barr Associates, Inc., 308.5 ± 5 nm). Off-resonance detection used a photomultiplier tube (PMT) (EMI 9813), whereas on-resonance fluorescence used a channel photomultiplier (CPM, PerkinElmer C1943P). Temporal profiles of OH/OD were generated by altering the delay between the photolysis and fluorescence lasers using a digital delay generator (BNC DG535) from 0 to 10 μ s. Scans were typically taken five times.

This work used 266 nm photolysis, due to the potential for methyl formate photolysis at 248 nm. Despite the small absorption cross-section at 248 nm, methyl formate photolysis does occur at this wavelength [93]. At 248 nm, secondary chemistry was detected in this work alongside the work of Le Calve et al. [8]. However, other works from Karlsruhe Institute of Technology (KIT), at much higher pressures (2, 5, and 10 bar), did not detect secondary chemistry.

3.2.2. Analysis of OH/OD traces

Pseudo-first order conditions with methyl formate in excess were utilised and OH/OD temporal profiles were single exponential decays up to 490 K. An example single exponential decay is shown in the inset of Figure 3.3, and is fit with the single exponential equation, E3.1, to extract the pseudo-first order rate coefficient for a given concentration of methyl formate.

$$OH_t = OH_0 \times \exp(-k't) \quad E3.1$$

Experiments were repeated at ~ 5 – 6 concentrations of methyl formate, and the pseudo-first order rate coefficients were plotted against concentration in a bimolecular plot. An example bimolecular plot is shown in Figure 3.3 with a linear

fit, the slope of which is the bimolecular rate coefficient. OH and OD decays in the absence of any methyl formate were single exponential and fit with E3.1 to extract the pseudo-first order rate coefficient, k_D , which represents diffusion and the reaction of OH with the precursor. k_D , was typically subtracted from the pseudo-first order rate coefficient, leading to intercepts within error of zero, such as the plot shown in Figure 3.3.

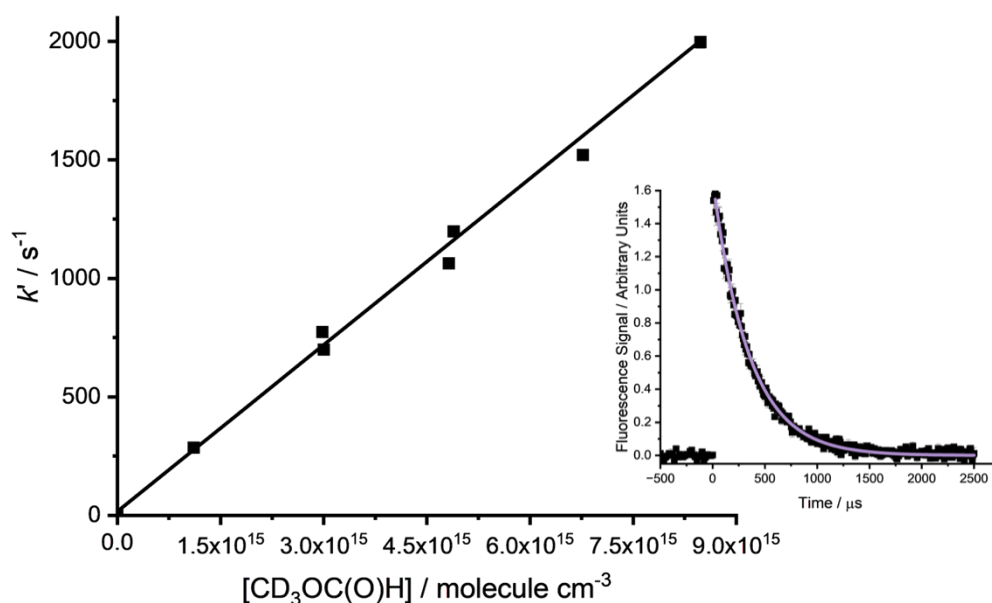
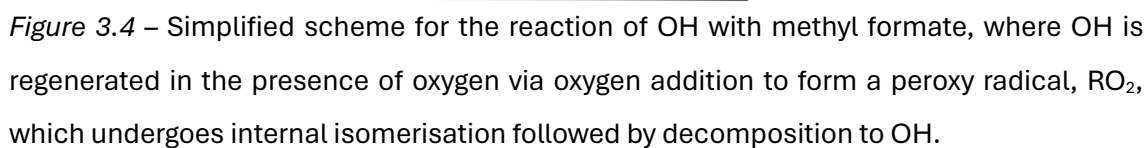


Figure 3.3 – Example bimolecular plot for the reaction of OH + CD₃OC(O)H at 393 K. The slope/bimolecular rate coefficient is equal to $(2.34 \pm 0.08) \times 10^{-13} \text{ cm}^3 \text{ molecule}^{-1} \text{ s}^{-1}$, determined over $(1.11 - 8.48) \times 10^{15} \text{ molecule cm}^3$. Although there, the uncertainties in k' are smaller than the size of the symbols.

Above 490 K, biexponential decays were observed. Biexponential decays can be attributed to the regeneration of OH via the internal isomerisation of peroxy radicals. Although no oxygen has been added to the reaction cell, the background oxygen concentration is approximately $1 \times 10^{14} \text{ molecules cm}^{-3}$ estimated from experiments outlined in Chapter 4. Biexponential decays were fit with a simplified scheme, illustrated in Figure 3.4, to extract the pseudo-first order rate coefficient for the reaction of OH with methyl formate.



The temperature-dependent kinetics of OH/OD + methyl formate ($k_{\text{OH+MF}}/k_{\text{OD+MF}}$) have been determined in this work between 296 – 588 K. Rate coefficients $k_{\text{OH+MF}}$ and $k_{\text{OD+MF}}$ increase with increasing temperature as shown in Figure 3.5 alongside non-Arrhenius temperature-dependent fits to the data:

$$k_{\text{OD}+\text{MF}} = ((4.35 \pm 6.62) \times 10^{-15}) \times \exp((1270 \pm 480)/T) \times (T/300)^{(5.30 \pm 1.07)}$$

80

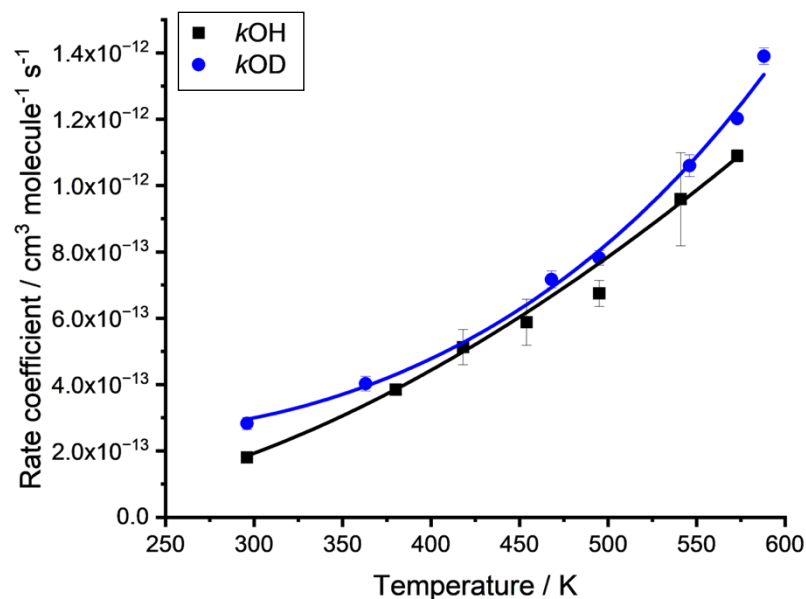


Figure 3.5 – Temperature-dependent kinetics of OH (black squares) and OD (blue circles) + methyl formate between 296 – 588 K.

Table 3.1 – Room temperature rate coefficients in the literature and this work for OH + methyl formate.

Reference	Technique	$10^{13} k_{OH+MF, 298 \text{ K}} / \text{cm}^3 \text{ molecule}^{-1} \text{ s}^{-1}$
Wallington et al. [19]	FP and RF detection of OH	2.27 ± 0.34
Le Calvé et al. [8]	LFP (248 or 352 nm) and OH LIF	1.73 ± 0.21
Good et al. [92]	Flowtube with RF detection of OH	1.77 ± 0.28
Szilágyi et al. [96]	Flowtube with RF detection of OH	1.83 ± 0.33
Eurochamp Recommendation [16]	Review	1.80 ± 0.30
This Work	LFP (266 nm) and OH LIF	1.81 ± 0.27

Comparisons of this work with the literature are shown in Figure 3.6. Although the k_{OH+MF} rate coefficients in this work are slightly larger than an

extrapolated fit of the Le Calvé et al. [8] data, this work is in good agreement with Le Calvé et al. [8] at room temperature. The room temperature rate coefficients, $k_{\text{OH+MF}}$, are presented in Table 3.1. Excluding the higher rate coefficient determined by Wallington et al. [19], there is good agreement between this work and the literature studies spanning a range of experimental methods. Wallington et al. [19] used flash photolysis at ~ 165 nm to generate their OH from H_2O . As mentioned earlier, this work moved from 248 nm photolysis to 266 nm due to secondary chemistry observed at 248 nm potentially caused by methyl formate photolysis. The absorption cross-section of methyl formate increases from $\sim 9 \times 10^{-21} \text{ cm}^2 \text{ molecule}^{-1}$ at 248 nm to $\sim 9 \times 10^{-18} \text{ cm}^2 \text{ molecule}^{-1}$ at 165 nm [97]. Therefore, secondary chemistry may influence the kinetics determined by Wallington et al. [19].

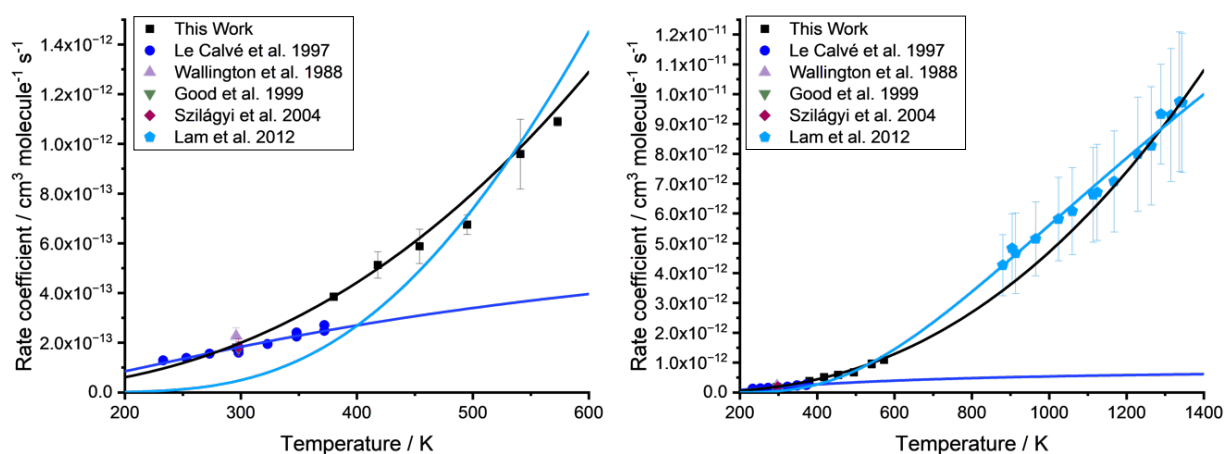


Figure 3.6 – The temperature dependence of OH + methyl formate determined in this work (black squares) and the literature. The dark blue solid line represents the temperature-dependent fit to the Le Calvé et al. [8] dataset (253 – 372 K). The light blue solid line represents the temperature dependence of the Lam et al. [9] data (876 – 1371 K). Both Le Calvé et al. [8] and Lam et al. [9] temperature-dependent fits have been extrapolated to 200 – 1400 K. The black solid line is a temperature-dependent fit to the rate coefficients determined in this work, Le Calvé et al. [8] and Lam et al. [9]. The left figure shows the overall kinetics between 200 and 600 K and the right figure shows the overall kinetics over an extended temperature range between 200 and 1400 K.

This work bridges the gap in the temperature dependence of $k_{\text{OH+MF}}$ between 372 and 876 K. Accurately determining the kinetics between 372 and 876 K is

important for low-temperature combustion studies. Figure 3.6 demonstrates that the temperature-dependent fits of Le Calve et al. [8] and Lam et al. [9] do not accurately predict the kinetics between 372 – 876 K.

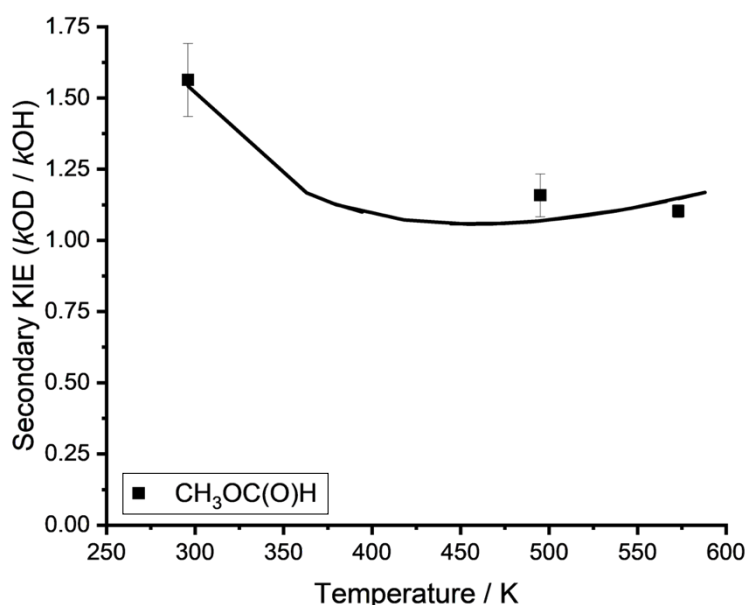


Figure 3.7 – The secondary KIE (k_{OD}/k_{OH}) for the reactions of OH/OD + methyl formate. The solid line is calculated from the temperature-dependent fits of k_{OH} and k_{OD} , whereas the individual black squares represent experimental values where the rate coefficients for OH and OD have been obtained at the same temperature.

As illustrated in Figures 3.5 and 3.7, the rate coefficient k_{OD+MF} is slightly larger than k_{OH+MF} . Figure 3.7 shows the secondary KIE (k_{OD}/k_{OH}) which decreases with increasing temperature between 296 and ~ 420 K before levelling off and subtly increasing slightly. The O-D bond is shorter than the O-H bond due to the lower zero point energy. The bond frequency is also reduced due to the increased reduced mass of OD compared with OH. As bond frequencies impact the stretching and bending frequencies within the transition states, the OD + methyl formate transition states have reduced energies compared with the OH + methyl formate transition states. This is discussed further in the next section.

3.4. Theoretical calculations to explain the temperature dependence of OH + methyl formate by Dr Robin Shannon

Theoretical calculations presented in this chapter are the work of Dr Robin Shannon. Dr Robin Shannon calculated the potential energy surface for OH + MF at the CCSD(T)-F12/aug-cc-pVTZ//M06-2X/6-31+G** level of theory, with higher-level “ANL0-like” calculations for the energies of the transition state barriers. Energies are zero-point energy corrected.

3.4.1. Theoretical methods

To complement the experimental measurements, statistical rate theory calculations have been performed in the form of RRKM/ME (Rice, Ramsperger, Kassel, Marcus, Master Equation) calculations. For these calculations, the potential energy surface of the OH + MF reaction was mapped out at the CCSD(T)-F12/aug-cc-pVTZ//M06-2X/6-31+G** level of theory. In this case, the CCSD(T) energies were obtained using Molpro, [98] while the DFT geometry optimisations and frequency calculations were performed in Gaussian [81]. All DFT calculations utilized the “ultrafine” integration grid in Gaussian. For key species, the reactants, and the transition states, we have employed higher-level calculations based on the ANL schemes of Klippenstein and co-workers [99]. For these calculations, the structures and obtained harmonic frequencies were reoptimized at the CCSD(T)-F12/cc-pVDZ-F12 level of theory. High-level single-point energies were obtained at these optimised structures using the following expression (E3.2):

$$E_{\text{ANL-like}} = E_{\text{CCSD(T)-F12/cc-pVQZ-F12}} + \Delta E_{\text{anharm}} + \Delta E_{\text{quad}} + \Delta E_{\text{so}} + \Delta E_{\text{DK}} \quad \text{E3.2}$$

where

$$\Delta E_{\text{anharm}} = \text{ZPE}_{\text{CCSD(T)-F12/cc-pVDZ-F12}}^{\text{harmonic}} + (\text{ZPE}_{\text{B3LYP/6-311+G**}}^{\text{anharmonic}} - \text{ZPE}_{\text{B3LYP/6-311+G**}}^{\text{harmonic}}) \quad \text{E3.3}$$

$$\Delta E_{\text{quad}} = E_{\text{CCSDT(Q)/aug-cc-pVDZ}} - E_{\text{CCSD(T)/aug-cc-pVDZ}} \quad \text{E3.4}$$

$$\Delta E_{\text{so}} = E_{\text{CCSD(T,full)/aug-cc-pCVTZ}} - E_{\text{CCSD(T)/aug-cc-pCVTZ}} \quad \text{E3.5}$$

$$\Delta E_{\text{DK}} = E_{\text{CCSD(T,DK)/cc-pVTZ-DK}} - E_{\text{CCSD(T)/cc-pVTZ-DK}} \quad \text{E3.6}$$

For anharmonic corrections to the zero-point vibrational energies, ΔE_{anharm} , ZPEs were obtained using vibrational perturbation theory (VPT) [100] as implemented in Gaussian [81]. For these VPT calculations, the B3LYP/6-311+G**

level of theory was used since previous work [99] has indicated that there can be numerical instabilities at the M06-2X level [82]. Higher-order excitations were corrected by taking the difference between CCSDT(Q)/aug-cc-pVDZ and CCSD(T)/aug-cc-pVDZ calculation using the MRCC code [101]. ΔE_{so} and ΔE_{DK} refer to corrections for spin-orbit coupling and relativistic effects, respectively, and these calculations were performed in Molpro with DK specifying the inclusion of Douglas Kroll one-electron integrals [102]. Compared with the original ANL approaches, our calculations are slightly less accurate. The main source of error is that we were unable to use basis sets quite as large as those in the ANL0 and ANL1 schemes, and we have made more extensive use of the explicitly correlated F12 methods to mitigate this.

For all the species considered in this work, only the lowest-energy conformer was considered explicitly. Given the conformational complexity of the species involved in this reaction system, multidimensional torsional potentials were included and were utilised by the coupled classical rotors method implemented in MESMER. To generate these coupled potentials, 100 (two coupled rotors) or 1000 (three coupled rotors) constrained geometry optimisations were performed for a given species corresponding to 36° steps in each torsional coordinate for the coupled rotors. For each constrained optimisation, the coupled torsional coordinates were held rigid. These coupled torsional potentials were fit with a multidimensional Fourier series using the ChemDyME package [103], and the resulting potentials were read by the coupled rotor methods in MESMER to generate fully coupled torsional density of states.

The highest-level “ANL-like” calculations and multidimensional rotor calculations were only performed for the two transition states as, for the temperatures and pressures considered here, the kinetics of the system were found to be insensitive to the pre-reaction complexes in that a change in the well depth by $\pm 4 \text{ kJ mol}^{-1}$ had a negligible impact on the calculated rate coefficients. For methyl formate, both torsions were considered to be separable. For the formate group abstraction transition state (TS_{CHO}), two coupled rotors were considered, with the methyl rotor considered separable with a 1-D hindered rotor treatment, while for the

methyl abstraction transition state (TS_{CH_3}), all three hindered rotors were considered coupled. All constrained optimisations for the hindered rotor calculations were performed at the M06-2X/6-31+G** level.

To consider tunneling a Wentzel–Kramers–Brillouin (WKB) approach [104], as implemented in MESMER, was used. The 1-D tunneling potentials were obtained from intrinsic reaction coordinate (IRC) calculations at the M06-2X/6-31+G** level of theory, and these potentials were corrected for ZPE effects using projected frequency calculations along the IRC. These tunneling potentials were scaled to the high-level energy differences between the transition states and their corresponding pre-reaction complex, and this scaling was maintained whenever transition state energies were altered in our master equation calculations such that the tunneling potential in MESMER was always consistent with the ZPE-corrected energy difference between pre-reaction complex and transition state.

In this work, MESMER was used to solve the energy grained master equation (EGME) for the OH + MF system. As a starting point, rovibrational densities of states were obtained under the rigid rotor harmonic oscillator approximation. Any rotatable bonds were additionally considered explicitly as 1-D or coupled hindered rotors, as described above. These hindered rotor motions were projected out of the molecular Hessian using the methodology of Sharma, Raman, and Green [105]. We coupled the internal modes of a given species to the other internal modes of that species using the coupled classical rotors approach [106] recently implemented in MESMER. This coupling considers how the vibrational modes of a species change upon rotation about an internal bond and this treatment negates the need for a multiconfigurational-type approach which approximates such coupling by considering different conformers of a species as distinct [107]. Currently, our coupled rotor approach neglects coupling between internal rotor modes and other normal modes. For the MESMER simulations, a grain size of 50 cm^{-1} was used, and the energy span was truncated at 25 kJ mol^{-1} above the highest barrier in the system.

3.4.2. Potential energy surface for the reaction of OH + methyl formate

The potential energy surfaces for formate abstraction (Figure 3.8, blue) and methyl abstraction (Figure 3.8, purple) are presented in Figure 3.8. The error in the transition state energies is estimated to be approximately 1 – 2 kJ mol⁻¹. However, they have been fit to the experimental data outlined in this chapter. The OH abstraction reactions proceed via pre- and post-reaction complexes. For formate abstraction, the pre-reaction complex has an energy of -10.4 kJ mol⁻¹ and a transition state barrier of 6.0 kJ mol⁻¹. The pre-reaction complex following methyl abstraction has an energy of -17.1 kJ mol⁻¹ and a barrier of 1.2 kJ mol⁻¹. Despite the presence of the pre-reaction complexes, the positive temperature dependence in the rate coefficients, $k_{\text{OH+MF}}$, indicates that the stabilisation of the pre-reaction complexes does not occur. Furthermore, this work found the kinetics were insensitive to changing the energy of the pre-reaction complex by ± 4 kJ mol⁻¹. The theoretical study of OH + methyl formate by Wu et al. [108] also determined the role of the pre-reaction complex was unimportant above ~ 200 K. Between ~ 233 and 300 K, the Wu et al. [108] predictions of the rate coefficient, $k_{\text{OH+MF}}$, are larger than the experimental value determined by Le Calve et al. [8]. However, the Wu et al. [108] energies have an uncertainty of 0.5 kcal mol⁻¹ (2.1 kJ mol⁻¹), corresponding to a factor of 8.7 uncertainty in $k_{\text{OH+MF}}$ at 233 K. Despite the absolute disagreement between Le Calve and Wu, the temperature-dependent rate coefficients, $k_{\text{OH+MF}}$, determined by Le Calve et al. [8] demonstrate the temperature dependence is becoming shallower below 298 K and hint at a potential increase with decreasing temperature. Jimenez et al. [10] observed the rate coefficient increasing with decreasing temperature between 22 and 66 K. Acceleration of the reaction rate at low temperatures is likely due to the stabilisation of the pre-reaction complexes followed by tunnelling.

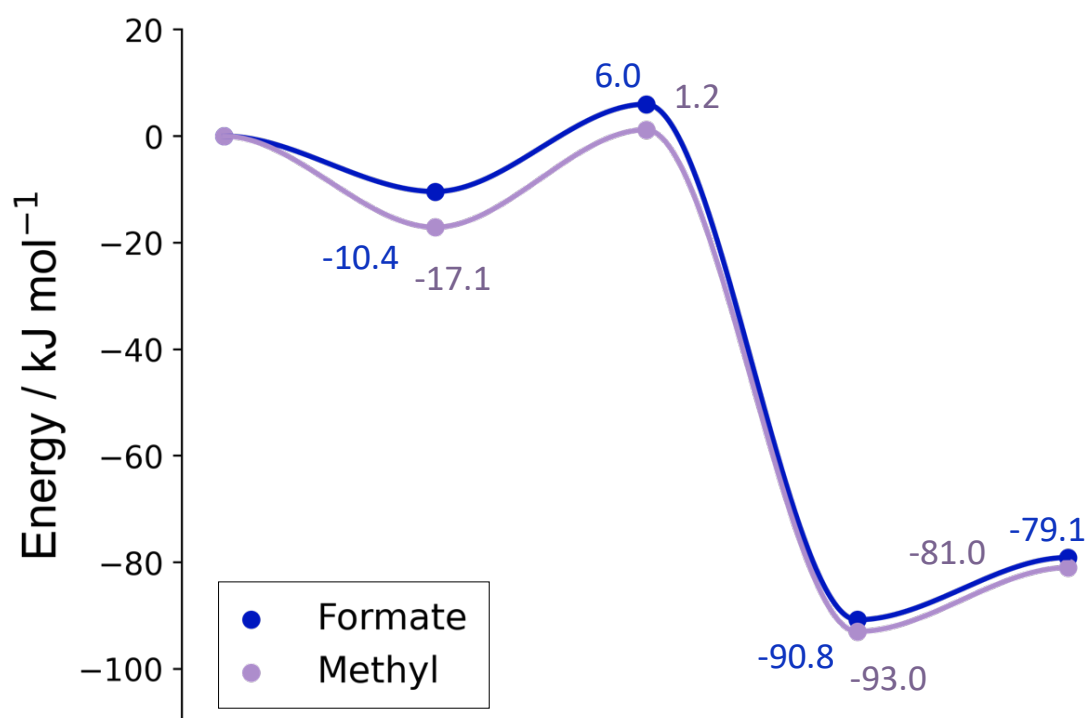


Figure 3.8 – Potential energy surface for formate (blue) and methyl (purple) abstraction by OH. Calculated by Dr Robin Shannon at the CCSD(T)-F12/aug-cc-pVTZ//M06-2X/6-31+G** level of theory, with higher-level “ANI0-like” calculations for the energies of the transition state barriers.

The lowest energy transition state structures for methyl and formate abstraction are presented in Figure 3.9. The transition state energy for methyl abstraction is lower in energy due to stronger hydrogen bonding in the transition state structure (Figure 3.9, Methyl TS A). Hydrogen bonding between the H atom in OH and the carbonyl oxygen atom (2.2 Å in length), coupled with the hydrogen bond interaction between the O in OH and the methyl hydrogen being abstracted, leads to a stabilised ring-like structure. The higher BDE for methyl abstraction (99.8 kcal mol⁻¹ / 418 kJ mol⁻¹) compared with formate abstraction (99.4 kcal mol⁻¹ / 416 kJ mol⁻¹) was, in this case, not indicative of more energy required for abstraction.

The transition state for formate abstraction has weaker hydrogen bonding and is higher in energy. The hydrogen bond in the formate transition state between the H in OH and the ether oxygen is longer (2.7 Å) and hence weaker, than in the methyl transition state. However, formate abstraction is entropically favoured as instead of being locked up in a ring-like transition state, it has a methyl group that

can spin freely. As the temperature increases, formate abstraction is expected to increase due to this entropic benefit.

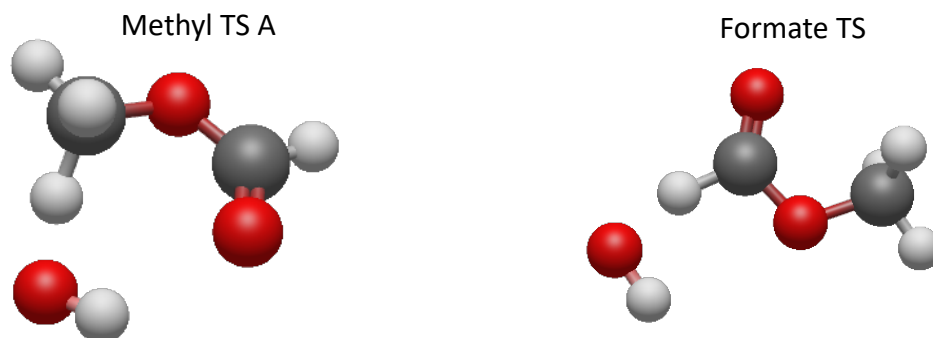


Figure 3.9 – Lowest energy transition states for OH abstraction from methyl formate. Abstraction at the methyl site has two transition states – a low-energy transition state (A) shown on the left and a high-energy transition state (B) presented in Figure 3.17. Abstraction from the formate site has one transition state, shown on the right.

The decreasing secondary KIE illustrated in Figure 3.7, supports the controlling role of hydrogen bonding in the methyl transition state. The secondary KIE at room temperature is ~ 1.5 , indicating OD/OH is involved in the transition state – as described above. As the temperature increases and the secondary KIE decreases, this signals that abstraction at the methyl site may be decreasing, and formate abstraction may be increasing. Increasing formate abstraction corresponds with a decrease in the secondary KIE as the transition state structure is not as heavily influenced by hydrogen bonding and the OH/OD molecule is not as involved in the structure (Figure 3.9, far right). However, there is a reduction in the transition state barriers for both formate and methyl abstraction by OD. As thermal energy increases with temperature, the transition state energies become less significant in controlling the reaction. Decreased importance of the barrier height is a result of more molecules having sufficient energy to overcome the energy barrier and may explain the decreasing secondary KIE with increasing temperature. The theoretical predictions of the reaction's site-specific kinetics are described in more detail, following the discussion of the kinetics of OH + the deuterated isotopomers of methyl formate.

3.5. OH kinetics of the deuterated isotopomers: OH + CH₃OC(O)D, CD₃OC(O)H and CD₃OC(O)D

The kinetics of OH + CH₃OC(O)D (dMF), CD₃OC(O)H (d3MF) and CD₃OC(O)D (d4MF) are presented in Figure 3.10 alongside OH + CH₃OC(O)H (MF). Solid lines through the rate coefficients are non-Arrhenius temperature-dependent fits:

$$k_{\text{OH} + \text{dMF}} = ((6.05 \pm 12.57) \times 10^{-14}) \times \exp((269 \pm 645)/T) \times (T/300)^{(3.18 \pm 1.54)}$$

$$k_{\text{OH} + \text{d3MF}} = ((1.68 \pm 0.51) \times 10^{-15}) \times \exp((1306 \pm 97)/T) \times (T/300)^{(6.03 \pm 0.21)}$$

$$k_{\text{OH} + \text{d4MF}} = ((2.54 \pm 2.22) \times 10^{-14}) \times \exp((156 \pm 264)/T) \times (T/300)^{(4.05 \pm 0.68)}$$

With increasing isotopic substitution, the rate coefficient generally decreases as would be expected according to the KIE. The similarity between the rate coefficients of CH₃OC(O)D and CD₃OC(O)H hints at a similar branching ratio for abstraction from the methyl and formate sites.

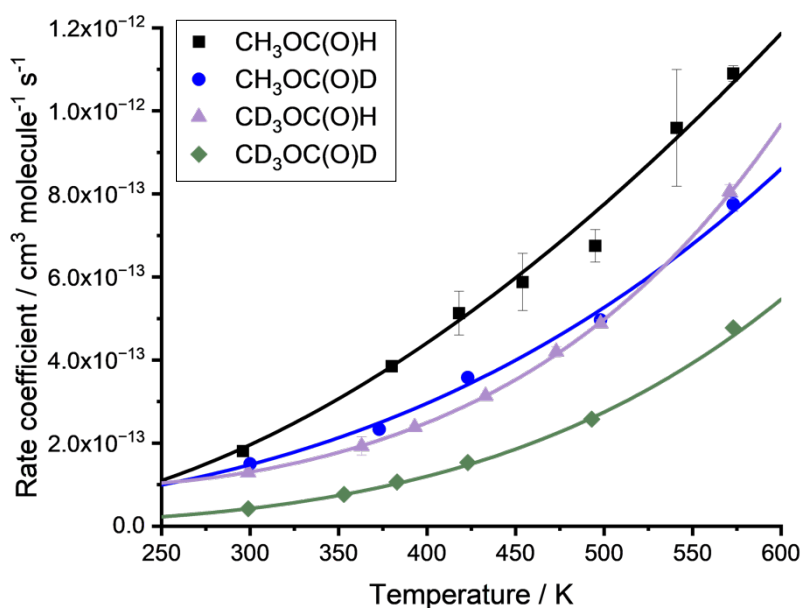


Figure 3.10 – Rate coefficients for the reactions of OH + CH₃OC(O)H (black squares), CH₃OC(O)D (blue circles), CD₃OC(O)H (purple triangles) and CH₃OC(O)D (green diamonds).

Figure 3.11 presents the primary KIE for each isotopomer – CH₃OC(O)H/CH₃OC(O)D (blue circles), CH₃OC(O)H/CD₃OC(O)H (purple triangles) and CH₃OC(O)H/CD₃OC(O)D (green diamonds). The individual points correspond with experimental values where the rate coefficients of CH₃OC(O)H and the

isotopomer have been determined at the same temperature, and the fitted lines are calculated from the non-Arrhenius temperature-dependent fits to the experimental data shown in Figure 3.10. The KIE for the fully deuterated isotopomer, $\text{CH}_3\text{OC}(\text{O})\text{H}/\text{CD}_3\text{OC}(\text{O})\text{D}$, shows the largest KIE, decreasing with increasing temperature. As the temperature increases and more thermal energy is available, changes in the zero point energy become less significant. Therefore, the KIE decreases.

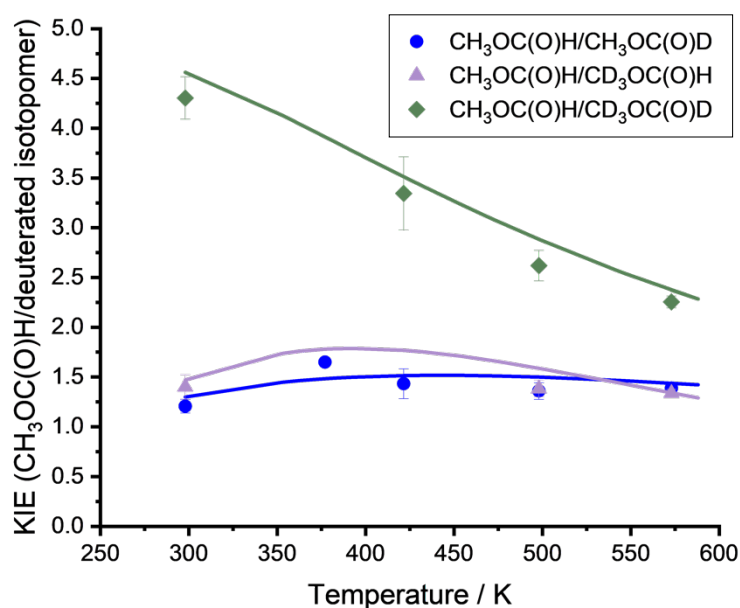


Figure 3.11 – The primary KIE calculated by dividing the rate coefficient, $k_{\text{OH} + \text{MF}}$, with the rate coefficient for each isotopomer. $k_{\text{OH} + \text{MF}}/k_{\text{OH} + \text{dMF}}$ is shown in blue, $k_{\text{OH} + \text{MF}}/k_{\text{OH} + \text{d}_3\text{MF}}$ is shown in purple, and $k_{\text{OH} + \text{MF}}/k_{\text{OH} + \text{d}_4\text{MF}}$ is shown in green. The solid lines are calculated from the non-Arrhenius temperature-dependent fits to the experimental data.

Comparisons between the KIE determined in this work for methyl formate (MF/d₄MF) and the KIE of other oxygenated molecules are presented in Table 3.2 around room temperature (293 – 300 K). The decrease in the KIE between fully deuterated ethane (4.61 ± 0.56) and propane (2.82) is attributed to a decrease in the C-H BDE for hydrogen abstraction by OH. Figure 3.12 illustrates how the KIE changes as a function of the BDE for the main reactive site within the organic molecules outlined in Table 3.2. BDEs are taken from Luo [95]. As the BDE increases, so does the KIE, however, the relationship is not linear. This could be because not all the

BDEs that contribute to the KIE for a given molecule are represented in Figure 3.13. Non-linearity could also hint at other factors controlling the KIE, for example hydrogen bonded pre-reaction complexes. The KIE determined in this work for methyl formate is 4.30 ± 0.21 with BDEs of 416 kJ mol^{-1} and 418 kJ mol^{-1} . Compared with the literature values in Figure 3.12, the KIE for methyl formate is high for a BDE of $416 - 418 \text{ kJ mol}^{-1}$, potentially indicating the KIE is also influenced by hydrogen bonding.

Table 3.2 – The Primary KIE for OH + methyl formate and other organic molecules.

Molecule	T / K	Primary KIE	Reference
Ethane ($\text{C}_2\text{H}_6 / \text{C}_2\text{D}_6$)	293	4.61 ± 0.56	Tully et al. [83]
Propane ($\text{C}_3\text{H}_8 / \text{C}_3\text{D}_8$)	298	2.82^a	Droege and Tully [84]
Methanol	294	2.15 ± 0.13	Hess and Tully [109]
Ethanol	298	2.36 ± 0.06	Carr et al. [110]
Formaldehyde ($\text{HCHO} / \text{DCDO}$)	298	1.66 ± 0.01 , 1.62 ± 0.08	Feilberg et al. [111], D’Anna et al. [112]
Acetaldehyde ($\text{CH}_3\text{CHO} / \text{CD}_3\text{CDO}$)	298	1.65 ± 0.08	D’Anna et al. [112]
Dimethyl ether ($\text{CH}_3\text{OCH}_3 / \text{CD}_3\text{OCD}_3$)	298	2.66 ± 0.19	Carr et al. [113]
Dipropyl ether ($\text{C}_6\text{H}_{14}\text{O} /$ $\text{C}_6\text{D}_{14}\text{O}$)	296	1.93 ± 0.18	Harry et al. [114]
Dibutyl ether ($\text{C}_8\text{H}_{18}\text{O} /$ $\text{C}_8\text{D}_{18}\text{O}$)	296	2.21 ± 0.24	Harry et al. [114]
Acetic acid ($\text{CH}_3\text{C}(\text{O})\text{OH} /$ $\text{CD}_3\text{C}(\text{O})\text{OD}$)	300	7.00 ± 1.27	Szabo et al. [115]
Methyl formate ($\text{CH}_3\text{OC}(\text{O})\text{H} / \text{CD}_3\text{OC}(\text{O})\text{D}$)	298	4.30 ± 0.21	This work ^b

a) No error is reported.

b) Calculated from the temperature dependent fits.

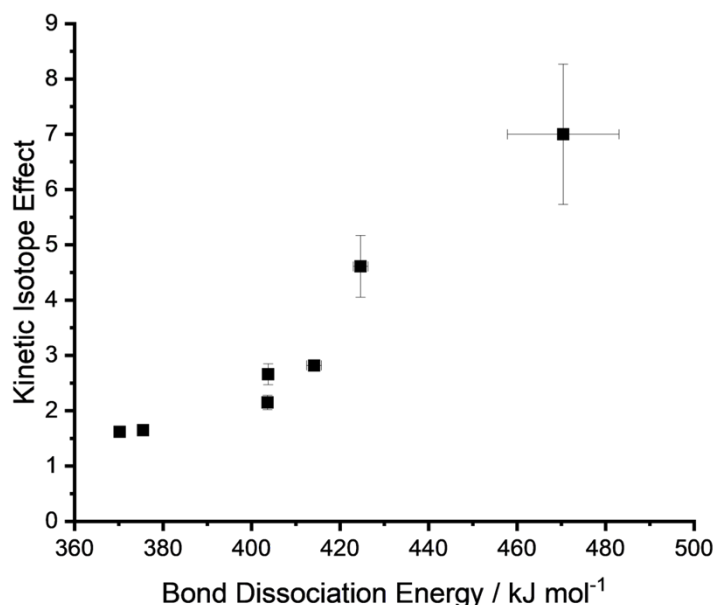


Figure 3.12 – BDEs (C-H) for the major abstraction site in a series of organic molecules alongside their KIEs presented in Table 3.2.

3.6. Extracting site-specific information from deuterated kinetics

The rate coefficients of OH + methyl formate isotopomers can be written as the sum of their site-specific rate coefficients:

$$k(\text{CH}_3\text{OC}(\text{O})\text{H}) = k(\text{CH}_3) + k(\text{H}) \quad \text{E3.7}$$

$$k(\text{CH}_3\text{OC}(\text{O})\text{D}) = k(\text{CH}_3) + k(\text{D}) \quad \text{E3.8}$$

$$k(\text{CD}_3\text{OC}(\text{O})\text{H}) = k(\text{CD}_3) + k(\text{H}) \quad \text{E3.9}$$

$$k(\text{CD}_3\text{OC}(\text{O})\text{D}) = k(\text{CD}_3) + k(\text{D}) \quad \text{E3.10}$$

$$k(\text{CH}_3\text{OC}(\text{O})\text{H}) + k(\text{CD}_3\text{OC}(\text{O})\text{D}) = k(\text{CH}_3\text{OC}(\text{O})\text{D}) + k(\text{CD}_3\text{OC}(\text{O})\text{H}) \quad \text{E3.11}$$

$$k(\text{CH}_3) + k(\text{H}) + k(\text{CD}_3) + k(\text{D}) = k(\text{CH}_3) + k(\text{D}) + k(\text{CD}_3) + k(\text{H}) \quad \text{E3.12}$$

E3.11 is a similar equation to that used by Tully [83] to demonstrate that each site-specific rate coefficient is independent of each other and hence independent of the isotopic content of each reaction site. However, writing the overall rate coefficients as the sum of the site-specific rate coefficients does not mean the site-specific rate coefficients remain the same between each isotopomer. The sum of $k_{\text{MF}} + k_{\text{d4MF}}$ and the sum of $k_{\text{dMF}} + k_{\text{d3MF}}$ are plotted in Figure 3.13. Both sums are equal within error, which either suggests the reactions are not coupled, or there is a common coupling factor.

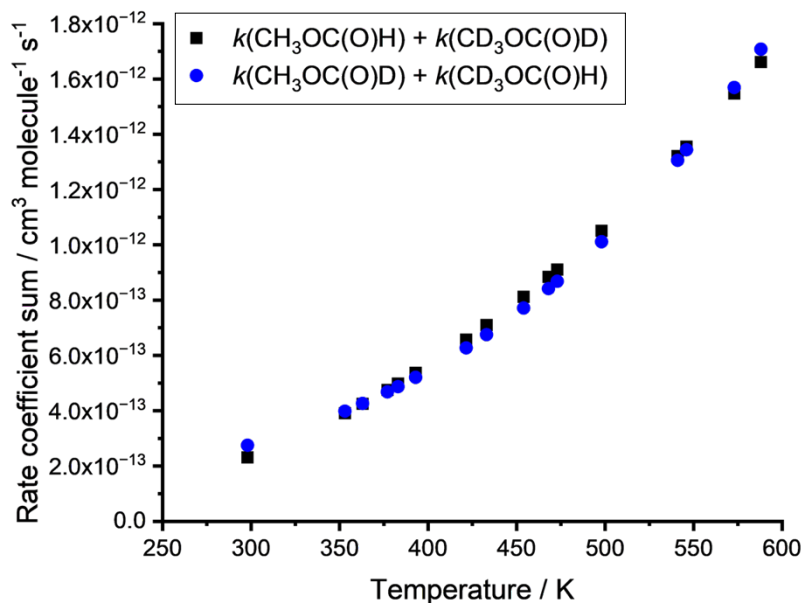


Figure 3.13 – The sum of rate coefficients $k(\text{CH}_3\text{OC(O)H})$ and $k(\text{CD}_3\text{OC(O)D})$ are shown in black squares, whilst the sum of rate coefficients $k(\text{CH}_3\text{OC(O)D})$ and $k(\text{CD}_3\text{OC(O)H})$ are shown in blue. Both pairs of rate coefficients are within error of each other, indicating the reaction sites are independent of a common coupling factor that applies.

The equations F1 and F2 determine the KIE between rate coefficients of MF/dMF (F1) and d3MF/d4MF (F2), probing the KIE from deuteration at the formate site.

$$F1 = \frac{k(\text{CH}_3\text{OC(O)H})}{k(\text{CH}_3\text{OC(O)D})} \quad \text{E3.13}$$

$$F2 = \frac{k(\text{CD}_3\text{OC(O)H})}{k(\text{CD}_3\text{OC(O)D})} \quad \text{E3.14}$$

Equations M1 and M2 probe the KIE of deuterating the methyl site.

$$M1 = \frac{k(\text{CH}_3\text{OC(O)H})}{k(\text{CD}_3\text{OC(O)H})} \quad \text{E3.15}$$

$$M2 = \frac{k(\text{CH}_3\text{OC(O)D})}{k(\text{CD}_3\text{OC(O)D})} \quad \text{E3.16}$$

To experimentally determine whether the reaction sites are coupled or not, the equations F1 and F2 can be manipulated to cancel out the effect of deuteration at the formate site, illustrated qualitatively in E3.17. This leaves the effect of switching from $\text{CH}_3 \rightarrow \text{CD}_3$ (E3.18).

$$\frac{R_H}{R_D} \times \frac{R_D}{R_H} \quad \text{E3.17}$$

$$\frac{F_2}{F_1} = \frac{CD_3OC(O)H}{CD_3OC(O)D} \div \frac{CH_3OC(O)H}{CH_3OC(O)D} = \frac{CD_3OC(O)H}{CD_3OC(O)D} \times \frac{CH_3OC(O)D}{CH_3OC(O)H} \quad \text{E3.18}$$

Likewise, the effect of switching from H → D can be isolated by cancelling deuteration at the methyl site represented qualitatively in E3.19 and calculated in E3.20.

$$\frac{CH_3R}{CD_3R} \times \frac{CD_3R}{CH_3R} \quad \text{E3.19}$$

$$\frac{M_2}{M_1} = \frac{CH_3OC(O)D}{CD_3OC(O)D} \div \frac{CH_3OC(O)H}{CD_3OC(O)H} = \frac{CH_3OC(O)D}{CD_3OC(O)D} \times \frac{CD_3OC(O)H}{CH_3OC(O)H} \quad \text{E3.20}$$

Writing each overall rate coefficient as the sum of the site-specific rate coefficients outlined in E3.7 – E3.10 leads to E3.21. If the reaction sites are independent and deuteration at one site has no impact on the other, then the result of F2/F1 and M2/M1, plotted in Figure 3.14, should be equal to 1.

$$\frac{F_2}{F_1} = \frac{M_2}{M_1} = \frac{k(CD_3)k(D) + k(H)k(CH_3)}{k(CD_3)k(H) + k(D)k(CH_3)} \quad \text{E3.21}$$

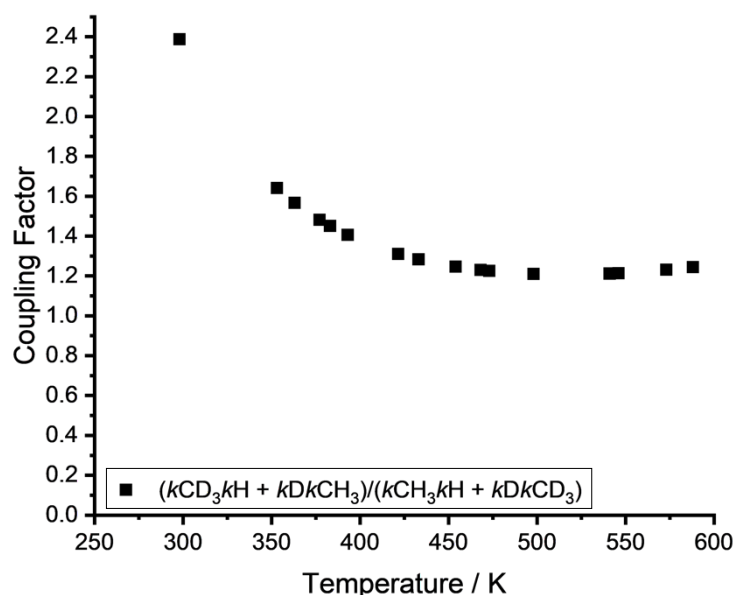


Figure 3.14 – The coupling factor between the methyl (CH₃) and formate (H) reaction sites within methyl formate, determined via E3.18 and E3.20.

F₂/F₁ (E3.18) and M₂/M₁ (E3.20) both have equal coupling factors that are greater than 1, as shown in Figure 3.14. At 300 K, the coupling between the two

reaction sites is 2.38, and decreases with increasing temperature. Expressing E3.7 and E3.10 and E3.8 and E3.9 as the sum of their site-specific rate coefficients provides proof that they are equal, despite being calculated from different combinations of isotopomers. The coupling between the reaction sites decreases with temperature as KIEs become less important with increasing temperature. As more thermal energy is available, differences in the zero point energies of the C-D bonds becomes less significant, and the KIE decreases.

Despite there being a large body of deuterated experiments within the literature, fewer experiments fully explored every combination of isotopomers which is required to untangle the coupling between reaction sites. Nonetheless, coupling between reaction sites appears a unique feature of molecules with more than one or a complex functional group. For molecules with one functional group, coupling factors, calculated via a similar procedure to E3.18 and E3.20, are approximately within error of 1. For propane, coupling varies from 1.08 to 1.01 whilst coupling in ethanol varies from 1.03 to 1.04. As both propane and ethanol have three reactive sites, multiple combinations of coupling can occur, therefore there is not one coupling factor. Acetaldehyde has a coupling factor of 1.03, indicating little coupling between reaction sites.

Coupling in prototypical multifunctional compounds such as methyl formate can potentially be explained by the reaction mechanism. Coupling based on reduced mass cannot explain the larger coupling factor observed in methyl formate compared with molecules with simple functional groups. Acetic acid ($\text{CH}_3\text{C}(\text{O})\text{OH}$) also has reaction sites which are coupled. The kinetics of the deuterated isotopomers of acetic acid reveal the reaction mechanism primarily proceeds via hydrogen abstraction from the acidic OH group. The acetic acid coupling factor is 1.67 at 300 K. This is slightly lower than the coupling in methyl formate. Both esters and carboxylic acids have a carbonyl group ($\text{C}=\text{O}$) adjacent to an oxygen atom, enabling resonance structures. The sharing of electron density between the carbonyl and adjacent oxygen atom is likely extended through the molecule. Coupling between the two reaction sites in this way could explain why altering the

R_1 group in an ester ($R_1OC(O)R_2$) impacts the reaction at the R_2 group. Both reaction mechanisms also involve hydrogen bonding due to the higher O:C ratios.

3.7. Experiments by the Olzmann group at the Karlsruhe Institute of Technology to determine the kinetics of OH + isotopomers of methyl formate

The experimental setup at KIT was similar to that used in this work. In brief, the apparatus consisted of a heatable slow-flow reactor made of stainless steel with a T-shaped arrangement of three quartz windows. The photolysis laser and the fluorescence excitation laser were propagated anti-parallel through the cell via two opposite parallel windows, and the fluorescence was monitored perpendicular to the laser axis through the third window.

In contrast to the Leeds experiments, HNO_3 (synthesised from H_2SO_4 and KNO_3) was used as the OH precursor, and He served as the bath gas. The OH radicals were produced by pulsed photolysis of the precursor with a KrF-excimer laser (Lambda Physik, Compex102) at 248 nm and detected by laser induced fluorescence excited at 282 nm with a frequency-doubled (BBO crystal) dye laser (Lambda Physik ScanMate2E, Coumarin 153 in ethanol). The dye laser was pumped by an XeCl excimer laser (Lambda Physik, Compex102) at 308 nm. The fluorescence after passing through a monochromator (Carl Zeiss, MQ4III, 308 ± 4 nm) was monitored with a photomultiplier tube (Hamamatsu, R22A). The time delay between the pulses of the photolysis and fluorescence excitation laser was set with a delay generator (Stanford, DG535); the repetition rate was 10 Hz.

The gases were stored in stainless steel cylinders, and flows were regulated with mass-flow controllers to avoid accumulation of reaction products in the cell. Pseudo-first order conditions, with $[MF]$ typically in the range 5×10^{14} to 5×10^{16} $cm^{-3} \gg [OH] < 3 \times 10^{13}$ cm^{-3} , were used. The estimated ratios of the initial concentrations of $[MF]_0/[OH]_0$ were always between 150 and 2000, and only single exponential decays of the OH LIF signals were observed. Typical results are illustrated in [Figure 2](#). The notable intercept in the bimolecular plots is essentially due to the use of HNO_3 as the OH precursor. As discussed in Bansch and Olzmann

[116], the reaction of OH with NO₂ impurities formed in the HNO₃ storage cylinder is mainly responsible for this effect. Influences on the rate coefficients (the slope) were minimised by carefully keeping the HNO₃ and hence the NO₂ concentration constants within one series of measurements for differing MF concentrations. Measurements were also performed with both increasing and decreasing MF concentrations, which obtained, within the error margin, identical results; that is, no kind of hysteresis was observed. Moreover, HNO₃ was always freshly synthesised and HNO₃/He mixtures older than 7 days were discarded. The purities of the chemicals used were as follows: CH₃OCHO (Sigma-Aldrich, ≥99.0%), CH₃OCDO (CDN Isotopes, 98.6%, 99.4%-d1), CD₃OCHO (CDN Isotopes, 99.6%, 99.9%-d3), CD₃OCDO (CDN Isotopes, 99.7%, 99.8%-d4), He (Air Liquide, >99.999%), H₂SO₄ (Roth, 98%), KNO₃ (Roth, ≥99%).

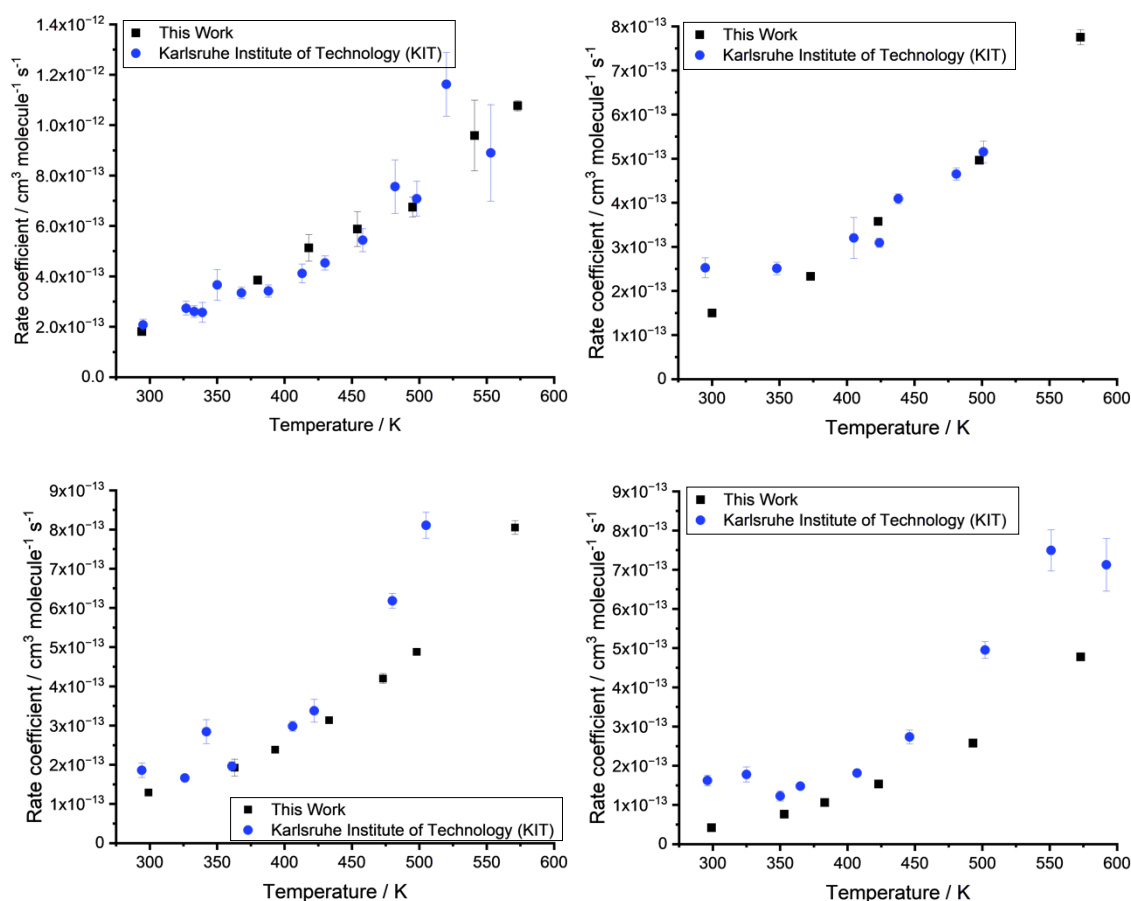


Figure 3.15 – A comparison of rate coefficients for the reactions of OH with CH₃OC(O)H (top left), CH₃OC(O)D (top right), CD₃OC(O)H (bottom left) and CD₃OC(O)D (bottom right) determined in this work (black squares) and by KIT (blue circles).

A comparison between the kinetics determined in the present work at the University of Leeds and at KIT is presented in Figure 3.15. There is generally good agreement between the two experimental studies. However, the kinetics of OH + CD₃OC(O)D is slightly more scattered in the KIT experiments.

3.8. Results of the Theoretical Calculations by Dr Robin Shannon

The potential energy surface for the reaction of OH with methyl formate is outlined above. Dr Robin Shannon fitted the MESMER simulations to the experimental kinetics of each isotopomer presented in this chapter. The built-in Levenberg-Marquardt algorithm in MESMER could not be used as this could only deal with one isotopic system at a time. Instead, a bespoke Python script was used to simultaneously fit the transition state energies in the MESMER input to the experimental data for all isotopic variants. This script ensures that the relative transition state energies for the different isotopic substitutions remained constant as constrained by the difference in ZPEs from the CCSD(T)-F12 harmonic frequencies and the B3LYP anharmonic corrections. A copy of this Python script can be found in the supporting information of Robertson et al. [13].

The MESMER calculated rate coefficients for each methyl formate isotopomer are presented in Figure 3.16. The solid lines represent rate coefficients based on the fitted *ab initio* barriers whilst dashed lines represent *ab initio* calculations with no barrier adjustments. There is generally excellent agreement (within experimental error) between the theoretically calculated rate coefficients and the experimental determinations. With increasing deuteration, the barrier heights increase as outlined in Table 3.3. Although the reaction sites have been experimentally determined as coupled, deuteration at one site leads to a small reduction in the transition state barrier at the other reaction site compared with barriers in undeuterated methyl formate. The fitted barriers for methyl and formate abstraction from CH₃OC(O)H are 0.9 ± 0.6 kJ mol⁻¹ and 4.1 ± 0.9 kJ mol⁻¹, respectively. These barrier heights are fitted to both experimental data from Leeds and KIT, excluding the kinetics of CD₃OC(O)D determined by KIT.

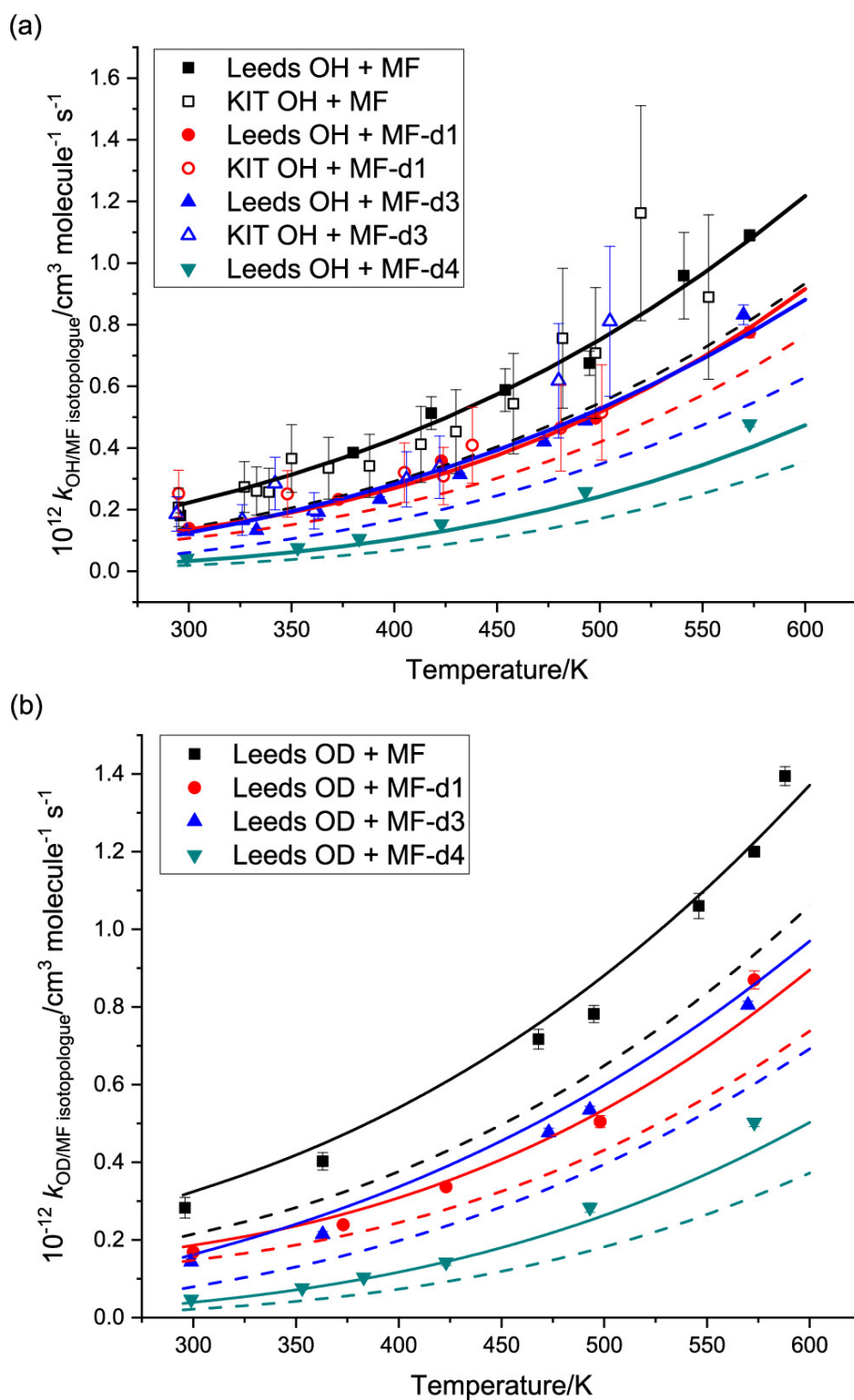


Figure 3.16 – Experimental rate coefficients determined in the present work (filled-in symbols) and by KIT (hollowed symbols) alongside theoretically calculated rate coefficients. Solid lines represent calculated rate coefficients from fitted barriers whilst dashed lines represent calculated rate coefficients from *ab initio* calculations. The top panel is OH-initiated reactions whilst the bottom panel is OD-initiated reactions.

Table 3.3 – Barrier heights (*ab initio* calculated) for each isotopomer of methyl formate.

Isotopomer	Methyl abstraction TS / kJ mol ⁻¹	Formate abstraction TS / kJ mol ⁻¹
OH + CH ₃ OC(O)H	1.3	6.0
OH + CH ₃ OC(O)D	1.2	10.1
OH + CD ₃ OC(O)H	7.2	5.5
OH + CD ₃ OC(O)D	7.2	9.6

Table 3.4 – Branching ratios for the reaction of OH + CH₃OC(O)H calculated by MESMER for methyl and formate abstraction.

Temperature / K	BR for methyl abstraction	BR for formate abstraction
294	0.49	0.51
350	0.43	0.57
400	0.40	0.60
450	0.38	0.62
500	0.38	0.62
550	0.38	0.62
600	0.39	0.61

Between 294 and 450 K the ratio of methyl abstraction decreases. However, between 450 and 550 K the ratio levels off before increasing. At low temperatures (below 294 K), methyl abstraction is favoured due to the lower transition state energy for abstraction. However, the ring-like structure, due to hydrogen bonding, of the methyl abstraction transition state has an entropic cost. Whilst abstraction from the formate site has a higher energy, it is entropically favoured as the methyl group is not locked up in a ring so can spin freely. The entropic benefit of the formate transition state explains why formate abstraction increases with temperature. A higher energy conformer of methyl abstraction is shown in Figure 3.17. This higher energy conformer is accessed by rotation in two torsional coordinates. Therefore, the coupled rotors approach outlined above is required to accurately calculate the branching ratios of methyl formate. In contrast to the rigid ring-like structure of the transition state for methyl abstraction presented in Figure 3.9, the high energy

conformer is more flexible and only has one hydrogen bond interaction between the oxygen of OH and the methyl hydrogen being abstracted.

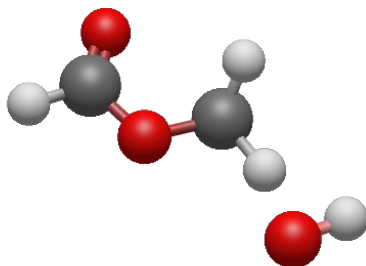
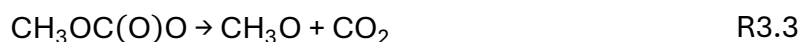
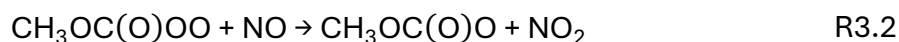
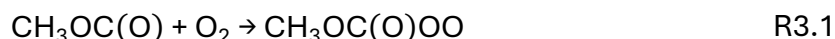


Figure 3.17 – High energy conformer for methyl abstraction accessed via rotation of two torsional coordinates.

3.9. Atmospheric impacts

The atmospheric fate of methyl formate is dominated by OH-initiated oxidation. As methyl formate is primarily used in industrial settings, its release into the atmosphere is most likely to occur in areas with high NO_x. With an atmospheric OH concentration of $\sim 1 \times 10^6$ molecule cm⁻³, the atmospheric lifetime of methyl formate is ~ 64 days. Therefore, it may be transported to low NO_x environments or be exposed to colder temperatures present higher in altitude.

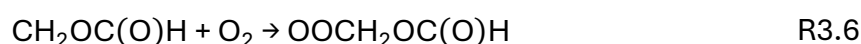
The products of methyl formate OH-initiated oxidation following abstraction at the formate and methyl reaction sites have been determined by Wallington et al. [11]. Abstraction at the formate site leads to the radical CH₃OC(O)•. Subsequent oxygen addition forms CH₃OC(O)OO• (R3.1), which in the presence of NO_x, reacts with NO to form the alkoxy radical CH₃OC(O)O• (R3.2). The alkoxy radical decomposes to CO₂ and CH₃O. CH₃O reacts with oxygen to form formaldehyde (HCHO) and HO₂. Wallington et al. [11] also observed minor production of CH₃OC(O)O₂NO₂ from the reaction of CH₃OC(O)OO• with NO₂.



Whilst there is less literature information on the fate of methyl formate in low NO_x environments, the MCM predicts CH₃OC(O) undergoes decomposition to CH₃ and CO₂. As will be shown in Chapter 4, this is not the case and CH₃OC(O) is likely to be intercepted by oxygen under atmospheric conditions. Therefore, under low NO_x environments CH₃OC(O)OO can participate in radical-radical chemistry. For example, its reaction with HO₂ (R3.5) can lead to the regeneration of OH radicals, contributing to the oxidising capacity of the atmosphere.



Abstraction from the methyl site leads to the CH₂OC(O)H radical which also reacts with oxygen to form OOCH₂OC(O)H. In the presence of NO_x, OOCH₂OC(O)H reacts with NO to form OCH₂OC(O)H. This radical can either undergo an alpha-ester rearrangement to form formic acid or react with oxygen to form formic acid anhydride. Tyndall et al. [47] determined the reaction with oxygen (R3.9) dominates over alpha-ester rearrangement with ~ 67% of the OCH₂OC(O)H undergoing R3.9 and ~ 33% of OCH₂OC(O)H undergoing alpha-ester rearrangement (R3.8).



This work has determined abstraction by OH at the formate site dominates slightly, occurring 51% of the time at 294 K. This is in good agreement with the approximate branching ratios determined by Tyndall et al. [47] of ~ 50:50 (ranging from 60:40 to 40:60). The MCM predicts a branching ratio for formate abstraction of 45%. Whilst this is slightly lower than in this work, once errors in the experimental and theoretically calculated rate coefficients are accounted for, this is in approximate agreement. As demonstrated in Figure 3.18, with decreasing temperature methyl abstraction increases. This will lead to an increase in the yield of formic acid. As concentrations of formic acid are currently underrepresented in atmospheric models, understanding sources of formic acid is important in closing this discrepancy [91].

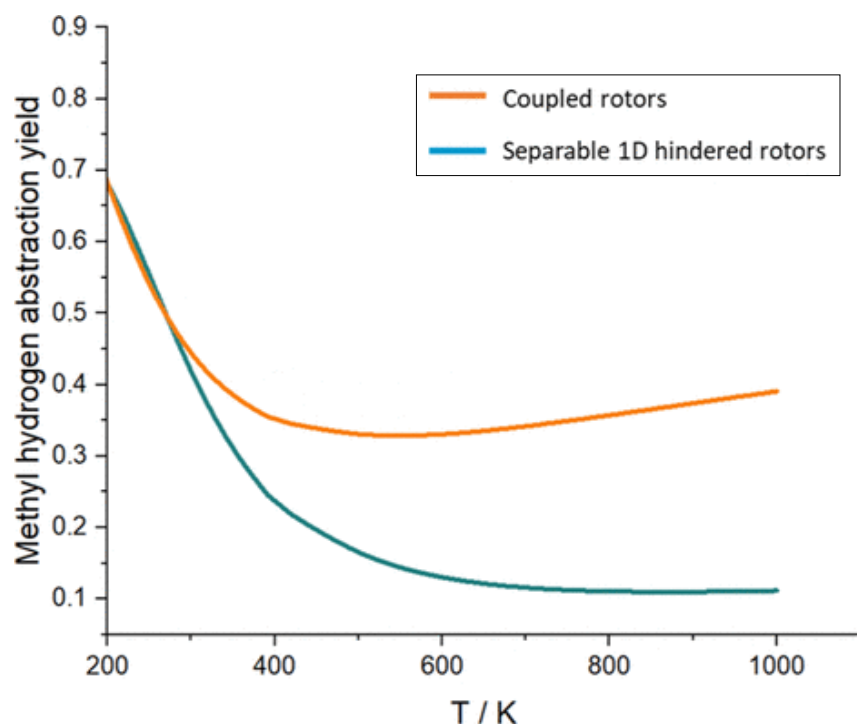


Figure 3.18 – Abstraction ratios from the methyl site in methyl formate as a function of temperature (200 – 1000 K). Reproduced from Robertson et al. [13].

3.10. Conclusions

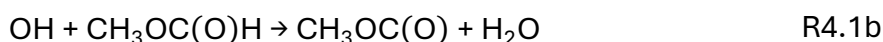
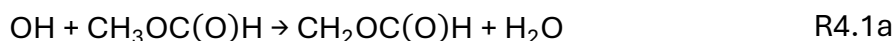
This chapter presents the experimental overall kinetics of OH/OD with $\text{CH}_3\text{OC(O)H}$, $\text{CH}_3\text{OC(O)D}$, $\text{CD}_3\text{OC(O)H}$ and $\text{CD}_3\text{OC(O)D}$. With increasing deuteration, the overall rate coefficients decreased as expected according to the KIE. This work also demonstrates the reaction sites within methyl formate cannot be thought of as distinct from one another, as they are coupled with a coupling factor of 2.38. The secondary KIE ($k_{\text{OD}}/k_{\text{OH}}$) was positive for all isotopomers, indicating the OH/OD radical plays a role within the transition state. Determination of the transition states by Dr Robin Shannon confirmed this and hydrogen bonding was determined to be most influential in the transition state leading to methyl abstraction. The decrease in the secondary KIE as a function of temperature indicated formate abstraction may increase with temperature. Through MESMER fitting to the experimental data, the site-specific kinetics of methyl formate with OH are quantified with 49% abstraction occurring at the methyl site at 294 K. This is calculated to increase with decreasing temperature and decrease with increasing temperature. This work also demonstrated the importance of including coupled hindered rotors in theoretical calculations. Whilst there is excellent agreement between the experimental and theoretical overall kinetics of methyl formate, the

experimental site-specific kinetics of methyl formate have still not been determined.

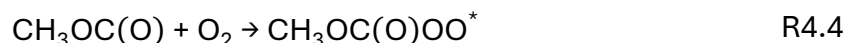
Chapter 4 Branching ratios for OH abstraction from methyl formate via yield studies of OH and OD from deuterated isotopomers

4. Introduction

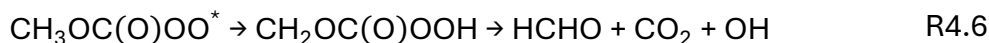
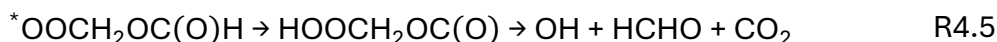
The overall experimental and theoretically determined kinetics of OH + methyl formate and its isotopomers have been outlined in Chapter 3. However, the experimental site-specific kinetics have not been defined. Determining the site-specific kinetics for the reaction of OH with methyl formate is important to quantify its atmospheric impact. The OH-initiated oxidation of methyl formate is shown in Figure 4.1 and proceeds initially via hydrogen abstraction from the methyl or formate group to produce one of two R radicals, CH₂OC(O)H and CH₃OC(O), respectively.



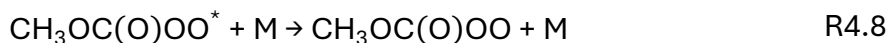
Under atmospheric conditions, R typically reacts with oxygen to form an excited RO₂ with excess vibrational energy, RO₂^{*} (R4.3 & R4.4).



RO₂^{*} can undergo an internal isomerisation to a carbon radical centred species, QOOH, followed by decomposition to OH.



Internal isomerisation is in competition with collisional stabilisation to the thermalised RO₂ via reaction with the bath gas, M.



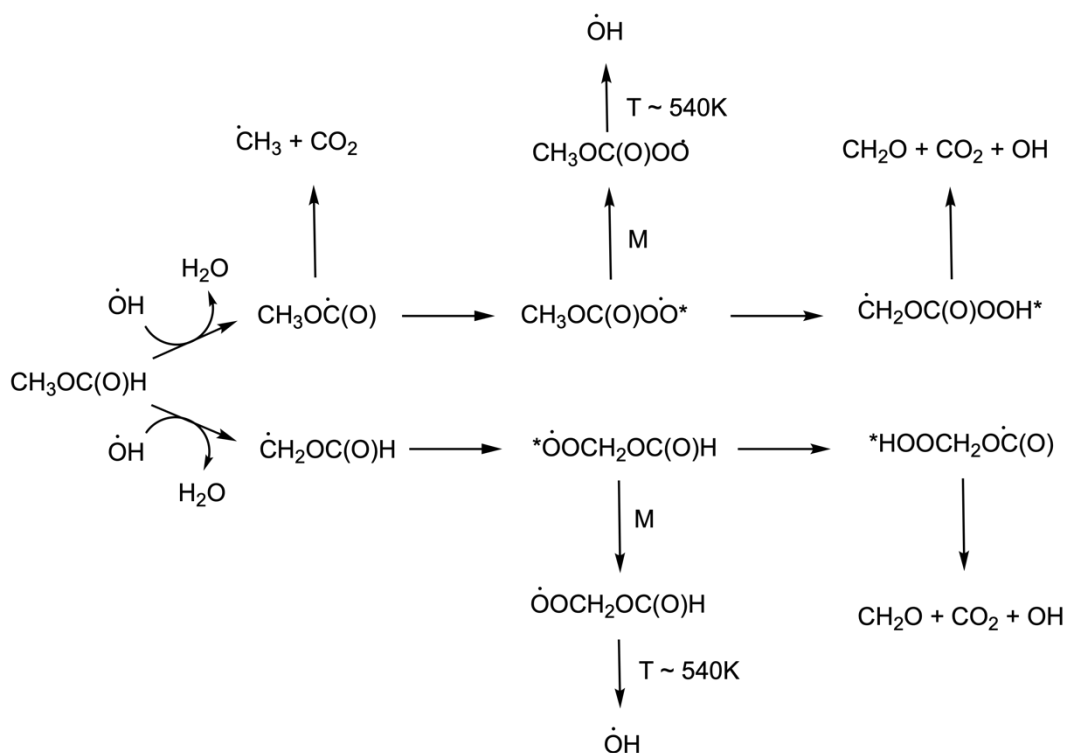


Figure 4.1 – The OH + CH₃OC(O)H reaction scheme under experimental conditions 298 – 523 K and 2 – 150 Torr in the presence of the bath gas (Ar) and oxygen (0 – 1.6 × 10¹⁶ molecule cm⁻³). Above ~ 420 K, the CH₃OC(O) radical undergoes thermal decomposition preventing its addition reaction with O₂ to form the peroxy radical. Peroxy radicals can undergo collisional stabilisation or chemically activated internal isomerisation followed by decomposition to OH. Above ~ 540 K the stabilised peroxy radicals have enough thermal energy to undergo internal isomerisation followed by decomposition to OH. The other products of decomposition, HCHO and CO₂, are proposed based on the structure of the peroxy radicals.

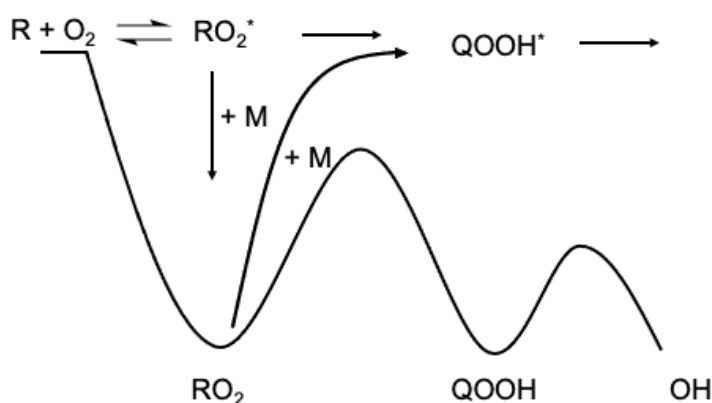


Figure 4.2 – Schematic potential energy surface for the regeneration of OH following the general reaction of R + O₂.

The competition between internal isomerisation and collisional stabilisation can be determined via the production of OH as a function of pressure. Under atmospheric conditions, where $[M]$ is large, RO_2^* radical stabilisation is dominant. Stabilisation of methyl formate generated RO_2^* to the thermalised RO_2 is also dominant under experimental conditions above approximately 100 Torr. Therefore, any additional OH observed at pressures above 100 Torr can be attributed to the thermalised RO_2 , which overcomes the energy barrier for isomerisation to QOOH and subsequent decomposition. The competition between reaction pathways following the reaction of $\text{R} + \text{O}_2$ is illustrated in Figure 4.2. For methyl formate, additional OH was observed at temperatures above ~ 540 K. At these temperatures, the $\text{CH}_3\text{OC}(\text{O})$ radical formed following formate abstraction undergoes rapid thermal decomposition and cannot be intercepted by O_2 under the experimental conditions. Consequently, the OH yields observed can be attributed to abstraction at the methyl group. The overall reaction scheme is summarised in Figure 4.1.

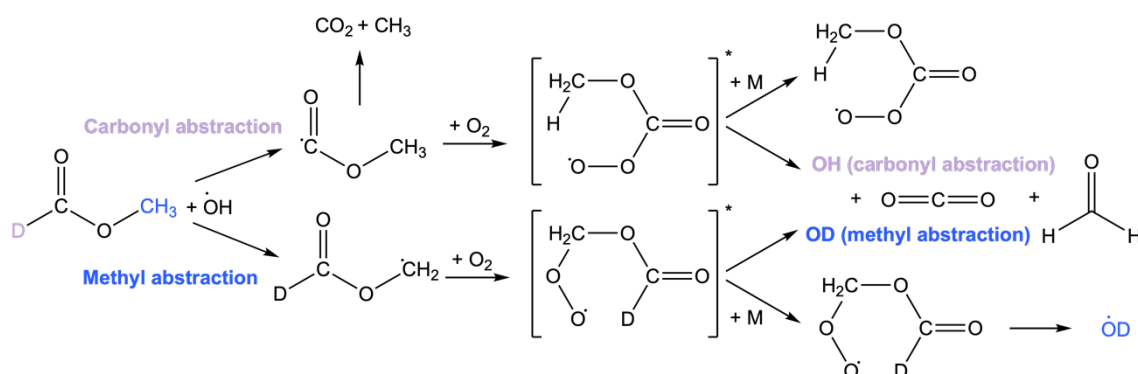


Figure 4.3 – Reaction scheme for $\text{OH} + \text{CH}_3\text{OC}(\text{O})\text{D}$ in the presence of oxygen. Abstraction at the methyl site leads to the regeneration of OD (blue) whilst abstraction from the formate site leads to the regeneration of OH (purple).

As discussed in Chapter 3, selectively deuterated isotopomers of methyl formate can be used to determine the kinetics of the individual elementary reactions of $\text{CH}_2\text{OC}(\text{O})\text{H}$ and CH_3OCO . This provides valuable information on the contribution of abstraction at either site. Understanding the initial branching ratio is important to determine the atmospheric impact of methyl formate, as subsequent reactions of each radical differ and lead to different products with different atmospheric impacts. Selective deuteration of methyl formate via the isotopomers $\text{CH}_3\text{OC}(\text{O})\text{D}$ and $\text{CD}_3\text{OC}(\text{O})\text{H}$, leads to site-specific regeneration of OH and OD. An

example of this is shown in Figure 4.3 for $\text{CH}_3\text{OC}(\text{O})\text{D}$, where OH is regenerated following formate abstraction and OD is regenerated following methyl abstraction.

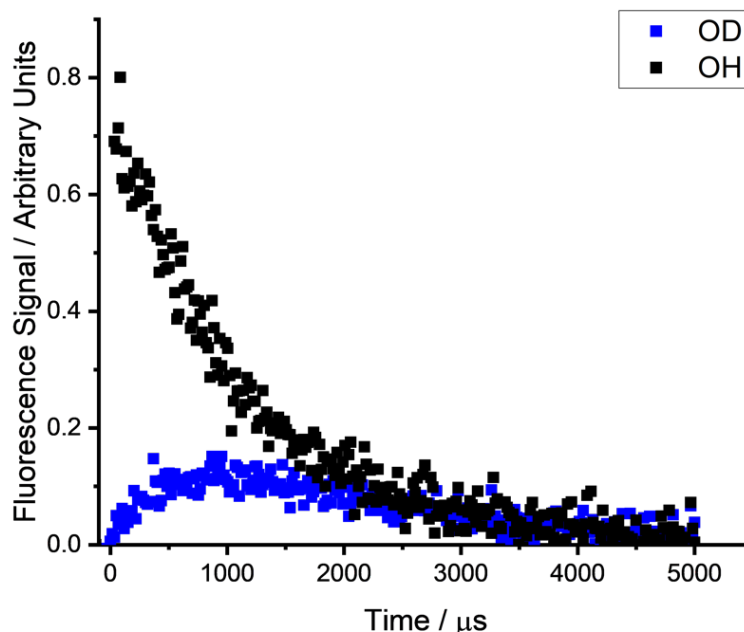


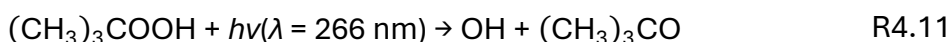
Figure 4.4 – Corresponding OH (black) and OD (blue) traces from the OH-initiated oxidation of $4.24 \times 10^{15} \text{ molecule cm}^{-3}$ $\text{CH}_3\text{OC}(\text{O})\text{D}$ in the presence of $2.09 \times 10^{16} \text{ molecule cm}^{-3}$ of oxygen at 2.8 Torr and 373 K.

For the OH-initiated reaction of $\text{CH}_3\text{OC}(\text{O})\text{D}$ the regeneration of OH is seen as a biexponential decay at low $[\text{O}_2]$ ($[\text{O}_2] \sim 1 \times 10^{15} \text{ molecule cm}^{-3}$). Production of OD from the analogous radical grows from a zero OD background. An example of OH and OD production from $^*\text{OOCH}_2\text{OC}(\text{O})\text{D}$ and $\text{CH}_3\text{OC}(\text{O})\text{OO}^*$ is shown in Figure 4.4. Comparisons of OH and OD yields are used extensively throughout this chapter to determine the reactions of both radicals. Due to the decrease in the total rate coefficient with increasing deuterated substitution, as outlined in the previous chapter, OH and OD yields from the deuterated isotopomer $\text{CD}_3\text{OC}(\text{O})\text{H}$ are limited to two Cl-initiated experiments. Following the oxidation of $\text{CD}_3\text{OC}(\text{O})\text{D}$, the formation of OH and OD was too slow to be resolved over the reaction timescale. Therefore, yield measurements were not experimentally feasible.

4.1. Experimental

4.1.1. Experimental Methods

The experimental setup in this chapter is the same as outlined in Chapter 3 and therefore only a brief description is used here. Laser flash photolysis at 266 nm has been used in conjunction with laser induced fluorescence (LIF) of OH and OD. H₂O₂ (Sigma-Aldrich, 50% wt in H₂O) and tert-butyl peroxide (tBuOOH, (CH₃)₃COOH (Alfa Aesar, 70% wt in H₂O)) were used as OH precursors and (COCl)₂ (Sigma-Aldrich 98%) as the Cl precursor. Experiments to determine yields as a function of pressure and temperature were performed over 3.2 – 65.8 Torr and 298 – 523 K under pseudo-first order conditions with the ester in excess. Concentrations of added oxygen were varied, ranging from no additional oxygen, beyond the background impurity, to additions of up to $\sim 5 \times 10^{16}$ molecule cm³.



Throughout all the experiments there remained a background oxygen concentration. The source of background oxygen is due to a cell leak rate of 51 mTorr min⁻¹. Background oxygen levels ranged from $\sim 2.4 \times 10^{14}$ molecule cm⁻³ for a flow rate of 80 mL min⁻¹ to $\sim 1.2 \times 10^{15}$ molecule cm⁻³ at a flow rate of 400 mL min⁻¹. Oxygen may also come from the bubbler delivery of H₂O₂ as it decomposes (R4.9); H₂O₂ decomposition can be exacerbated upon contact with the metal pipework. However, the background oxygen concentration remains in the presence of alternative precursors (CH₃)₃COOH (R4.11) and (COCl)₂, whose reactions are outlined in Appendix B.

Remaining reactants included CH₃OC(O)H (Sigma-Aldrich 99%), CH₃OC(O)D (Sigma-Aldrich 99%), CD₃OC(O)H (Sigma-Aldrich 99%), CD₃OC(O)D (QMX Laboratories 99%), C₂H₅OC₂H₅ (Sigma-Aldrich $\geq 99\%$), O₂ (BOC, 99.5%), argon (BOC 99.998%) and helium (BOC 99.999%).

4.1.2. Data analysis

For OH-initiated experiments, OH decay traces were biexponential at low oxygen concentrations due to the regeneration of OH via the internal isomerisation of the excited RO_2^* . An example biexponential decay is shown in Figure 4.5 alongside insets illustrating the residuals for a biexponential and single exponential fit. Biexponential fits have been derived according to the scheme outlined in Figure 4.6. The rate coefficient for the initial hydrogen abstraction reaction by OH is denoted k_{MF} and leads to a radical R. The radical reacts with oxygen with a rate coefficient, k_{R} , to produce RO_2^* . As the $\text{R} + \text{O}_2$ reaction is not a rate determining step, the production of RO_2^* can be described by k_{Ar} , which combines k_{MF} and k_{R} . A derivation of the biexponential equation is shown in Appendix A alongside fits where k_{MF} and k_{R} are separated and combined, showing no influence on the yield of OH. Collisional stabilisation of RO_2^* is described as k_{Stab} whilst the chemically activated internal isomerisation and decomposition is described as k_{Regen} . The biexponential fit shown in Figure 4.5, extracts k_{Ar} , k_{Regen} and k_{Stab} .

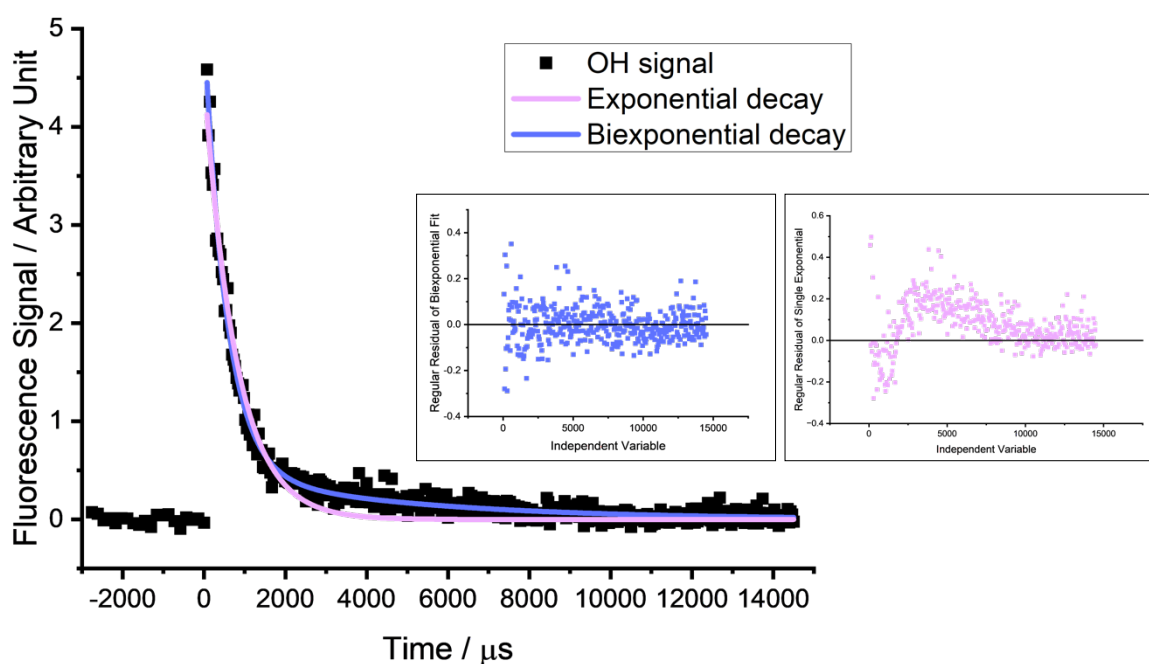
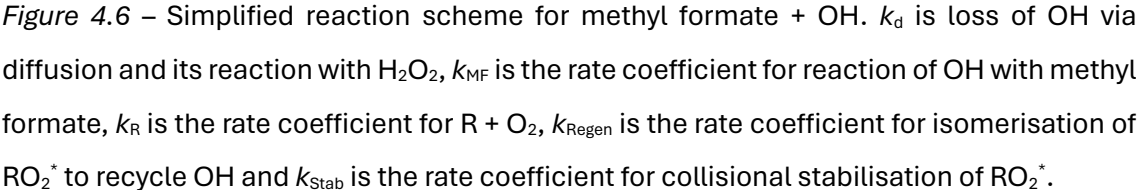


Figure 4.5 – Biexponential decay following the OH-initiated oxidation of 1.87×10^{15} molecule cm^{-3} methyl formate at 90 Torr and 515 K.



Yields of OH were determined by taking the ratio of OH formed from RO_2^* (k_{Regen}) divided by the total loss of RO_2^* ($k_{\text{Regen}} + k_{\text{Stab}}$) (E4.1).

When $\sim 1 \times 10^{15}$ molecule cm^{-3} molecular oxygen was added, the OH decays became single exponential. This is due to an increase in the rate of $\text{R} + \text{O}_2$ which rapidly forms RO_2^* and consequently leads to the regeneration of OH on a faster timescale such that $k_{\text{R}}[\text{R}][\text{O}_2] + k_{\text{Regen}}[\text{RO}_2^*] + k_{\text{Stab}}[\text{RO}_2^*] \gg k_{\text{MF}}[\text{CH}_3\text{OC}(\text{O})\text{H}]$. Therefore, the only rate-determining step becomes the loss of OH with methyl formate in the presence of oxygen, k_{O_2} . The relationship between k_{Ar} and k_{O_2} can be described by E4.2 with the resulting relationship for the OH yield shown in E4.3.

$$Y_{OH} = 1 - \frac{k_{O_2}}{k_{Ar}} \quad \text{E4.3}$$

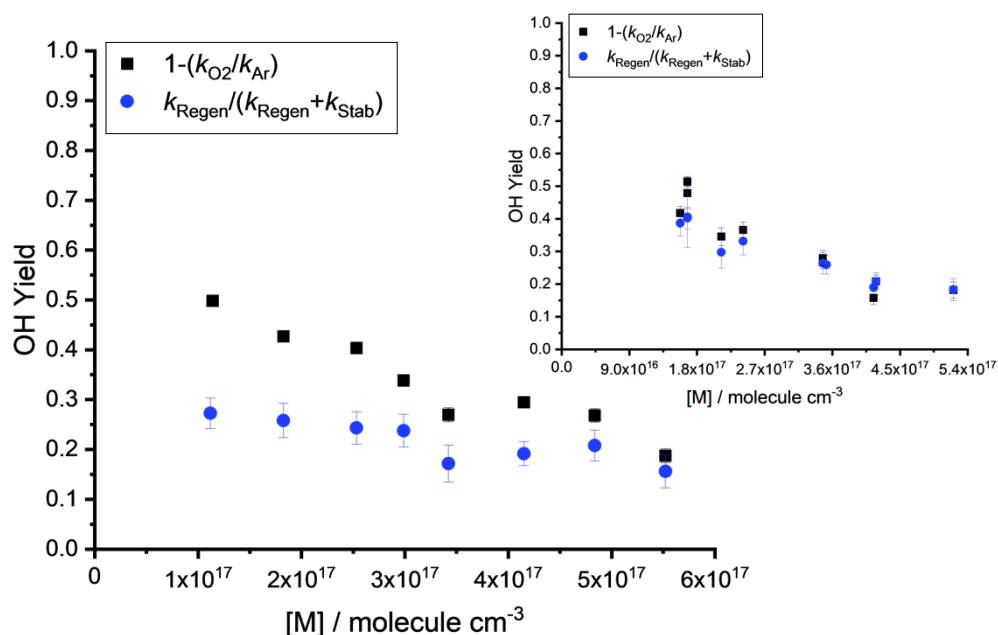


Figure 4.7 – OH yields as a function of pressure from the OH-initiated reaction of $\text{CH}_3\text{OC(O)H}$ in argon. Yields in black are calculated via E3 whilst yields in blue are calculated with E1. The inset at 298 K shows good agreement between the two methods whilst the main figure at 423 K, shows a discrepancy between the yields calculated via the two methods. The discrepancy is due to the thermal decomposition of $\text{CH}_3\text{OC(O)}$. In the presence of oxygen larger yields of OH are observed due to the reaction of $\text{CH}_3\text{OC(O)} + \text{oxygen}$ regenerating OH.

Determining the yields via the biexponential fit (E4.1) can lead to an underprediction of the OH yield if decomposition of the R radical occurs. The Figure 4.7 inset shows OH yields calculated via both methods agree at 298 K. However, there is a disagreement in the OH yields at 423 K as thermal decomposition of $\text{CH}_3\text{OC(O)}$ now occurs and a higher concentration of oxygen than is present in the background is required to intercept R. Due to this potential to underpredict the OH yield, the OH yields presented in this work have been determined from the pseudo-first order rate with and without added oxygen (E4.3).

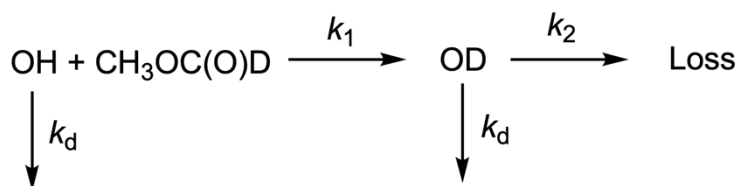


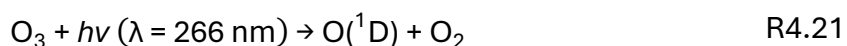
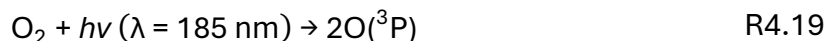
Figure 4.8 – Simplified reaction scheme for the growth and decay of OD from the OH-initiated oxidation of $\text{CH}_3\text{OC(O)D}$. k_d represents diffusional loss.

OD traces from the OH-initiated oxidation of CH₃OC(O)D were fit with E4.4, derived from the simplified reaction scheme shown in Figure 4.8. This scheme was also used to fit OH and OD traces from Cl initiated reactions where the rate determining step was the initial hydrogen abstraction.

$$\text{OD} \times \left(\left(\frac{-k_1}{(k_1 - k_2 + k_d)} \right) \times (\exp^{(-k_1 + k_d)t} - \exp^{-k_2 t}) \right) + b \quad \text{E4.4}$$

4.1.3. OD signal calibration

OD yields were determined via laser induced fluorescence of OD at $\lambda \sim 307$ nm, which grows from a zero OD background, as seen in Figure 4.4. The time profiles of OD traces were fit to extract the maximum signal height which was divided by a 100% signal reference to determine the yield ratio of OD formed. The OH signal at time zero represents 100% signal so was used as the reference after the calibration ratio of OH:OD was determined. To calibrate OH and OD responses, ozone was produced via the photolysis of oxygen at 185 nm with a mercury lamp and flowed into the reaction cell where it was photolysed at 266 nm to O(¹D) that reacted with fixed, excess amounts of H₂O or D₂O to OH and OD respectively (R4.19 – R4.23).



Spectra of OH and OD were then taken by scanning over a range of OH and OD lines, under identical PMT settings and LIF output conditions. This was repeated between 298 and 473 K and 6 – 133 Torr. The chosen lines are shown in Figure 4.9 and correspond to laser induced fluorescence of OD (Q₁(1)) at 307.248 nm and OH (R₁(1)) at 307.290 nm. They have an experimental 1:1 ratio and are independent of temperature and pressure, within two standard deviations. LIFBASE predicted OH and OD spectra between 307.175 and 307.450 nm are shown in Figure 4.10 at 300 K

[14]. LIFBASE predicts an OH/OD ratio of 1.08 at 300 K and 0.94 at 500 K, consistent with a 1:1 ratio within the 2σ experimental error.

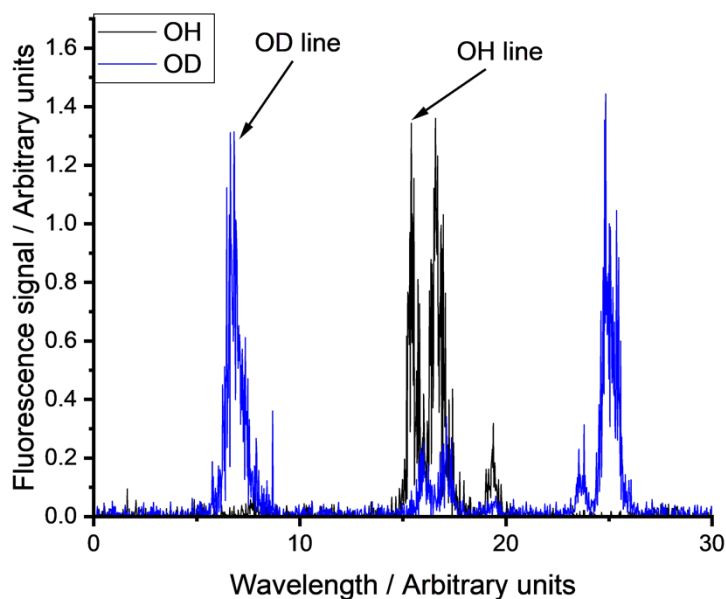


Figure 4.9 – Example spectra of OH and OD at 20 Torr and 298 K show a 1:1 relationship between the OH and OD signal. The OH and OD lines chosen in this work are shown with arrows and correspond to the $A^2\Sigma^+ (v'=0) \leftarrow X^2\Pi_i (v''=0)$ transition with rotational assignments $R_1(1)$ and $Q_1(1)$, respectively.

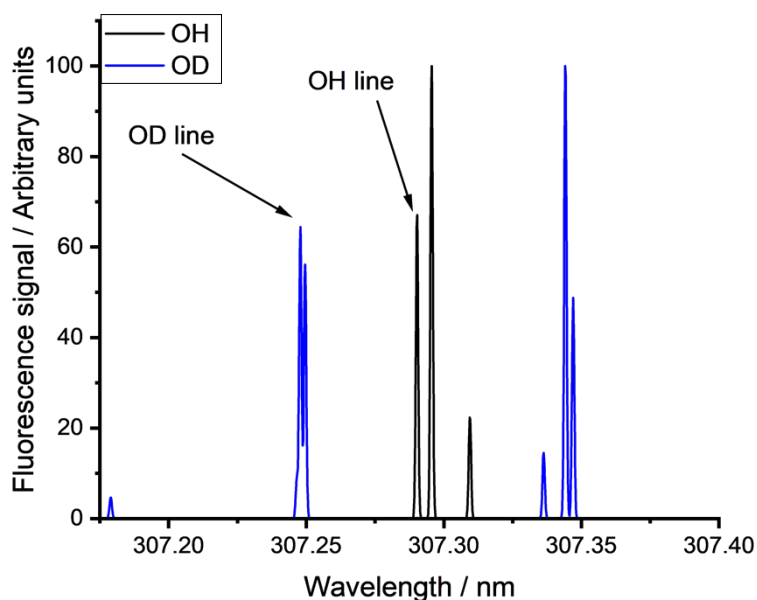


Figure 4.10 – OH (black) and OD (blue) spectra under vacuum between 307.1 – 307.4 nm at 300 K, as predicted by LIFBASE [14]. The OH and OD lines chosen in this work are shown with arrows and correspond to the $A^2\Sigma^+ (v'=0) \leftarrow X^2\Pi_i (v''=0)$ transition with rotational assignments $R_1(1)$ and $Q_1(1)$, respectively.

4.2. Initial temperature-dependent rate coefficients for $\text{CH}_3\text{OC(O)}$ and $\text{CH}_2\text{OC(O)D} + \text{O}_2$ in the low-pressure (well-skipping) region

4.2.1. $\text{R} + \text{O}_2$ kinetics

The radicals $\text{CH}_3\text{OC(O)}$ and $\text{CH}_2\text{OC(O)H}$ are formed following initial hydrogen abstraction from the carbonyl and methyl sites in methyl formate. Their atmospheric fate is addition with oxygen to form $\text{CH}_3\text{OC(O)OO}$ and $\text{OOCH}_2\text{OC(O)H}$. Determining the rate coefficients for these reactions is a key step in understanding the atmospheric oxidation of methyl formate. The Cl-initiated oxidation of $\text{CH}_3\text{OC(O)D}$ has been used to determine the reactions of both radicals, $\text{CH}_3\text{OC(O)}$ and $\text{CH}_2\text{OC(O)D}$, with oxygen. Using the same laser induced fluorescence and laser flash photolysis experimental set-up described in section 4.2.1 and for a fixed pressure (between 8 and 84 Torr), temperature (between 298 and 573 K), and concentration of Cl and $\text{CH}_3\text{OC(O)D}$, experiments were repeated under varying oxygen concentrations from 5.94×10^{13} molecule cm^{-3} to 5.05×10^{16} molecule cm^{-3} to determine the rate coefficients for reactions of $\text{CH}_3\text{OC(O)}$ (from OH detection) and $\text{CH}_2\text{OC(O)D}$ (from OD detection) with oxygen. Decay traces of OH were fit globally (OD traces were also fit globally, independent to OH) with a triexponential equation derived by Dr Mark Blitz, according to the reaction scheme outlined in Figure 4.11. The equation can be found in Appendix A. The Cl-initiated oxidation of $\text{CH}_3\text{OC(O)D}$, is faster than the OH-initiated oxidation, therefore increasing the rate of k_{Cl} and ensuring k_{R} is the rate determining step. Values of k_{R} and k_{D} are extracted following the independent global analysis of OH and OD traces, with k_{Cl} fixed and k_{D} fixed at zero for OD trace analysis ($\text{CH}_2\text{OC(O)D}$ does not undergo thermal decomposition). The background oxygen concentration was allowed to float, leading to background oxygen concentrations in the range 6.4×10^{13} to 7.6×10^{14} molecule cm^{-3} .

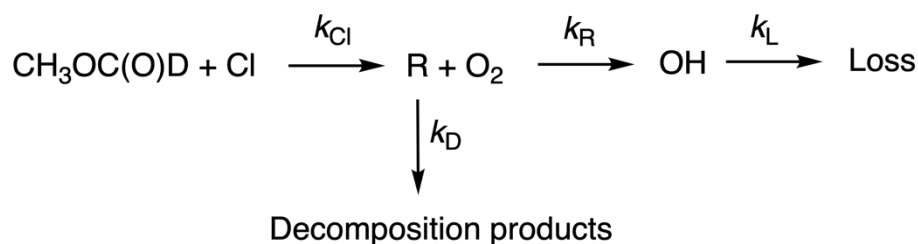


Figure 4.11 – Reaction schematic used to derive the equation to fit the traces of OH and OD globally to determine k_{R} and k_{D} .

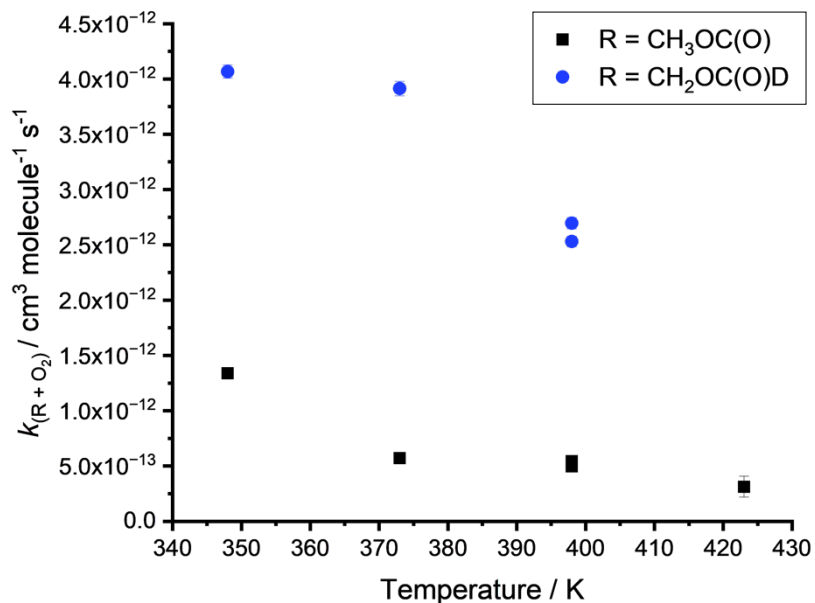


Figure 4.12 – Temperature-dependent rate coefficients for the reactions of R radicals CH₃OC(O) (black squares) and CH₂OC(O)D (blue circles) with O₂ determined between 8 and 9 Torr.

This work has primarily explored the temperature dependence of the R + O₂ rate coefficients, which decrease with increasing temperature, as shown in Figure 4.12 at 8 – 9 Torr. This is expected from barrierless reactions as increases in energy, due to increasing temperature, promote re-dissociation back to the reactants. Figure 4.12 also illustrates the difference in reactivity between an ether-centred radical, CH₂OC(O)D + O₂, and the formate-centred radical, CH₃OC(O) + O₂. At 8 Torr and 348 K, the rate coefficients are $(4.07 \pm 0.06) \times 10^{-12} \text{ cm}^3 \text{ molecule}^{-1} \text{ s}^{-1}$ and $(1.34 \pm 0.03) \times 10^{-12} \text{ cm}^3 \text{ molecule}^{-1} \text{ s}^{-1}$, respectively. As the rate coefficients were determined at 8 Torr, direct comparisons between the present work and high-pressure limiting rate coefficients presented in the literature cannot be made. However, a similar trend demonstrating increased reactivity for ether-centred radicals is observed. For example, the rate coefficients for CH₃OCH₂ and CH₃CH₂OCHCH₃ + O₂ as determined by Potter et al. [117] are $(0.94 \pm 0.04) \times 10^{-11} \text{ cm}^3 \text{ molecule}^{-1} \text{ s}^{-1}$ and $(3.10 \pm 0.55) \times 10^{-11} \text{ cm}^3 \text{ molecule}^{-1} \text{ s}^{-1}$, respectively, compared to $(5.07 \pm 0.16) \times 10^{-12} \text{ cm}^3 \text{ molecule}^{-1} \text{ s}^{-1}$ for CH₃C(O) + O₂ and $(5.37 \pm 0.15) \times 10^{-12} \text{ cm}^3 \text{ molecule}^{-1} \text{ s}^{-1}$ for C₂H₅C(O) + O₂, determined by Romero et al. [118]. These results suggest a stronger activating effect from an ether group over a carbonyl

group, likely due to the electron-donating effect of the ether oxygen. The difference between the ether and carbonyl-centred (formate) radicals determined in this work is $2.70 \times 10^{-12} \text{ cm}^3 \text{ molecule}^{-1} \text{ s}^{-1}$, smaller than the $4.33 \times 10^{-12} \text{ cm}^3 \text{ molecule}^{-1} \text{ s}^{-1}$ difference in rate coefficient between $\text{CH}_3\text{OCH}_2 + \text{O}_2$ and $\text{CH}_3\text{C}(\text{O}) + \text{O}_2$. The smaller difference in this work could be attributed to the proximity of the ether and carbonyl functional groups, which share electrons. However, further experiments to determine the high pressure rate coefficients are required to make a definitive conclusion.

Figure 4.13 presents rate coefficients as a function of pressure, determined for the $\text{CH}_3\text{OC}(\text{O}) + \text{O}_2$ (left) reaction, and $\text{CH}_2\text{OC}(\text{O})\text{D} + \text{O}_2$ (right). The rate coefficients increase with pressure due to stabilisation of the excited RO_2^* radicals removing the energy required for dissociation back to R and O_2 .

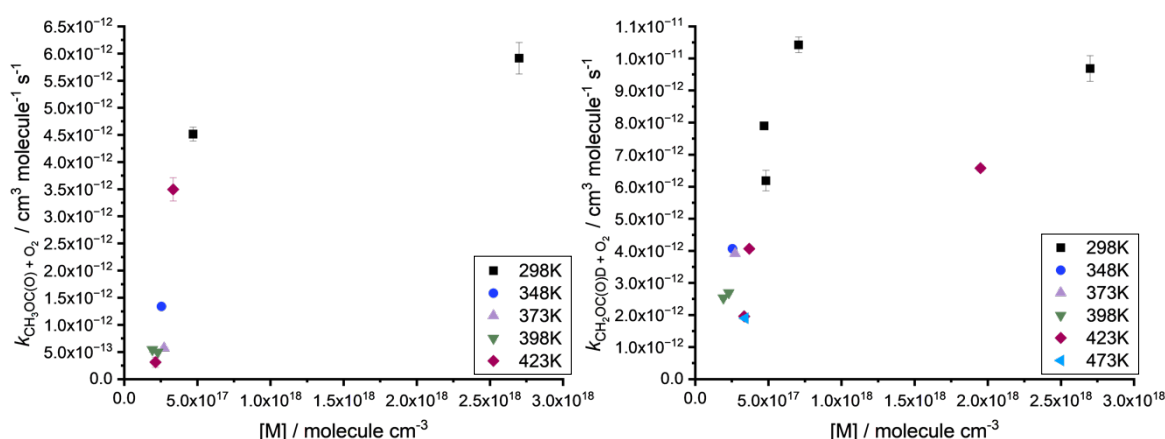


Figure 4.13 – Bimolecular rate coefficients for $\text{CH}_3\text{OC}(\text{O}) + \text{O}_2$ (left) and $\text{CH}_2\text{OC}(\text{O})\text{D} + \text{O}_2$ (right) determined from the global analysis of respective OH and OD traces as a function of pressure and temperature.

4.2.2. Evidence for R decomposition

Figure 4.14 shows bimolecular plots for both R + O_2 radicals using the individual analysis of each trace at 298 K (Figure 4.14, right) and 423 K (Figure 4.14, left). No background oxygen was included in the individual analysis, therefore, traces at zero added oxygen have been omitted. A significant feature of the plots in Figure 4.14 is the dramatic change in intercept between 298 K and 423 K for the $\text{CH}_3\text{OC}(\text{O})$ radical (Figure 4.14, black squares). The high intercept represents the

rate of $\text{CH}_3\text{OC}(\text{O})$ decomposition which is $\sim 30,000 \text{ s}^{-1}$ at 423 K, increasing from $\sim 10,000 \text{ s}^{-1}$ at 398 K (Appendix C, Figure C.1). The intercepts of $\sim 2000 \text{ s}^{-1}$ for both radicals at 298 K and the $\text{CH}_2\text{OC}(\text{O})\text{D}$ radical at 423 K is due to the background oxygen concentration. At 423 K, the intercept of the $\text{CH}_2\text{OC}(\text{O})\text{D} + \text{O}_2$ bimolecular plot is $\sim 2800 \text{ s}^{-1}$. Using the slope of the plot, $3.83 \times 10^{-12} \text{ cm}^3 \text{ molecule}^{-1} \text{ s}^{-1}$, and assuming the true intercept is zero implies a background oxygen concentration of $7.31 \times 10^{14} \text{ molecule cm}^{-3}$.

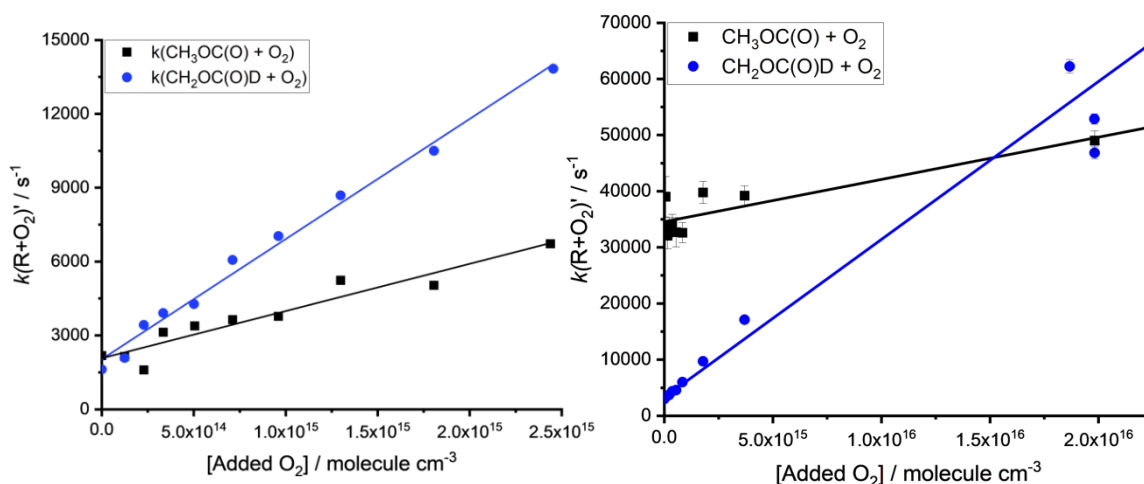


Figure 4.14 – Bimolecular plots for $\text{CH}_3\text{OC}(\text{O})$ (black squares) and $\text{CH}_2\text{OC}(\text{O})\text{D}$ (blue circles) + O_2 at 423 K (left) and 298 K (right). Both bimolecular plots were determined at 14 Torr.

Combustion-focused computational studies suggest $\text{CH}_3\text{OC}(\text{O})$, formed following hydrogen abstraction from the formate group, undergoes chemically activated decomposition (R4.24) [119].



Chemically activated decomposition occurs when a molecule is formed with sufficient energy to initiate another reaction. In this case, the excess energy of the $\text{CH}_3\text{OC}(\text{O})$ radical may lead to dissociation [120]. However, as illustrated in Figure 4.14, $\text{CH}_3\text{OC}(\text{O})$ decomposition does not occur at room temperature and is a thermal process. Due to increasing thermal energy, the rate of $\text{CH}_3\text{OC}(\text{O})$ radical decomposition increases with increasing temperature. This work determined values for $\text{CH}_3\text{OC}(\text{O})$ decomposition via the global analysis of OH traces which also determined $k(\text{CH}_3\text{OC}(\text{O}) + \text{O}_2)$ simultaneously. High uncertainty in the background oxygen concentration led to high uncertainty in the value for $\text{CH}_3\text{OC}(\text{O})$

decomposition, leading to large experimental errors. To reduce this uncertainty, Dr Lavinia Onel performed similar experiments with lower additions of oxygen beginning at $\sim 1 \times 10^{13}$ molecule cm^{-3} . Figure 4.15 illustrates the decomposition rates of $\text{CH}_3\text{OC}(\text{O})$ as a function of temperature, determined in this work and by Dr Lavinia Onel.

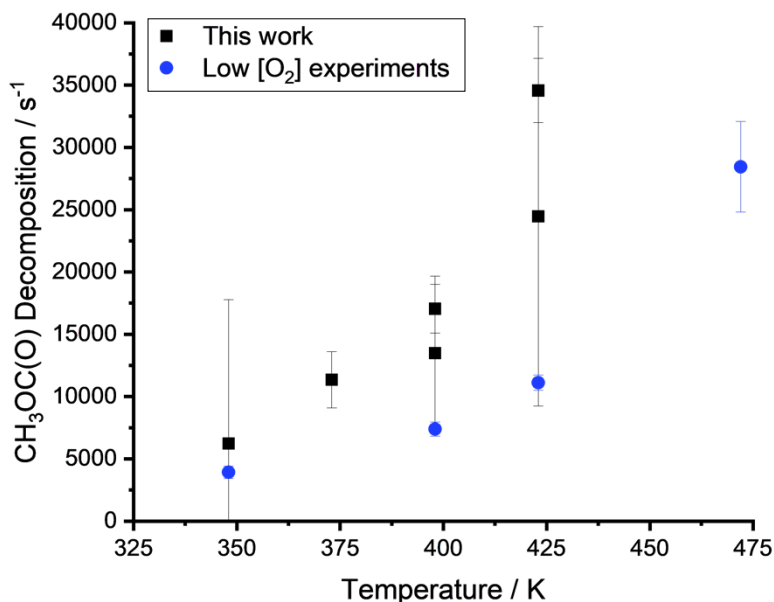


Figure 4.15 – Decomposition rates of $\text{CH}_3\text{OC}(\text{O})$ as determined from this work (black squares) and experiments by Dr Lavinia Onel under lower oxygen additions ($\sim 1 \times 10^{13} - 1 \times 10^{15}$ molecule cm^{-3}).

At high temperatures when all of the $\text{CH}_3\text{OC}(\text{O})$ radical undergoes thermal decomposition, OH yields from $\text{OH} + \text{CH}_3\text{OC}(\text{O})\text{H}$ can be attributed to abstraction from the methyl site, leading to high temperature branching ratios for methyl abstraction.

4.3. Experimental yields from the OH and Cl initiated oxidation of $\text{CH}_3\text{OC}(\text{O})\text{H} + \text{O}_2$

The association reactions between $\text{R} + \text{O}_2$, outlined in section 4.2.1, produce excited RO_2^* radicals, $\text{CH}_3\text{OC}(\text{O})\text{OO}^*$ and $^*\text{OOCH}_2\text{OC}(\text{O})\text{H}$. These excited radicals are formed with enough energy to undergo internal isomerisation reactions via five-membered transition states, leading to the production of QOOH and, consequently, OH via QOOH decomposition. Experimental yields of OH, from the internal

isomerisation of excited RO_2^* radicals, decrease with increasing pressure due to an increase in collisional stabilisation via R4.7 and R4.8. Yields from the OH and Cl-initiated oxidation of $\text{CH}_3\text{OC(O)H}$ are illustrated in Figures 4.16 and 4.17, respectively, at 298, 353 and 448 K, following Stern-Volmer analysis as derived in Appendix A. Individual yields at all temperatures are tabulated in Appendix C. Where multiple Stern-Volmer plots were obtained for a single temperature, for example at 298 K, they have been combined and unless otherwise stated, all errors are statistical at the 1σ level. Scatter outside the statistical errors could be due to variations in the background oxygen level. To maintain a sufficient concentration of methyl formate for pseudo-first order conditions and achieve low pressures, the flow rate was increased with increasing pressure. This meant background oxygen levels varied between each pressure on the Stern-Volmer plot. Changing background oxygen concentrations likely leads to varying amounts of the $\text{CH}_3\text{OC(O)}$ radical being captured by oxygen addition, which competes with $\text{CH}_3\text{OC(O)}$ decomposition. Experimental yields for Cl-initiated oxidation have been corrected to account for the $\text{Cl} + \text{tBuOOH}$ branching ratio and quenching of methyl formate and added oxygen as outlined in the Appendix B. These corrections are likely responsible for the increased scatter in the Cl-initiated yields at 298 K.

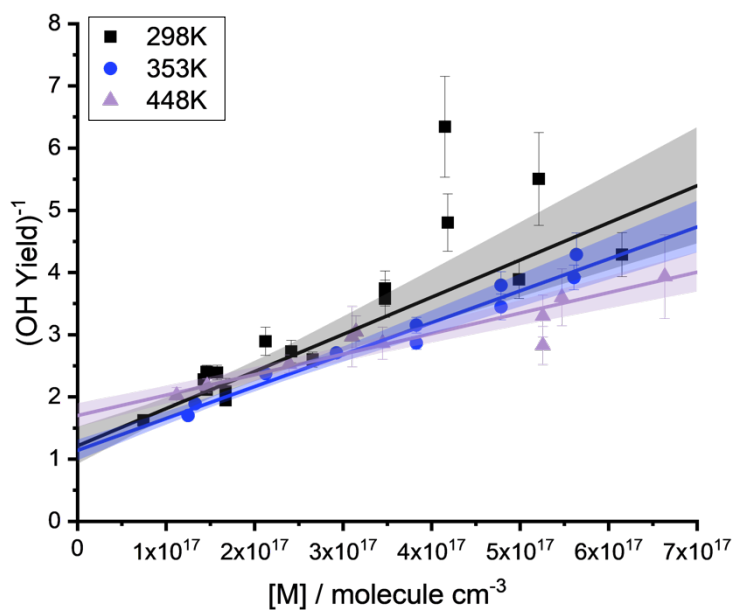


Figure 4.16 – Stern-Volmer plots of the reciprocal OH yield following the OH-initiated oxidation of $\text{CH}_3\text{OC}(\text{O})\text{H}$ in argon at 298, 353 and 448 K. The shaded regions illustrate the 95% confidence limits.

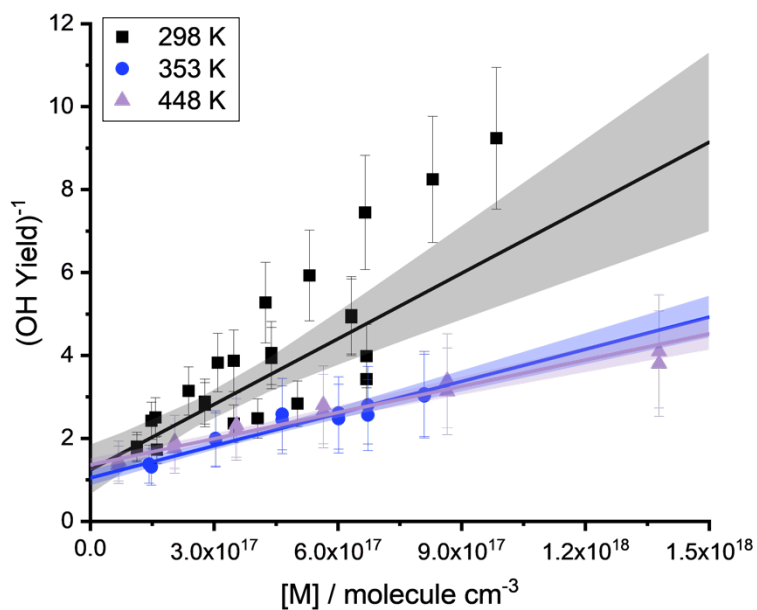


Figure 4.17 – Stern-Volmer plots of the reciprocal OH yield following the Cl-initiated oxidation of $\text{CH}_3\text{OC}(\text{O})\text{H}$ in argon between 298 and 453 K. The shaded regions illustrate the 95% confidence limits.

The Stern-Volmer slope, as derived in Appendix A and according to the scheme in Figure 4.6, is defined in E4.5 and describes the ratio of collisional stabilisation to OH recycling from the chemically activated RO_2^* .

$$\frac{1}{Y_{\text{OH}}} = 1 + \frac{k_{\text{Stab}}}{k_{\text{Regen}}} [\text{M}] \quad \text{E4.5}$$

The gradient of the slopes in Figures 4.16 and 4.17 generally decrease with increasing temperature.

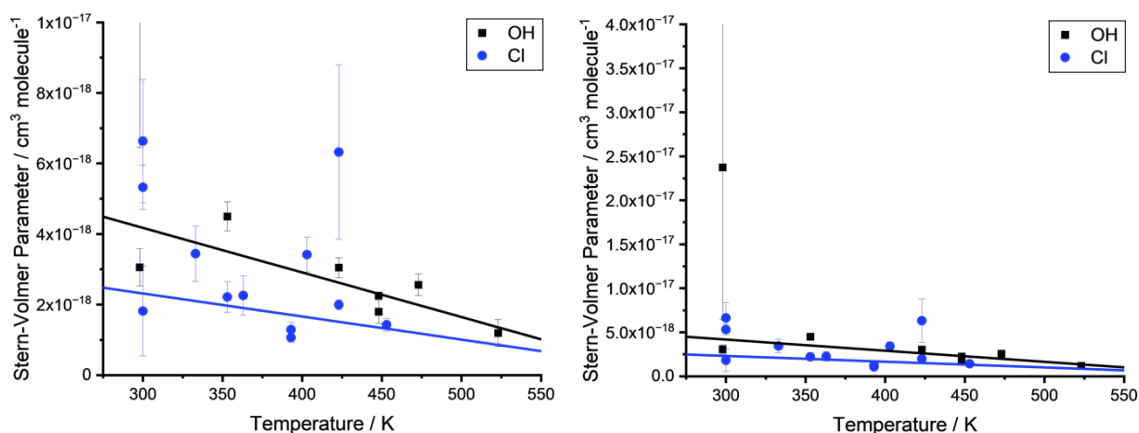


Figure 4.18 – Stern-Volmer parameters from the OH (black squares) and Cl-initiated (blue circles) oxidation of $\text{CH}_3\text{OC(O)H}$. The main figure has a y-axis limit of $1 \times 10^{-17} \text{ cm}^3 \text{ molecule}^{-1}$. The inset shows all of the data, with a y-axis limit of $4.5 \times 10^{-17} \text{ cm}^3 \text{ molecule}^{-1}$. Rather than having physical meaning, the linear lines provide a qualitative representation of the general trend as a function of temperature.

Normalised Stern-Volmer slopes, divided by their intercepts, are summarised in Figure 4.18 as a function of temperature. Whilst Figures 4.16 and 4.17 show a combination of yields for a given temperature, Figure 4.18 shows the slopes determined from a single experiment. Although a few outliers remain, the trend is clear and illustrated qualitatively via linear slopes that decrease with increasing temperature. As the temperature is increased, more energy is available to the excited RO_2^* radicals, consequently increasing the rate of internal isomerisation to QOOH and decomposition to OH relative to collisional stabilisation. Hence k_{Regen} becomes greater than k_{Stab} and the Stern-Volmer slope decreases with increasing temperature. As abstraction from both the methyl and formate sites leads to OH regeneration, the Stern-Volmer slopes shown here represent a combination of radicals following methyl and formate abstraction.

There is general agreement between the Cl and OH-initiated Stern-Volmer slopes. This can be explained via similar branching ratios for the Cl and OH-initiated oxidation and similar Stern-Volmer slopes of each radical.

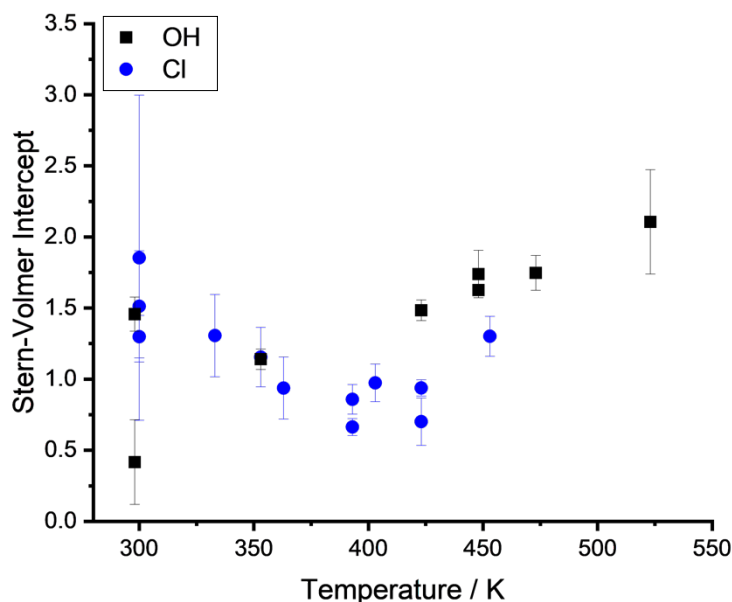


Figure 4.19 – Temperature-dependent Stern-Volmer intercepts from OH and Cl-initiated oxidation of $\text{CH}_3\text{OC}(\text{O})\text{H}$.

Stern-Volmer intercepts represent the amount of OH recycling at zero pressure. An intercept above 1 suggests less than 100% recycling, whilst an intercept less than 1 would suggest an additional source of OH. The intercepts from the OH and Cl-initiated oxidation of $\text{CH}_3\text{OC}(\text{O})\text{H}$ are shown in Figure 4.19, with errors at the 95% confidence level. Intercepts below 1 are most likely due to experimental error; from the reagents added to the reaction cell, methyl formate, the OH precursor H_2O_2 , argon and oxygen, only methyl formate can recycle OH. It is worth noting that the intercepts for the Cl-initiated reaction are subject to additional error due to corrections for the $\text{Cl} + \text{tBuOOH}$ branching ratio and quenching factors applied to place the yields on an absolute scale. This may be the reason that proportionally more of the Cl-initiated intercepts lie below 1. Furthermore, as the tBuOOH reference is subject to decomposition at temperatures above approximately 455 K, the Cl-initiated reactions have an upper temperature limit of 453 K. OH-initiated intercepts are independent of temperature until around 423 K, when they increase with increasing temperature. Whilst the Cl-initiated intercepts

are more scattered, they follow the same trend within the experimental errors. The increasing intercepts can be attributed to the decomposition of the $\text{CH}_3\text{OC}(\text{O})$ radical, preventing 100% OH recycling. Decomposition of the $\text{CH}_3\text{OC}(\text{O})$ radical reduces the OH yield unless sufficient oxygen is added for the oxygen addition reaction (R4.4) to become competitive. Loss of $\text{CH}_3\text{OC}(\text{O})$ via R4.24 causes the Stern-Volmer intercepts to increase and the OH yield at zero pressure to decrease with temperature.

Understanding the competition between decomposition of the $\text{CH}_3\text{OC}(\text{O})$ radical and addition with oxygen ($k(\text{R}+\text{O}_2)$) allows branching ratios from the Stern-Volmer intercepts to be quantified. If all the $\text{CH}_3\text{OC}(\text{O})$ radical is lost to decomposition, the reciprocal of the Stern-Volmer intercept is the branching ratio for methyl abstraction. The competition between the decomposition of $\text{CH}_3\text{OC}(\text{O})$ and the reaction with oxygen is exemplified in the data at 423 K, shown in Figure 4.20.

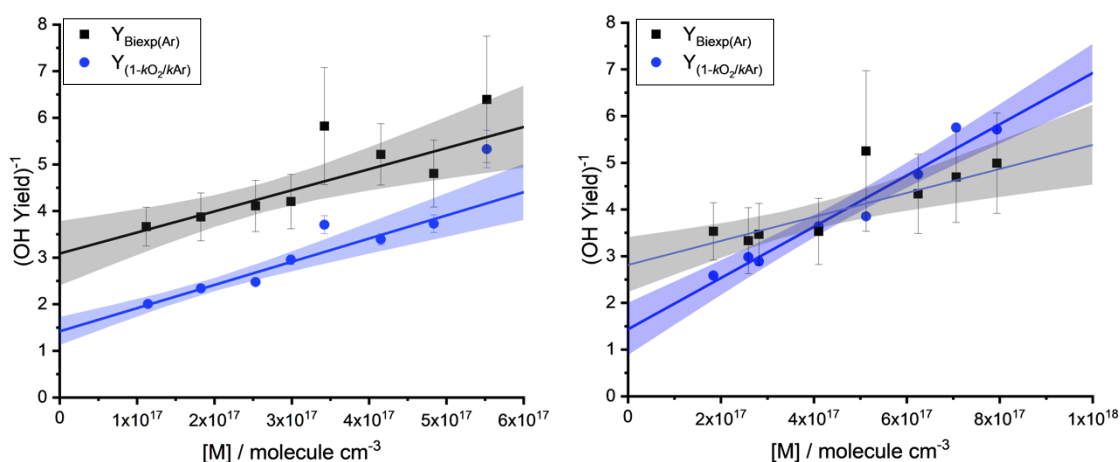


Figure 4.20 – Stern-Volmer plot at 423 K (left) and 473 K (right) from the OH-initiated oxidation of $\text{CH}_3\text{OC}(\text{O})\text{H}$. OH yields extracted from biexponential traces (E1, black squares) observed in the absence of added oxygen are lower than OH yields in the presence of added oxygen (E3, blue circles). When oxygen is added, $\text{CH}_3\text{OC}(\text{O})$ decomposition is intercepted by the $\text{CH}_3\text{OC}(\text{O}) + \text{O}_2$ reaction, resulting in higher yields of OH.

There is a clear distinction in Figure 4.20 between the yields determined via analysis in the absence and presence of $\sim 1.6 \times 10^{16}$ molecule cm^{-3} added oxygen (Figure 4.20, blue circles) and from biexponential decays in the absence of any

added oxygen (Figure 4.20, black squares). In the absence of added oxygen, the $\text{CH}_3\text{OC}(\text{O})$ radical formed following formate abstraction, thermally decomposes. As the pressure increases throughout the Stern-Volmer plot, the rate of $\text{R} + \text{O}_2$ increases. At the lowest pressure on the Stern-Volmer plot at 423 K, the rate coefficient of $\text{CH}_3\text{OC}(\text{O}) + \text{O}_2$ is $\sim 3 \times 10^{-13} \text{ cm}^3 \text{ molecule}^{-1} \text{ s}^{-1}$. When oxygen is added (blue circle data), the pseudo-first order rate coefficient of $\text{CH}_3\text{OC}(\text{O}) + \text{O}_2$ is 4590 s^{-1} . At the highest pressure on the Stern-Volmer plot, when the rate coefficient of $\text{CH}_3\text{OC}(\text{O}) + \text{O}_2$ is $\sim 2.5 \times 10^{-12} \text{ cm}^3 \text{ molecule}^{-1} \text{ s}^{-1}$, the pseudo-first order rate coefficient becomes 40000 s^{-1} . As the rate of $\text{R} + \text{O}_2$ changes over the Stern-Volmer plot, so does the proportion of $\text{CH}_3\text{OC}(\text{O})$ being lost to decomposition. For Figure 4.20 (left) this change is from (84 – 38)%, using a decomposition rate coefficient for $\text{CH}_3\text{OC}(\text{O})$ of 25000 s^{-1} . However, the decomposition of $\text{CH}_3\text{OC}(\text{O})$ is also a pressure dependent process so will also increase across the Stern-Volmer plot. Both processes may cancel out leading to similar slopes at 423 K.

In the absence of any added oxygen (assuming a background oxygen concentration of $\sim 1 \times 10^{14} \text{ molecule cm}^{-3}$) almost all (99% at the highest pressure) of the $\text{CH}_3\text{OC}(\text{O})$ radical is lost to decomposition. Therefore, the Stern-Volmer intercept obtained in the absence of any added oxygen is a more accurate measure of the branching ratio of methyl abstraction. At 423 K, the intercept suggests a branching ratio for methyl abstraction of $(32 \pm 28)\%$, where the error is at the 95% confidence limit. At 473 K, the Stern-Volmer intercept from $Y_{1-(k_{\text{O}_2}/k_{\text{Ar}})}$ ($1.53 - 1.65 \times 10^{16} \text{ molecule cm}^{-3}$ of added oxygen) overestimates the branching ratio for methyl abstraction (0.69 ± 0.27). However, the branching ratio from biexponential yields is 0.36 ± 0.08 .

Due to the high activation energy for $\text{CH}_3\text{OC}(\text{O})$ decomposition, k_{Decomp} , has a strong temperature dependence. At 498 K, when $\text{CH}_3\text{OC}(\text{O}) + \text{O}_2$ is no longer competitive at any point on the Stern-Volmer plot with $\text{CH}_3\text{OC}(\text{O})$ decomposition, the biexponential yield is independent of pressure. The internal isomerisation of the thermalised RO_2 also increases with temperature/thermal energy. Biexponential yields ($Y_{\text{Biexp}(\text{Ar})}$, black squares) represent OH regenerated from the thermalised RO_2 ,

OOCH₂OC(O)H. There is a subtle negative gradient in the $Y_{\text{Biexp(Ar)}}$ Stern-Volmer plots shown in Figure 4.21 as the unimolecular isomerisation of a thermalised RO₂ radical is a pressure-dependent reaction. OH yields from the chemically activated *OOCH₂OC(O)H are still captured via the change in the rate with and without added oxygen ($Y_{1-(k_{\text{O}_2}/k_{\text{Ar}})}$, blue circles). The branching ratios for methyl abstraction, calculated from the Stern-Volmer ($Y_{1-(k_{\text{O}_2}/k_{\text{Ar}})}$) intercepts and the high pressure biexponential yields ($Y_{\text{Biexp(Ar)}}$) are in good agreement within their experimental errors - as illustrated in Figure 4.21, in the Stern-Volmer plots at 498 K and 523 K.

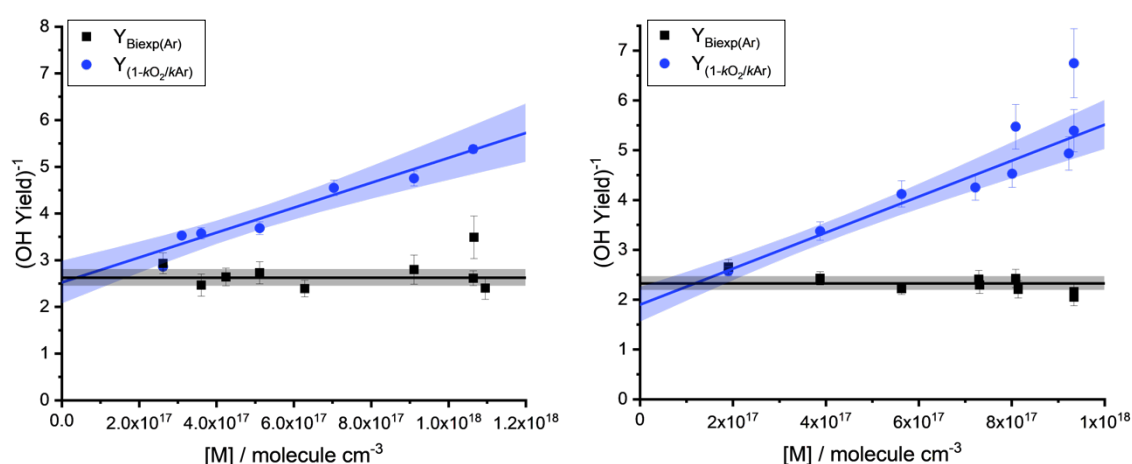


Figure 4.21 – Stern-Volmer plots at 498 K (left) and 523 K (right) in blue. Yields from biexponential decays in the absence of added oxygen represent OH yields from the thermalised RO₂ (OOCH₂OC(O)H) and are shown in black.

A summary of the branching ratios for methyl abstraction determined from the OH + CH₃OC(O)H yield experiments is presented in Figure 4.22 alongside the MESMER predicted branching ratios. At 423 and 473 K the branching ratio is calculated from the Stern-Volmer intercepts of biexponential yields, $Y_{\text{Biexp(Ar)}}$. Branching ratios at 498 and 523 K are calculated from both the Stern-Volmer intercept and OH yields from the thermalised RO₂, OUCH₂OC(O)H. MESMER branching ratios are obtained by fitting the temperature-dependent kinetics of the methyl formate isotopomers as outlined in Chapter 3 and the yields of OH outlined in this chapter. Excluding the branching ratio at 523 K, the experimental and MESMER calculated yields agree within the experimental errors. Despite the disagreement at 523 K, there is great agreement between the MESMER modelled

yields as a function of pressure. Details of the MESMER fits can be found in Appendix C.

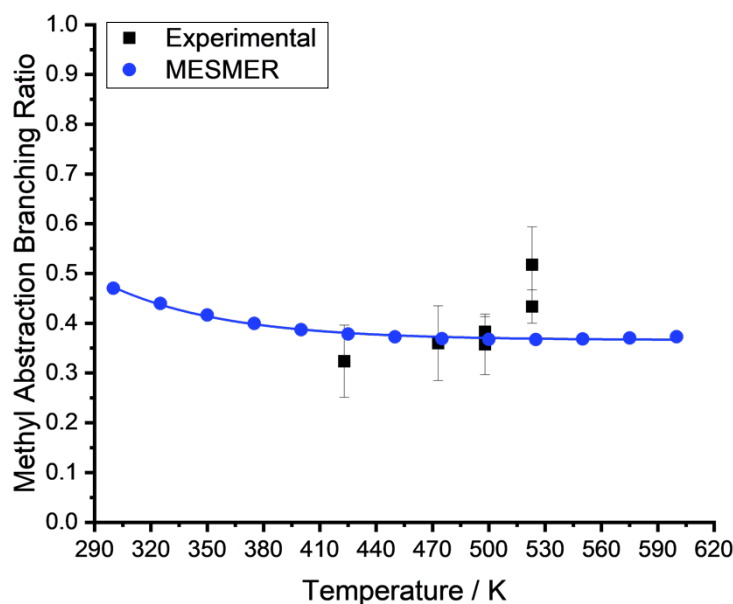
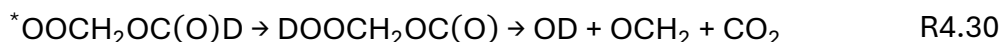
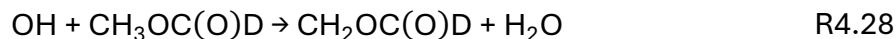
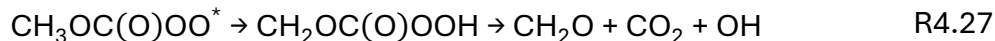
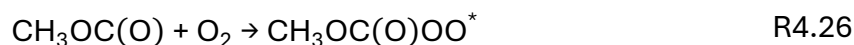
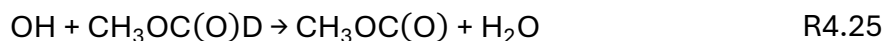


Figure 4.22 – Experimental branching ratios for methyl abstraction discussed above (black) alongside MESMER predicted values (blue).

4.4. Experimental yields from the OH and Cl initiated oxidation of CH₃OC(O)D + O₂

The oxidation of CH₃OC(O)D leads to the production of OH following formate abstraction (R4.25 – R4.27) and OD following methyl abstraction (R4.28 – R4.30), as illustrated in Figure 4.3.



The detection of OH and OD can be used to determine the separate RO₂ characteristics of CH₃OC(O)OO* and *OOCH₂OC(O)D. For OH-initiated experiments, yields of OH were determined from E4.3 using the rate coefficient for OH removal in the absence and presence of added oxygen. OD yields were calculated as the ratio of the maximum OD signal, extracted from E4.4, compared

to the maximum OH signal under the same concentrations of oxygen and methyl formate. The simple growth and decay reaction scheme, shown in Figure 4.4 and E4.4, proved to be sufficient and always within error of more complex reaction schemes (Appendix C, Figure C.4). Numerical integration within MATLAB and Python were used to test more complex reaction schemes which accounted for $k(R + O_2)$ and OD regeneration from thermal RO_2 and chemically activated RO_2^* decomposition. Details of these scripts and comparative fits to the data can be found in Appendix C Figures C.3 and C.4. For Cl-initiated experiments, both OH and OD yields, shown in Appendix C Figure C.5, were determined by comparing their respective signal heights once corrected for quenching by oxygen and methyl formate and referenced against the signal height of OH from tBuOOH, corrected for the Cl + tBuOOH branching ratio.

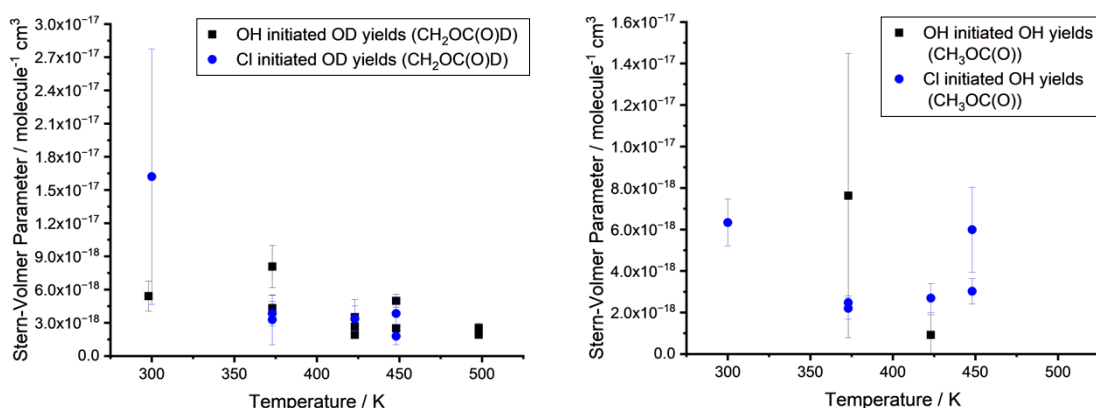


Figure 4.23 – Comparisons of Stern-Volmer parameters from the OH and Cl-initiated oxidation of $CH_3OC(O)D$. OD yields representing methyl abstraction are shown on the left and OH yields representing formate abstraction are shown on the right.

Stern-Volmer parameters (normalised Stern-Volmer slopes divided by their intercepts) from OH and Cl-initiated oxidation, are presented in Figure 4.23. OD yields formed following methyl abstraction and the internal isomerisation and decomposition of $^*OOCH_2OC(O)D$ are shown on the left whilst the right figure shows OH yields formed following formate abstraction and the internal isomerisation and decomposition of $CH_3OC(O)OO^*$. Figure 4.23 illustrates good agreement between the OH and Cl-initiated yields within their experimental errors. Due to experimental challenges in detecting the OH yields, OD yield data are more

abundant and prone to less error. The yields of OH were smaller than OD, and the detection method for OH-initiated experiments was less sensitive as the rate of OH decay is subject to larger errors than the signal heights.

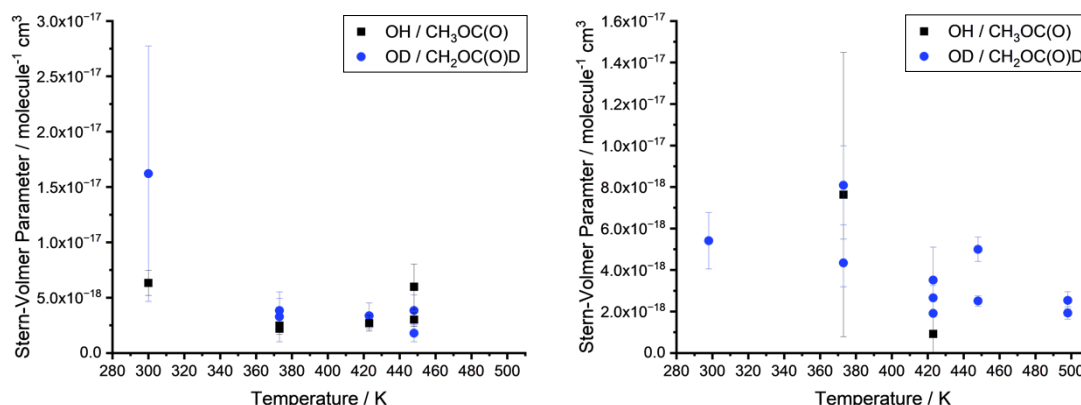
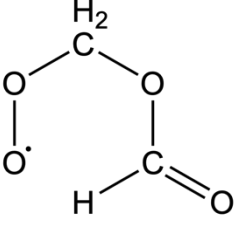
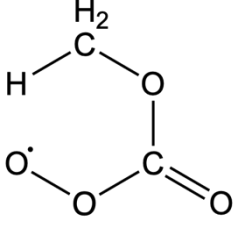


Figure 4.24 – Comparison of Stern-Volmer parameters following methyl and formate abstraction. Comparisons following Cl-initiated oxidation are shown on the left, and the right shows comparisons from OH-initiated oxidation.

Whilst Figure 4.23 highlights the agreement between the yields following OH and Cl-initiated oxidation, Figure 4.24 demonstrates the comparison between OH and OD yields. Stern-Volmer parameters following hydrogen abstraction from the formate site are shown in black, whereas Stern-Volmer parameters following hydrogen abstraction from the methyl site are shown in blue. Parameters following Cl-initiated oxidation are on the left hand side of Figure 4.24 and parameters following OH-initiated oxidation are on the right. The parameters following methyl abstraction are greater than those following formate abstraction with the difference decreasing with increasing temperature. However, due to the large overlapping errors, this conclusion is not definitive. As the Stern-Volmer parameters are indicative of the ratio between internal isomerisation and collisional stabilisation, the experimental evidence suggests the rate of internal isomerisation to QOOH and subsequent decomposition may be faster for the $^{\bullet}\text{OOCH}_2\text{OC}(\text{O})\text{D}$ radical following methyl abstraction than the $\text{CH}_3\text{OC}(\text{O})\text{OO}^{\bullet}$ radical formed following formate abstraction.

Table 4.1 – Barrier heights for the internal isomerisation of RO₂ radicals to QOOH following OH-initiated oxidation of CH₃OC(O)H at the methyl and formate abstraction sites. *ab initio* and fitted barriers determined in this work are compared with the work of Yang et al. [22].

Abstraction Site	Transition State	Ab Initio Barrier / kJ mol ⁻¹	Fitted Barrier / kJ mol ⁻¹	Yang et al. / kJ mol ⁻¹
Methyl Abstraction		91.8	98.0	95.4
Formate Abstraction		115.6	109.5	117.2

The *ab initio* stationary points along the methyl formate potential energy surface have been calculated by Robin Shannon at the CCSD(T)-f12/aug-CC-pVTZ//M062X/6-31+G** level of theory using Molpro [98] for the CCSD(T) calculations and Gaussian [81] for the DFT calculations. The barrier heights for RO₂ internal isomerisation to QOOH have also been fit within MESMER and are shown in Table 4.1 alongside the work of Yang et al. [22]. Yang et al. [22] calculated the stationary points along the potential energy surface of methyl formate oxidation at the CCSD(T)-F12/cc-pVTZ-F12//B2PLYP-D3/cc-pVTZ level of theory. As illustrated in Table 4.1, the barrier height for CH₃OC(O)OO internal isomerisation is larger than OOCH₂OC(O)H. This supports the experimental evidence illustrated in Figure 4.24. As more thermal energy is available to the QOOH species, the difference between their relative barrier heights becomes less significant, and their Stern-Volmer parameters become more similar with increasing temperature. Yang et al. [22] found the lowest barrier for QOOH decomposition to OH is below the barriers for internal isomerisation from RO₂ to QOOH. Therefore, QOOH decomposition can be considered instantaneous as the QOOH radicals will decompose rather than undergo the reverse reaction to re-form RO₂. This work considered the QOOH radicals as sinks, assuming OH formation is instantaneous.

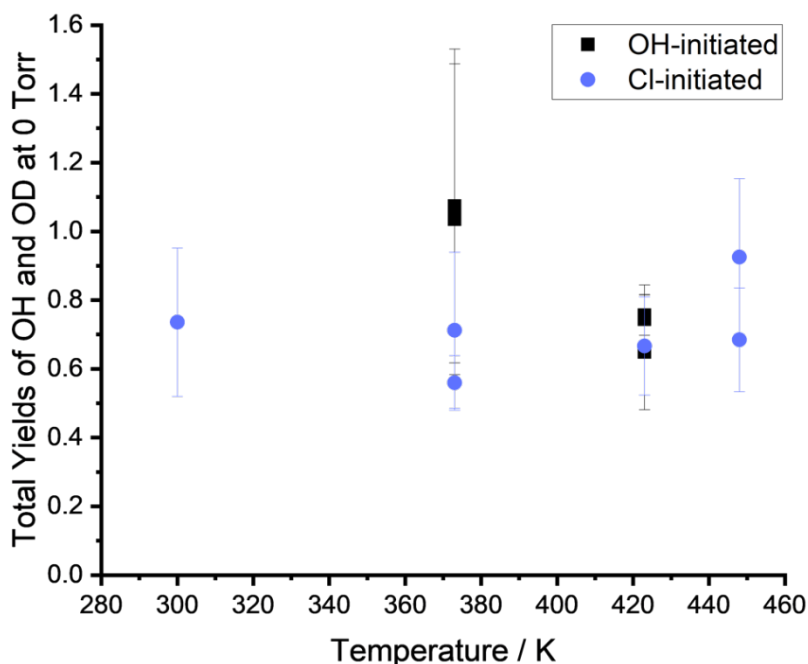


Figure 4.25 –Yield sums of the reciprocal Stern-Volmer intercepts for OH and OD yields from the OH (black squares) and Cl-initiated (blue circles) oxidation of $\text{CH}_3\text{OC}(\text{O})\text{D}$.

The ratio of Stern-Volmer intercepts from OH (formate abstraction) and OD (methyl abstraction) yields should provide valuable information on the branching ratio of initial abstraction by OH and Cl. If the $\text{CH}_3\text{OC}(\text{O})$ radical formed following formate abstraction does not undergo any decomposition, then the sum of recycling between the OH and OD yields should be equal to 100%. The total recycling, calculated by summing the reciprocal of the Stern-Volmer intercepts from OH and OD yields, is shown in Figure 4.25 for OH and Cl-initiated oxidation of $\text{CH}_3\text{OC}(\text{O})\text{D}$. For Cl-initiated reactions, OH yields are systematically 30% lower than 100%, independent of temperature. The Stern-Volmer intercepts following Cl-initiated oxidation are prone to larger errors than the corresponding OH-initiated intercepts. This is due to the multiple corrections, outlined in Appendix B, Cl signals undergo to place the yields on an absolute scale. For OH-initiated reactions, the total recycling decreases from 373 K to 423 K, with 1×10^{16} molecule cm^{-3} added oxygen, as expected due to the decomposition of the $\text{CH}_3\text{OC}(\text{O})$ radical preventing 100% recycling.

Competition between the decomposition of $\text{CH}_3\text{OC(O)}$ and $k(\text{R}+\text{O}_2)$ is illustrated in Figure 4.26. At both 423 K (Figure 4.26, left) and 398 K (Figure 4.26, right), the yields of OH increase as a function of added oxygen. Due to a large time difference between measuring the methyl formate calibration and the yields of OH/OD as a function of oxygen at 398 K, the yields presented in Figure 4.26 (right) at 398 K are qualitative only. However, the general trend at 398 K suggests $\text{CH}_3\text{OC(O)}$ decomposition becomes competitive with oxygen addition, $k(\text{R}+\text{O}_2)$, between 373 K and 398 K. The yields of OD remain constant with increasing added oxygen, implying no decomposition of $\text{CH}_2\text{OC(O)D}$ occurs. $\text{CH}_2\text{OC(O)D}$ is not expected to undergo thermal decomposition as it likely has a much higher barrier to decomposition than $\text{CH}_3\text{OC(O)}$. Although $\text{CH}_2\text{OC(O)D}$ decomposition has not been quantified theoretically, experimental OD yields are independent of added oxygen. Yields as a function of added oxygen were determined from Cl-initiated experiments, at ~ 8 Torr. As RO_2^* is stabilised by collisions with argon to RO_2 , which does not undergo thermal decomposition to OH/OD at 423 K, the sum of OH and OD yields presented in Figure 4.26 (left) is not 100%. The average yield of OD presented in Figure 4.26 at 423 K is 0.34 ± 0.04 . The predicted yield at 8 Torr from the Stern-Volmer slope is 0.31 ± 0.09 . Good agreement between the average OD yield at varying concentrations of added oxygen up to 8.87×10^{15} molecule cm^{-3} and the predicted yield calculated from Stern-Volmer slopes and intercepts obtained at 423 K at $\sim 1.6 \times 10^{16}$ molecule cm^{-3} of added oxygen, further demonstrates the independence of OD yields as a function of added oxygen.

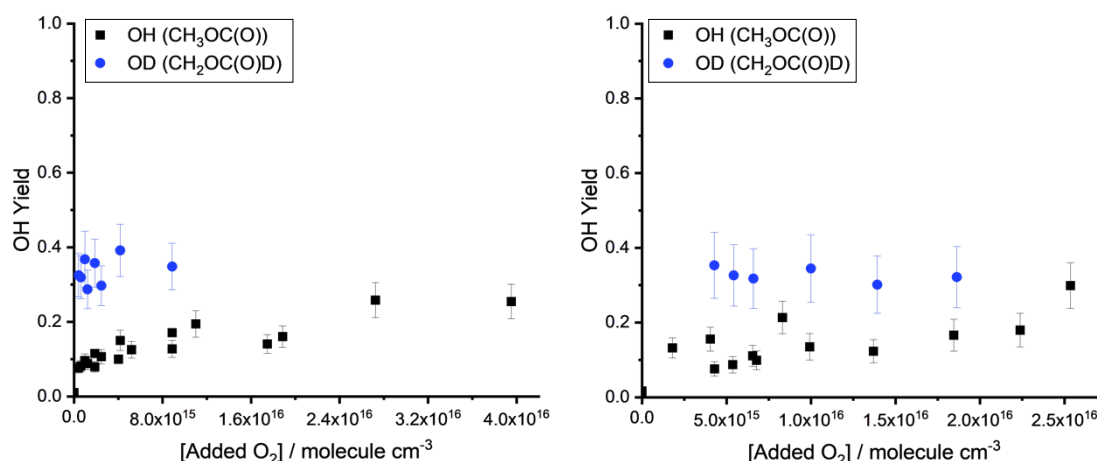


Figure 4.26 – OH (black squares) and OD (blue circles) yields following the reaction of Cl + CH₃OC(O)D as a function of added oxygen are quantitative at 423 K (left) and qualitative at 398 K (right).

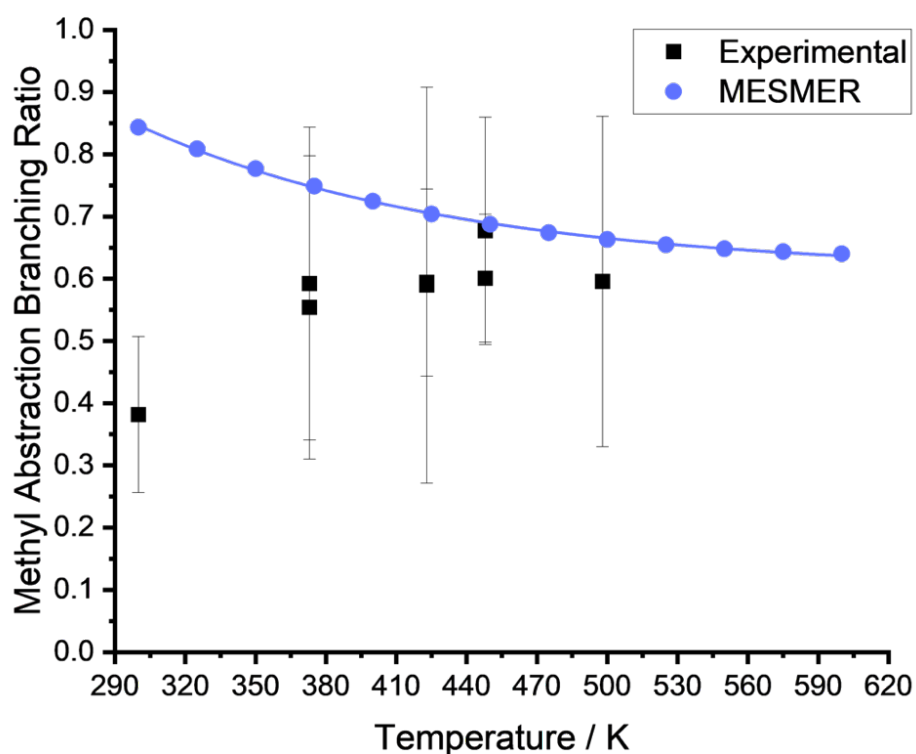


Figure 4.27 – Branching ratios for the OH-initiated oxidation of CH₃OC(O)D. The ratios are calculated from the reciprocal of their respective OH / OD Stern-Volmer intercepts.

The branching ratios for methyl abstraction from CH₃OC(O)D are calculated from the reciprocal of the OD Stern-Volmer intercepts and are presented in Figure 4.27. Excluding the branching ratio at 300 K, there is good agreement between the

experimental branching ratios and those calculated by MESMER. There is a significant increase in abstraction at the methyl site from $\text{OH} + \text{CH}_3\text{OC}(\text{O})\text{D}$ compared to $\text{OH} + \text{CH}_3\text{OC}(\text{O})\text{H}$. At 423 K, the average branching ratio from $\text{CH}_3\text{OC}(\text{O})\text{D}$ is 0.54 ± 0.06 , whilst the branching ratio for $\text{CH}_3\text{OC}(\text{O})\text{H}$ is 0.33 ± 0.07 . As the energy required to abstract deuterium is greater than hydrogen, there is a shift in the branching ratio leading to an increase in methyl abstraction. Whilst methyl abstraction from $\text{CH}_3\text{OC}(\text{O})\text{D}$ appears relatively constant with increasing temperature, methyl abstraction from $\text{CH}_3\text{OC}(\text{O})\text{H}$ increases slightly.

4.5. OH/OD yields from the thermalised RO_2 isotopomers

Kinetic experiments outlined in Chapter 3, produced biexponential decays at high temperatures (above 433 K) and high pressures (above ~ 100 Torr). OH regeneration under these experimental conditions is due to the thermalised RO_2 overcoming the barrier to internal isomerisation. Following the OH-initiated oxidation of $\text{CH}_3\text{OC}(\text{O})\text{H}$, OH regeneration is observed above 541 K. Deuterated isotopomers appear to show biexponential behaviour at temperatures lower than undeuterated methyl formate, implying the energy barrier for thermalised $\text{RO}_2 \rightarrow \text{QOOH}$ is lower in the deuterated isotopomers. For each isotopomer, biexponential behaviour was exclusively observed following methyl abstraction, consistent with the above experiments that showed rapid $\text{CH}_3\text{OC}(\text{O})$ decomposition, preventing recycling of OH/OD from the formate site. For $\text{CH}_3\text{OC}(\text{O})\text{H}$ and $\text{CD}_3\text{OC}(\text{O})\text{H}$, OH decays became biexponential due to the isomerisation of thermalised radicals $\text{OOCH}_2\text{OC}(\text{O})\text{H}$ and $\text{OOCd}_2\text{OC}(\text{O})\text{H}$. OD decays remained single exponential due to the thermal decomposition of $\text{CH}_3\text{OC}(\text{O})$ and $\text{CD}_3\text{OC}(\text{O})$. For $\text{CH}_3\text{OC}(\text{O})\text{D}$ and $\text{CD}_3\text{OC}(\text{O})\text{D}$, OD decays became biexponential due to the isomerisation of thermalised radicals $\text{OOCH}_2\text{OC}(\text{O})\text{D}$ and $\text{OOCd}_2\text{OC}(\text{O})\text{D}$. OH decays remained single exponential due to the thermal decomposition of $\text{CH}_3\text{OC}(\text{O})$ and $\text{CD}_3\text{OC}(\text{O})$.

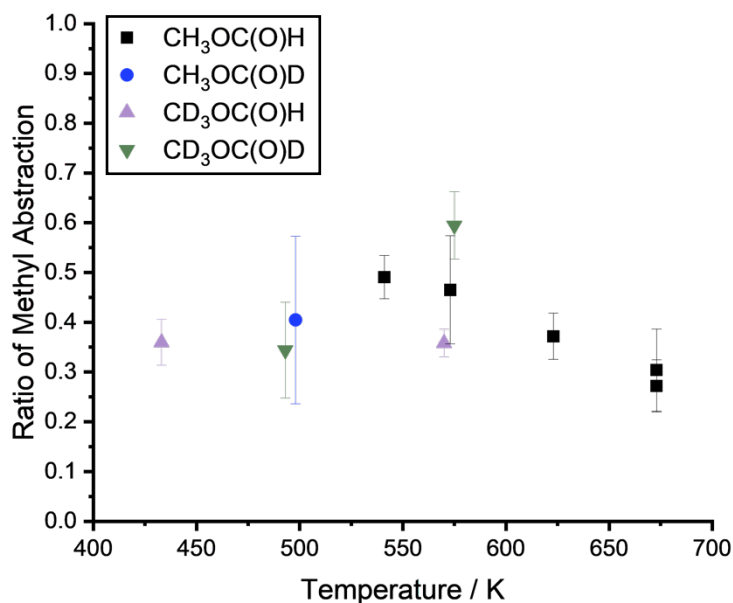


Figure 4.28 – Branching ratios for methyl abstraction from the different isotopomers of methyl formate.

Figure 4.28 presents the branching ratios for methyl abstraction from the isotopomers of methyl formate as a function of temperature, showing little deviation with increasing isotopic substitution. This is quite surprising as MESMER predicted branching ratios that deviate significantly with isotopic substitution.

For CH₃OC(O)H and CH₃OC(O)D, experimental branching ratios have been obtained via the Stern-Volmer intercepts (outlined above) and from kinetic experiments describing the thermalised RO₂ radicals at high pressures. Experimental branching ratios have been combined and are compared against MESMER predicted branching ratios calculated from both *ab initio* barriers and fitted barriers for each isotopomer in Figure 4.29.

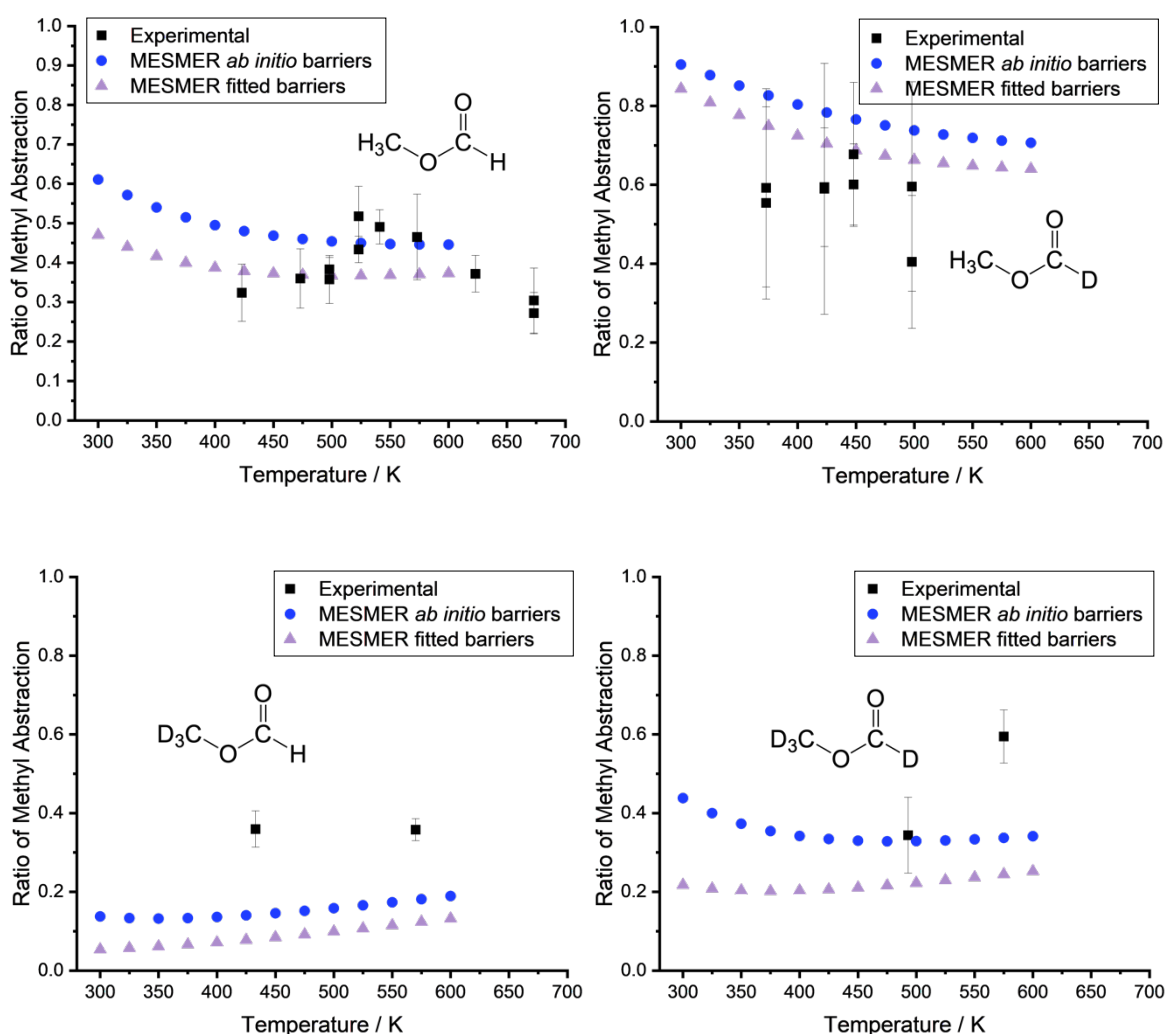


Figure 4.29 – High temperature branching ratios for methyl abstraction from isotopomers $\text{CH}_3\text{OC}(\text{O})\text{H}$ (top left), $\text{CH}_3\text{OC}(\text{O})\text{D}$ (top right), $\text{CD}_3\text{OC}(\text{O})\text{H}$ (bottom left) and $\text{CD}_3\text{OC}(\text{O})\text{D}$ (bottom right) compared with MESMER predicted values using *ab initio* and fitted barriers.

4.6. Atmospheric Implications

As discussed in Chapter 3, the atmospheric oxidation of methyl formate leads to different atmospheric impacts depending on the initial site of abstraction. Formate abstraction leads to carcinogenic formaldehyde whilst methyl abstraction leads to formic acid and formic acid anhydride [11]. This work quantifies the branching ratios from the OH-initiated oxidation – the dominant loss process for esters in the atmosphere. For $\text{CH}_3\text{OC}(\text{O})\text{H}$, high temperature experimental branching ratios are in good agreement with the MESMER predictions, providing confidence in their extrapolation to atmospherically relevant temperatures. The

experimental branching ratios are compared in Figure 4.30 with the MESMER predictions and predictions by the Jenkin et al. [15] SAR.

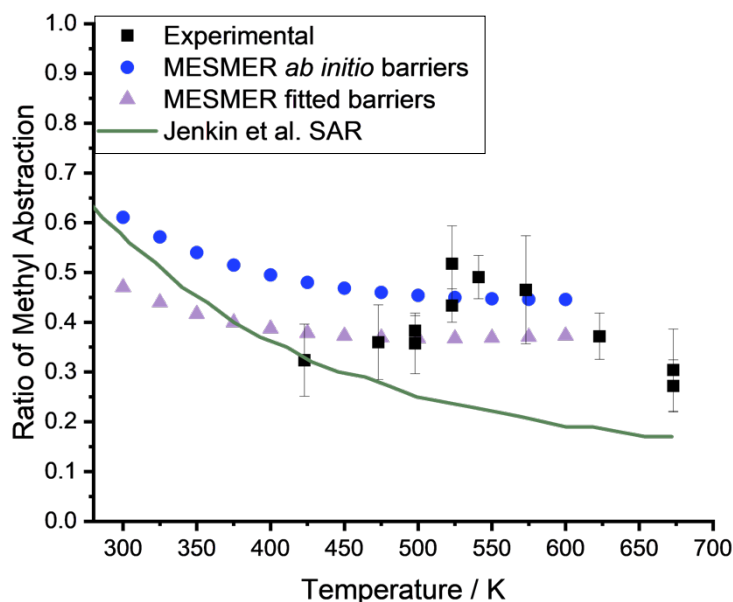


Figure 4.30 – Experimental branching ratios (black squares) for OH-initiated oxidation at the methyl site in methyl formate, $\text{CH}_3\text{OC(O)H}$. MESMER predicted branching ratios are shown in blue and purple alongside the Jenkin et al. [15] SAR predictions.

At room temperature, the branching ratio calculated via the Jenkin et al. [15] SAR predicts methyl abstraction dominates with a branching ratio of 0.58. This branching ratio is slightly higher than the MESMER calculated value of 0.47. With increasing temperature, the Jenkin et al. [15] SAR also overpredicts the decrease in methyl abstraction. However, the Jenkin et al. [15] SAR is only trained on data up to 400 K. Therefore, extrapolation above 400 K is beyond the scope of the SAR. Although the Jenkin et al. [15] SAR is implemented in the MCM, the MCM predicts a branching ratio for methyl abstraction of 0.55, also higher than in this work but within a reasonable error range [121].

The MCM predicts the $\text{CH}_3\text{OC(O)}$ radical decomposes under atmospheric conditions. However, this work demonstrates $\text{CH}_3\text{OC(O)}$ will react with oxygen in the atmosphere to form the peroxy radical, $\text{CH}_3\text{OC(O)OO}$. Although under high NO_x conditions products of formate abstraction will be HCHO via either mechanism

(decomposition or peroxy radical formation followed by reactions with NO and O₂), under low NO_x conditions the CH₃OC(O)OO radical may react with other peroxy radicals leading to accretion products or the regeneration of OH via R4.31.



Whilst the atmospheric oxidation of methyl formate is well characterised under high NO_x conditions, products of peroxy radical reactions under low NO_x conditions have not been quantified.

The experimental site-specific kinetics determined in this work will be used to train a more accurate SAR for the prediction of overall and site-specific kinetics for the reactions of OH radicals with esters.

4.7. Conclusions

The site-specific kinetics following the OH-initiated oxidation of methyl formate have been experimentally determined between 423 and 523 K. Above 423 K, the CH₃OC(O) radical thermally decomposes. The rate of thermal decomposition has been measured via the intercepts of $k(\text{R}+\text{O}_2)$ bimolecular plots (Figure 4.14) and global fitting of OH and OD yields (Figure 4.27), both determined following the oxidation of CH₃OC(O)D. OH yields following formate abstraction and the internal isomerisation of CH₃OC(O)OO are dependent on oxygen, as CH₃OC(O) decomposition is competitive with oxygen addition. OD yields are independent of added oxygen as the barrier for OOCH₂OC(O)D decomposition is likely too high to be competitive. Therefore, the only pathway for CH₂OC(O)D is reaction with oxygen.

Within experimental error, there is good agreement between the experimentally determined site-specific kinetics of CH₃OC(O)H and the MESMER predicted values. The experimental site-specific kinetics of CH₃OC(O)D determine a slightly higher branching ratio for methyl abstraction upon deuteration at the formate site. However, the experimental branching ratio is not as large as predicted by MESMER. Experimental branching ratios for methyl abstraction are 0.32 ± 0.07 from CH₃OC(O)H and 0.59 ± 0.15 from CH₃OC(O)D at 423 K. MESMER predicted branching ratios are 0.38 and 0.70, respectively. MESMER generally predicts larger shifts in the branching ratios than the experimentally determined values. However,

for $\text{CD}_3\text{OC}(\text{O})\text{H}$ and $\text{CD}_3\text{OC}(\text{O})\text{D}$, experimental data are sparse due to difficulties in determining Stern-Volmer plots of the deuterated isotopomers with slower rate coefficients for their reactions with OH .

Chapter 5 The site-specific kinetics of OH + isopropyl formate

5. Introduction

Isopropyl formate, $(\text{CH}_3)_2\text{CHOC}(\text{O})\text{H}$, is the first in the series of formates ($\text{ROC}(\text{O})\text{H}$) with a branched R group/alkyl chain. There are three sites available for reaction with OH: hydrogen abstraction from one of the two methyl groups ($(\text{CH}_3)_2$), the tertiary hydrogen (CH), and the formate hydrogen ($\text{C}(\text{O})\text{H}$). With only three reactive sites, isopropyl formate is a good bridge between determining the site-specific kinetics of methyl formate, which has two reaction sites, and larger esters.

Understanding the site-specific kinetics of isopropyl formate is important to advance our knowledge of ester reactivity, particularly how the isopropyl group influences reactivity. Whilst, to my knowledge, no ambient measurements of isopropyl formate exist, it is potentially emitted through its use in perfumes and food flavouring. The scent of isopropyl formate is characterised by The Good Scents Company as ethereal, sweet, solvent-like and fruity with a sweet and fruity (berry) flavour [122]. Quantifying emissions from perfume sources is challenging, as manufacturers do not release details of their perfume ingredients to protect private formulations. However, isopropyl formate is likely one of the many VOCs that make up the composition of ambient air. Isopropyl formate is also formed *in situ* in the atmosphere following the atmospheric oxidation of isobutyl isopropyl ether, with a yield of $\sim 48\%$ [123]. Ether solvents have attracted lots of interest in our move towards net zero. Many solvents, such as toluene, are toxic to human health and derived from fossil fuels, so they need to be phased out for net zero to be possible. Solvents contributed the largest percentage of VOC emissions in England in 2019 [32]. As the use of ethers and esters increases, so too will their emissions into the atmosphere. Atmospheric chemical mechanisms such as the MCM rely on SARs to model the oxidation of esters. To develop more accurate SARs, we need reliable experimental data for SAR training. Studies to advance our understanding of ester reactivity, such as this work on the site-specific kinetics of isopropyl formate, are critical to growing the body of literature on esters whose emissions and relevance are likely to increase.

5.1. Literature studies of isopropyl formate kinetics

The rate coefficient for the reaction of OH with isopropyl formate has been determined at room temperature by Stemmler et al. [123], Szilagyi et al. [124], Pimentel et al. [17] and Zhang et al. [125]. Stemmler et al. [123] performed relative rate experiments in a Teflon bag reactor at 297 ± 3 K and 725 ± 10 Torr. Methyl nitrite was photolysed by UV lamps (350 – 450 nm) to produce OH via R5.1 – R5.3.



Products were detected by gas chromatography with flame ionisation detection (GC-FID). Plotting the decay of isopropyl formate against the dipropyl ether reference gave a linear slope equal to 0.11 ± 0.01 . Using the 1994 Atkinson [126] recommended rate coefficient for OH + dipropyl ether of $1.85 \times 10^{-11} \text{ cm}^3 \text{ molecule}^{-1} \text{ s}^{-1}$, Stemmler et al. [123] determined the rate coefficient for the reaction of OH + isopropyl formate to be $(2.0 \pm 0.1) \times 10^{-12} \text{ cm}^3 \text{ molecule}^{-1} \text{ s}^{-1}$. However, the 5% error reported in the final rate coefficient is unreflective of the 10% error in the slope, which, combined with the 40% error in the recommended rate coefficient for the dipropyl ether reference, gives a rate coefficient of $(2.04 \pm 0.84) \times 10^{-12} \text{ cm}^3 \text{ molecule}^{-1} \text{ s}^{-1}$. Using the Eurochamp [16] recommended value for OH + dipropyl ether of $(2.0 \pm 0.3) \times 10^{-11} \text{ cm}^3 \text{ molecule}^{-1} \text{ s}^{-1}$ (15% error) gives an updated relative rate value of $(2.20 \pm 0.39) \times 10^{-12} \text{ cm}^3 \text{ molecule}^{-1} \text{ s}^{-1}$ which is shown in Figure 5.1.

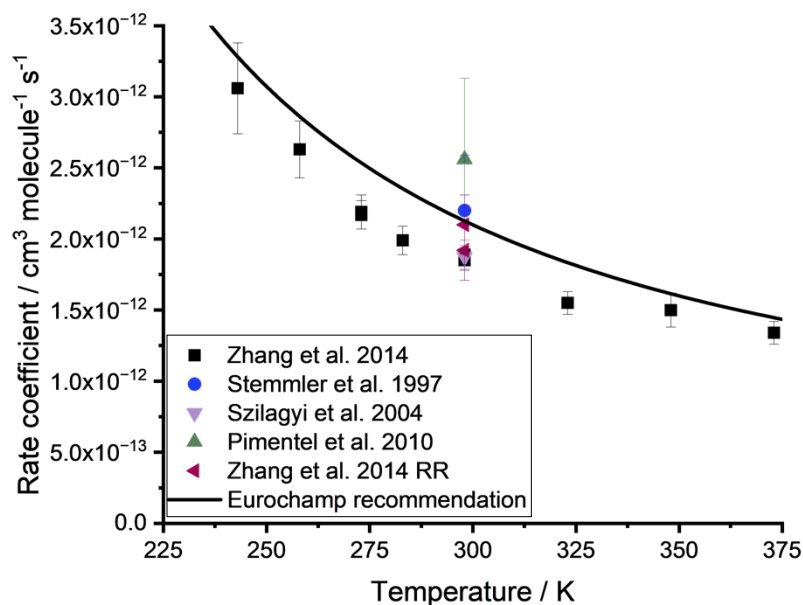


Figure 5.1 – Literature rate coefficients for the reaction of OH + isopropyl formate alongside the Eurochamp recommended temperature dependence [16].

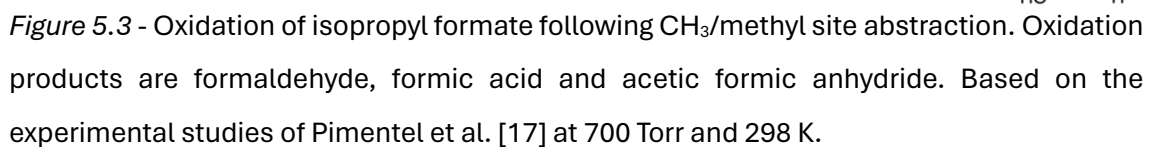
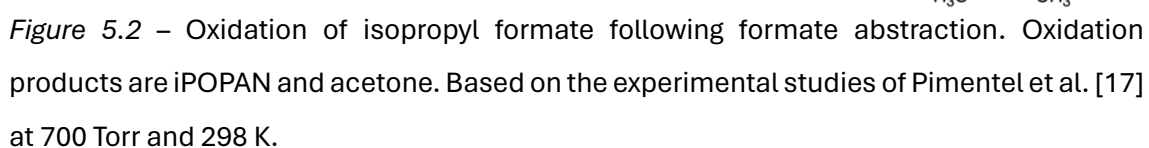
Szilagyi et al. [124] determined the absolute kinetics using a discharge flow method with resonance fluorescence. OH was generated by reacting H atoms with excess NO_2 via R5.4, and He was used as the bath gas at a total pressure of 1.91 Torr.



Pimentel et al. [17] determined the rate coefficient for OH + isopropyl formate via a relative rate study in a cylindrical steel chamber coupled with an FTIR spectrometer. Their OH radicals were generated via the photolysis of methyl nitrite (R5.1 – R5.3) by a Xe arc lamp. They measured a linear slope of 0.30 ± 0.05 relative to ethene. Using a value for $k(\text{OH} + \text{ethene})$ of $7.9 \times 10^{-12} \text{ cm}^3 \text{ molecule}^{-1} \text{ s}^{-1}$ [127], Pimentel et al. [17] reported a value of $(2.4 \pm 0.6) \times 10^{-12} \text{ cm}^3 \text{ molecule}^{-1} \text{ s}^{-1}$. Their error represents the statistical error in the measured value and the reference reaction. The recommended value has since been updated by Eurochamp [16] and is now $(8.5 \pm 1.3) \times 10^{-12} \text{ cm}^3 \text{ molecule}^{-1} \text{ s}^{-1}$, leading to an updated rate coefficient of $(2.56 \pm 0.57) \times 10^{-12} \text{ cm}^3 \text{ molecule}^{-1} \text{ s}^{-1}$ for the reaction of OH + isopropyl formate, shown in Figure 5.1.

Zhang et al. [125] determined the room temperature rate coefficient using both absolute and relative methods. Their relative rate study was performed in a reaction chamber at 760 Torr using ultra-pure air. OH was formed from the photolysis of H₂O₂ at 254 nm. Propane and pentane were used as reference compounds, which gave linear slopes of 1.89 ± 0.02 and 0.51 ± 0.02 , respectively. These slopes give rate coefficients for OH + isopropyl formate of $(2.10 \pm 0.32) \times 10^{-12}$ cm³ molecule⁻¹ s⁻¹ and $(2.03 \pm 0.41) \times 10^{-12}$ cm³ molecule⁻¹ s⁻¹ using the Calvert 2008 recommended rate coefficients of $(1.11 \pm 0.17) \times 10^{-12}$ cm³ molecule⁻¹ s⁻¹ for propane and $(3.97 \pm 0.79) \times 10^{-12}$ cm³ molecule⁻¹ s⁻¹ for pentane [128]. Using the Eurochamp [16] recommendations for propane and pentane updates the OH + isopropyl formate rate coefficients to $(2.10 \pm 0.21) \times 10^{-12}$ cm³ molecule⁻¹ s⁻¹ relative to propane and $(1.92 \pm 0.21) \times 10^{-12}$ cm³ molecule⁻¹ s⁻¹ relative to pentane. The absolute measurements made by Zhang et al. [125] used laser flash photolysis of H₂O₂ at 248 nm with off-resonance laser induced fluorescence of OH in He bath gas. This technique was used to measure the temperature dependence of the reaction between 243 and 373 K. Zhang et al. [125] observed a negative temperature dependence, which is shown in Figure 5.1 alongside all literature studies.

The chamber experiments by Zhang et al. [125] also determined product yields via FTIR spectroscopy, gas chromatography coupled with photoionisation detectors (GC-PID) and gas chromatography coupled with mass spectrometry (GC-MS). Due to a lack of IR reference spectra for unknown products, their chamber study was only able to determine the product yield of acetone, with a yield of $(39 \pm 2)\%$. The chamber study by Pimentel et al. [17] also observed products formed following reactions of OH and Cl + isopropyl formate. Figures 5.2 – 5.4 show the atmospheric oxidation pathways of isopropyl formate, adapted from Pimentel et al. [17] for abstraction from the formate, methyl and tertiary reaction sites.



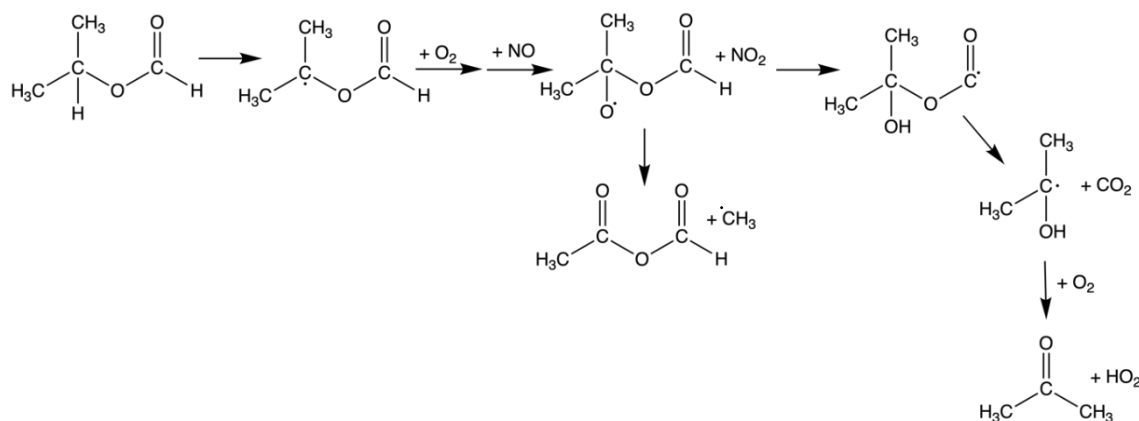


Figure 5.4 – Oxidation of isopropyl formate following CH/tertiary site abstraction. Oxidation products are acetone and acetic formic anhydride. Based on the experimental studies of Pimentel et al. [17] at 700 Torr and 298 K.

Whilst Pimentel et al. [17] focused on Cl-initiated oxidation, they also performed supplementary experiments on OH-initiated oxidation. Formate abstraction following Cl-initiated oxidation was quantified by irradiating mixtures of Cl_2 , isopropyl formate and N_2 . Isopropyl chloroformate, $(\text{CH}_3)_2\text{CHOC}(\text{O})\text{Cl}$, was detected with a yield of $(30 \pm 3)\%$ at 298 K. In the presence of O_2 , N_2 and NO_2 , formate abstraction leads to products of iPOPAN ($(\text{CH}_3)_2\text{CHOC}(\text{O})\text{O}_2\text{NO}_2$) and acetone, which sum to 38%. However, as 30% of the reaction is known to proceed via formate abstraction, this leaves a remainder of 8% ($38 - 30\%$ known formate abstraction), which can be attributed to acetone formation following tertiary abstraction. Oxidation pathways following tertiary abstraction are illustrated in Figure 5.3 and lead to the production of acetic formic anhydride (AFAN). AFAN was produced with a yield of $(30 \pm 4)\%$, in close agreement with the yield of CH_3O ($(35 \pm 5)\%$), a co-product from the same reaction pathway. Therefore, abstraction from the tertiary site is approximately 40% calculated from the sum of the AFAN yield + 8% acetone or the sum of CH_3O yield + 8% acetone. The main products formed following methyl abstraction are formaldehyde and formic acid, as illustrated in Figure 5.3. The oxygen-independent yield of formaldehyde is $\sim 20\%$ and is attributed to the decomposition of the $\text{HC}(\text{O})\text{OCH}(\text{CH}_3)\text{CH}_2\text{O}^\bullet$ radical. Further reaction of formaldehyde's co-product, $\text{HC}(\text{O})\text{OC}^\bullet\text{H}(\text{CH}_3)$, leads to the radical $\text{HC}(\text{O})\text{OCO}^\bullet\text{H}(\text{CH}_3)$, which can undergo alpha-ester rearrangement to formic acid or react with oxygen to produce formic acid anhydride. Formic acid is only formed via methyl abstraction with a yield of $(15 \pm 5)\%$, implying that almost all of the

$\text{HC(O)OCO}^\bullet\text{H(CH}_3\text{)}$ radical undergoes alpha-ester rearrangement. The sum of the yields accounts for 75 – 85% of the reacted isopropyl formate and leaves 10% of the reaction branching ratios unaccounted for. Multifunctional nitrates were observed and may account for the remainder of the reaction, although it is unknown which reaction pathways they are formed via.

Due to the formation of HO_2 following Cl-initiated oxidation, Pimentel et al. [17] estimated 30% of the attack in the Cl-initiated experiments could be due to OH-initiated oxidation. Taking this into account, they revised the experimental branching ratios following Cl-initiated oxidation to be $(30 \pm 5)\%$ for formate abstraction, $(20 \pm 5)\%$ for methyl abstraction and $(50 \pm 5)\%$ for tertiary abstraction. The OH-initiated oxidation of isopropyl formate produced yields of AFAN (43%), acetone (43%) and HCOOH (15 – 20%). Increased formation of AFAN is attributed to increased abstraction at the tertiary site, estimated between 55 – 65%. The yield of iPOPAN following OH-initiated oxidation was 20 – 25%. The yield of iPOPAN following Cl-initiated oxidation is not reported in isolation, although from the table of yields reported by Pimentel et al. [17], is on average $\sim 7.5\%$. However, Pimentel et al. [17] report that the 20 – 25% yield of iPOPAN suggests a similar branching ratio for formate abstraction following Cl and OH-initiated oxidation.

Chamber experiments by Pimentel et al. [17] demonstrate abstraction from the tertiary hydrogen dominates the OH-initiated oxidation of isopropyl formate. However, how this branching ratio changes as a function of temperature and the branching ratios of formate and methyl abstraction are not as well characterised. This work expands the temperature-dependent kinetics of isopropyl formate from between 243 and 373 K to 230 and 575 K. The site-specific kinetics of isopropyl formate + OH are also determined as a function of temperature between 298 and 575 K.

5.2. Experimental

5.2.1. Synthesis of isopropyl formate isotopomers

Due to the lack of availability in purchasing deuterated isotopomers of isopropyl formate, $(\text{CH}_3)_2\text{CHOC(O)D}$, was synthesised to determine the site-

specific reaction kinetics of isopropyl formate. To test the synthesis method, undeuterated isopropyl formate, $(\text{CH}_3)_2\text{CHOC(O)H}$, was also synthesised. Isopropyl alcohol is reacted with formic acid in a Fischer esterification reaction [18]. The reaction is summarised in Figure 5.5, and the reaction mechanism is illustrated in Figure 5.6. Concentrated sulphuric acid is used as a catalyst to protonate formic acid. The lone pair on the alcohol group in isopropyl alcohol attacks the protonated formic acid in a nucleophilic addition reaction that forms a tetrahedral intermediate. A series of proton transfers occur before water is eliminated and sulphuric acid reforms, producing isopropyl formate.

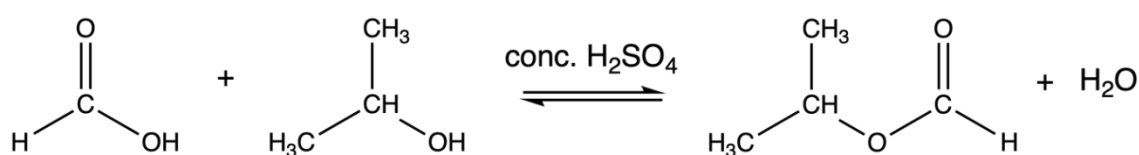


Figure 5.5 – Esterification reaction between formic acid and isopropyl alcohol, forming isopropyl formate and water.

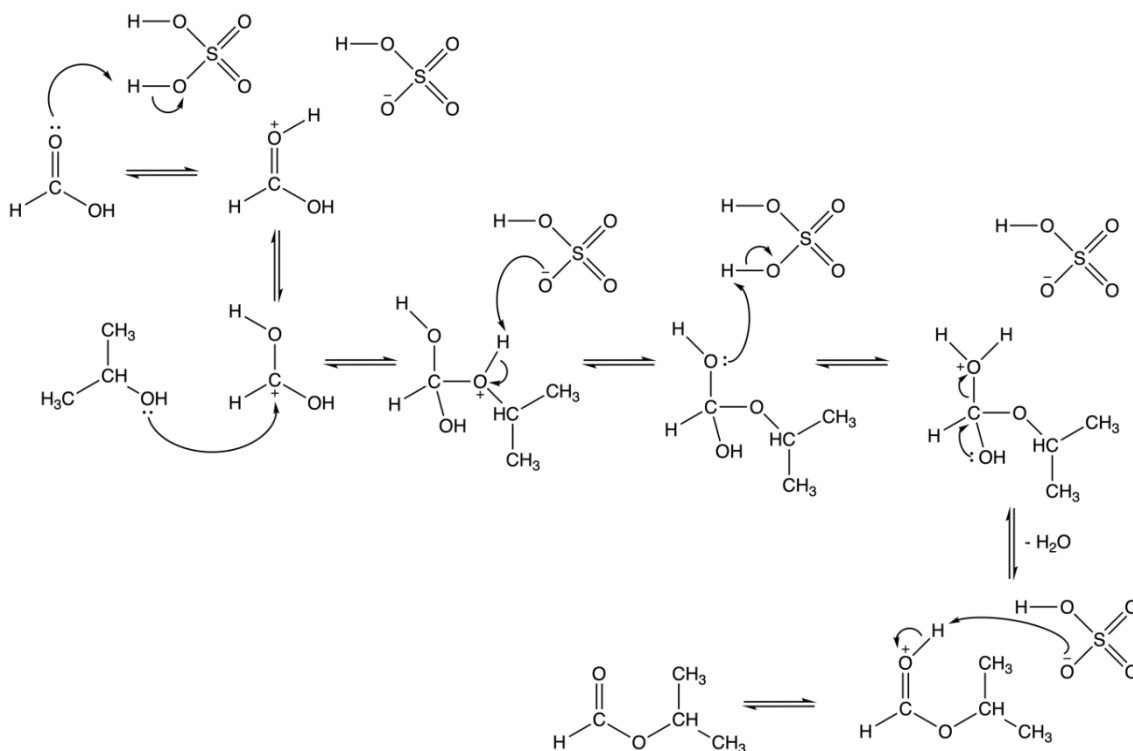


Figure 5.6 – The reaction mechanism for the Fischer esterification reaction between formic acid and isopropyl alcohol, catalysed by sulphuric acid [18].

To synthesise isopropyl formate, 20 ml of isopropyl alcohol (Thermofisher, 99%) and 40 ml of formic acid (Fisher Scientific, 98 – 100%) were added to a round-bottom flask containing a magnetic stirrer bar. The round-bottomed flask sat within

a metal heat block on a heater stirrer plate (Figure 5.7). Whilst the mixture was heated, 2 ml of concentrated sulphuric acid (Fisher Scientific, 95%) was added dropwise. The mixture was refluxed at approximately 349 K for 8 hours and left to cool overnight. Sodium carbonate was dissolved in deionised water and added in small, sequential additions until effervescence was no longer observed. Effervescence was due to the production of CO_2 following the neutralisation of unreacted sulphuric acid. Following the addition of sodium carbonate, the mixture separated into two distinct layers consisting of an organic layer and an aqueous layer. The higher-density aqueous layer containing aqueous sodium carbonate and formic acid was drained, leaving the organic layer containing the isopropyl formate product. The organic layer was washed with aqueous sodium carbonate three times before being transferred to a clean round-bottom flask. Isopropyl formate was distilled between 341.5 – 345.0 K, making sure to keep the temperature below the boiling point of isopropyl alcohol (358 K), which may also remain in the organic layer. NMR analysis of isopropyl formate can be found in Appendix D.

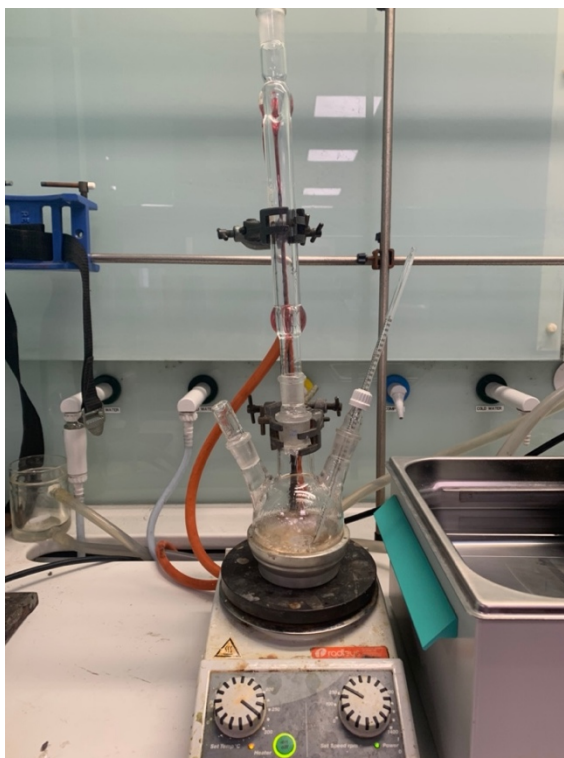


Figure 5.7 – Reflux set up for the synthesis of isopropyl formate.

The kinetics and yields of synthesised isopropyl formate were compared with isopropyl formate purchased from Sigma-Aldrich (98%) and found to be in good

agreement. Deuterated isopropyl formate, $(\text{CH}_3)_2\text{CHOC}(\text{O})\text{D}$, was synthesised following the same methodology outlined above, using deuterated formic acid ($\text{CD}_3\text{C}(\text{O})\text{OD}$) (Apollo Scientific Limited, >99.0 Atom% D (95% in D_2O)) instead of $\text{CH}_3\text{C}(\text{O})\text{OH}$. NMR analysis of $(\text{CH}_3)_2\text{CHOC}(\text{O})\text{D}$ showed a purity of > 98%.

5.2.2. Low temperature reaction cell and UV absorption measurements

The kinetics presented in this chapter cover a wider temperature range than the kinetics presented in Chapters 3 and 4 due to the implementation of a new reaction cell. The new experimental setup is illustrated in Figure 5.8. Gas bulbs of isopropyl formate (Sigma-Aldrich, 98% and synthesised, 98%) and deuterated isopropyl formate (synthesised, 98%) were made to known concentrations in argon (BOC 99.998%), as outlined previously in Chapter 2. The vapour pressure of isopropyl formate was calculated via the Antoine Equation to be 139.17 Torr [129]. Bulbs of isopropyl formate were typically made with 2% isopropyl formate and 98% argon. The argon bath gas and isopropyl formate were flowed through calibrated mass flow controllers into a mixing manifold. The OH/OD precursor was delivered to the mixing manifold via a bubbler flowing argon over liquid H_2O_2 (Sigma-Aldrich, 50% wt in H_2O) mixed with D_2O (Sigma-Aldrich 99.9 atom% D). The flow rate of the bubbler, and hence OH/OD concentration, was set by a valve which controlled the flow of gas out of the bubbler. Once the flow rate from the bubbler had been set, the pressure in the reaction cell was noted, and the flow out of the bubbler turned off. This led to a pressure reduction within the cell. The flow of argon was increased until the pressure within the reaction cell was the same as when the bubbler was flowing. The change in the argon flow rate with/without bubbler delivery corresponded to the flow rate of the peroxide precursor.

The mixing manifold flowed the gas through PTFE piping to a glass UV absorption cell, 1 m in length. A mercury lamp was fitted to the front of the cell and sent probe light towards the CCD detector (Hamamatsu S7031). The CCD detector was fitted with a 185 nm interference filter. However, absorbance at 254 nm was also observed. The theory behind UV absorption measurements is described in detail in Chapter 2. In this work, UV absorption measurements were used to ensure that the delivery of isopropyl formate was stable. The light intensity at 185 and 254

150

nm was monitored in the absence and presence of isopropyl formate. Delivery of isopropyl formate stabilised within two minutes of setting a new flow. Following absorption experiments, two minutes was used as a standard time between new isopropyl formate flows/points on the bimolecular plot.

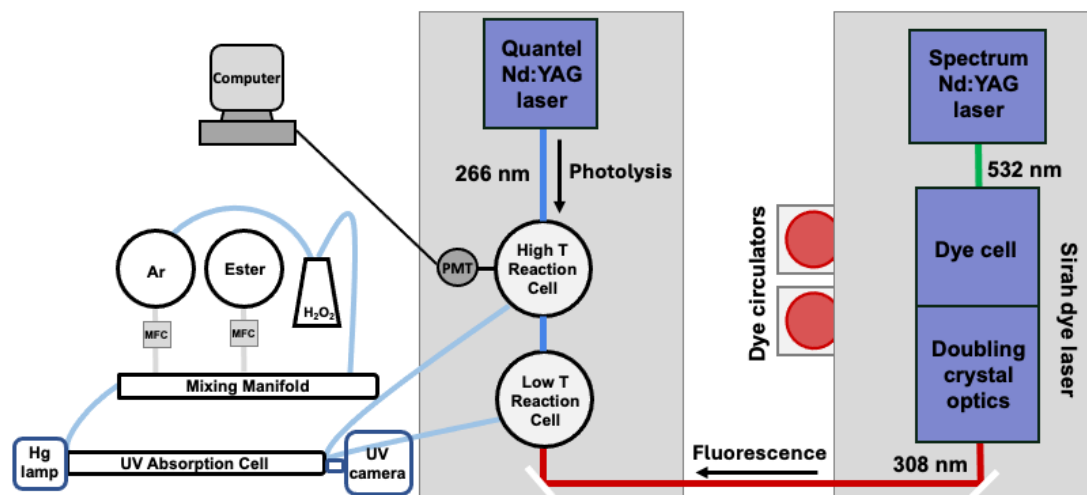


Figure 5.8 – Experimental setup to determine gas-phase kinetics of OH/OD + ester.

The gas mixture flowed through the UV absorption cell and into the low-temperature or high-temperature reaction cell. Each reaction cell had a gas inlet which was connected to the UV absorption cell outlet via PTFE piping. The reaction cell not in use had a stopper placed on its gas inlet. The pressure inside the cell was controlled by throttling the gas exit to a rotary vane pump. The rotary pump was connected to both reaction cells and selectively pumped the cell the gas was flowed through. The temperature of the low temperature reaction cell was controlled by a silicon thermal fluid (SYLTHERMÔ) pumped around the cell by a recirculating thermostating unit. The temperature in the high temperature reaction cell was controlled by a ceramic oven.

OH and OD radicals were generated by the photolysis of the $\text{H}_2\text{O}_2/\text{D}_2\text{O}_2$ precursor at 266 nm by a pulsed Nd:YAG laser (Quantel Q-smart 850 at 10 Hz). OH and OD radicals were then monitored via on-resonance laser induced fluorescence at ~ 308 nm (307.290 nm for OH ($\text{R}_1(1)$)) and 307.248 nm for OD ($\text{Q}_1(1)$)). The wavelengths of OH and OD were chosen to match the calibrated wavelengths with

a 1:1 relationship, as outlined in Chapter 4. The radicals were excited by a Nd:YAG pumped dye laser (Sirah, Cobra Stretch, DCM special dye), and their fluorescence was monitored using a channel photomultiplier (PerkinElmer C1943O). The time delay between the photolysis and fluorescence laser was generated by a digital delay generator (BNC DG535). Typically, five scans were taken for a given temporal profile. OH decays were analysed via E4.1 and E4.3, whose derivations are outlined in Appendix B. OD decays were analysed via the same equations as OH with additional analysis via E4.4 when OD grew from a zero background. Some OD decays required more complex MATLAB analysis, which is discussed below.

5.2.3. Computational calculations

The potential energy surface of the OH + isopropyl formate reaction has been mapped out at the M062X/6-31+G** level of theory. The energies, DFT geometry optimisations and frequency calculations were performed in Gaussian [81], utilising the “ultrafine” integration grid. Where multiple transition states have been found for a given reaction site, only the lowest is presented.

5.3. Temperature dependent kinetics of OH/OD with isopropyl formate

This work has determined the temperature-dependent reaction kinetics of isopropyl formate with OH and OD between 230 and 575 K and 2.6 and 200 Torr. Rate coefficients determined in this work are shown in Figure 5.9 alongside other literature studies. At 298 K, this work agrees with the studies of Pimentel et al. [17] and Stemmler et al. [123], however, the studies by Zhang et al. [125] and Szilagyi et al. [124] determined rate coefficients lower than in this work. Whilst neither study reports any oxygen present, if any background oxygen were present, OH is expected to regenerate following the internal isomerisation of the excited RO_2^* to a QOOH species followed by decomposition to OH, illustrated in Figure 5.10.

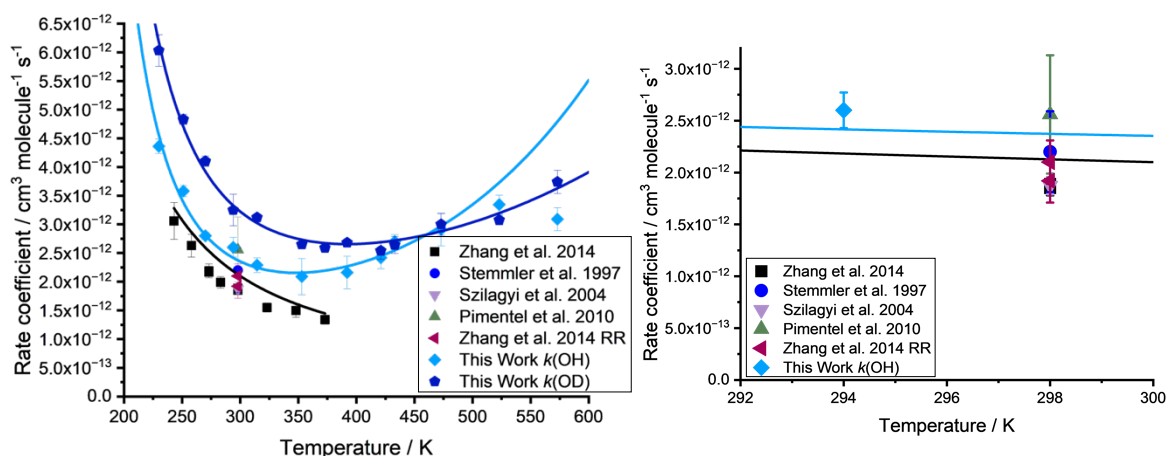


Figure 5.9 – Rate coefficients for the reactions of OH and OD + isopropyl formate determined in this work between 230 – 575 K and 110 – 120 Torr Ar shown alongside literature studies for OH + isopropyl formate. The inset shows a focused view between 290 – 300 K at OH + isopropyl formate determined in this work and the literature. Solid lines represent non-Arrhenius temperature-dependent fits.

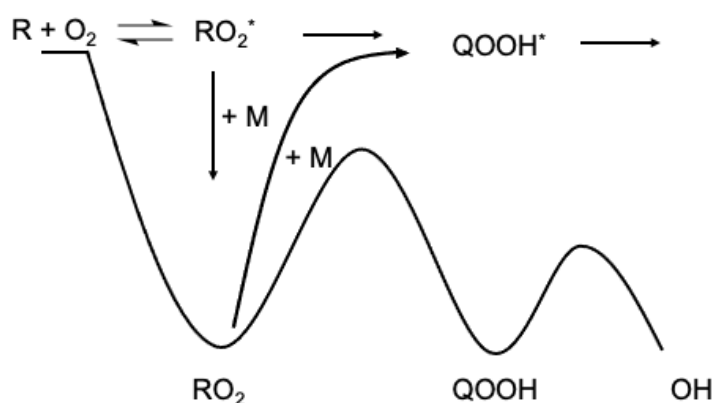


Figure 5.10 – Generic potential energy surface for a hydrogen abstraction reaction leading to the production of OH.

Szilagyi et al. [124] used He bath gas at a pressure of 1.91 Torr with single exponential fits. The OH decays presented by Szilagyi et al. [124] are taken over a relatively short timeframe of the overall reaction time (0.4 lifetimes) such that if biexponential behaviour were present, it would not be observed. Furthermore, their example biexponential plot for OH + isopropyl formate has an intercept of $\sim 80 \text{ s}^{-1}$, which is higher than the reported rate of diffusion and reaction with impurities value of 26.2 s^{-1} and a significant fraction of the measured k' range of 99 – 275 s^{-1} . If any oxygen was present in their system, OH recycling at 298 K and 1.91 Torr would be

highly efficient, resulting in an observed rate coefficient lower than the true value. They report an error of 4.4%. As the discrepancy, $\sim 54 \text{ s}^{-1}$, between the measured rate of diffusion and reaction with impurities and the observed bimolecular intercept ranges from 55 – 20% of the observed k' , the reported 4.4% error is unlikely to reflect the true experimental error.

Zhang et al. [125] also used He as the bath gas with single exponential fits. Although no pressure is stated in the Zhang et al. [125] study, similar studies from the same group at the time use a pressure of $\sim 100 \text{ Torr}$ [130, 131]. At 298 K and 120 Torr of Ar, this work found $(19 \pm 10)\%$ recycling of OH. As Ar is more efficient at collisional stabilisation than He, this effect is expected to increase in He. With increasing temperature, the rate of RO_2^* to OH increases, leading to an increase in the amount of OH recycling for a given pressure. This effect could explain the increasing discrepancy between this work and Zhang et al. [125] with increasing temperature. However, the discrepancy remains approximately constant with decreasing temperature despite the expectation that OH recycling would decrease. The relative rate study by Zhang et al. [125] at 700 Torr of He determined a higher room temperature rate coefficient of $(2.10 \pm 0.21) \times 10^{-12} \text{ cm}^3 \text{ molecule}^{-1} \text{ s}^{-1}$ relative to propane and $(1.92 \pm 0.21) \times 10^{-12} \text{ cm}^3 \text{ molecule}^{-1} \text{ s}^{-1}$ relative to pentane, compared with $(1.87 \pm 0.11) \times 10^{-12} \text{ cm}^3 \text{ molecule}^{-1} \text{ s}^{-1}$ in their absolute study. However, both their absolute and relative rate coefficients agree within experimental errors.

In agreement with Zhang et al. [125], this work also observes a negative temperature dependence. The rate coefficient decreases from $(4.36 \pm 0.13) \times 10^{-12} \text{ cm}^3 \text{ molecule}^{-1} \text{ s}^{-1}$ at 230 K to $(2.09 \pm 0.32) \times 10^{-12} \text{ cm}^3 \text{ molecule}^{-1} \text{ s}^{-1}$ at 353 K before increasing to $(3.51 \pm 0.32) \times 10^{-12} \text{ cm}^3 \text{ molecule}^{-1} \text{ s}^{-1}$ at 523 K. The negative temperature dependence can largely be attributed to hydrogen abstraction at the tertiary site. Figure 5.11 shows the potential energy surface for the initial hydrogen abstraction by OH at the three reaction sites within isopropyl formate. Abstraction from the tertiary site (purple) has a negative activation energy of $-12.1 \text{ kJ mol}^{-1}$ compared with 3.0 kJ mol^{-1} and 0.5 kJ mol^{-1} for abstraction from the formate (blue)

and methyl (green) sites, respectively. The transition states are shown in Figure 5.12 and are all influenced by hydrogen bonding to varying extents.

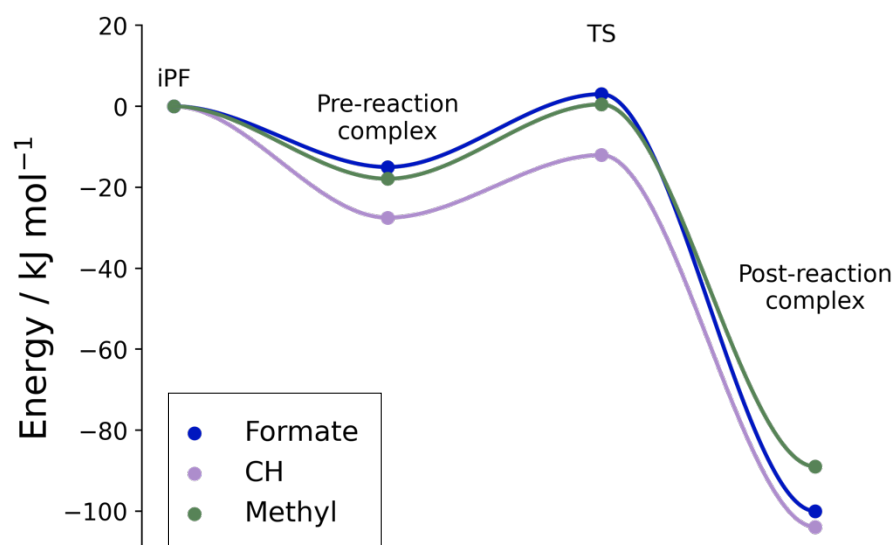


Figure 5.11 – Potential energy surface for the initial hydrogen abstraction of OH + isopropyl formate from the formate reactive site (blue), the tertiary site (purple) and the methyl site (green).

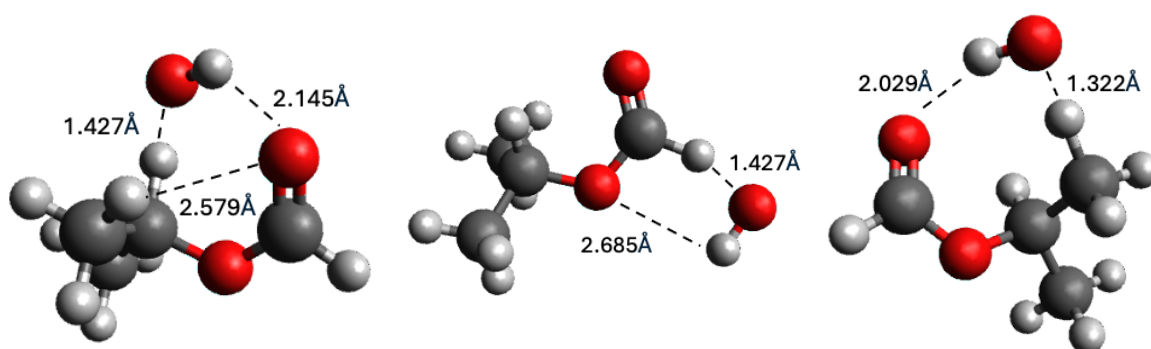


Figure 5.12 – Transition state structures for hydrogen abstraction from isopropyl formate by OH at the tertiary, formate and methyl sites from left to right.

Fitting the positive section of the temperature dependence with an Arrhenius fit gives an activation energy of 5.2 kJ mol⁻¹, if the anomalous *k*OH at 573 K is ignored, or 3.6 kJ mol⁻¹ including *k*OH at 573 K. Alternative, higher energy transition states for formate and methyl abstraction of 4.6 kJ mol⁻¹ and 11.4 kJ mol⁻¹, respectively, have been found. As demonstrated in Chapter 3, outlining methyl formate kinetics, multi-conformer effects become increasingly important at higher temperatures. Therefore, the higher energy conformers for formate and methyl abstraction likely contribute to the positive temperature dependence observed at high temperatures.

Hydrogen bonding involving the carbonyl oxygen is stronger than hydrogen bonding involving the ether oxygen. The carbonyl oxygen atom is a stronger hydrogen acceptor than the ether oxygen due to increased electron density in the double bond compared with the single-bonded ether oxygen. The transition state for tertiary abstraction has a hydrogen bond between the hydrogen in OH and the carbonyl oxygen, which is 2.145 Å. There is also a weaker hydrogen bond/hydrogen bond interaction between one of the methyl hydrogens and the carbonyl oxygen, which is 2.579 Å. The interaction distance between the oxygen in OH and the tertiary hydrogen being abstracted is 1.403 Å. In the formate transition state, there is a hydrogen bond between the hydrogen in OH and the ether oxygen, which is 2.685 Å. The interaction distance between the oxygen in OH and the formate hydrogen being abstracted is 1.427 Å. Despite the transition state for methyl abstraction being higher in energy than for tertiary abstraction, the hydrogen bond between hydrogen in OH and the carbonyl oxygen is 2.029 Å, shorter than the hydrogen bond between the carbonyl oxygen and hydrogen in the tertiary transition state (2.145 Å). The hydrogen bond interaction distance between the OH oxygen and abstracting methyl hydrogen is 1.322 Å, which is also shorter than in the tertiary transition state (1.403 Å). Despite the shorter hydrogen bonding in the methyl transition state, the abstraction of a methyl hydrogen requires more energy than the tertiary C-H bond. The BDE for a methyl hydrogen is 420.6 kJ mol⁻¹ compared with 403.7 kJ mol⁻¹ for the tertiary hydrogen and 407.5 kJ mol⁻¹ for the formate hydrogen [95]. Tertiary abstraction has the lowest BDE, which could be due to electron donation from the adjacent ether group and the inductive effect of the methyl groups. The additional hydrogen bond interaction between the methyl hydrogen and carbonyl oxygen may also help stabilise the tertiary transition state. These combined effects lead to tertiary abstraction dominating at room temperature, as determined by Pimentel et al. [17]. As the rate coefficient increases with decreasing temperature, tertiary abstraction increases.

Table 5.1 – Hydrogen bond and hydrogen bond interaction distances in the transition states for abstraction from the formate, tertiary and methyl sites in isopropyl formate.

Abstraction site	Hydrogen bond description	Hydrogen bond distance / Å
Formate (C(O)H)	O-H---OC(O)H, OH hydrogen to ether oxygen	2.685
Formate (C(O)H)	H-O—HC(O)O<, OH oxygen to hydrogen being abstracted	1.427
Tertiary (CH)	O-H --- (O)C<, OH hydrogen to carbonyl oxygen	2.145
Tertiary (CH)	CH ₃ ---(O)C<, methyl hydrogen to carbonyl oxygen	2.579
Tertiary (CH)	H-O---H-C<, OH oxygen to hydrogen being abstracted	1.403
Methyl (CH ₃)	O-H---(O)C<, OH hydrogen to carbonyl oxygen	2.029
Methyl (CH ₃)	H-O---H ₃ C<, OH oxygen to hydrogen being abstracted	1.322

The ratio between k_{OH} and k_{OD} is illustrated in Figure 5.13, demonstrating a positive KIE (k_{OD} / k_{OH}) between 220 K and 425 K, that decreases with increasing temperature until k_{OH} becomes greater than k_{OD} from 425 K. As previously discussed in Chapter 3, the positive secondary KIE is indicative that the OH/OD bond partakes in the transition state, rather than acting as a spectator bond. As the role of hydrogen bonding is greatest for tertiary and methyl abstraction, the decreasing positive KIE is indicative that abstraction at the tertiary and methyl sites decreases with increasing temperature. The increase in the secondary KIE at the

highest temperature corresponds with a deviation in k_{OH} from the predicted trend (see Figure 5.9).

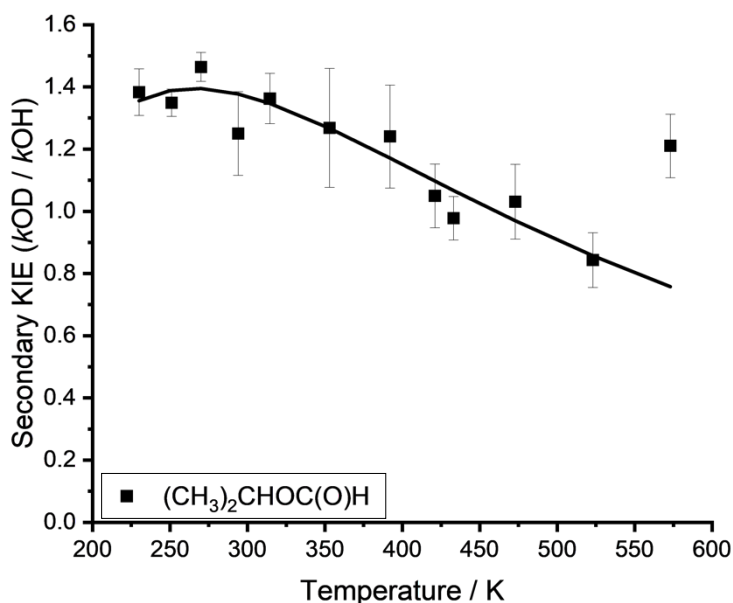
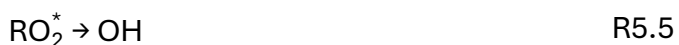


Figure 5.13 – The secondary KIE, k_{OD}/k_{OH} . Individual points on the graph are experimentally measured values of k_{OD}/k_{OH} and the fitted line is k_{OD}/k_{OH} calculated from the temperature-dependent fits shown in Figure 5.9.

5.4. Yields of OH from the reaction of OH + isopropyl formate

The reactions of OH and OD with isopropyl formate regenerate OH when oxygen is present in the system, as discussed above and illustrated in Figure 5.10. Yields of OH can come from the excited RO_2^* (R5.5) or the thermalised RO_2 (R5.6).



Yields of OH from the excited RO_2^* will decrease as a function of pressure as RO_2^* is collisionally stabilised to the thermalised RO_2 . As the temperature increases, internal isomerisation of the RO_2^* becomes more competitive with collisional stabilisation. However, yields of OH from the thermalised RO_2 will increase with pressure and temperature.

5.4.1. Pressure dependence of OH + isopropyl formate at low temperatures

The rate coefficient for OH + isopropyl formate ($k_{\text{OH+IPF}}$) determined in the absence of added oxygen was found to be pressure dependent at 232 K and 252 K as shown in Figures 5.14 and 5.15, respectively. At 232 K, the rate coefficient at 2.6, 20, 43 and 113 Torr has been determined by fitting OH decays with a single exponential. Single exponential fits provided the lowest reduced chi-squared value whilst biexponential fits gave non-sensical, negative values for k_{Regen} , and k_{Stab} . The rate coefficient at 13 Torr, which is an anomaly from the trend, was determined by fitting OH decays with a biexponential. The yields of OH at 232 K are shown on the bottom of Figure 5.13. At 2.6 and 20 Torr the yield is calculated via E5.2, where the high pressure rate coefficient, k_{HighP} , is an average of the rate coefficients determined at 43 and 113 Torr.

$$Y_{\text{OH}} = 1 - \frac{k_{\text{Obs}}}{k_{\text{HighP}}} \quad \text{E5.2}$$

The yield at 13 Torr is determined from the biexponential decay via E3.1. As the yields at 232 K decrease as a function of pressure, they likely come from R5.5, the internal isomerisation of the excited RO_2^* . The pressure dependence is due to the yields of OH which influence the measured rate coefficient. As yields decrease with increasing pressure, the influence of OH on the measured rate coefficient decreases. OD is not regenerated following the reaction of OH + isopropyl formate, therefore, OD decays are not influenced by OD regeneration and the measured rate coefficient is the same regardless of the experimental pressure.

Figure 5.14 shows the rate coefficients determined at 252 K as a function of pressure alongside the corresponding yields. All OH decays at 252 K were fit with a single exponential as despite the pressure dependence and implied OH yield, no biexponential behaviour was observed. The absence of biexponential behaviour suggests that OH is being regenerated on a faster timescale than at higher temperatures. The faster regeneration of OH could be due to an increase in $k_{\text{R+O}_2}$ at low temperatures. Observation of yields at 232 and 252 K and the observation of the lower rate coefficient for single exponential OH decays, provide support for the discrepancy between this work and the works of Zhang et al. [125] and Szilagyi et al. [124].

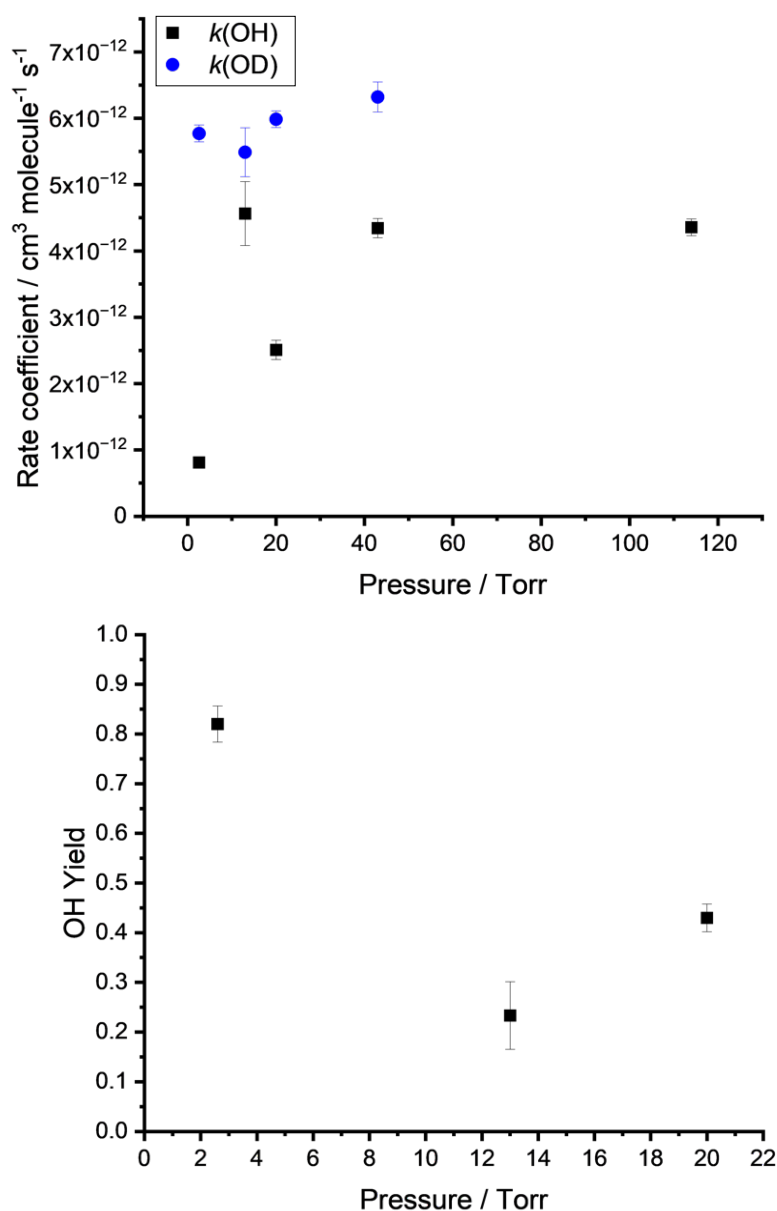


Figure 5.14 – Rate coefficients determined at 232 K (top) and corresponding yields of OH (bottom) as a function of pressure in the absence of any added oxygen.

5.4.2. OH yields as a function of pressure and oxygen at 298 K

Yields at 298 K are shown in Figure 5.15 and decrease with increasing pressure as the excited RO_2^* is collisionally stabilised, preventing OH formation. Between 77 and 96 Torr, the OH yield increases slightly with pressure before plateauing at 0.19 ± 0.04 . This high pressure yield can be attributed to the thermalised RO_2 (R5.6). OH yields from the thermalised RO_2 will increase with pressure as internal isomerisation of RO_2 is a unimolecular pressure-dependent reaction. As there are three reaction sites within isopropyl formate, there are three

RO₂ species that can undergo internal isomerisation and decompose to OH. Excluding the yields above 90 Torr, the Stern-Volmer intercept (shown in Figure 5.15) is 1.41 ± 0.68 with the error at the 95% confidence limit. Above 40 Torr, there is likely a small contribution to the OH yields from the thermalised RO₂, which leads to a slightly higher Stern-Volmer intercept than expected. As the Stern-Volmer intercept describes the competition between k_{Stab} and k_{Regen} (from the excited RO₂^{*}), OH yields suspected to come from the thermalised RO₂ have been excluded. Excluding thermalised RO₂ yields gives a lower Stern-Volmer intercept of 1.12 ± 0.30 . However, even with the points between 40 and 90 Torr, the Stern-Volmer intercept at 298 K is within error of 1. If the Stern-Volmer intercept was greater than 1, this suggests a loss of OH, which could occur through the decomposition of the ROC(O) radical formed following the initial hydrogen abstraction.

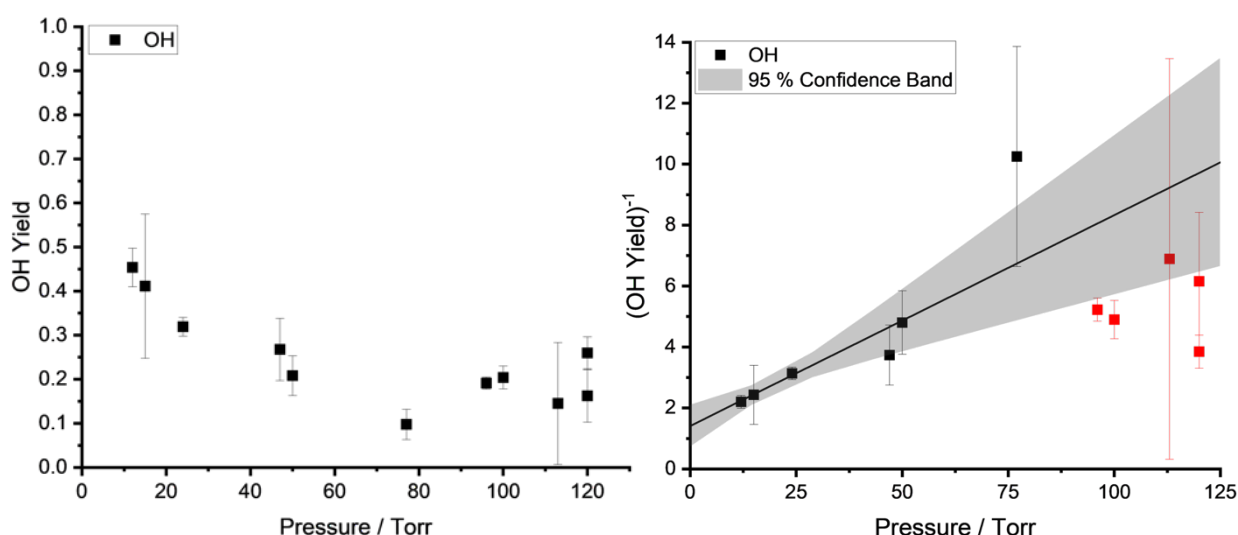


Figure 5.15 – Yields of OH as a function of pressure. The left figure shows OH yields whilst the right figure shows the reciprocal of the OH yield, i.e., the Stern-Volmer plot. Yields above 90 Torr, shown in red, have been excluded from the Stern-Volmer slope as these come from a thermalised RO₂. The Stern-Volmer slope shown on the right is equal to 0.073 ± 0.012 with an intercept of 1.30 ± 0.68 .

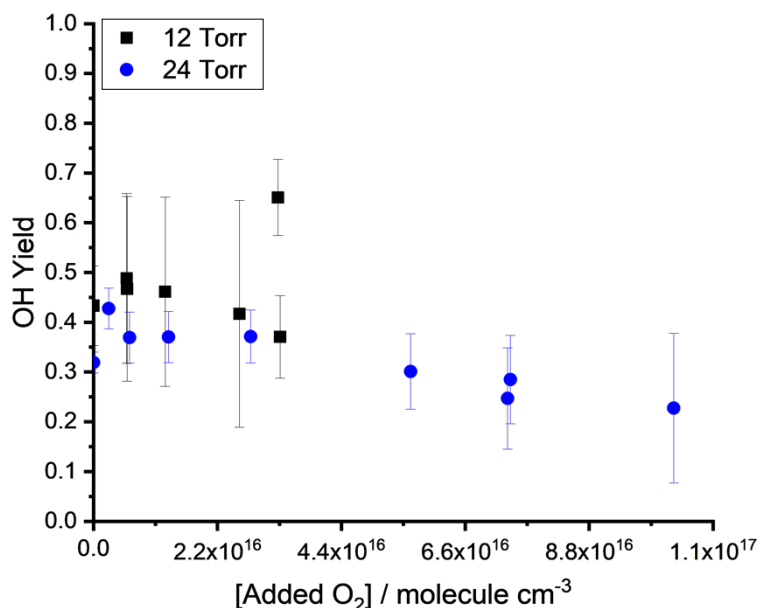


Figure 5.16 – Yields of OH at 12 (black squares) and 24 (blue circles) Torr as a function of added oxygen at 298 K. Yields have been calculated from the difference in the pseudo-first order rate coefficient in the absence and presence of oxygen (E2).

Experiments measuring the OH yield as a function of added oxygen at 12 and 24 Torr (Figure 5.16) show the yield is independent of added oxygen, providing further evidence that no radical is being lost to decomposition at 298 K. The small decrease in the OH yield with increasing concentrations of added oxygen is likely due to increased collisional stabilisation of the RO₂^{*}, as oxygen is more efficient at collisional stabilisation than the argon bath gas.

5.4.3. OH yields as a function of added oxygen and pressure between 393 and 523 K

OH decays remain biexponential in the absence and presence of added oxygen above 393 K. Biexponential behaviour in the presence of added oxygen indicates that increasing the rate of k_{R+O_2} does not increase the timescale of OH regeneration because k_{Regen} from the collisionally stabilised RO₂ increases with increasing thermal energy. OH yields from RO₂ also increase with pressure as the unimolecular isomerisation is a pressure dependent reaction. OH yields calculated from the biexponential tail Y_{Biexp} (Figure 5.17, black) represent the fraction of OH from the thermalised RO₂ (R5.6). The OH yield can also be calculated from the difference

between the pseudo-first order rate coefficient ($k_{\text{OH}+\text{iPF}}$) in the absence and the presence of added oxygen, $Y_{1-(k\text{O}_2/k\text{Ar})}$ (Figure 5.17, blue), which represents the fraction of OH from the excited RO_2^* (R5.5). The sum of the two yields, $Y_{\text{Sum}(\text{O}_2)}$ is shown in Figure 5.17 in lilac.

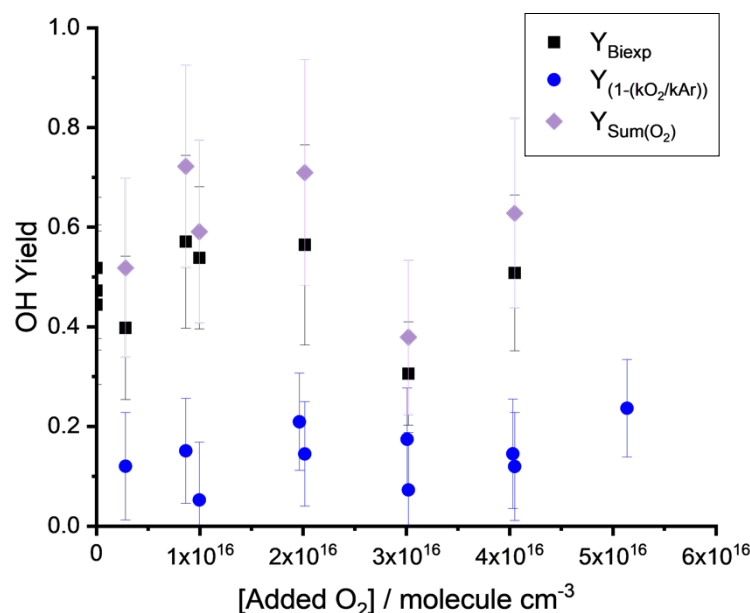


Figure 5.17 – Yields as a function of added oxygen at 393 K and 113 Torr.

At 393 K, the $Y_{1-(k\text{O}_2/k\text{Ar})}$ yield (from RO_2^*) increases with oxygen. Adding oxygen makes the reaction of $(\text{CH}_3)_2\text{CHOC}(\text{O})$ with oxygen, formed following formate abstraction, competitive with its thermal decomposition. When these processes are competitive, the OH yield is expected to increase with added oxygen. Therefore, observation of an oxygen dependence at 393 K suggests radical decomposition of $(\text{CH}_3)_2\text{CHOC}(\text{O})$ is occurring and is competitive with the reaction of $(\text{CH}_3)_2\text{CHOC}(\text{O}) + \text{O}_2$. The experimentally measured unimolecular decomposition of $\text{CH}_3\text{OC}(\text{O})$ is presented in Chapter 4, demonstrating the exponential increase in the rate of decomposition. Although the rate of $(\text{CH}_3)_2\text{CHOC}(\text{O})$ has not been experimentally measured, the temperature dependence of $(\text{CH}_3)_2\text{CHOC}(\text{O})$ decomposition is likely similar to $\text{CH}_3\text{OC}(\text{O})$ decomposition. Yields at 413 K are shown in Figure 5.18 and are independent of oxygen, indicating $(\text{CH}_3)_2\text{CHOC}(\text{O})$ decomposition is too fast to be competitive with oxygen addition at 413 K.

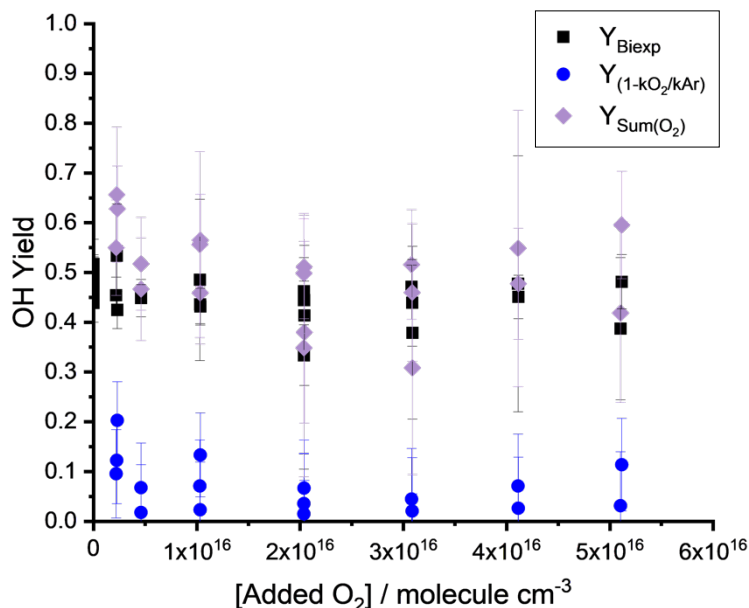


Figure 5.18 – Yields as a function of added oxygen at 413 K and 120 Torr.

OH yields at 423 K as a function of pressure are presented in Figure 5.19. As described above, yields from biexponential OH decays in the presence of added oxygen ($Y_{\text{Biexp}(\text{O}_2)}$, pink triangles) are from the thermalised RO_2 and increase with pressure. Yields from biexponential decays in the absence of added oxygen ($Y_{\text{Biexp}(\text{Ar})}$, black squares) also represent OH from the thermalised RO_2 radicals and increase with pressure. Yields in the absence and presence of added oxygen ($Y_{1-(k\text{O}_2/k\text{Ar})}$, blue circles) decrease with increasing pressure due to the removal of RO_2^* via collisional stabilisation. Yields in the presence of added oxygen ($Y_{\text{Sum}(\text{O}_2)}$, lilac diamonds) are higher than yields in the absence of added oxygen. However, above 80 Torr, $Y_{\text{Biexp}(\text{Ar})}$ and $Y_{\text{Sum}(\text{O}_2)}$ agree within their experimental error range. As oxygen is more efficient at energy transfer than argon, in the presence of added oxygen, both the collisional stabilisation of RO_2^* (removing OH yields) and the isomerisation of the thermalised RO_2 (increasing OH yields) may be faster. This would lead to yields in the presence of added oxygen becoming independent of pressure at a lower pressure than in the presence of no added oxygen, as illustrated in Figure 5.19. As the yields are independent of added oxygen at 413 K, the increase in the presence of oxygen is unlikely due to capturing $(\text{CH}_3)_2\text{CHOC}(\text{O})$ radical from decomposition. The increase is likely due to representing a higher proportion of yields from RO_2^* . As the biexponential yields in the absence of added oxygen are larger than in the presence

of added oxygen, they may also be representing some OH from RO_2^* . In the presence of added oxygen, due to an increase in $k_{\text{R}+\text{O}_2}$, the two processes of OH regeneration $\text{RO}_2^* \rightarrow \text{OH}$ and $\text{RO}_2 \rightarrow \text{OH}$ can be resolved over the experimental timescale. However, when the formation of RO_2 is slower in the absence of added oxygen, the source of regenerated OH is not resolved.

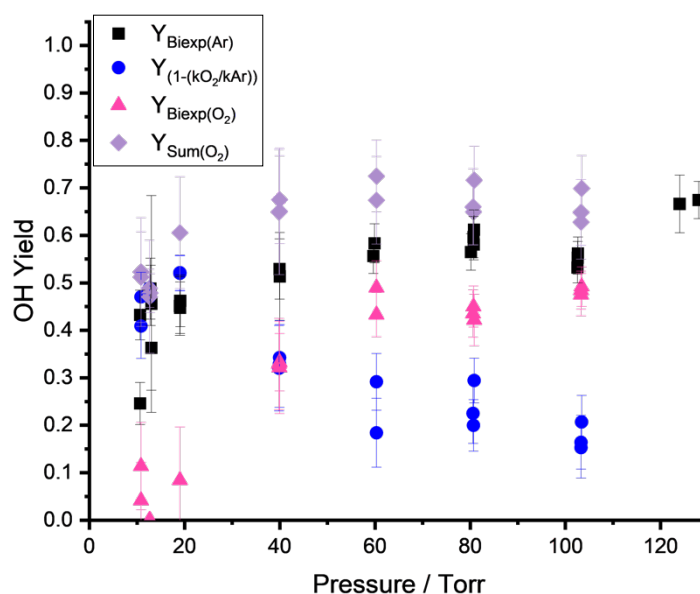


Figure 5.19 – Yields of OH calculated via different methods at 423 K. Yields at this temperature are independent of added oxygen.

The Stern-Volmer intercept of the yields, $Y_{1-(k\text{O}_2/k\text{Ar})}$, shown in Figure 5.19 in blue is 1.55 ± 0.27 with an unweighted fit or 1.59 ± 0.11 with an instrumental fit. Both Stern-Volmer fits are shown in Figure 5.20. As the Stern-Volmer intercept is above 1, this provides further evidence that thermal decomposition of the $(\text{CH}_3)_2\text{CHOC(O)}$ radical is occurring at this temperature. Thermal decomposition of $\text{CH}_3\text{OC(O)}$, outlined in Chapter 4, was also noticeable at 423 K via an increase in the Stern-Volmer intercept. However, the yields of OH outlined in Chapter 4 increased with added oxygen at 398 and 423 K. The oxygen dependence of the yields in this chapter, illustrated in Figures 5.17, 5.18 and 5.21 at 393, 413 and 473 K from isopropyl formate oxidation, is not as significant as yields from methyl formate oxidation.

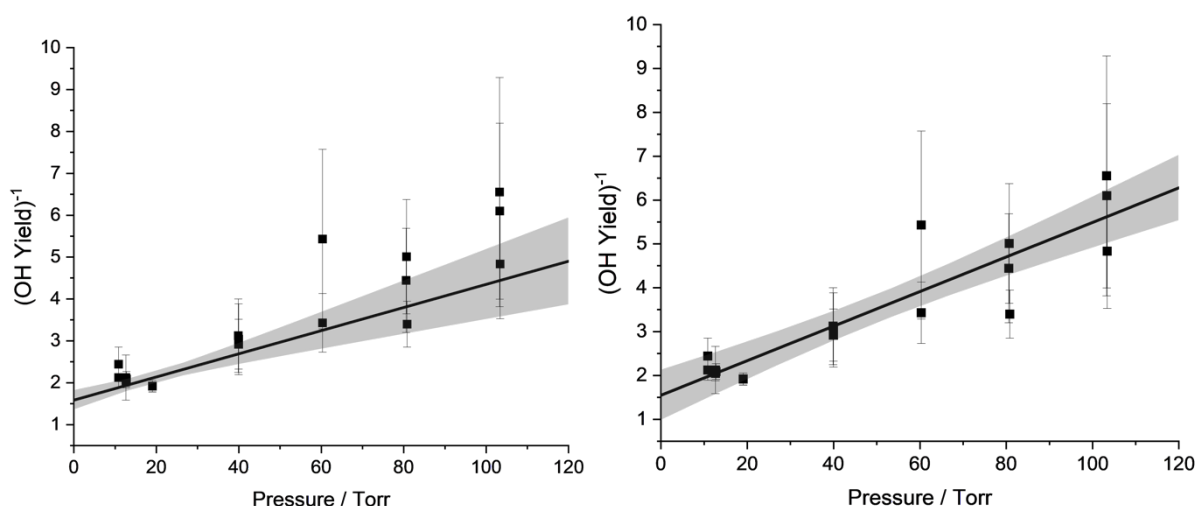


Figure 5.20 – Stern-Volmer plots at 423 K with an instrumental fit (left) and unweighted fit (right). The instrumental fit has a slope equal to 0.028 ± 0.005 and an intercept equal to 1.59 ± 0.22 . The unweighted fit has a slope equal to 0.039 ± 0.004 and an intercept equal to 1.55 ± 0.57 .

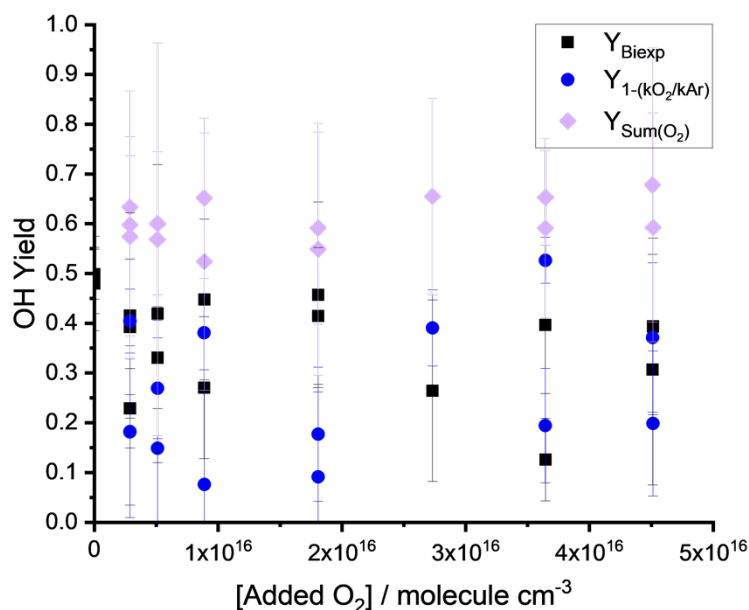


Figure 5.21 - Yields as a function of added oxygen at 473 K and 120 Torr. Yields are independent of added oxygen and can be attributed to abstraction at the tertiary and methyl reaction sites. The radical formed following formate abstraction, $(\text{CH}_3)_2\text{CHOC}(\text{O})$, thermally decomposes preventing OH regeneration.

The weaker oxygen dependence in the isopropyl formate system suggests that decomposition of the $(\text{CH}_3)_2\text{CHOC}(\text{O})$ radical may be occurring at a faster rate

than the $\text{CH}_3\text{OC}(\text{O})$ radical. Pimentel et al. [17] observed decomposition of $(\text{CH}_3)_2\text{CHOC}(\text{O})$ at 340 K and 700 Torr. Whilst this work has not explored the decomposition of $(\text{CH}_3)_2\text{CHOC}(\text{O})$ at 340 K, the pressure of their system is much higher than in this work (700 vs 120 Torr). As decomposition of $\text{ROC}(\text{O})$ is a unimolecular reaction, increasing pressure will increase the rate of reaction. Pimentel et al. [17] also observed the decomposition of $(\text{CH}_3)_3\text{COC}(\text{O})$ at 298 K, indicating $(\text{CH}_3)_3\text{COC}(\text{O})$ decomposition is faster than $(\text{CH}_3)_2\text{CHOC}(\text{O})$ decomposition. Despite these experimental observations, theoretical calculations by Dr Robin Shannon at the CCSD(T)-F12/aug-cc-pVTZ//M06-2X/6-31+G** level of theory found the barriers to $\text{ROC}(\text{O})$ decomposition to be independent of the R group. Formate abstraction contributes a lower percentage in the isopropyl formate reaction compared with methyl formate. Hence, less $(\text{CH}_3)_2\text{CHOC}(\text{O})$ is produced in this system and changes as a function of added oxygen are likely more subtle. However, further evidence for radical decomposition comes from experiments of the deuterated isotopomer, $(\text{CH}_3)_2\text{CHOC}(\text{O})\text{D}$, outlined below.

Yields determined at 523 K, as a function of pressure, are presented in Figure 5.22. The separate contributions of the excited RO_2^* (R5.5) and the thermalised RO_2 (R5.6) are not as obvious at 523 K compared with 423 K. As the temperature has increased, the rate of internal isomerisation has increased, and OH from RO_2^* and RO_2 is now occurring on a similar timescale. Therefore, separate contributions from RO_2^* and RO_2 to the OH yield cannot be distinguished at 523 K. The increase in the rate of internal isomerisation as a function of temperature is also evident by examining the yields presented at 393 K in Figure 5.17 and 473 K in Figure 5.21. Although the sum of the yields is similar at both 393 and 473 K, the contribution from the excited RO_2^* has increased at 473 K as internal isomerisation is faster due to the increase in thermal energy.

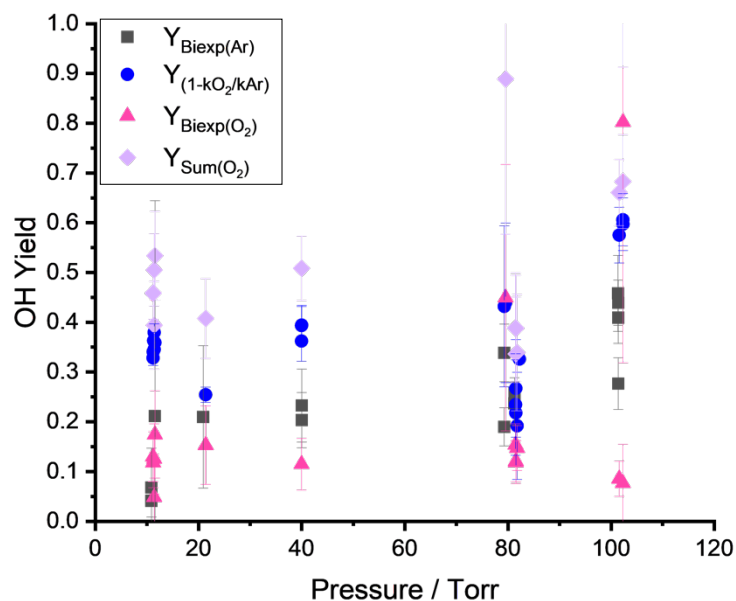


Figure 5.22 - Yields of OH following the reaction of OH with isopropyl formate calculated via different methods at 523 K.

5.4.4. Yields of OH from thermalised RO₂ species at high pressures

OH yields from the reaction of OH + isopropyl formate can come from three peroxy (RO₂) radicals: (CH₃)₂CHOC(O)OO formed from formate abstraction, (CH₃)₂C(OO)OC(O)H from tertiary abstraction or OOCH₂(CH₃)CHOC(O)H from methyl abstraction. For (CH₃)₂CHOC(O)OO, only one isomerisation transition state with a barrier of 61.5 kJ mol⁻¹, has been found where the oxygen radical abstracts the tertiary hydrogen to form the carbon centred QOOH radical, (CH₃)₂COC(O)OOH. For (CH₃)₂C(OO)OC(O)H, the oxygen radical can abstract either the formate hydrogen or a methyl hydrogen. Abstraction of the formate hydrogen is lower in energy with an isomerisation barrier of 76.7 kJ mol⁻¹, compared with 153.3 kJ mol⁻¹ to abstract a methyl hydrogen. Abstraction of a methyl hydrogen has a significantly higher barrier as it is five-membered transition state. Steric hinderance leads to an increase in the barrier for isomerisation in five-membered compared with six-membered transition states. For OOCH₂(CH₃)CHOC(O)H, isomerisation can abstract the tertiary hydrogen, with a barrier of 143.3 kJ mol⁻¹ (a five-membered transition state), or another methyl hydrogen, with a barrier of 114.1 kJ mol⁻¹ (a six-membered transition state). The barriers to internal isomerisation for each of the thermalised peroxy

radicals are shown in Table 5.2. It is assumed that once the barrier to isomerisation is overcome, decomposition of the QOOH radical is instantaneous.

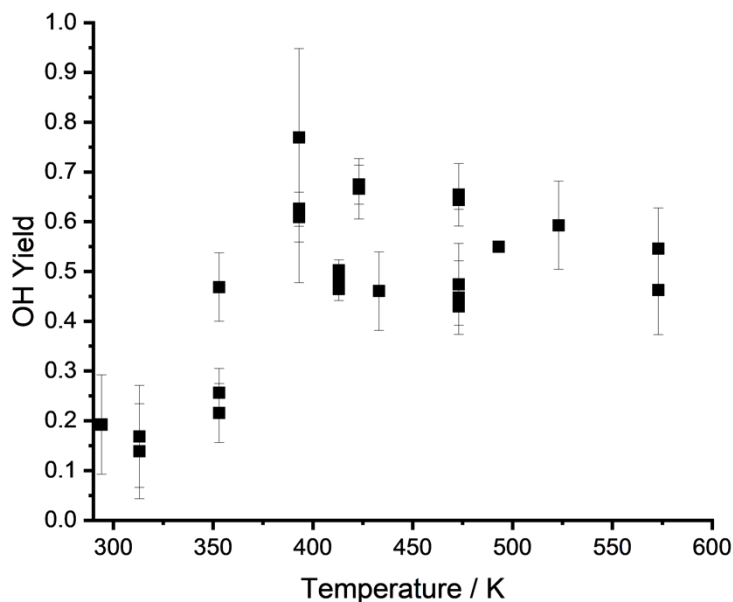
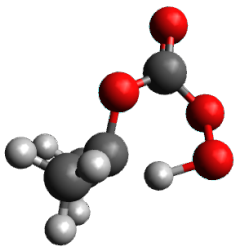
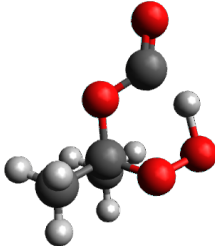
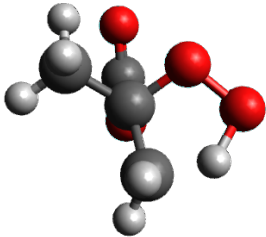
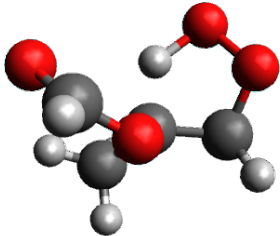
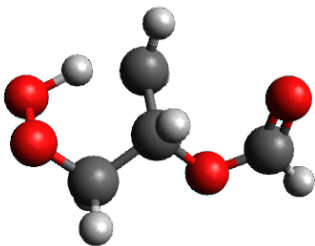


Figure 5.23 – Yields of OH from OH + isopropyl formate obtained by fitting biexponential decays above 120 Torr.

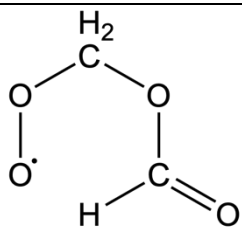
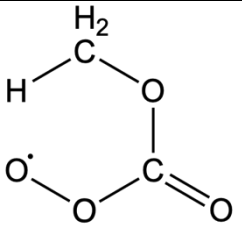
The barrier for internal isomerisation of the $(\text{CH}_3)_2\text{CHOC}(\text{O})\text{OO}$ radical is the lowest in energy. Therefore, yields of OH from the thermalised RO_2 at 298 and 313 K, shown in Figure 5.23, are likely due to isomerisation of $(\text{CH}_3)_2\text{CHOC}(\text{O})\text{OO}$ – formed following formate abstraction. This would give branching ratios for formate abstraction of 0.19 ± 0.10 at 298 K and 0.15 ± 0.02 at 313 K. This is in good agreement with the room temperature branching ratio for formate abstraction of $\sim 20 - 25\%$ assigned by Pimentel et al. [17] via the observation of iPOPAN, illustrated in Figure 5.2.

Table 5.2 - Barriers for internal isomerisation of the thermalised RO₂ radicals formed following abstraction from the formate, methyl and tertiary sites in isopropyl formate.

Abstraction Site	Transition State	<i>ab initio</i> Barrier / kJ mol ⁻¹
Formate Abstraction		61.5
Tertiary Abstraction		76.7
Tertiary Abstraction		153.3
Methyl Abstraction		143.3
Methyl Abstraction		114.1

High pressure yields of OH from the reaction of OH + methyl formate were observed from 541 K. The barriers for isomerisation of peroxy radicals $\text{CH}_3\text{OC(O)OO}$ and $\text{OOCH}_2\text{OC(O)H}$ are $115.6 \text{ kJ mol}^{-1}$ and 91.8 kJ mol^{-1} , respectively. The lowest barrier for isomerisation of $\text{OOCH}_2(\text{CH}_3)\text{CHOC(O)H}$ is $114.1 \text{ kJ mol}^{-1}$, whereas the lowest barrier for isomerisation of $(\text{CH}_3)_2\text{C(OO)OC(O)H}$ is 76.7 kJ mol^{-1} . Chapter 4 discussed how yields of OH from methyl formate can be attributed to methyl abstraction, via the isomerisation of $\text{OOCH}_2\text{OC(O)H}$. As the isomerisation of $\text{OOCH}_2(\text{CH}_3)\text{CHOC(O)H}$ is 14 kJ mol^{-1} higher in energy than $\text{OOCH}_2\text{OC(O)H}$, yields of OH, shown in Figure 5.23, are unlikely to come from methyl abstraction. However, the methyl formate barriers are determined at a much higher level of theory, CCSD(T)-F12/aug-cc-pVTZ//M06-2X/6-31+G**, compared with M062X/6-31+G** for isopropyl formate barriers. Therefore, barriers for isopropyl formate peroxy radicals are not as reliable, and the comparison is not direct.

Table 5.3 - Barriers for internal isomerisation of the thermalised RO_2 radicals formed following abstraction from the methyl and formate sites in methyl formate.

Abstraction Site	Transition State	<i>ab initio</i> Barrier / kJ mol^{-1}	Fitted Barrier / kJ mol^{-1}	Yang et al. / kJ mol^{-1}
Methyl Abstraction		91.8	98.0	95.4
Formate Abstraction		115.6	109.5	117.2

Between 393 and 541 K, the OH yields observed likely come from a combination of tertiary and formate abstraction. However, as decomposition of the radical formed following formate abstraction may dominate over oxygen addition, the yields can be attributed to tertiary abstraction. Table 5.4 presents branching ratios for tertiary abstraction calculated from the yield average at each temperature. At 393 K the branching ratio for tertiary abstraction is ~ 70%, higher than the ~ 55 [17] 65% ratio determined by Pimentel et al. [17] at 298 K. The study by Pimentel et al. [17] accounted for 75 – 85% of the reacted isopropyl formate. It is possible that some products, such as multifunctional nitrates, following tertiary abstraction, were not quantified, leading to a slight underestimation of tertiary abstraction. The rate coefficient for OH + isopropyl formate decreases between 300 and 393 K, indicating that tertiary abstraction is dominant. However, the secondary KIE also decreases slightly in this range, suggesting that the importance of hydrogen bonded transition states (observed for tertiary and methyl abstraction) decreases. This work determined formate abstraction contributes ~ 20% of the total reaction at 298 K. If the branching ratio for tertiary abstraction is accurate at 393 K, and remains approximately constant between 298 and 393 K, this leaves a 10 – 20% remainder for methyl abstraction. Given the strong hydrogen bonding in the methyl transition state and the lower transition state energy for initial abstraction by OH than formate abstraction, it is perhaps surprising that reaction at the methyl site contributes the smallest amount to the total reactivity. However, entropically the formate transition state is likely favoured as the methyl and tertiary groups are not locked up in hydrogen bonds and therefore, can spin freely. The ratio of formate abstraction may be lower than 20% as the yields determined at 298 and 313 K do have significant errors.

Table 5.4 – Branching ratios for tertiary abstraction as a function of temperature calculated from the yield average of OH yields for a given temperature. OH yields were determined from biexponential decays in the absence of added oxygen above 120 Torr.

Temperature / K	Branching Ratio for tertiary abstraction
393	0.67 ± 0.09
413	0.49 ± 0.02
423	0.67 ± 0.01
433	0.46 ± 0.08
473	0.53 ± 0.11
523	0.59 ± 0.09
573	0.50 ± 0.06

5.5. Kinetics of OH/OD with deuterated isopropyl formate, $(\text{CH}_3)_2\text{CHOC}(\text{O})\text{D}$

5.5.1. OH + $(\text{CH}_3)_2\text{CHOC}(\text{O})\text{D}$

The kinetics of OH/OD + $(\text{CH}_3)_2\text{CHOC}(\text{O})\text{D}$ have been determined between 230 and 573 K and 80 and 127 Torr. Figure 5.24 shows the temperature-dependent kinetics determined in this work for OH + $(\text{CH}_3)_2\text{CHOC}(\text{O})\text{H}$ (black squares) and $(\text{CH}_3)_2\text{CHOC}(\text{O})\text{D}$ (blue circles). Deuteration at the formate site leads to a reduction in the rate coefficient that generally increases with increasing temperature. C-D has a lower zero-point energy than C-H, meaning the C-D BDE is higher than the analogous C-H BDE. Therefore, more energy is required to react at the formate site in $(\text{CH}_3)_2\text{CHOC}(\text{O})\text{D}$ vs $(\text{CH}_3)_2\text{CHOC}(\text{O})\text{H}$, leading to a reduction in the rate coefficient. As the extent of the KIE increases with temperature, this indicates that abstraction at the formate site also increases with temperature.

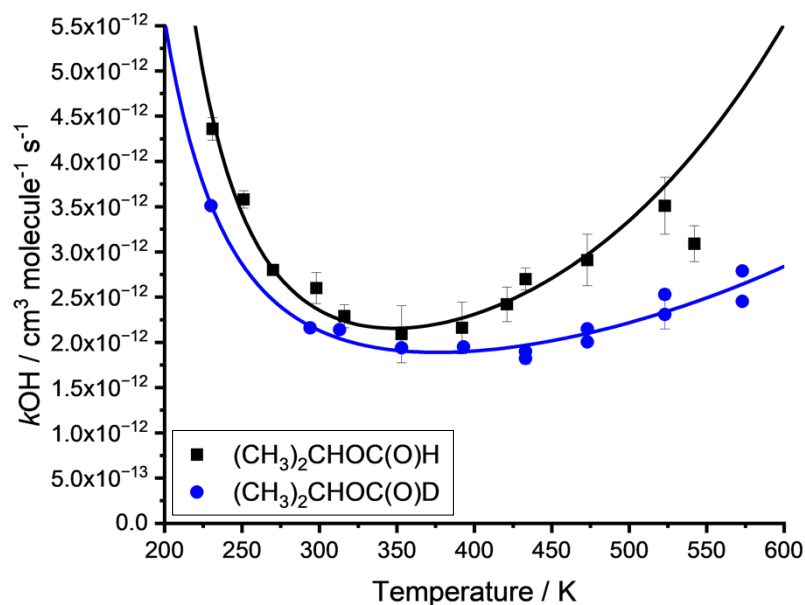


Figure 5.24 – Temperature-dependent kinetics for the reactions of OH + (CH₃)₂CHOC(O)H (black squares) fitted with the expression $((2.13 \pm 1.53) \times 10^{-15}) \times \exp((2117 \pm 212)/T) \times (T/300)^{(5.89 \pm 0.61)} \text{ cm}^3 \text{ molecule}^{-1} \text{ s}^{-1}$ and (CH₃)₂CHOC(O)D (blue circles) fitted with the expression $((9.24 \pm 2.45) \times 10^{-15}) \times \exp((1636 \pm 79)/T) \times (T/300)^{(4.39 \pm 0.23)} \text{ cm}^3 \text{ molecule}^{-1} \text{ s}^{-1}$.

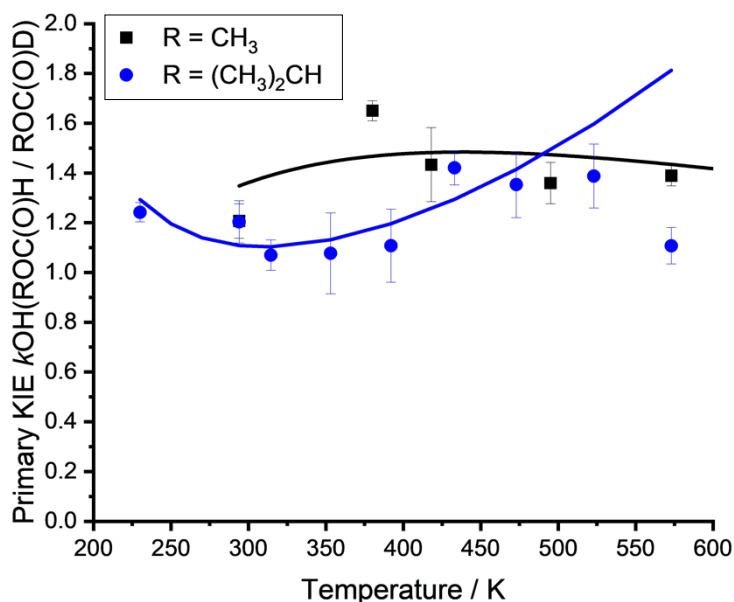


Figure 5.25 – The *k*OH KIE (ROC(O)H/ROC(O)D) for R = CH₃ (methyl formate) shown in black squares and R = (CH₃)₂CH (isopropyl formate) shown in blue circles. The KIE is calculated from experimental values of *k*OD/*k*OH for a given temperature and the temperature-dependent fits of *k*OD and *k*OH, which are shown as solid lines.

The KIE ($\text{ROC(O)H} / \text{ROC(O)D}$) for the OH-initiated oxidation of methyl formate ($\text{R} = \text{CH}_3$) and isopropyl formate ($\text{R} = (\text{CH}_3)_2\text{CH}$) is shown in Figure 5.25 as a function of temperature. Individual points correspond to measured values of $k_{\text{OH}}(\text{ROC(O)H} / \text{ROC(O)D})$, whilst the fitted lines represent the KIE based on the temperature-dependent fits of k_{OH} . The decrease in the KIE between 230 and 300 K could be attributed to the geometric isotope effect (GIE). The GIE describes the influence of deuteration on hydrogen bonding [132]. Deuteration leads to an increase in the distance between the hydrogen bond donor and acceptor. This is due to a reduction in the availability of the electron distribution, which is driven by the lower zero-point energy and vibrational frequency. Although the formate hydrogen only partakes in a hydrogen bonding interaction in the formate transition state, the decrease in electron availability may reduce the polarisation of the adjacent carbonyl oxygen, which partakes in hydrogen bonding in both the tertiary and methyl transition states. Hydrogen bonding within transition states plays a more important role in controlling reactivity at lower temperatures. Therefore, weaker hydrogen bonding due to a secondary GIE may lead to a reduction in the rate coefficient at temperatures where hydrogen bonding influences the reaction, such as between 230 and 300 K due to the transition states for tertiary and methyl abstraction, not formate abstraction.

The comparative k_{OH} KIE for methyl formate and isopropyl formate is shown in Figure 5.25. At 298 K, this work, which is in good agreement with Pimentel et al. [17], estimates ~ 20% of the OH-initiated oxidation of isopropyl formate occurs at the formate site. At 298 K, the KIE is 1.11. At 298 K, the KIE for methyl formate is 1.35 and corresponds with a branching ratio for formate abstraction of ~ 53%. Although the extent of the KIE does not quantitatively correspond with the magnitude of formate abstraction, the higher KIE in the methyl formate system corresponds with the higher fraction of abstraction at the formate site.

5.5.2. OD + (CH₃)₂CHOC(O)D

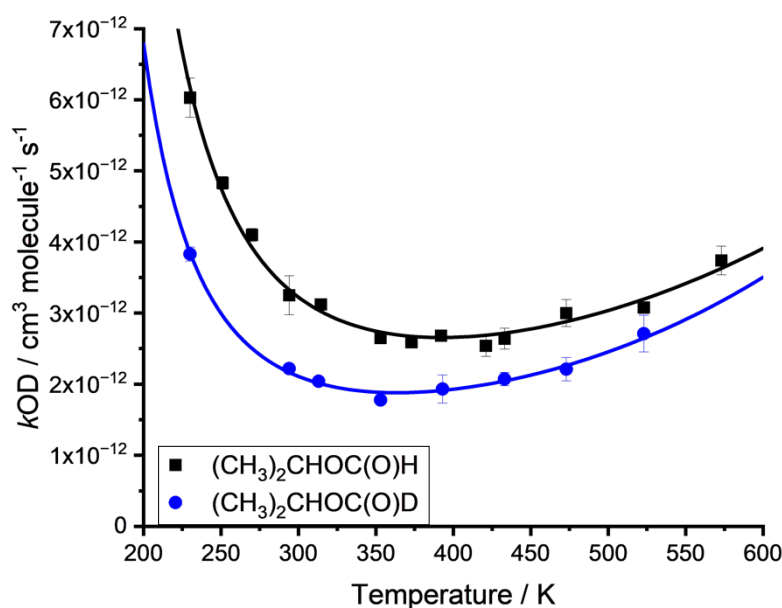


Figure 5.26 – Temperature-dependent kinetics for the reactions of OD + (CH₃)₂CHOC(O)H (black squares) fitted with the expression $((5.25 \pm 1.74) \times 10^{-15}) \times \exp((1926 \pm 97)/T) \times (T/300)^{(4.91 \pm 0.28)} \text{ cm}^3 \text{ molecule}^{-1} \text{ s}^{-1}$ and (CH₃)₂CHOC(O)D (blue circles) fitted with the expression $((1.80 \pm 0.56) \times 10^{-15}) \times \exp((2120 \pm 91)/T) \times (T/300)^{(5.83 \pm 0.27)} \text{ cm}^3 \text{ molecule}^{-1} \text{ s}^{-1}$. Kinetics were determined between 80 and 127 Torr of argon.

The rate coefficients for OD + (CH₃)₂CHOC(O)H and (CH₃)₂CHOC(O)D are shown in Figure 5.26. At 393 K, OD decays became biexponential due to the regeneration of OD. The regeneration of OD following OH and OD-initiated oxidation of (CH₃)₂CHOC(O)D can be attributed to the (CH₃)₂C(OO)OC(O)D peroxy radical that undergoes an internal isomerisation to abstract deuterium from the deuterated formate site. The regeneration of OD complicates OD trace analysis, particularly as the temperature is increased and OD regeneration becomes faster. From 393 K, k_{OD} has been determined by fitting the initial time profile of OD with a single exponential fit. Due to the increasing interference of OD regeneration, the uncertainty in the rate coefficient for OD + (CH₃)₂CHOC(O)D increases with temperature. OD trace analysis is discussed in Appendix D, which details OD trace analysis at high temperatures.

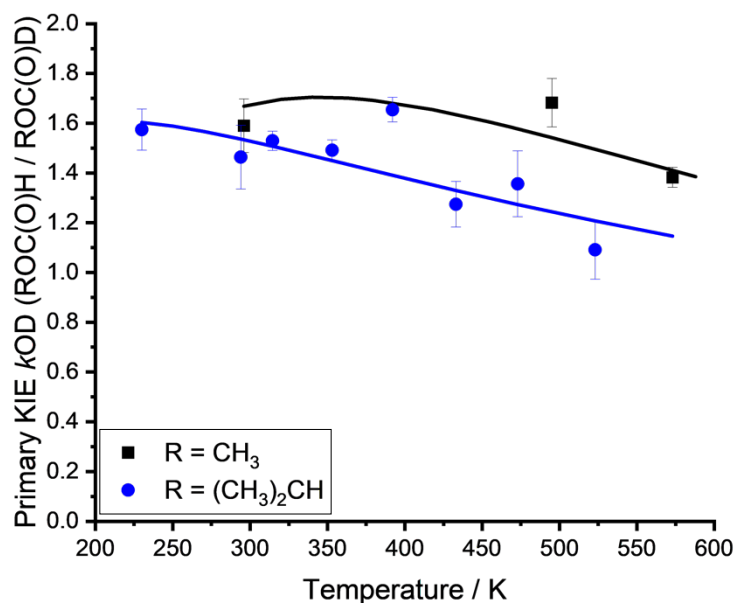


Figure 5.27 – The kOD KIE ($ROC(O)H/ROC(O)D$) for $R = CH_3$ (methyl formate) shown in black squares and $R = (CH_3)_2CH$ (isopropyl formate) shown in blue circles. The KIE is calculated from experimental values of kOD/kOH for a given temperature and the temperature-dependent fits of kOD and kOH , which are shown as solid lines.

The primary KIE ($(CH_3)_2CHOC(O)H/(CH_3)_2CHOC(O)D$) for kOD is shown in Figure 5.27. At low temperatures the primary KIE is larger for kOD than kOH . The high primary KIE suggests that the hydrogen bonded transition states for tertiary abstraction and methyl abstraction dominate at low temperatures. As the temperature increases, the primary KIE decreases due to formate abstraction increasing.

The secondary KIE (kOD / kOH) is illustrated in Figure 5.28 for $(CH_3)_2CHOC(O)H$ (black squares) and $(CH_3)_2CHOC(O)D$ (blue circles). The secondary KIE provides information on the extent of hydrogen bonding in the transition states. The reduction in the secondary KIE in deuterated isopropyl formate could be indicative that deuteration at the formate site has led to weaker hydrogen bonding due to the GIE, as discussed above. The reduced secondary KIE could also indicate that hydrogen-bonded transition states are not dominant in $(CH_3)_2CHOC(O)D$. However, this is unlikely. If deuteration has impacted the branching ratios, formate abstraction would decrease, leading to an increase in

tertiary and methyl abstraction, which both have hydrogen-bonded transition states. Although the secondary KIE from the fitted temperature dependence of k_{OD} and k_{OH} appears to decrease with temperature before increasing, the individual values are within error flat across the temperature range.

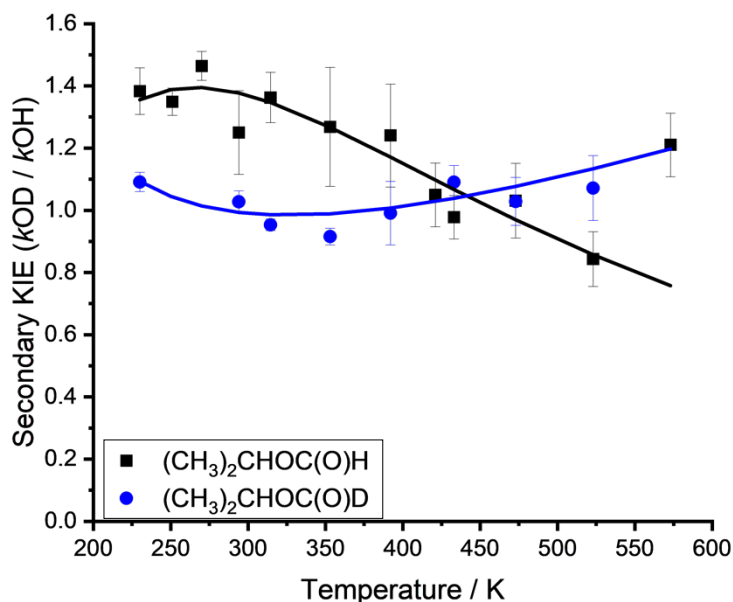


Figure 5.28 – The secondary KIE for $(CH_3)_2CHOC(O)H$ (black squares) and $(CH_3)_2CHOC(O)D$ (blue circles). The KIE is calculated from experimental values of k_{OD}/k_{OH} for a given temperature and the temperature dependent fits of k_{OD} and k_{OH} , which are shown as solid lines.

5.6. Yields of OD from OH and OD-initiated oxidation of $(CH_3)_2CHOC(O)D$

Following OH and OD-initiated oxidation of $(CH_3)_2CHOC(O)D$, OD regeneration is observed at 393 K and above. OD regeneration comes from the internal isomerisation of $(CH_3)_2C(OO)OC(O)D$, formed following tertiary abstraction. Therefore, OD yields are analogous with branching ratios for tertiary abstraction from $(CH_3)_2CHOC(O)D$. The good agreement between the yields of OH from $(CH_3)_2CHOC(O)H$ and OD from $(CH_3)_2CHOC(O)D$ above 393 K, suggests deuteration at the formate site has little impact on the branching ratio for tertiary abstraction.

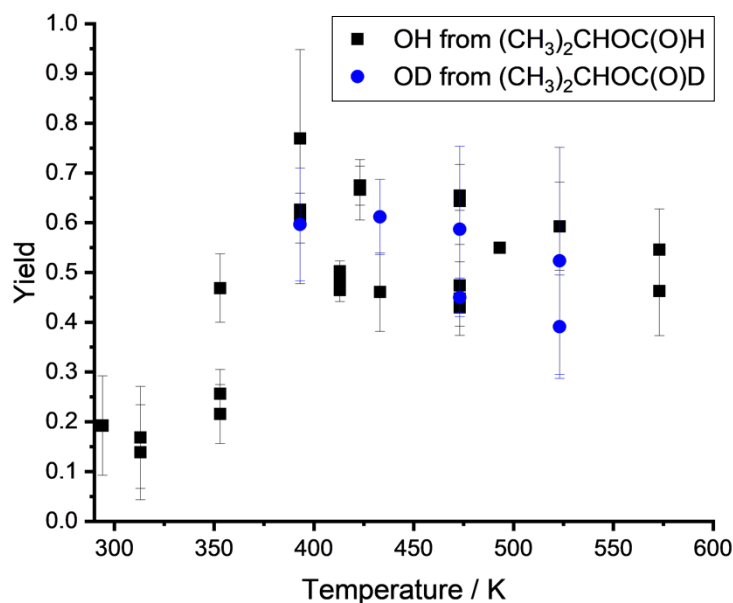


Figure 5.29 – Yields of OH from the OH and OD-initiated oxidation of $(\text{CH}_3)_2\text{CHOC}(\text{O})\text{H}$ (black squares) and yields of OD from the OH and OD-initiated oxidation of $(\text{CH}_3)_2\text{CHOC}(\text{O})\text{D}$ (blue circles) as a function of temperature.

The regeneration of OH is not observed across the experimental temperature range following the oxidation of $(\text{CH}_3)_2\text{CHOC}(\text{O})\text{D}$. OH yields at 298 and 313 K from the oxidation of $(\text{CH}_3)_2\text{CHOC}(\text{O})\text{H}$ have been attributed to formate abstraction, as discussed above. The absence of OH yields following the oxidation of $(\text{CH}_3)_2\text{CHOC}(\text{O})\text{D}$ suggests deuteration at the formate site has shifted the branching ratio for formate abstraction. The branching ratio for formate abstraction from $(\text{CH}_3)_2\text{CHOC}(\text{O})\text{H}$ is $\sim 20\%$ at room temperature. Based on the oxidation studies of methyl formate outlined in Chapters 3 and 4, deuteration at the formate site is expected to decrease the branching ratio for formate abstraction. As the formate branching ratio is already quite low, a further decrease likely produces OH yields below 10% that are too low to be observed. When formate abstraction does occur at higher temperatures, the $(\text{CH}_3)_2\text{CHOC}(\text{O})$ radical undergoes thermal decomposition and therefore no OH is observed. The absence of OH regeneration also provides evidence for the hypothesis that the yields of OH following $(\text{CH}_3)_2\text{CHOC}(\text{O})\text{H}$ oxidation are only due to tertiary abstraction. If the yields were also due to methyl abstraction, OH regeneration would be observed following the oxidation $(\text{CH}_3)_2\text{CHOC}(\text{O})\text{D}$.

5.7. Atmospheric impacts

Reaction with OH is the dominant atmospheric loss process of isopropyl formate. Using the rate coefficient determined in this work, and a concentration of OH of 1×10^6 molecule cm^{-3} , the lifetime of isopropyl formate is ~ 4.26 days. Sources of isopropyl formate are likely from volatile consumer products and so may contribute to indoor and outdoor air pollution. The atmospheric oxidation mechanism of isopropyl formate was proposed by Pimentel et al. [17] at 298 K in the presence of NO_x. The dominant abstraction site is the tertiary site, primarily producing acetone. Abstraction from the formate site also produces acetone, although can lead to iPOPAN which is harmful to human health and could transport NO_x long distances.

Branching ratios determined in this work for tertiary abstraction are presented in Figure 5.30 alongside Pimentel et al. [17] and SAR predicted branching ratios by Jenkin et al. [15]. Combining the branching ratios determined in this work and by Pimentel et al. [17], the branching ratio for tertiary abstraction appears relatively flat between ~ 298 and 393 K. The secondary KIE determined in this work is also approximately constant in this temperature regime. The secondary KIE is influenced by hydrogen bonding in the transition states. This work determined that abstraction at the tertiary hydrogen has a negative activation energy due to the hydrogen-bonded transition state. Furthermore, the overall temperature dependence is in the valley of the “U-shape” between 298 and ~ 350 K, indicating little change in the branching ratio. Below 298 K the overall rate coefficient increases with decreasing temperature, indicating that tertiary abstraction increases. Above ~ 350 K the rate coefficient also increases with increasing temperature, which is attributed to increasing formate abstraction. Increasing formate abstraction with increasing temperature is demonstrated through experiments with deuterated isopropyl formate, $(\text{CH}_3)_2\text{CHOC}(\text{O})\text{D}$.

The branching ratio for tertiary abstraction is predicted by the Jenkin et al. [15] SAR to have a stronger temperature dependence than is experimentally observed, leading to an inaccurate prediction of the branching ratios. Whilst this work determined formate abstraction increases with temperature and is the next

180

largest site of reaction, Jenkin et al. [15] predict methyl abstraction to be larger than formate abstraction. At 298 K, Jenkin et al. [15] predict formate abstraction accounts for 5% of the reaction, tertiary abstraction accounts for 74% and methyl abstraction accounts for 23%. This work determined formate abstraction accounts for ~19% at 298 K. The overprediction of methyl abstraction by Jenkin et al. [15], will lead to an underprediction in the rate of acetone production.

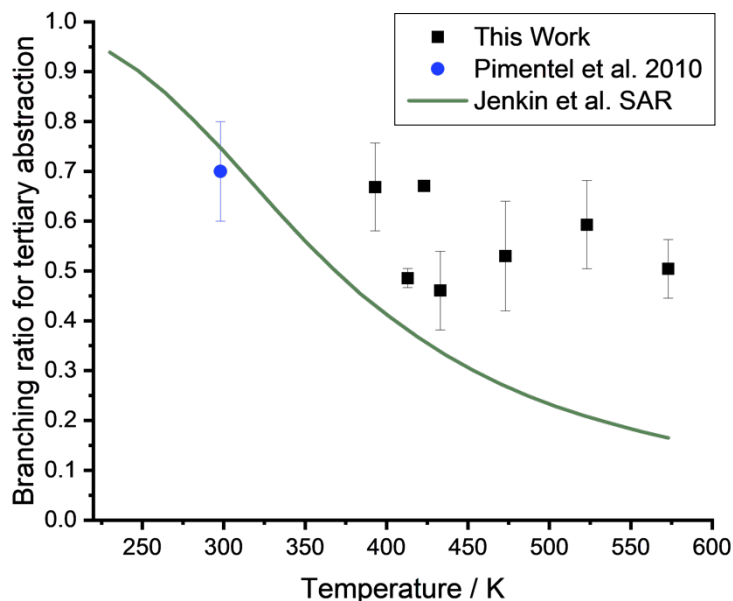


Figure 5.30 – Branching ratios for tertiary abstraction from isopropyl formate experimentally determined in this work between 393 and 573 K (black squares), by Pimentel et al. [17] at 298 K (blue circle), and SAR predictions by Jenkin et al. [15] (solid green line).

5.8. Conclusions

The site-specific kinetics of isopropyl formate have been determined between 298 and 573 K. At 298 and 313 K the yields of OH are attributed to formate abstraction and are 0.19 ± 0.10 and 0.15 ± 0.02 . The errors are statistical at the 1σ level. However, as the errors do not account for systematic errors, they are likely too low. Adding an additional 10% error gives yields of 0.19 ± 0.12 and 0.15 ± 0.04 . Pimentel et al. [17] determined a branching ratio for formate abstraction of ~20 – 25%, within error of the value determined in this work at 298 K. Although the branching ratio determined in this work at 313 K is lower than at 298 K, this work determined formate abstraction increases as a function of temperature.

Yields above 393 K are attributed to tertiary abstraction as the $(\text{CH}_3)_2\text{CHOC}(\text{O})$ radical undergoes thermal decomposition at these temperatures and the barrier for isomerisation of the thermalised $\text{OOCH}_2\text{CH}_3\text{CHOC}(\text{O})\text{H}$ is much higher than $(\text{CH}_3)_2\text{C}(\text{OO})\text{OC}(\text{O})$. Furthermore, no yields of OH are observed following the oxidation of $(\text{CH}_3)_2\text{CHOC}(\text{O})\text{D}$ which would be expected following methyl abstraction. Tertiary abstraction decreases with increasing temperature from 0.67 ± 0.09 at 393 K to 0.50 ± 0.06 at 573 K. Pimentel et al. [17] determined tertiary abstraction accounted for $\sim (55 - 65)\%$ of the reaction at 298 K. As tertiary abstraction is unlikely to increase between 298 and 393 K, little change in the branching ratio for tertiary abstraction is expected between 298 and 393 K. The overall temperature dependence is also comparatively flat between 298 and 393 K, in the valley of its “U-shape”. Yields of OD from the OH-initiated oxidation of $(\text{CH}_3)_2\text{CHOC}(\text{O})\text{D}$ agree with the OH yields from the oxidation of $(\text{CH}_3)_2\text{CHOC}(\text{O})\text{H}$, suggesting deuteration does not have a significant impact on the branching ratio.

Chapter 6 An updated ester Structure Activity Relationship

6. Introduction

The large variety of molecules in the atmosphere makes the experimental determination of overall kinetics, let alone site-specific kinetics, unfeasible. Consequently, atmospheric chemical mechanisms such as the MCM rely on SAR predictions [74]. Due to limitations in experimental data, SARs are primarily trained on the overall kinetics of simple, monofunctional molecules. However, molecules in the atmosphere often have more than one functional group. Applying SARs to multifunctional molecules is beyond their current scope and introduces significant errors in chemical mechanisms (e.g., the MCM). These errors are quickly extrapolated into atmospheric models and other applications (for example, comparisons with field measurements), which use the MCM to benchmark our understanding of atmospheric chemistry [67].

SARs are trained on the overall kinetics of molecules. Consequently, current SARs are not trained to accurately predict site-specific kinetics. Excluding experimental site-specific kinetics from SAR development leads to SARs which do not represent our understanding of atmospheric chemistry; current SARs represent a simplified version of our understanding. Incorporating experimental site-specific kinetics into SARs is challenging, as it requires careful evaluation of the literature. McGillen et al. [7] compiled a database of overall experimental gas-phase kinetics of organic molecules for use in SAR development. However, no equivalent database exists that includes experimental site-specific information.

Many of the challenges SAR development faces are exemplified by the esters. Although esters are one functional group, they are composed of two functional groups – an ether and a carbonyl group. Therefore, esters are prototypical multifunctional compounds. Failings of the current SAR approach in predicting the site-specific kinetics of esters are exacerbated in predictions of more multifunctional compounds.

6.1. Comparing ester reactivity with other oxygenated molecules

Oxygenated molecules are prevalent in the atmosphere. Therefore, understanding the reactivity of oxygenated molecules is fundamental in advancing our understanding of atmospheric chemistry. Experimental kinetics of OH radicals with formates (determined in the present work, Chapters 3 – 5, and from the literature), demonstrate the current SAR by Jenkin et al. [15] inadequately represents the site-specific kinetics of formates. Whilst this work contributes towards identifying this discrepancy between the SAR predicted site-specific kinetics and those determined experimentally, it is important to note that there were already suggestions of this within the literature. The atmospheric chamber study by Pimentel et al. [17], conducted in 2010, determined that the site-specific kinetics for formate abstraction from isopropyl formate and tertbutyl formate were different, whereas the Jenkin et al. [15] SAR assumes a constant rate coefficient for formate abstraction. Formate abstraction from isopropyl formate and tertbutyl formate are significantly larger than the SAR prediction by Jenkin et al. [15], developed in 2018. When the ester SAR was updated in 2018, there were already experimental site-specific kinetics available in the literature that were excluded from SAR development. Until the present work, group additivity SARs have exclusively implemented overall kinetics in their development. It is outside the scope of this work to review the extensive literature on the site-specific kinetics of simple functional groups (e.g., ketones, aldehydes, ethers and alcohols) and compare experimental and SAR predicted values. However, examining how their overall reactivity changes as a function of the adjacent R group provides useful context in developing the formate SAR.

6.1.1. Alcohol and ether reactivity

Alcohols (R-OH) and ethers (R-O-R) activate abstraction from adjacent C-H bonds due to electron donation from the lone pairs of electrons on the oxygen atom. Despite their similar mechanisms of influence, alcohols and ethers are represented differently within the current Jenkin et al. [15] SAR. The influence of the alcohol functional group is represented via primary and secondary substituent factors. For ether predictions, Jenkin et al. [15] implement site-specific rate coefficients for hydrogen abstraction from reactive sites adjacent to the ether functionality and

secondary substituent factors to account for long-range effects. At 298 K, the Jenkin et al. [15] SAR predicts the site-specific rate coefficient for hydrogen abstraction adjacent to an alcohol group to be $2.77 \times 10^{-12} \text{ cm}^3 \text{ molecule}^{-1} \text{ s}^{-1}$ ($k_{\text{Secondary}} \times F(-\text{OH})$), and $5.62 \times 10^{-12} \text{ cm}^3 \text{ molecule}^{-1} \text{ s}^{-1}$ for abstraction adjacent to an ether group. The larger activating effect of the ethers compared with alcohols is illustrated in Figure 6.1.

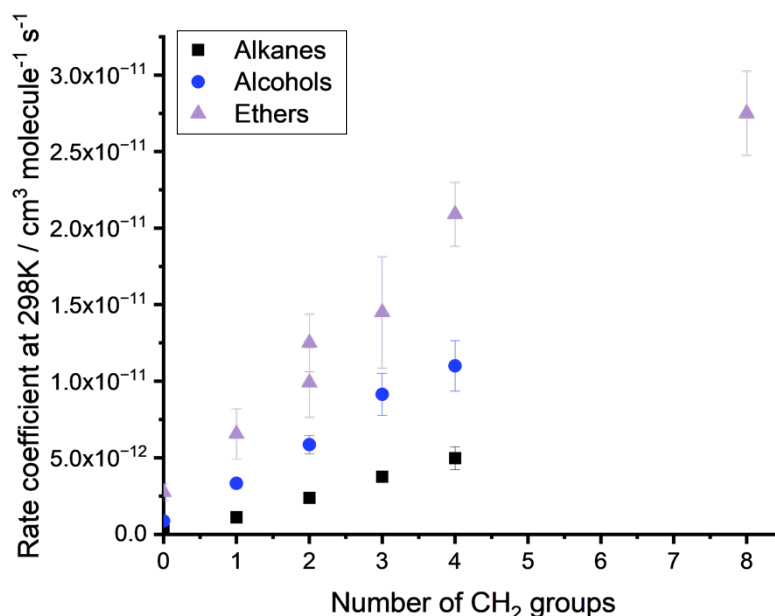


Figure 6.1 – Rate coefficients for the reactions of OH + linear alkanes, alcohols and ethers, as recommended by Eurochamp [16]. Rate coefficients are plotted as a function of the number of CH₂ groups. Ether rate coefficients with two CH₂ groups are from diethyl ether and methoxy propane.

The influence of alcohol and ether functionality extends beyond the adjacent reaction sites. Evidence for impacts further along the alkyl chain comes from the linear increases in k_{298} as a function of chain length. With each additional CH₂ group, the overall rate coefficients of ethers and alcohols increase more than the 298 K rate coefficient for an additional CH₂ group in alkanes. This is demonstrated via the larger slope for linear increases (+CH₂) in alcohols and ethers compared with the corresponding alkanes (Figure 6.1). The impact of adding each CH₂ group can also be calculated via E6.1, where R represents alkyl groups and X represents a functional group such as OH or -O-.

$$k\text{CH}_2 = k\text{RCH}_2\text{X} - k\text{RX} \quad \text{E6.1}$$

For example, E6.2 and E6.3 represent $k\text{CH}_2$ for one and two CH_2 groups in linear alcohols.

$$k\text{CH}_2 = k\text{CH}_3\text{CH}_2\text{OH} - k\text{CH}_3\text{OH} \quad \text{E6.2}$$

$$k\text{CH}_2 = k\text{CH}_3\text{CH}_2\text{CH}_2\text{OH} - k\text{CH}_3\text{CH}_2\text{OH} \quad \text{E6.3}$$

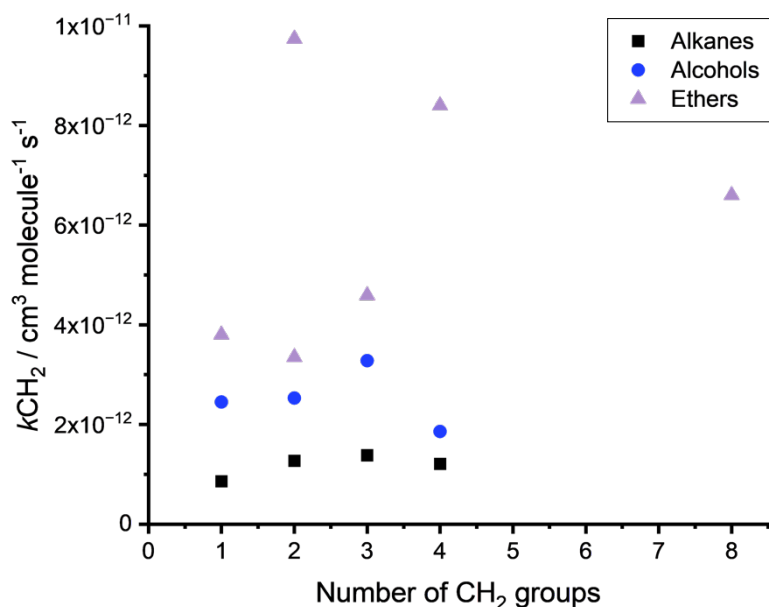


Figure 6.2 – Rate coefficients for each additional CH_2 group ($k\text{CH}_2$) in the reactions of $\text{OH} +$ linear alkanes, alcohols (ROH) and ethers (ROR), plotted as a function of the number of CH_2 groups. Additional points for ethers with two CH_2 groups are from diethyl ether and methoxy propane.

Figure 6.2 plots $k\text{CH}_2$ for each additional CH_2 group in a linear series of alkanes (ethane, propane, butane, hexane), alcohols (methanol, ethanol, propanol, butanol, propanol) and ethers (dimethyl ether, methoxy ethane, methoxy propane, methoxy butane, diethyl ether, dipropyl ether and dibutyl ether). Within the experimental errors, the activation of $k\text{CH}_2$ from one to three CH_2 groups is approximately the same. However, after three CH_2 groups, the activating effect appears to decrease. The hydroxyl group influences the rate of reaction at reaction sites α , β and γ from the OH functionality [59, 133]. This is further demonstrated by comparing the rate coefficients between alcohols and diols, with diol rate coefficients larger than monoalcohols. SARs, such as Kwok and Atkinson's [21],

which utilise the alcohol substituent factor in diol calculations, underpredict the diol rate coefficient. Underprediction indicates the diol rate coefficients are larger due to the effects of the OH groups extending beyond the alpha position [59]. Effects of multiple OH groups likely combine to increase the rate of reaction further. However, combining the effects in a multiplicative manner (e.g. $k_{\text{Secondary}} \times F(-\text{CH}_2\text{OH}) \times F(-\text{CH}_2\text{OH})$) leads to an overprediction of the rate coefficient [15]. As illustrated in Figure 6.2, similar long range effects are observed for the ethers [134]. To account for long range effects, secondary substituent factors were incorporated into ether SARs by Calvert et al. [59] and Jenkin et al. [15].

6.1.2. Aldehyde and ketone reactivity

The influence of aldehyde (RC(O)H) and ketone (RC(O)R) functionality on adjacent sites of reactivity differs from alcohols and ethers. Rather than activating the adjacent reaction site, ketones and aldehydes activate C-H bonds from the reaction site beta (β) to the carbonyl functionality [135, 136]. Increased reactivity at the β site is due to the stabilisation of the transition state via a ring like structure involving the OH radical, the C-H bond at the β site, and the carbonyl group [137, 138]. At 298 K, the secondary substituent factor ($-\text{CH}_2\text{C(O)}$) is 3.4 compared with 1.0 for the adjacent substituent factor ($-\text{C(O)}$) [15]. The activation of the β site is demonstrated by comparing the rate coefficients at 298 K for ketones and alkanes. Figure 6.3 illustrates that adding one CH_2 group to a ketone molecule has little impact on the overall rate coefficient, whereas adding two CH_2 groups leads to an increase in k_{298} . The increase remains for three CH_2 groups, before decreasing with each additional CH_2 group. Larger k_{CH_2} values, above the corresponding alkanes, may be due to inductive effects of additional CH_2 groups stabilising the hydrogen bonded structure at the β site. The curvature in k_{298} as a function of the number of CH_2 groups implies that no longer range effects are occurring within the molecule. However, Calvert et al. [59] noted discrepancies between overall experimental and SAR predicted values increased for larger ketones (2-heptanone, 2-octanone etc.) and suggested this may be due to activation of the carbonyl group beyond the β site.

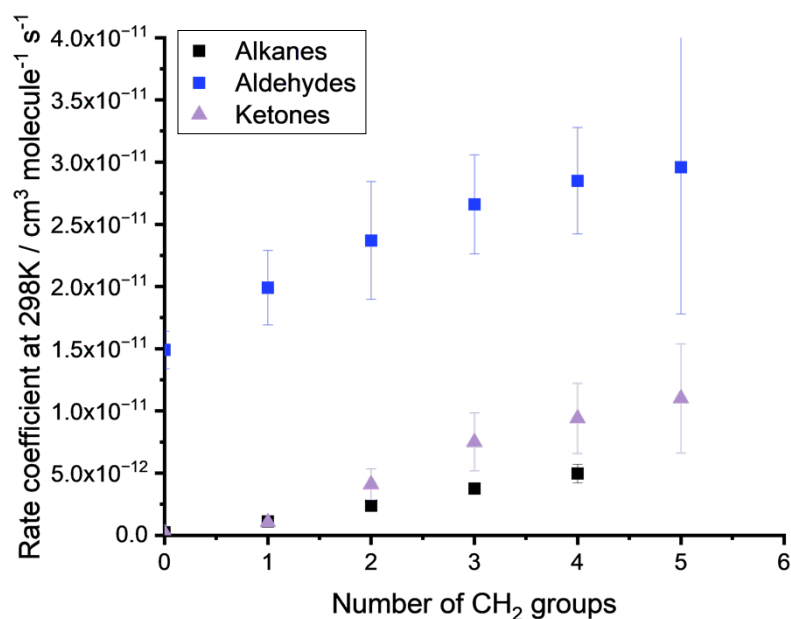


Figure 6.3 – Rate coefficients for the reactions of OH + linear alkanes, aldehydes and ketones as recommended by Eurochamp [16]. Rate coefficients are plotted as a function of the number of CH₂ groups.

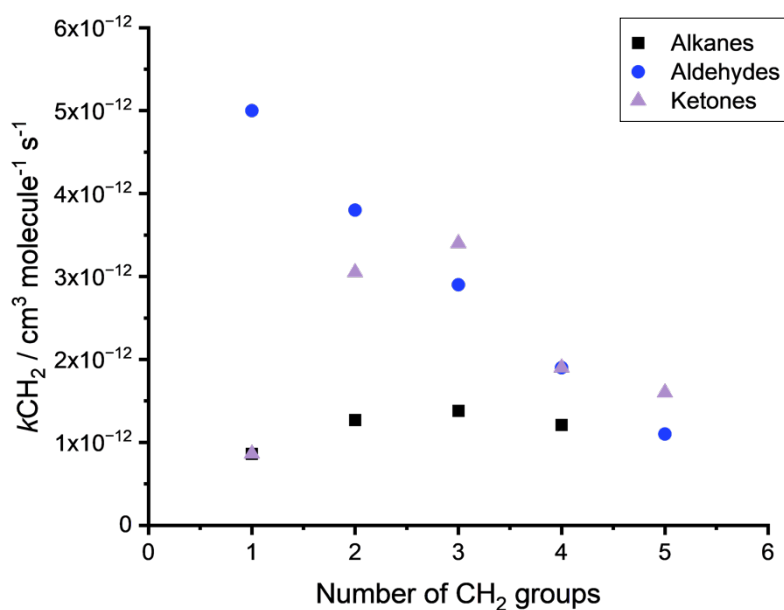


Figure 6.4 – Rate coefficients for each additional CH₂ group (k_{CH_2}) in the reactions of OH + linear alkanes, aldehydes (RC(O)H) and ketones (RC(O)R), plotted as a function of the number of CH₂ groups.

Activation at the β site is not as noticeable in the aldehydes due to aldehydic abstraction dominating the overall rate coefficient. The oxygen atom in the carbonyl group pulls electron density away from the carbon atom, creating a dipole.

Consequently, the carbon atom becomes more electropositive leading to a weakening of the aldehydic C-H bond. Due to the weak aldehydic bond, abstraction from the aldehydic site dominates throughout the aldehydes.

6.1.3. Ester reactivity

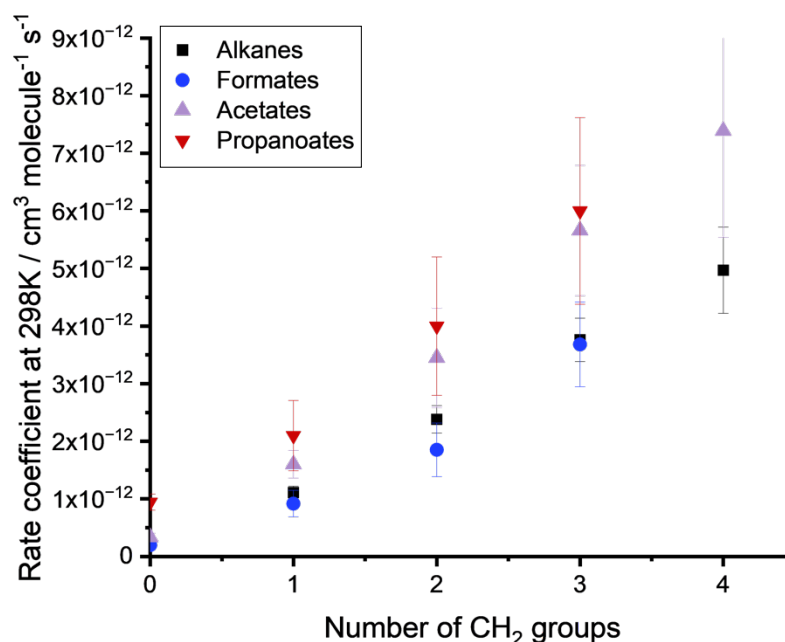


Figure 6.5 – Rate coefficients for the reactions of OH + linear alkanes, formates (ROC(O)H), acetates (ROC(O)CH₃) and propanoates (ROC(O)CH₂CH₃) as recommended by Eurochamp [16] and this work. Rate coefficients are plotted as a function of the number of CH₂ groups.

Esters (R₁OC(O)R₂) influence on site-specific reactivity is comparable to both ethers and ketones. However, their influence on overall reactivity is significantly reduced compared with simple functional groups. Figure 6.5 illustrates the rate coefficients at 298 K for alkanes and esters with varying R₂ groups – formates (ROC(O)H), acetates (ROC(O)CH₃) and propanoates (ROC(O)CH₂CH₃). The number of CH₂ groups are relative to the R₁ group in the esters, so methyl propanoate (CH₃OC(O)CH₂CH₃) has zero R₁ CH₂ groups, whilst ethyl propanoate (CH₃CH₂OC(O)CH₂CH₃) has one R₁ CH₂ group. Rate coefficients for the formates are the lowest in the series. Although aldehydes, which also contain a C(O)H group, exhibit significantly higher overall rate coefficients than the alkanes, this is not the case for the formates. This is due to the adjacent ether functionality. As outlined above, the reactivity of the aldehydes is due to the dipole created between the

carbonyl oxygen and carbon atoms, weakening the adjacent C-H bond. With the ether group adjacent to the carbonyl, there is no strong dipole. Instead, resonance occurs between the ether oxygen and the carbonyl oxygen. Electron density is shared across the molecule via resonance (Figure 6.6), resulting in the site-specific rate coefficient for formate abstraction depending on the adjacent R group.

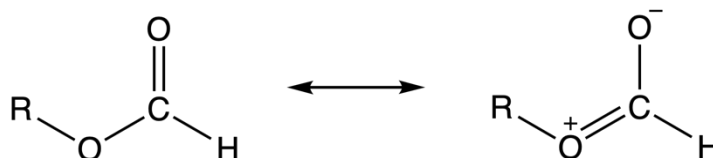


Figure 6.6 – Resonance structures of a formate (ROC(O)H).

6.1.4. Site-specific kinetics of formates

The temperature-dependent site-specific kinetics of methyl formate have been determined between 294 and 573 K. At 298 K, formate abstraction (ROC(O)-H) is the dominant site of reactivity, accounting for 53% of the overall reaction (Chapters 3 and 4). Pimentel et al. [17] experimentally determined the site-specific kinetics of isopropyl formate and tertbutyl formate, which are presented in Figure 6.7 alongside the site-specific kinetics of methyl formate and the Jenkin et al. [15] SAR predictions. The combination of experimental site-specific kinetics by Pimentel et al. [17] and the present work (Chapter 5) demonstrates that formate abstraction is dependent on the adjacent R group. The current SAR by Jenkin et al. [15] underpredicts formate reactivity in all formates, and the discrepancy increases with increasing size of the adjacent R group. The underprediction by Jenkin et al. [15] is due to their use of a constant rate coefficient for formate abstraction. For methyl formate, the discrepancy between the experimental site-specific rate coefficient and the Jenkin et al. [15] SAR is 11%, increasing to 25% for isopropyl formate and 37% in tertbutyl formate. Although there are no experimental site-specific kinetics for ethyl formate, n-propyl formate, n-butyl formate or isobutyl formate at 298 K, all of these rate coefficients are expected to be larger than the Jenkin et al. [15] predictions.

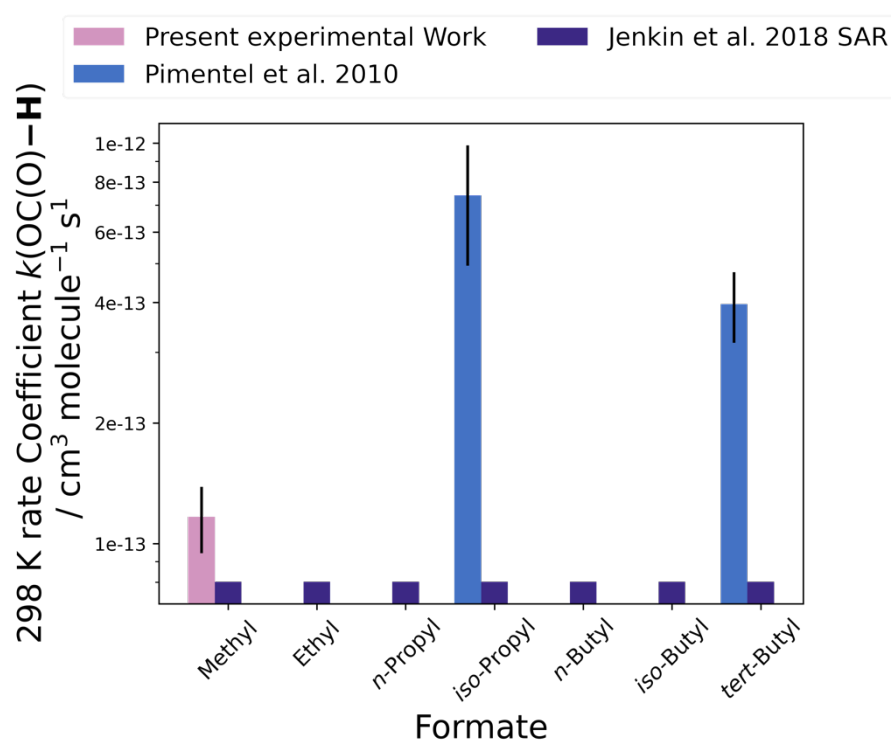


Figure 6.7 – Experimentally determined rate coefficients for formate abstraction at 298 K.

The present work determined the site-specific kinetics for formate abstraction from ethyl formate (390 – 580 K), isopropyl formate (423 – 498 K) and tertbutyl formate (420 – 583 K), which are presented in Figure 6.8 at 423 K. The prevailing trend at 423 K is that the formate rate coefficient increases with increasing electron donation from the adjacent R group. Determination of this trend at 423 K supports the hypothesis that the experimental site-specific kinetics at 298 K also depend on the electron-donating ability of the R group. However, the formate rate coefficient in isopropyl formate has been experimentally determined by Pimentel et al. [17] to be larger than the formate rate coefficient in tertbutyl formate. The tertbutyl group is a better electron donor than isopropyl, suggesting the influences at 298 K may not be as straightforward. Despite this discrepancy, the current SAR approach of implementing a constant rate coefficient for formate abstraction is theoretically incorrect, leading to inaccurate predictions of formate reactivity. Accurately determining the branching ratio for formate abstraction is important to quantify concentrations of formaldehyde, a carcinogen and irritant, formed in the atmospheric oxidation of esters. Figures 6.7 and 6.8 highlight how important it is to implement experimental site-specific kinetics into SAR

development, otherwise SARs inaccurately represent our understanding of atmospheric chemistry.

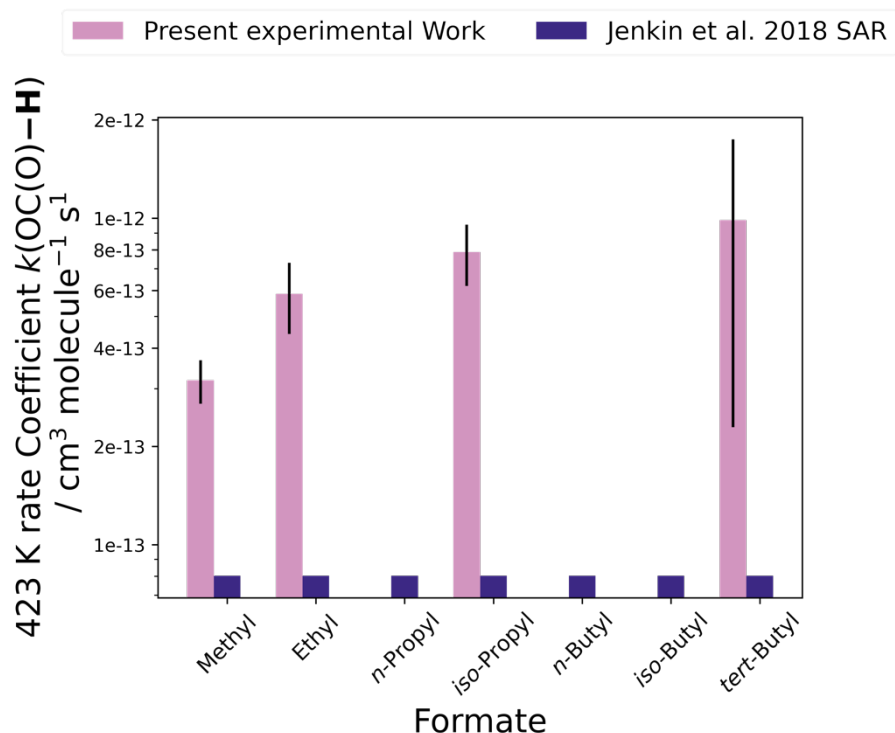


Figure 6.8 – Experimentally determined rate coefficients for formate abstraction at 423 K. Although presented here, the Jenkin et al. [15] SAR is trained up to 400 K.

Additional experimental evidence for the dependence of formate reactivity on the adjacent R group comes from the kinetic isotopomer studies presented in Chapter 3. The experimental kinetics of deuterated isotopomers of methyl formate demonstrate that the reaction sites are coupled, meaning deuteration at one site influences the rate of abstraction at the other (undeuterated) reaction site. Coupling of reaction sites indicates that the site-specific kinetics of formates cannot be accurately predicted with a SAR that assumes reaction sites are independent of one another. The experimental site-specific kinetics of the formates highlight the discrepancy with the current SAR, whilst also determining how formate reactivity is influenced.

6.1.5. Influences of adjacent R groups in higher esters

Experimental site-specific rate coefficients for formate abstraction clearly indicate that formate abstraction is dependent on the adjacent R group. The

potential wider implication of this result is that the site-specific kinetics of all esters depend on the adjacent R groups on either side of the ester functionality. In other words, changing the R_1 group in the representative ester, $R_1OC(O)R_2$, influences the site-specific rate coefficients in the R_2 group. If this is true, it poses a significant challenge in predicting the site-specific kinetics of esters and particularly the kinetics of diesters or esters which contain additional functional groups.

To test this assumption, the reactivity of R_1 is tested against different R_2 groups. Figure 6.9 compares the rate coefficient for each additional CH_2 group (k_{CH_2}) in a series of linear formates ($ROC(O)H$), acetates ($ROC(O)CH_3$), propanoates ($ROC(O)CH_2CH_3$) and butanoates ($ROC(O)CH_2CH_2CH_3$). If k_{CH_2} is similar between R_2 groups, it would indicate that R_2 does not influence R_1 . Changing the R_2 group ($R_1OC(O)R_2$) from H to CH_3 leads to an increase in k_{CH_2} , calculated from analogous R_1 groups. However, there is little increase in k_{CH_2} upon changing R_2 from CH_3 to CH_2CH_3 or $CH_2CH_2CH_3$. Despite no change for linear increases ($+CH_2$) in R_2 , there is a large change in k_{CH_2} when R_2 is an isopropyl group, $CH(CH_3)_2$. The difference between the 298 K overall rate coefficients methyl 2-methylpropanoate ($CH_3OC(O)CH(CH_3)_2$) and ethyl 2-methylpropanoate ($CH_3CH_2OC(O)CH(CH_3)_2$) is $5.91 \times 10^{-11} \text{ cm}^3 \text{ molecule}^{-1} \text{ s}^{-1}$, a significant increase from $R_2 = CH_3$ or CH_2CH_3 . The increase is so large that it has been excluded from Figure 6.9 as it alters the scale of the y-axis such that other differences in k_{CH_2} cannot be detected. Errors have also been excluded from Figure 6.9 as these are large and hinder the readability of the Figure. The calculated values of k_{CH_2} alongside their errors are presented in Table 6.1.

Comparisons of k_{CH_2} illustrated in Figure 6.9 suggest R_1 reactivity is influenced by R_2 . However, the influence depends more on the shape of the R group than on the size. Unfortunately, no more comparisons can be made due to a lack of experimental data. Additional experiments to determine the kinetics of ethyl 2-2-dimethyl propanoate ($CH_3CH_2OC(O)C(CH_3)_3$) so comparisons could be made with methyl 2-2-dimethyl propanoate ($CH_3OC(O)C(CH_3)_3$) would resolve the influence of the tertbutyl group.

Table 6.1 – Calculated rate coefficients at 298 K for each CH₂ group (k_{CH_2}) in a range of esters (R₁OC(O)R₂).

R ₁	R ₂	$k_{CH_2} / \text{cm}^3 \text{ molecule}^{-1} \text{ s}^{-1}$
CH ₃ CH ₂	H	$(7.21 \pm 2.32) \times 10^{-13}$
CH ₃ CH ₂ CH ₂	H	$(9.36 \pm 5.17) \times 10^{-13}$
CH ₃ CH ₂ CH ₂ CH ₂	H	$(1.83 \pm 0.87) \times 10^{-12}$
CH ₃ CH ₂	CH ₃	$(1.27 \pm 0.25) \times 10^{-12}$
CH ₃ CH ₂ CH ₂	CH ₃	$(1.85 \pm 0.86) \times 10^{-12}$
CH ₃ CH ₂ CH ₂ CH ₂	CH ₃	$(2.21 \pm 1.42) \times 10^{-12}$
CH ₃ CH ₂ CH ₂ CH ₂ CH ₂	CH ₃	$(1.73 \pm 2.17) \times 10^{-12}$
CH ₃ CH ₂	CH ₂ CH ₃	$(1.16 \pm 0.63) \times 10^{-12}$
CH ₃ CH ₂ CH ₂	CH ₂ CH ₃	$(1.90 \pm 1.35) \times 10^{-12}$
CH ₃ CH ₂ CH ₂ CH ₂	CH ₂ CH ₃	$(2.00 \pm 2.02) \times 10^{-12}$
CH ₃ CH ₂	CH ₂ CH ₂ CH ₃	$(1.14 \pm 1.75) \times 10^{-12}$
CH ₃ CH ₂ CH ₂	CH ₂ CH ₂ CH ₃	$(1.50 \pm 2.65) \times 10^{-12}$
CH ₃ CH ₂	CH(CH ₃) ₂	$(5.91 \pm 0.67) \times 10^{-11}$

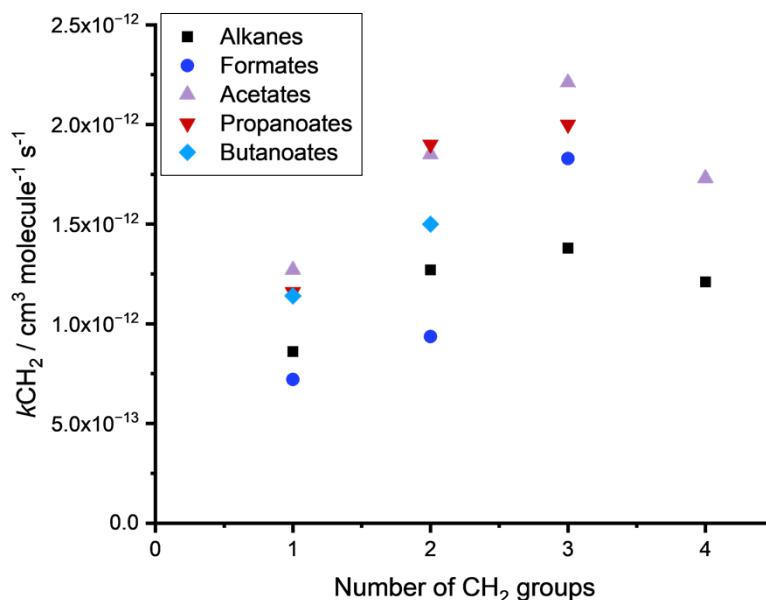


Figure 6.9 – Rate coefficients for each additional CH₂ group (k_{CH_2}) in the reactions of OH + linear alkanes, formates (ROC(O)H), acetates (ROC(O)CH₃) and propanoates (ROC(O)CH₂CH₃), plotted as a function of the number of CH₂ groups.

Although some general trends on the impact of R_2 on R_1 reactivity have been determined, there is still uncertainty in how far along the carbon chain influences occur. If R_2 is an isopropyl group this has a large impact on R_1 reactivity. However, it is not known whether the isopropyl group will still have an impact if it is further along the carbon chain. It is also unknown how far along the R_1 carbon chain R_2 can influence. For ketones, there is an increase in k_{CH_2} between one and two CH_2 groups/ carbon atoms, with decreasing influence after three CH_2 groups. The influence of alcohols and ethers also decreases after three CH_2 groups. The decrease in k_{CH_2} at four CH_2 groups in the acetates suggests the esters may also follow this trend. However, it is not clear whether this extends to the formates. Unlike the esters with alkyl groups on either side of the ester functionality, formate reactivity is influenced by both the size and shape of the R_1 group (Figure 6.8). Therefore, formates may be more sensitive to changes in electron donation. Current SARs typically account for the impacts alpha and beta to a functional group, through primary and secondary substituent factors. To reduce the number of SAR parameters tertiary substituent factors are not included in SARs.

6.1.6. The dominant site of reactivity in the esters

In esters, the dominant reaction site is alpha to the ester functionality due to ring-like hydrogen-bonded transition states, such as those exhibited in ketones. However, a similar ring-like structure can occur at the reaction site beta to the carbonyl functionality. From current literature studies, it is inferred that the dominant reaction site primarily depends on the stabilisation of the hydrogen-bonded structure via the inductive effect from adjacent R groups. For example, the oxidation of methyl pivalate (Figure 6.10) is estimated by Wallington et al. [139] to proceed via abstraction from the carbonyl side with an approximate ratio of ~ 75%. Wallington et al. [139] estimates this ratio to match their observed 51% yield of acetone. The influence of hydrogen bonding on the reaction of OH + methyl pivalate is further supported by the curvature in the experimentally determined temperature-dependent kinetics by Wallington et al. [139] and Mapelli et al. [140]. Many of the temperature-dependent kinetics of OH radicals with esters exhibit curvature between 200 and 600 K. Rather than indicating stabilisation of the hydrogen-bonded

pre-reaction complex, the curvature is most likely due to hydrogen-bonded transition states with negative activation barriers for hydrogen abstraction.

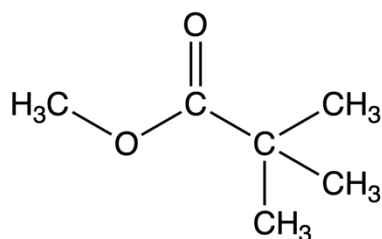


Figure 6.10 – The structure of methyl pivalate.

Although abstraction on the carbonyl side of the ester functionality can dominate the reaction, when there are equivalent groups on both sides of the ester functionality, abstraction on the ether side dominates. This is likely due to the additional activating effect of the ether oxygen. This is exemplified via the site-specific kinetics of methyl acetate ($\text{CH}_3\text{OC(O)CH}_3$) and ethyl propionate ($\text{CH}_3\text{CH}_2\text{OC(O)CH}_2\text{CH}_3$). As is common in the literature, there are more studies on the site-specific kinetics of Cl-initiated oxidation than OH-initiated oxidation. Nonetheless, Tyndall et al. [47] experimentally determined the reaction of OH with methyl acetate occurs ~60% at the $\text{CH}_3\text{O-}$ group. The OH-initiated oxidation of ethyl propionate has been studied theoretically by Andersen et al. [141] at the CCSD(T)-F12/VDZ-F12//BH&HLYP/aug-cc-pVTZ level of theory. Andersen et al. [141] determined 80% of the reaction proceeds via hydrogen abstraction at the CH_2 group adjacent to the ether functionality.

Accurately predicting the site-specific kinetics of esters is critical to determining their atmospheric impacts. Figure 6.11 illustrates the oxidation products from methyl formate. Hydrogen abstraction adjacent to the carbonyl group typically leads to aldehydes such as formaldehyde, whilst abstraction from reaction sites adjacent to the ether group leads to organic acids such as formic acid. Aldehydes and organic acids have very different atmospheric impacts. Formaldehyde and acetaldehyde are harmful to human health, with both classed as Group 1 (“carcinogenic to humans”) carcinogens by the International Agency for Research on Cancer [142]. On the other hand, organic acids contribute to the formation of SOAs and the acidity of clouds and rainwater. SOAs have both climate

Complexity in understanding ester reactivity explains why current SARs, which treat each reaction site as independent of all other reaction sites, fail to predict the site-specific kinetics of formates accurately, and likely higher esters too. Again, these problems may be exacerbated in the predictions of multifunctional compounds.

Although SARs are used to determine product yields following atmospheric oxidation, they are not trained to predict site-specific kinetics. The focus of current SARs on overall kinetics ignores experimental site-specific kinetics already in the literature. However, as this work demonstrates, the lack of experimental site-specific kinetics is a key challenge in future SAR development. Despite the failings of the current SAR, this work attempts to update the group additivity SAR. Group additivity SARs are widely used in the atmospheric chemistry community. One of the key reasons for this is their user-friendly nature and relatively low number of parameters [67]. The present work makes several adjustments to address some of the above challenges and test whether group additivity SARs can accurately predict the site-specific kinetics of esters, prototypical multifunctional compounds.

6.3. Methods for SAR Development

6.3.1. General group additivity methods

An overview of the origins of group additivity SARs used in gas phase reaction kinetics is presented in Chapter 1. The present work focuses on saturated esters. Therefore, this work only considers one reaction pathway - hydrogen abstraction by OH. This work builds upon the SAR update developed by Jenkin et al. [15]. Rate coefficients for k_{Primary} , $k_{\text{Secondary}}$ and k_{Tertiary} are consequently fixed to the expressions defined by Jenkin et al. [15] and presented in Table 6.2. Similarly, to Atkinson, Jenkin did not find a benefit in using individual substituent factors for adjacent $-\text{CH}_2-$, $-\text{CH}<$ or $>\text{C}<$ groups. This work does not adapt the substituent factor ($F(\text{CH}_2-, -\text{CH}<, >\text{C}<)$) defined by Jenkin et al. [15]. Substituent factors are determined in the present work by minimising the difference between experimental and calculated rate coefficients (E4). The Excel Solver varies the substituent factors to find the minimum difference. Global minima, rather than local, are found by varying the starting point for the substituent factor. As the aim of this SAR is for use in atmospheric chemical models, this work also incorporates an upper temperature limit of 400 K, as implemented by

Jenkin et al. [15]. However, as many of the experimental site-specific rate coefficients determined in this work are above 400 K, the SAR is also optimised between 200 and 600 K.

$$\text{Sum Squared Residuals} = \sum \left(\frac{k_{\text{SAR}} - k_{\text{Exp}}}{k_{\text{Exp}}} \right)^2 \quad \text{E6.4}$$

Table 6.2 – Fixed SAR parameters from Jenkin et al. [15] used in the updated ester SARs.

SAR Parameter	Temperature Dependent Expression
k_{Primary}	$(2.90 \times 10^{-12}) \times \exp(-925/T)$
$k_{\text{Secondary}}$	$(4.95 \times 10^{-12}) \times \exp(-555/T)$
k_{Tertiary}	$(3.17 \times 10^{-12}) \times \exp(-225/T)$
$F(\text{CH}_3)$	$1.00 \times \exp(0/T)$
$F(\text{CH}_2-, -\text{CH}<, >\text{C}<)$	$1.00 \times \exp(89/T)$

Potential biases in the SAR have been considered and avoided where possible. For example, equally spaced temperature intervals between the lowest and highest experimental temperatures have been used for each ester. In the 200 – 400 K SAR an upper temperature limit of 400 K is imposed whereas in the 200 – 600 K SAR an upper limit of 600 K is used. The 200 – 400 K SAR utilises ten temperature intervals whereas the 200 – 600 K SAR uses twenty equally spaced intervals.

6.3.2. The history of ester SARs

The ester group influences reactivity differently depending on which side of the functionality the C-H bond being abstracted by OH is adjacent to. In the first gas phase kinetics SAR by Atkinson [70], the ester substituent factor only accounted for C-H groups adjacent to the ether group via the substituent factor $F(-\text{OC}(\text{O}))$. Hydrogen abstraction from C-H groups adjacent to the carbonyl functionality used the standard substituent factor for a carbonyl group ($-\text{C}(\text{O})-$), which was constant for an ester, aldehyde or ketone despite their different reactivities. This was addressed in the SAR update by Kwok and Atkinson [21], specifying a separate substituent factor for the impact of the ester ($-\text{C}(\text{O})\text{O}-$) functionality adjacent to the carbonyl group.

The first update to ester SARs was provided by Le Calve et al. [8] who experimentally determined the total rate coefficients between 233 and 372 K for a series of formates using laser flash photolysis with laser induced fluorescence. The formates studied were: methyl formate, ethyl formate, n-propyl formate, n-butyl formate and tertbutyl formate. Le Calve incorporated a new substituent factor to account for formate reactivity ($F(-OC(O)H)$), derived from minimising the least squares (E4) between k_{Exp} and k_{SAR} for ethyl, n-propyl and n-butyl formate. Formate abstraction from ethyl, n-propyl and n-butyl formate was considered negligible and excluded from SAR calculations. The rationale to exclude formate abstraction was based on the increase in the overall rate coefficient at 298 K (k_{298}) with increasing chain length. Le Calve et al. [8] attributed the increase in k_{298} to hydrogen abstraction predominantly occurring on the chain adjacent to the ether group. Larger discrepancies between k_{Exp} and k_{SAR} for methyl and tertbutyl formate indicated formate abstraction was more important. After incorporating $F(-OC(O)H)$ into the methyl and tertbutyl formate SARs, Le Calve et al. [8] calculated the rate coefficient for formate abstraction ($k(OC(O)-H)$) from the difference between k_{Exp} and k_{SAR} . This gave different site-specific rate coefficients for formate abstraction in methyl ($0.9 \times 10^{-13} \text{ cm}^3 \text{ molecule}^{-1} \text{ s}^{-1}$) and tertbutyl formate ($2.43 \times 10^{-13} \text{ cm}^3 \text{ molecule}^{-1} \text{ s}^{-1}$). This was the first indication that the alkyl groups on either side of the ester functionality influence reactivity.

Table 6.3 – Comparison of ester SAR parameters used by Kwok and Atkinson [21], Le Calve et al. [8] and Jenkin et al. [15], demonstrating how ester SARs have evolved over time.

SAR Parameter	Kwok and Atkinson [21]	Le Calve et al. [8]	Jenkin et al. [15]
$F(-C(O)OR)$	0.74 (previously 0)	“	“
$F(-OC(O))$	1.6 (previously 1.5)	“	“
$F(-OC(O)H)$	NA	0.6	0.6
$k(OC(O)-H) / \text{cm}^3 \text{ molecule}^{-1} \text{ s}^{-1}$	$k_{Tert} \times F(-C(O)-) \times F(-O-)$	$(0.9 - 2.86) \times 10^{-13}$	8.02×10^{-14}

The group additivity SAR for the esters was subsequently updated by Jenkin et al. [15] who imposed an upper limit of 400 K, keeping the temperature range

focused on the atmosphere. SAR predictions of the total rate coefficient as a function of temperature agree well within a factor two, which is the standard accuracy SARs aim for. Although the study by Le Calve et al. [8] found the rate coefficient for formate abstraction likely varies between methyl and tertbutyl formate, indicating a dependence on the adjacent R group, Jenkin et al. [15] implemented a fixed rate coefficient for formate abstraction. Following the methods of Atkinson [70], Jenkin et al. [15] extrapolate the value determined for the simplest molecule in the homologous series. They assign the rate coefficient for formate abstraction, $k(\text{ROC}(\text{O})\text{-H})$, as $8.02 \times 10^{-14} \text{ cm}^3 \text{ molecule}^{-1} \text{ s}^{-1}$, irrespective of the adjacent R group. No details are provided in Jenkin et al. [15] as to how this rate coefficient was derived for methyl formate. As demonstrated above, this approach leads to an underestimation of the site-specific rate coefficient for formate abstraction, with increasing discrepancy as R increases in size and shape.

6.3.3. Differences between methods in the present work and the literature

In order to address the challenges outlined in section 6.2.3.3., the present work made some key modifications to the SAR:

1. Incorporation of experimental site-specific kinetics.
2. Expansion of the SAR temperature range to 200 – 600 K to incorporate all experimental site-specific kinetics determined in this work.
3. Site-specific rate coefficients for formate abstraction depending on whether the adjacent R group is primary, secondary or tertiary.
4. Secondary substituent factors $F(\text{CH}_2\text{OC}(\text{O})\text{H})$, $F(\text{CHOC}(\text{O})\text{H})$ and $F(\text{COC}(\text{O})\text{H})$ are added to the SAR to reflect the long-range influence of the ester functionality.
5. Three parameter expressions are implemented for all substituent factors and site-specific rate coefficients.

The largest difference is the incorporation of experimental site-specific kinetics. Including experimental site-specific rate coefficients means the SAR not only predicts the total rate coefficient accurately but also predicts accurate site-specific kinetics, which is key to determining the ratio of products formed and, hence, the atmospheric impact. Experimental site-specific kinetics are

implemented by constraining the SAR predictions within experimental uncertainties for a given temperature.

The technique the present work employs to determine the site-specific kinetics of esters utilises the decomposition of ROC(O) combined with the thermal isomerisation of peroxy radicals. Both processes occur at high temperatures outside of the atmospheric range. Therefore, there are more experimental site-specific kinetics for the formates above 400 K than there are below. This work has therefore optimised the SAR between 200 – 600 K to make use of these experimental measurements. The SAR optimised between 200 – 600 K is compared against the SAR optimised between 200 – 400 K to evaluate the approach. It is difficult to ensure esters with more experimental data are not weighted preferentially in SAR development. If the SAR is too heavily trained on a smaller sample of esters it may overfit the training data and not extrapolate as well to unknown esters; the ultimate goal of the SAR is to accurately predict the site-specific kinetics of esters for which no experimental data exists. Despite the incorporation of an equal number of $k(T)$ values for each ester, the SAR may be weighted more heavily towards esters which have constraints on site-specific kinetics. To reduce this weighting, experimental site-specific kinetics have been implemented at the equally spaced temperature intervals. However, the experimental site-specific kinetics do not always align with the equally spaced temperature intervals. Therefore, site-specific kinetics within ± 6 K of a pre-determined temperature interval, are implemented within the SAR.

To address the experimental dependence of formate abstraction on the adjacent R group, this work expands the rate coefficient to reflect whether the adjacent R group is primary ($k(\text{CH}_3\text{OC(O)-H})$), secondary ($k(\text{CH}_2\text{OC(O)-H})$) or tertiary ($k(\text{CH(X)(Y)OC(O)-H})$ or $k(\text{C(X)(Y)(Z)OC(O)-H})$). It is determined above that the site-specific kinetics of higher esters (e.g., acetates) likely depend only on the shape of the R group, not the size. However, formate site-specific rate coefficients at 423 K suggest the size of the R group is also influential in determining formate abstraction. The decision to focus on the shape of the R group, rather than size, is primarily an effort to minimise the number of additional SAR parameters. However, at atmospherically relevant temperatures there are not enough site-specific kinetics

for linear formates to make parameterisations on the influence of the size of the R group.

As illustrated in Figure 6.8, the influence of the ester functionality extends beyond the adjacent reaction site. Compared with the analogous alkanes, reaction sites alpha, beta and gamma to the ester group are activated. The extended ester influence is incorporated into the present SAR through secondary substituent factors $F(\text{CH}_2\text{OC}(\text{O})\text{H})$, $F(\text{CHOC}(\text{O})\text{H})$ and $F(\text{COC}(\text{O})\text{H})$. Lastly, the substituent factors and site-specific rate coefficients are extended to three-parameter expressions (E6.5) in an attempt to provide more flexibility for the SAR to predict both the negative and positive temperature dependent kinetics of the esters.

$$k = A \times \exp \frac{E}{RT} \times \left(\frac{T}{300} \right)^n \quad \text{E6.5}$$

Table 6.4 – Temperature range and parameters implemented in each SAR.

SAR	Temperature Range / K	SAR Parameters
Jenkin et al. [15]	200 – 400	$F(\text{OC}(\text{O})\text{H})$ & $k(\text{ROC}(\text{O})\text{-H})$
EsterSAR1.0	200 – 400	$F(\text{OC}(\text{O})\text{H})$, $k(\text{CH}_3\text{OC}(\text{O})\text{-H})$. $k(\text{CH}_2\text{OC}(\text{O})\text{-H})$ & $k(\text{CHOC}(\text{O})\text{-H})$ or $k(\text{COC}(\text{O})\text{-H})$
EsterSAR1.1	200 – 400	$F(\text{OC}(\text{O})\text{H})$, $k(\text{CH}_3\text{OC}(\text{O})\text{-H})$. $k(\text{CH}_2\text{OC}(\text{O})\text{-H})$, $k(\text{CHOC}(\text{O})\text{-H})$ or $k(\text{COC}(\text{O})\text{-H})$, $F(\text{CH}_2\text{OC}(\text{O})\text{H})$, $F(\text{CHOC}(\text{O})\text{H})$ & $F(\text{COC}(\text{O})\text{H})$
EsterSAR2.0	200 – 600	$F(\text{OC}(\text{O})\text{H})$, $k(\text{CH}_3\text{OC}(\text{O})\text{-H})$. $k(\text{CH}_2\text{OC}(\text{O})\text{-H})$ & $k(\text{CHOC}(\text{O})\text{-H})$ or $k(\text{COC}(\text{O})\text{-H})$
EsterSAR2.1	200 – 600	$F(\text{OC}(\text{O})\text{H})$, $k(\text{CH}_3\text{OC}(\text{O})\text{-H})$. $k(\text{CH}_2\text{OC}(\text{O})\text{-H})$, $k(\text{CHOC}(\text{O})\text{-H})$ or $k(\text{COC}(\text{O})\text{-H})$, $F(\text{CH}_2\text{OC}(\text{O})\text{H})$, $F(\text{CHOC}(\text{O})\text{H})$ & $F(\text{COC}(\text{O})\text{H})$

To test the impact of some of the changes to the updated SAR, several SARs have been optimised. There are four combinations presented for the updated SAR. Optimisations at 200 – 400 K and at 200 – 600 K, with and without secondary parameters. These SARs are denoted EsterSAR1.0, EsterSAR2.0, EsterSAR1.1 and EsterSAR2.1. Table 6.4 outlines the temperature dependence and parameters used in each SAR.

6.3.4. Experimental kinetics implemented in the present work

The last update to the formate SAR by Jenkin et al. [15] used the overall OH kinetics recommended by Calvert et al. [59] for six formates: methyl formate, ethyl formate, n-propyl formate, isopropyl formate, n-butyl formate and tertbutyl formate. No temperature-dependent data were used for isopropyl formate, only the rate coefficient at 298 K. The experimental formate kinetics used in Jenkin's SAR are presented as solid lines in Figure 6.12. The temperature-dependent kinetics of isopropyl formate and isobutyl formate were likely excluded by Jenkin et al. [15] as they hadn't been included in rate coefficient recommendations in 2018 when Jenkin et al. [15] updated the SARs. However, in 2014, Zhang et al. [143] determined the overall kinetics of isopropyl formate and isobutyl formate. In 2021, the Zhang et al. [143] study was included in recommendations by McGillen et al. [16] whose primary goal was to provide a dataset for SAR development. This work utilises the McGillen et al. [16] dataset which has since been updated. The latest update (AtmVOCKin-3.1.xls), available [here](#), is incorporated into the updated SARs alongside additional experimental kinetics outlined below.

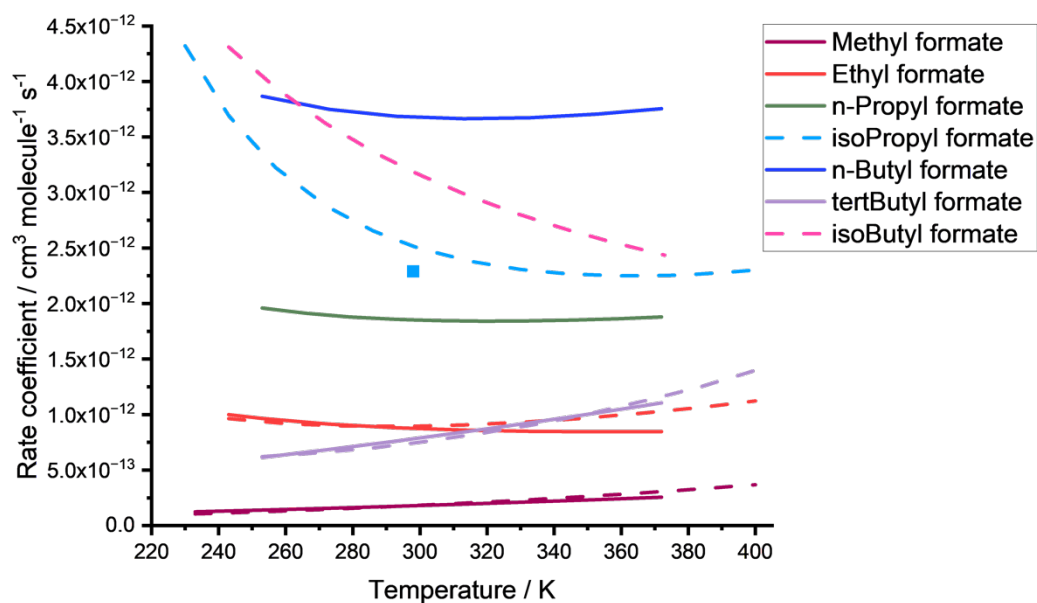


Figure 6.12 – Temperature-dependent data for the reactions of OH + formates. Each formate is represented with a different colour. Solid lines are the temperature-dependent recommendations of Calvert et al., which are used to train the Jenkin et al. [15] SAR. The temperature-dependent rate coefficients used in this work are shown above as dashed lines and are based on Eurochamp recommendations, with a few modifications to include overall kinetics in this work. The rate coefficients for methyl formate are updated to include kinetics outlined in Chapter 3. Ethyl formate kinetics are adapted to include the work of Dr Lavinia Onel (Appendix E), rate coefficients for isopropyl formate are adapted to include the kinetics outlined in Chapter 5 and tertbutyl formate kinetics are adapted to include the kinetics in Appendix E.

The temperature-dependent overall OH kinetics used in the formate SAR development are presented in Figure 6.12 as dashed lines. This work utilises the rate coefficients for isobutyl formate determined by Zhang et al. [143] and recommended by McGillen et al. [16], expanding the formate SAR dataset from six to seven formates. The temperature dependence for OH + methyl formate has been updated to a three-parameter expression, determined by fitting the data recommended by McGillen et al. [16] alongside the rate coefficients presented in Chapter 3. No updates are made to the recommended temperature dependencies of n-propyl and n-butyl formate, used in SAR development by Jenkin et al. [15] Temperature-dependent rate coefficients for OH + isopropyl formate are outlined in Chapter 5. OH regeneration influenced the rate coefficients determined by Zhang et

al. [143], leading to an underestimation of the rate coefficient. Therefore, the temperature dependence for isopropyl formate used in SAR development excludes the Zhang et al. [143] data and uses the rate coefficients determined in this work.

Table 6.5 – Summary of the experimental temperature-dependent data used in the present work to update the formate SAR. The temperature dependence of each rate coefficient is visualised in Figure 6.12.

Formate	Low T	High T	$k_T / \text{cm}^3 \text{ molecule}^{-1} \text{ s}^{-1}$	$k_{298} / \text{cm}^3 \text{ molecule}^{-1} \text{ s}^{-1}$
methyl formate	233	588	$(4.09 \times 10^{-13}) \times \exp \frac{-216}{T} \times \left(\frac{T}{300}\right)^{2.14}$	1.96×10^{-13}
ethyl formate	243	618	$(2.39 \times 10^{-15}) \times \exp \frac{1785}{T} \times \left(\frac{T}{300}\right)^{6.07}$	9.16×10^{-13}
n-propyl formate	253	372	$(2.17 \times 10^{-13}) \times \exp \frac{643}{T} \times \left(\frac{T}{300}\right)^2$	1.85×10^{-12}
isopropyl formate	230	573	$(3.96 \times 10^{-15}) \times \exp \frac{1934}{T} \times \left(\frac{T}{300}\right)^{5.32}$	2.52×10^{-12}
n-butyl formate	253	371	$(4.46 \times 10^{-13}) \times \exp \frac{633}{T} \times \left(\frac{T}{300}\right)^2$	3.68×10^{-12}
tertbutyl formate	253	623	$(6.72 \times 10^{-15}) \times \exp \frac{1415}{T} \times \left(\frac{T}{300}\right)^{6.26}$	7.44×10^{-13}
isobutyl formate	243	373	$(8.38 \times 10^{-13}) \times \exp \frac{398}{T}$	3.19×10^{-12}

Despite the influence of OH regeneration on the OH kinetics of isopropyl formate, this work has incorporated the kinetics of OH + isobutyl formate, also recommended by McGillen et al. [16] and determined by Zhang et al. [143]. The isopropyl structure has a tertiary C-H bond adjacent to the ether functionality, with a lower BDE due to electron donation from the adjacent alkyl groups and the ether functionality. No equivalent C-H bonds exist in isobutyl formate peroxy radicals. Therefore, the internal isomerisation of RO₂ from isobutyl formate peroxy radicals likely occurs at a higher temperature when more thermal energy is available to break

the C-H bonds. In case any OH regeneration has occurred an additional 10% error has been added to the kinetics of isobutyl formate. The overall kinetics utilised in the formate SAR are summarised in Table 6.5.

6.3.5. Site-specific kinetics for the formate SAR

The site-specific kinetics of methyl formate, ethyl formate, isopropyl formate and tertbutyl formate are used to develop the formate SAR and are presented in Tables 6.6 – 6.9 and Figures 6.13 – 6.16. Site-specific kinetics for methyl formate are outlined in Chapters 3 and 4.

Table 6.6 – Site-specific kinetics for OH + methyl formate implemented in the SAR.

Temperature / K	Branching Ratio (formate abstraction)	Reference
300	0.53 ± 0.12	MESMER ^a
325	0.56 ± 0.11	MESMER ^a
400	0.61 ± 0.10	MESMER ^a
425	0.62 ± 0.09	MESMER ^a
498	0.52 ± 0.23	This work experimental
523	0.53 ± 0.19	This work experimental
525	0.63 ± 0.09	MESMER ^a
541	0.51 ± 0.07	This work experimental
600	0.63 ± 0.09	MESMER ^a

^aMESMER calculated branching ratios are based on fitting the full methyl formate experimental dataset (kinetics and pressure-dependent yields). A blanket 20% error was added the theoretical yields. However, this does not capture a discrepancy between experiment and theory at 541 K. An additional 5% error had been applied to the experimental value at 541 K, alongside an increase to the theoretical error from 20% to 25%. The additional error is to account for systematic errors.

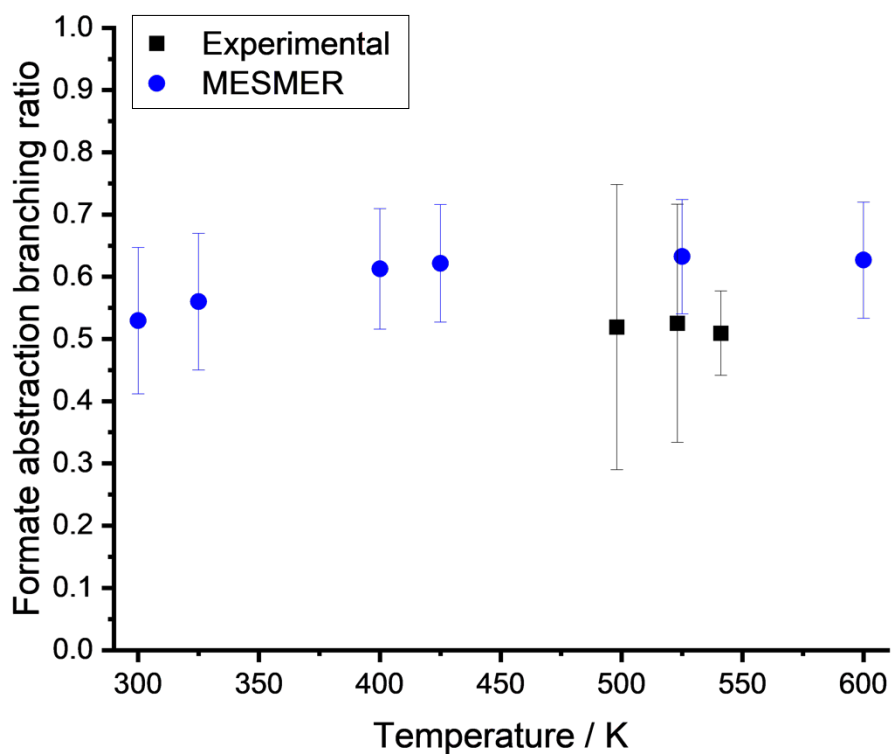


Figure 6.13 - The site-specific kinetics of methyl formate implemented in the SAR, as determined experimentally in the present work (Chapter 4) and theoretically by Dr Robin Shannon (labelled MESMER, based on isotopomer studies).

The site-specific kinetics of ethyl formate have been determined by Dr Lavinia Onel, using a similar methodology outlined in Chapters 3, 4 and 5. As with isopropyl formate, ethyl formate has three reaction sites and therefore OH yields can come from three peroxy radicals. Analysis of the ethyl formate experimental data is presented in Appendix E.

Table 6.7 – Site-specific kinetics for OH + ethyl formate implemented in the SAR.

Temperature / K	Branching Ratio (formate abstraction) ^a	Reference
390	0.54 ± 0.10	Dr Lavinia Onel experimental
431	0.45 ± 0.11	Dr Lavinia Onel experimental
508	0.52 ± 0.09	Dr Lavinia Onel experimental
547	0.51 ± 0.07	Dr Lavinia Onel experimental
580	0.48 ± 0.15	Dr Lavinia Onel experimental

^aGiven the error increase required for agreement between the experimental and theoretical branching ratios in methyl formate, an additional 10% has been added to the branching ratios.

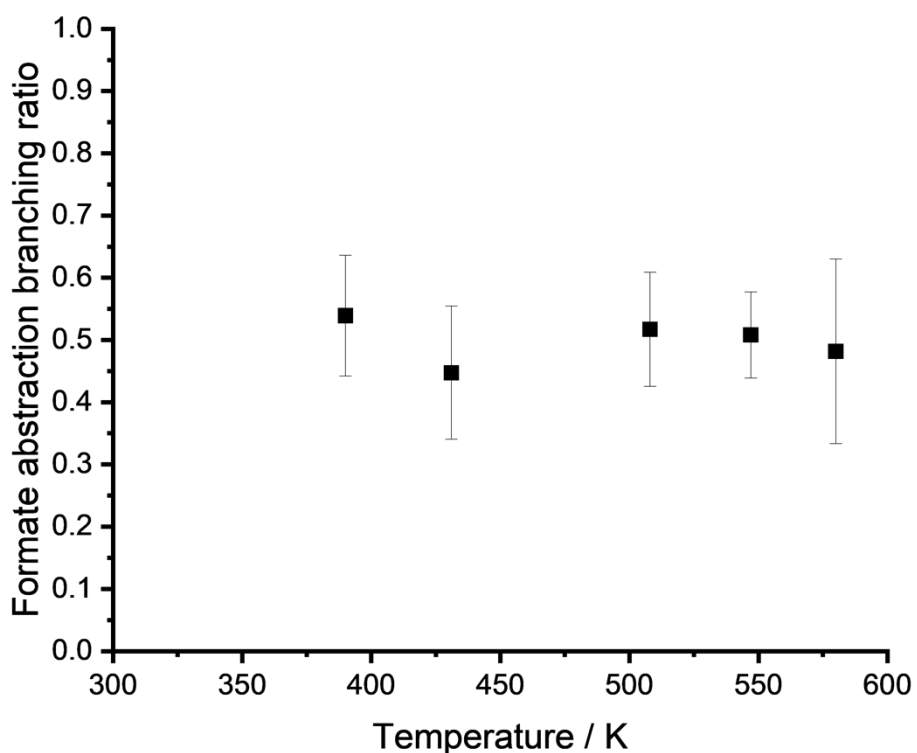


Figure 6.14 – The site-specific kinetics of ethyl formate implemented in the SAR, as determined experimentally by Dr Lavinia Onel.

Table 6.8 – Site-specific kinetics for OH + isopropyl formate implemented in the SAR.

Temperature / K	Branching Ratio (CH ₂ abstraction)	Reference
298	0.70 ± 0.10	Pimentel et al.
423	0.67 ± 0.07	This work
473	0.53 ± 0.16	This work
493	0.55 ± 0.11	This work

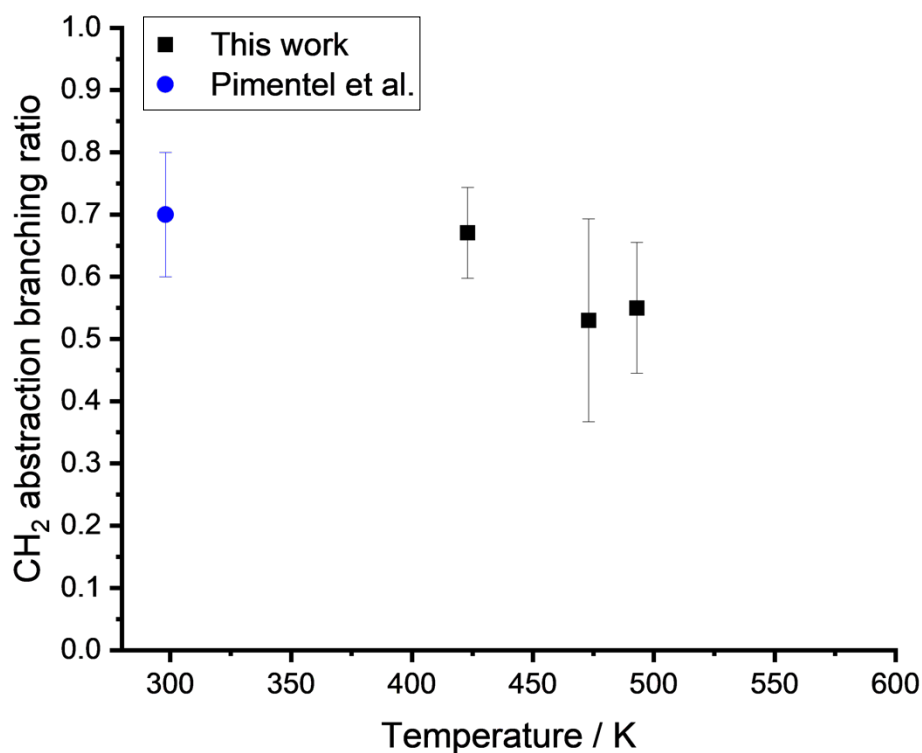


Figure 6.15 – The site-specific kinetics of isopropyl formate implemented in the SAR, as determined in this work and by Pimentel et al.

The site-specific kinetics of isopropyl formate, as outlined in Chapter 5, are presented as the ratio of CH₂ abstraction. All other site-specific kinetics are presented as branching ratios for formate abstraction. The site-specific kinetics of tertbutyl formate have been experimentally determined between 420 – 583 K. The experimental results and analysis are outlined in Appendix E. Where branching ratios are determined from the thermalised peroxy radicals at higher temperatures, an additional 10% error has been added to the yields.

Table 6.9 – Site-specific kinetics for OH + tertbutyl formate implemented in the SAR.

Temperature / K	Branching Ratio (formate abstraction)	Reference
298	0.50 ± 0.10	Pimentel et al.
420	0.60 ± 0.46	This work
450	0.66 ± 0.16	This work
473	0.40 ± 0.11	This work
523	0.55 ± 0.06	This work
548	0.68 ± 0.31	This work
583	0.63 ± 0.10	This work

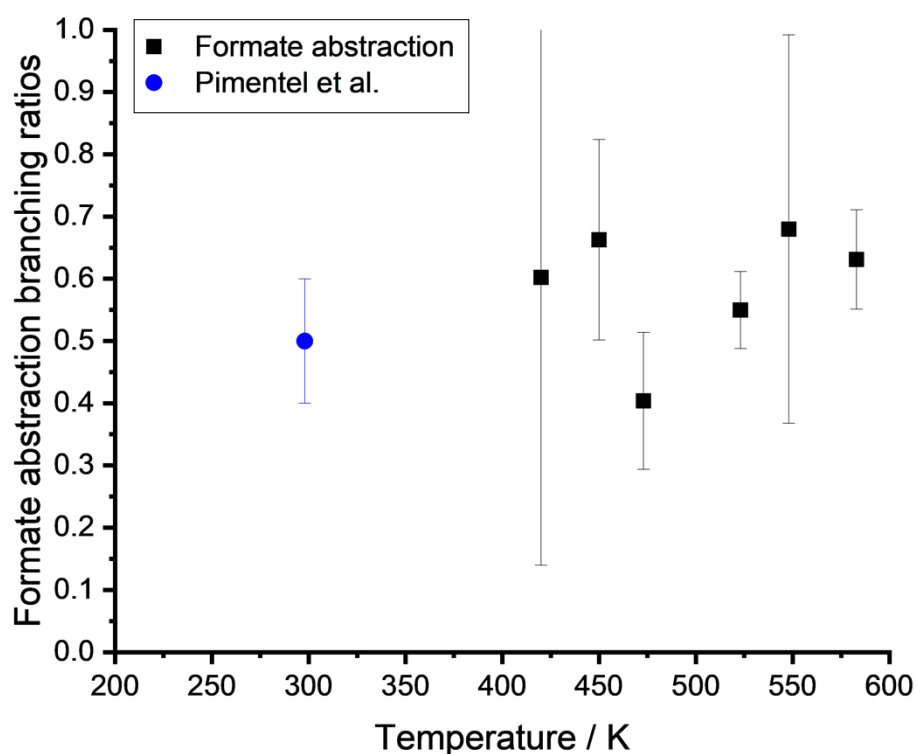


Figure 6.16 – The site-specific kinetics of tertbutyl formate implemented in the SAR, as determined in this work.

6.4. SAR Results

The overall temperature-dependent kinetics predicted by the SARs are presented in Figure 6.17. The updated SARs generally lead to improved predictions of the rate coefficients as a function of temperature compared with the current SAR by Jenkin et al. [15]. Improvement could be due to the increased number of

parameters providing more flexibility to the SAR. However, the updated SAR is also significantly more constrained by experimental site-specific kinetics. Although the current overall rate coefficient predictions by the Jenkin et al. [15] SAR are well within the factor of two range commonly used as a target, they struggle to predict both the negative and positive temperature dependence of some of the formates.

The SSR of each SAR in the present work are presented in Table 6.10. Incorporation of secondary substituent factors leads to a reduction in the SSR, which is most notable for the SAR optimised between 200 and 600 K. The site-specific kinetics of EsterSAR1.0 and EsterSAR2.0 which do not include secondary substituent factors will be discussed first.

Table 6.10 – Sum of the squared residuals (SSR) for each SAR in the present work.

EsterSAR1.0	EsterSAR1.1	EsterSAR2.0	EsterSAR2.1
4.17	0.66	44.67	3.12

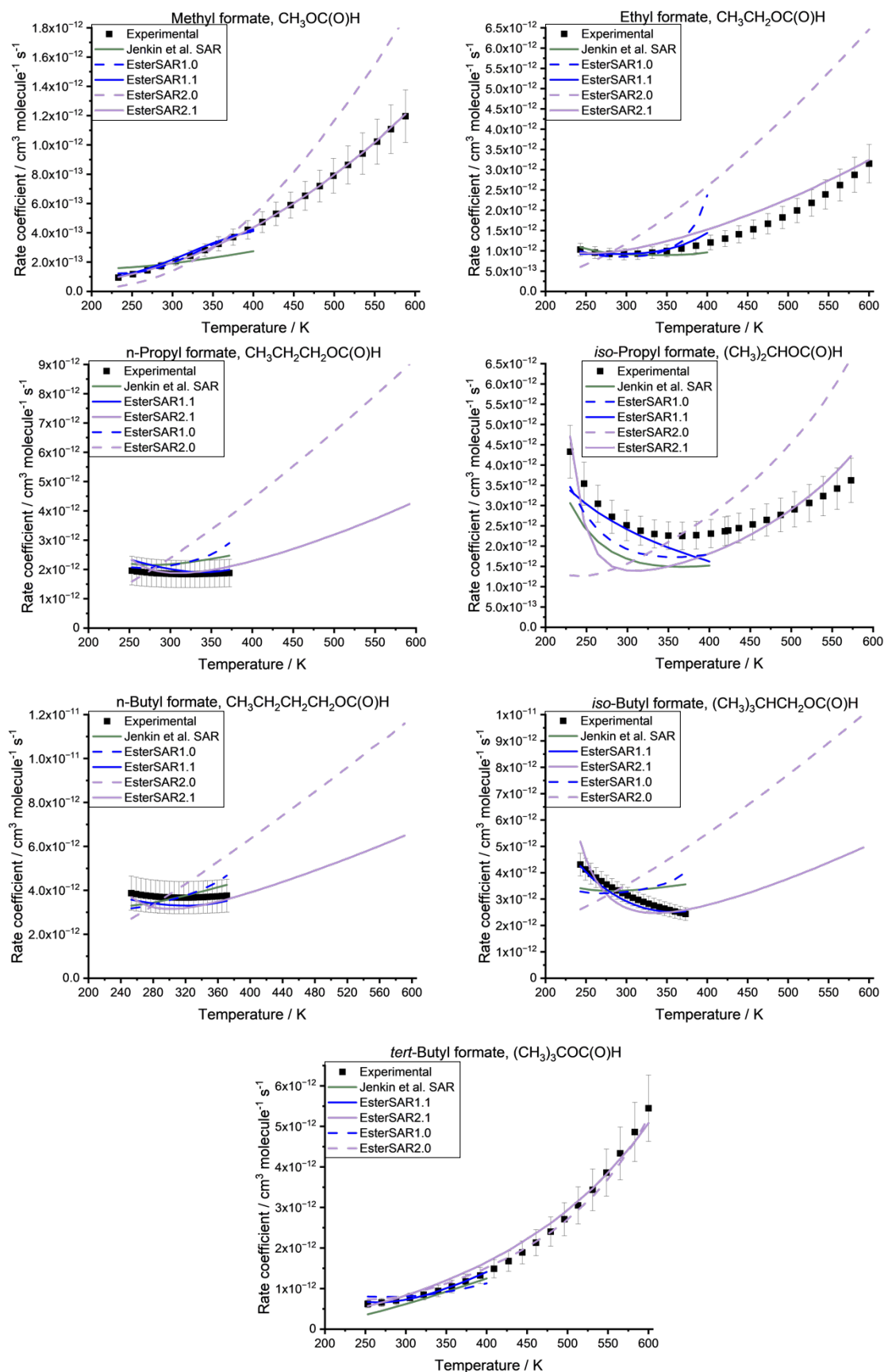


Figure 6.17 – Formate temperature-dependent kinetics determined experimentally (black squares) and via different SAR calculations.

6.5. EsterSAR1.0 and EsterSAR2.0

The SAR was first optimised between 200 – 400 K without including secondary effects and a solution was found within the experimental site-specific kinetic constraints (EsterSAR1.0). However, EsterSAR1.0 overpredicts the positive temperature dependence of $k(\text{CH}_2\text{OC}(\text{O})\text{-H})$ and predicts zero formate abstraction at 298 K in all linear formates. Formate abstraction from ethyl formate is constrained at 386 K to 0.54 ± 0.10 . EsterSAR1.0 predicts formate branching ratios of 0.44 at 386 K and 1.00 at 582 K. The branching ratios for each site of abstraction are presented in Figure 6.18 for each formate. Although no experimental site-specific kinetics exist at 298 K for the linear formates, based on the trends in formate abstraction outlined above, formate abstraction is likely larger than in methyl formate. Therefore, a lower $k(\text{CH}_2\text{OC}(\text{O})\text{-H})$ than $k(\text{CH}_3\text{OC}(\text{O})\text{-H})$ is theoretically unlikely. Optimising the SAR between 200 – 600 K (EsterSAR2.0) incorporates significantly more experimental site-specific kinetics for formate abstraction than EsterSAR1.0. Therefore, it is not surprising that EsterSAR2.0 does a better job than EsterSAR1.0 at predicting formate abstraction.

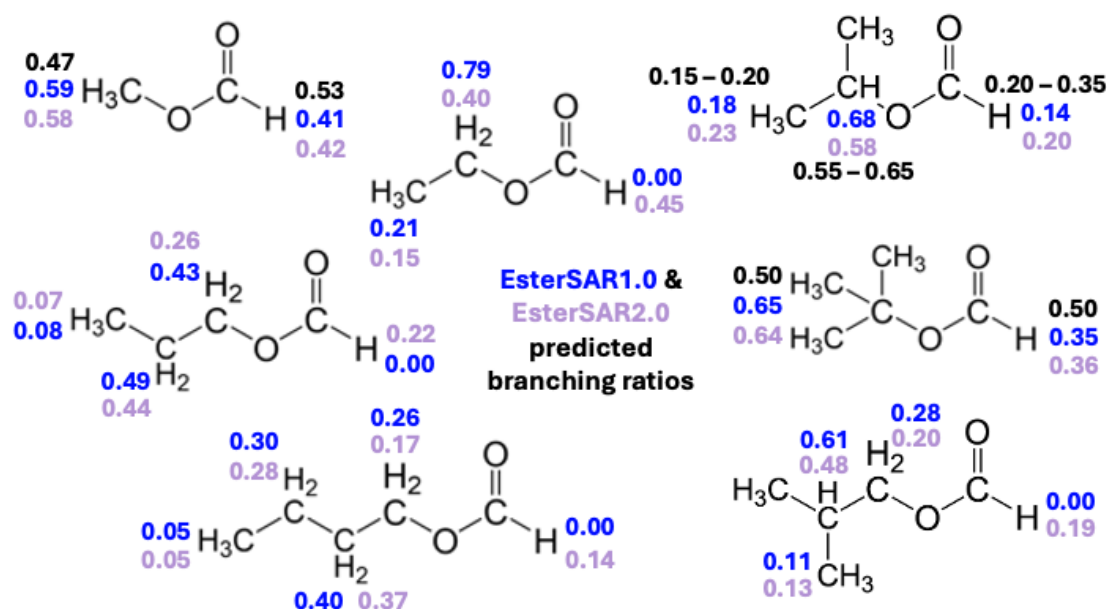


Figure 6.18 – Branching ratios for each formate included in the SAR. Experimental branching ratios are shown in black and SAR calculated branching ratios are shown in blue (EsterSAR1.0) and purple (EsterSAR2.0).

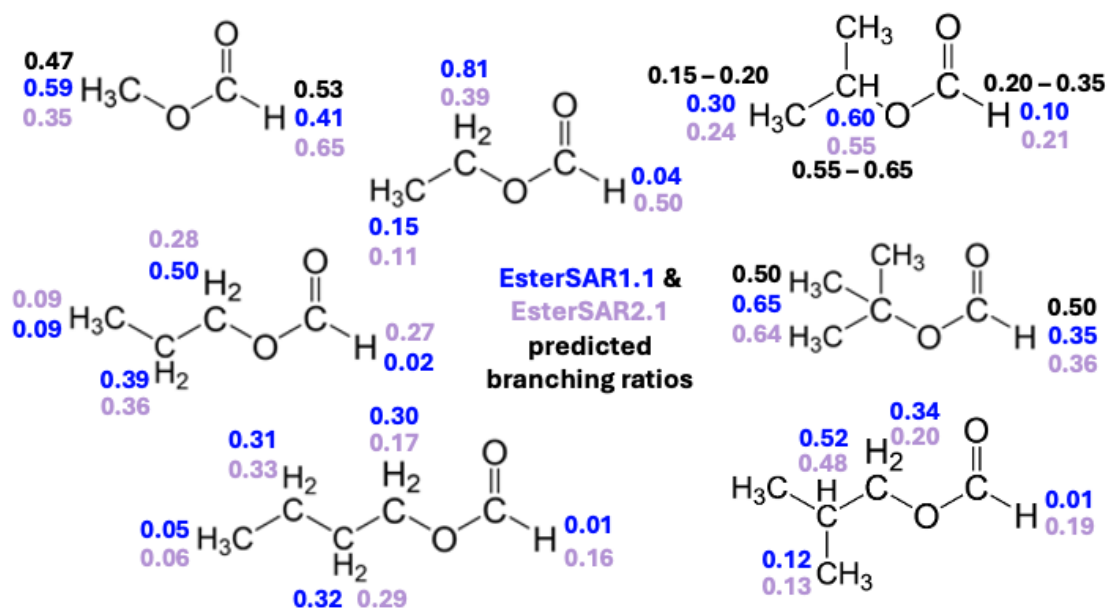


Figure 6.19 – Branching ratios for each formate included in the SAR. Experimental branching ratios are shown in black and SAR calculated branching ratios are shown in blue (EsterSAR1.1) and purple (EsterSAR2.1). Both SARs incorporate secondary substituent factors.

The other key site of abstraction to monitor is the site alpha to the ether oxygen/ester group. This site is shown experimentally to dominate in both formates and acetates and typically leads to the formation of organic acids. Accurately predicting this dominant site of abstraction is therefore important for accurate atmospheric modelling. As demonstrated in Figure 6.18, neither EsterSAR1.0 nor EsterSAR2.0 predicts the reaction site alpha to the ether group to dominate. The impact of abstraction at the site alpha to the ether group is represented via the substituent factor $F(-OC(O)H)$. A substituent factor below one indicates the reactivity of adjacent C-H bonds will decrease due to the functionality whilst a substituent factor above one indicates reactivity will increase due to functionality. Although hydrogen abstraction at the alpha site adjacent to the ether group dominates at room temperature and is activated by the ester functionality, $F(-OC(O)H)$ is determined to be less than one in all ester SARs (Le Calve, Jenkin, EsterSAR1.0, EsterSAR1.1, EsterSAR2.0 and EsterSAR2.1) at 298 K.

Comparisons of the overall rate coefficient for the formates compared with the analogous R group in alkanes are presented in Figure 6.20. As the formates have

a unique hydrogen abstraction site, there are no direct comparisons with alkanes. However, rate coefficients for the formates can be compared with alkanes that have the same R group as ROC(O)H, with a primary CH₃ site subtracted (E6.6). The experimental k_{CH_3} value has been derived via E6.7, i.e., half the ethane (CH₃CH₃) rate coefficient (k_{CH_3}), which is $1.25 \times 10^{-13} \text{ cm}^3 \text{ molecule}^{-1} \text{ s}^{-1}$.

$$k(\text{OH}+\text{R}) = k(\text{OH}+\text{RCH}_3) - k(\text{OH}+\text{CH}_3) \quad \text{E6.6}$$

$$k(\text{OH} + \text{CH}_3) = \frac{k(\text{OH} + \text{CH}_3\text{CH}_3)}{2} \quad \text{E6.7}$$

Despite the additional formate reaction site ($k(\text{OC(O)-H})$), the overall rate coefficients of both k_R and $k_{\text{ROC(O)H}}$ are typically within error of each other. Given the additional contribution from formate abstraction, the contribution of abstraction on the adjacent R group must be lower in the formates than the analogous alkanes. Within the SAR, the only way to represent this decrease is via $F(-\text{OC(O)H})$. Consequently, $F(-\text{OC(O)H})$ has a value less than one which leads to a reduction in the branching ratio adjacent to the formate functionality.

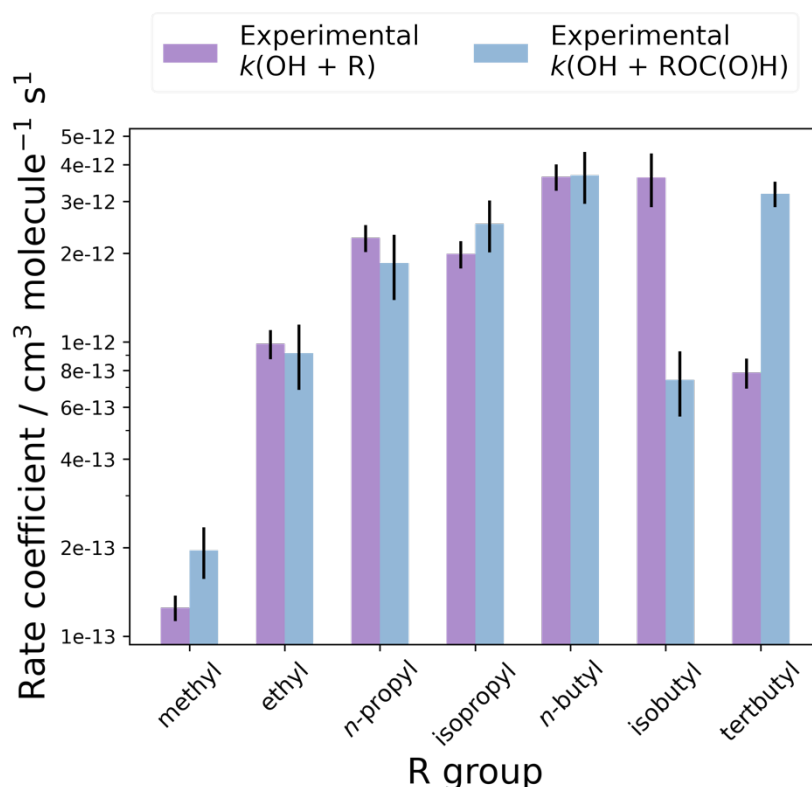


Figure 6.20 – Rate coefficients at 298 K for OH radical reactions with alkyl groups (R) (purple) and formates (blue). Rate coefficients for alkyl groups are calculated by subtracting k_{CH_3} from k_{RCH_3} , with k_{CH_3} calculated from $k_{CH_3CH_3}/2$.

Table 6.11 – Substituent factor $F(-OC(O)H)$ values for different SARs.

SAR	Substituent Factor $F(-OC(O)H)$
EsterSAR1.0	$(2.61 \times 10^{-4}) \times \exp\left(\frac{-2432}{T}\right) \times \left(\frac{T}{300}\right)^{5.61}$
EsterSAR1.1	$(7.92 \times 10^{-1}) \times \exp\left(\frac{-59}{T}\right) \times \left(\frac{T}{300}\right)^{-1.97}$
EsterSAR2.0	$(6.18 \times 10^{-1}) \times \exp\left(\frac{4}{T}\right) \times \left(\frac{T}{300}\right)^{1.27}$
EsterSAR2.1	$(5.17 \times 10^{-1}) \times \exp\left(\frac{-0.0018}{T}\right) \times \left(\frac{T}{300}\right)^{0.77}$
Jenkin et al. [15]	$(2.51 \times 10^{-2}) \times \exp\left(\frac{-1050}{T}\right)$

6.5.1. EsterSAR1.1 and EsterSAR2.1

Secondary substituent factors have been incorporated into the ester SAR to capture potential long-range effects of the ester functionality, as described above. Secondary factors may also help improve branching ratio predictions at the reaction site alpha to the ester functionality. Incorporating secondary substituent factors improves the predictions of the overall (Figure 6.17) and site-specific (Figure 6.19) kinetics between 200 – 400 K (EsterSAR1.0 → EsterSAR1.1) and 200 – 600 K (EsterSAR2.0 → EsterSAR2.1). This is particularly true for the SAR optimised between 200 – 600 K, which does a significantly worse job (without secondary factors) at predicting overall kinetics than the current SAR by Jenkin et al. [15].

The secondary substituent factor $F(-CH_2OC(O)H)$ is incorporated into the kinetic predictions of ethyl formate, n-propyl formate, n-butyl formate and isobutyl formate. Optimisations of $F(-CH_2OC(O)H)$ are therefore fitting both the overall kinetics of four formates and the site-specific kinetics of one formate (ethyl formate). In comparison, $F(-CHOC(O)H)$ and $F(-COC(O)H)$ are each fitting the overall and site-specific kinetics of one formate each – isopropyl formate ($F(-CHOC(O)H)$) and tertbutyl formate ($F(-COC(O)H)$). Consequently, the overall and site-specific SAR predictions of isopropyl formate and tertbutyl formate are more accurate in both EsterSAR1.1 and EsterSAR2.1. For the other formates, trade-

offs are made. Between 200 – 400 K (EsterSAR1.1), improvements in the overall kinetics are most notable for the larger formates, n-butyl formate and isobutyl formate. However, the site-specific kinetics of n-butyl formate and isobutyl formate do not predict abstraction alpha to the ester group to dominate. EsterSAR1.1 also underpredicts formate abstraction. In contrast, EsterSAR2.1 does a good job at predicting formate abstraction but does not predict the alpha reaction site to dominate.

Including the high temperature site-specific kinetics determined between 400 – 600 K, does lead to improvements in the prediction of formate abstraction at 298 K. Realistic extrapolations down to room temperature suggest this approach of implementing higher temperature experimental kinetics could be useful for other oxygenated or multifunctional compounds whose site specific kinetics may only be determined above 400 K. Expanding the SAR to 600 K also ensures the SAR determines the correct temperature dependent trends over a wider range of temperatures, and is perhaps more theoretically robust as a result. Although the focus of SAR development is to improve atmospheric models, this SAR may also be of interest to the low-temperature combustion community. Despite the inclusion of extensive experimental site-specific kinetics, the updated SARs fail to accurately predict the site-specific kinetics of the dominant reaction site. However, other than for isopropyl formate, no site-specific kinetics implemented in the SAR describe abstraction from the chain adjacent to the formate group. Experimentally determining the kinetics of the dominant reaction site in the esters would provide conclusive experimental data to fix this SAR.

6.6. Testing the updated formate SAR on the kinetics of n-butyl formate

6.6.1. Overall kinetics of n-butyl formate

This work has also experimentally determined the overall kinetics of n-butyl formate between 232 and 613 K. To test the updated SAR, this work's n-butyl formate kinetics were reserved, and the SAR was trained on the temperature-dependent recommendation by Calvert et al. [23], combining the temperature-dependent study by Le Calve et al. [8] and the room temperature determination of Wallington et al. [19]. The Calvert et al. [23] recommendation has been recommended by

Eurochamp [16] and is presented in Figure 6.21 alongside this work, the literature and SAR predictions determined in this work (EsterSAR2.1) and by Jenkin et al. [15].

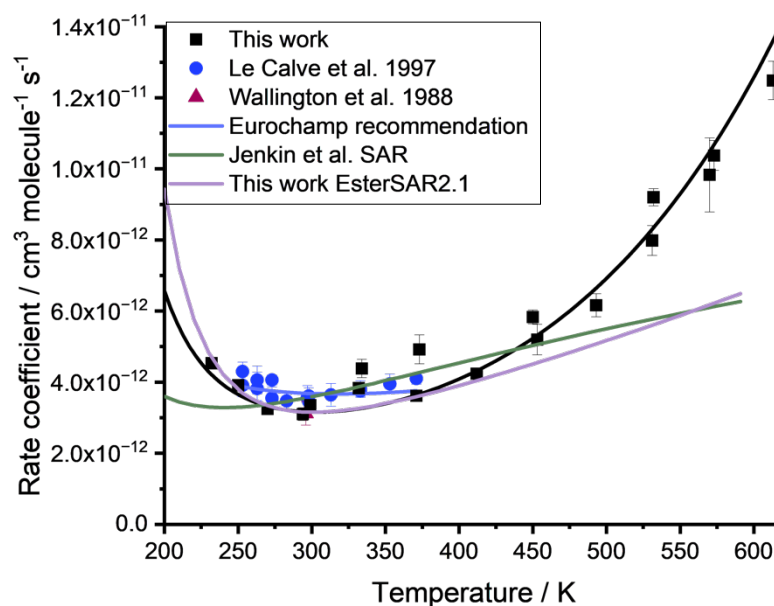


Figure 6.21 – Temperature-dependent rate coefficients for the reaction of OH + n-butyl formate determined in this work (black squares and solid black line), the literature (Le Calve et al. [8] (blue circles) and Wallington et al. [19] (burgundy triangles)), the Eurochamp [16] recommended temperature dependence (blue line), Jenkin et al. [15] SAR predictions (green line) and the EsterSAR2.1 predictions updated in this work (purple line).

EsterSAR2.1, as outlined above, is trained on the overall and site-specific experimental formate kinetics up to 600 K, whilst the Jenkin et al. [15] SAR is trained on overall kinetics up to 400 K. Despite the extended temperature range in this work, the Jenkin et al. [15] SAR does a slightly better job at predicting the temperature-dependent kinetics between 373 and ~ 570 K. However, neither SAR predict the strong positive temperature-dependence experimentally observed. An evaluation of each SAR's ability to predict the overall rate coefficient is shown in Figure 6.22. Figure 6.22 (left) plots the experimental rate coefficients calculated from the temperature-dependent fit between 200 and 600 K on the x-axis and the SAR predicted rate coefficient on the y-axis. Figure 6.22 (right) shows a similar figure for the experimental temperature range between 232 and 613 K. EsterSAR2.1 predicts the overall kinetics more accurately between 412 and 200 K, although the agreement begins to deviate below 250 K. The ability of the updated SAR to predict

the negative temperature dependence demonstrates an improvement over the current SAR.

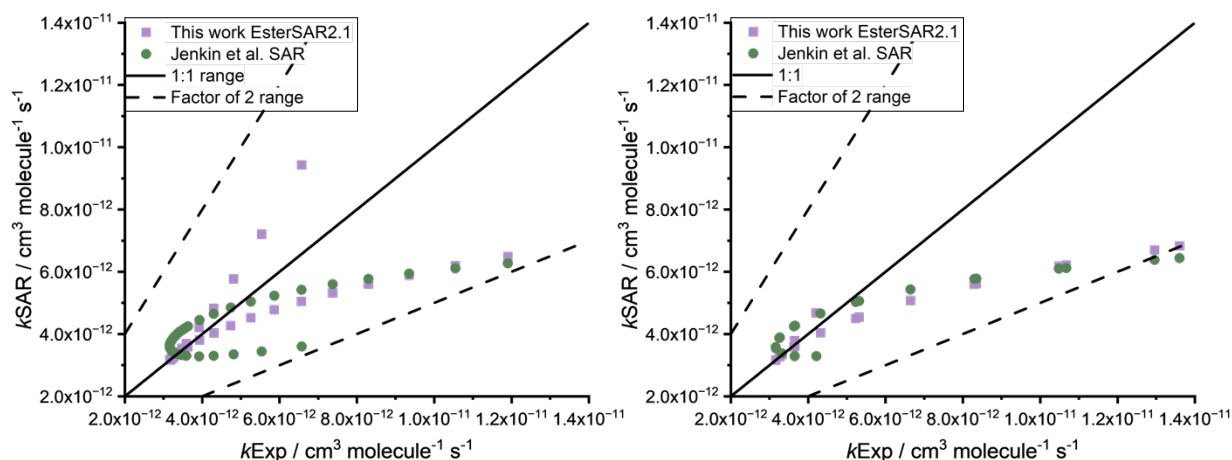


Figure 6.22 – SAR calculated rate coefficients for OH + n-butyl formate from this work (EsterSAR2.1) and Jenkin et al. [15] are plotted against experimental rate coefficients for OH + n-butyl formate calculated from the temperature-dependent fit to this work. The left figure shows rate coefficients between 200 and 600 K, whilst the right figure shows rate coefficients between 232 and 613 K.

6.6.2. Site-specific kinetics of n-butyl formate

This work has tentatively determined the site-specific kinetics of n-butyl formate between 493 and 613 K. Above 493 K, OH decays following the OH-initiated oxidation of n-butyl formate in the absence of any added oxygen at ~ 120 Torr became biexponential. Biexponential behaviour under these experimental conditions is due to the thermalised RO₂ radical undergoing internal isomerisation followed by decomposition to OH. Yields of OH are presented in Figure 6.21 (black squares) alongside the branching ratio for abstraction at the reaction site alpha to the ether group calculated by Zaras et al. [20] (blue circles). Zaras et al. [20] calculated the rate coefficients for hydrogen abstraction by OH at the G3//MP2/aug-cc-pVDZ level of theory coupled with statistical rate theory between 500 and 1300 K. The value plotted in Figure 6.21 at 298 K is an extrapolation of the temperature dependence of each site-specific rate coefficient calculated by Zaras et al. [20].

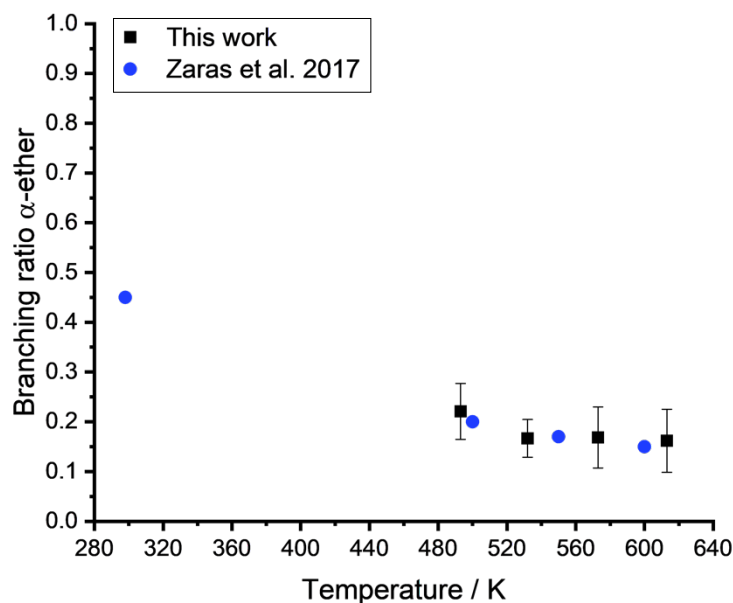


Figure 6.23 – OH yields determined in this work (black squares) following the OH-initiated oxidation of n-butyl formate at 120 Torr in the absence of added oxygen. Branching ratios for abstraction from the reaction site alpha to the ether oxygen calculated by Zaras et al. [20] are shown as blue circles.

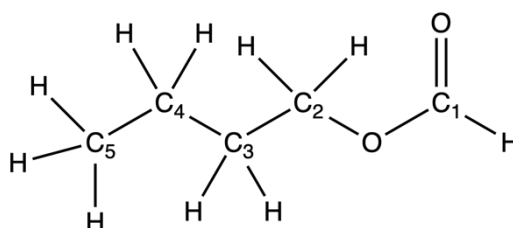


Figure 6.24 – The structure of n-butyl formate with each carbon numbered, C₁ starts at the formate carbon.

The structure of n-butyl formate is shown in Figure 6.24 with each carbon atom labelled C₁ – C₅. Hydrogen abstraction at each reaction site within n-butyl formate, can lead to multiple peroxy radicals, which can each undergo internal isomerisation followed by decomposition to OH. The peroxy radical with the lowest barrier for internal isomerisation is the peroxy radical formed following hydrogen abstraction adjacent to the ether group isomerising to abstract the formate hydrogen. Although there is agreement between the OH yields determined in this work and the branching ratio calculated by Zaras et al. [20], it is not conclusive that the OH yields are exclusively due to abstraction alpha to the ether group. Radicals formed following initial hydrogen abstraction further along the alkyl chain can also

undergo thermal decomposition, preventing the formation of a peroxy radical and hence regeneration of OH. At 500 K, Zaras et al. [20] calculated the rate coefficients for decomposition of $\text{CH}_3\text{CH}_2\text{CH}_2\text{CH}_2\text{OC}(\text{O})^\bullet$ and $\text{CH}_3\text{CH}_2\text{CH}^\bullet\text{CH}_2\text{OC}(\text{O})\text{H}$ are $35.81 \times 10^6 \text{ s}^{-1}$ and 6195 s^{-1} , respectively.

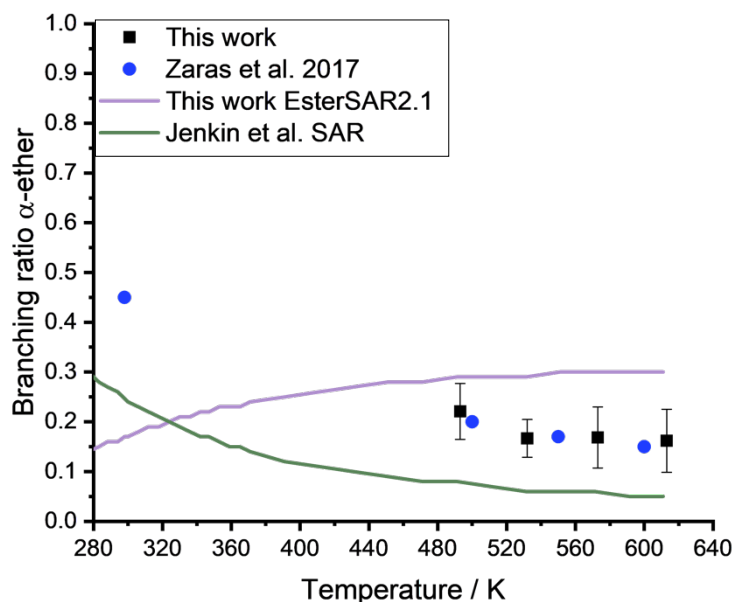


Figure 6.25 – Branching ratios for OH abstraction adjacent to the ether group in n-butyl formate. Branching ratios calculated by Zaras et al. [20] are shown as blue circles, this works SAR EsterSAR2.1 is shown in purple and the Jenkin et al. [15] SAR is shown in green.

Between ~ 360 and 500 K , the updated SAR does a better job at predicting the n-butyl formate site-specific kinetics. However, it predicts the opposite temperature dependence to the Jenkin et al. [15] SAR. Although the Jenkin et al. [15] SAR underpredicts the branching ratio for abstraction alpha to the ether group, it does get the temperature-dependent trend correct.

6.7. Implications of this work

The results for the formate SARs presented above highlight challenges in developing group additivity SARs that accurately predict site-specific kinetics. Through the incorporation of experimental site-specific kinetics for formate abstraction, predictions of the overall and site-specific formate rate coefficients are improved over the current SAR by Jenkin et al. [15]. However, the updated SAR

cannot accurately predict the site-specific kinetics of the other reaction sites. The poor extrapolation leaves little confidence in the SARs application beyond the training data.

Group additivity SARs are a parameterisation of experimental data. The substituent factors utilised in group additivity are based on the Arrhenius equation (E6.8).

$$k = A \times \exp\left(\frac{-Ea}{RT}\right) \quad \text{E6.8}$$

Whilst the Arrhenius equation is empirical, the parameters have physical meaning for simple abstraction reactions with a well-defined barrier. Molecules, such as alkanes, which have a positive temperature dependence and whose kinetics can be described by the Arrhenius equation can typically be described well by group additivity. However, oxygenated molecules are also influenced by hydrogen bonding interactions between oxygenated functional groups within the molecule and the OH radical. The impacts of oxygenated functional groups can also extend beyond adjacent sites of reactivity and as demonstrated for the esters, are not always independent of one-another.

The Arrhenius temperature dependence has been expanded to incorporate an additional parameter, n , to describe rate coefficients with both a negative and positive temperature dependence. This work uses a modified Arrhenius expression to parameterise the overall experimental temperature dependencies observed and expanded the substituent factors in the updated SAR to include n . However, the parameter n has no theoretical basis. For group additivity SARs to accurately predict site-specific kinetics of oxygenated molecules (such as esters) outside of their training datasets, a new mathematical expression may be required. In 1991, Bonchev & Rouvray wrote, “the mathematization of chemistry has paralleled the progress of chemistry” [68]. If the SAR parameterisations become more physically meaningful, the confidence in SAR predictions intuitively increases.

6.8. Alternative SAR Approaches

To more accurately predict the site-specific kinetics of esters, this work expanded the current Jenkin et al. [15] SAR to include several more parameters. However, increasing the number of parameters did not lead to a SAR that can accurately predict formate site-specific kinetics at each reaction site. Given the complexities outlined above in predicting the site-specific kinetics of esters and other oxygenated molecules, an alternative approach may be required. Alternative approaches can vary from adapting the current mathematical expression with the group additivity SAR to developing a new type of SAR based on quantum chemical data or utilising a machine learning approach.

6.8.1. Topological Indices

Topological indices can be used in SAR development in a wide variety of ways. Figure 6.26 plots the Zagreb index alongside transition state energies for hydrogen abstraction at the formate (black squares), alpha-ether (blue circles) and beta-ether (purple triangles) reaction sites in the series of formates. Energies are calculated at the M062X/6-31+G** level of theory. Figure 6.26 also presents the rate coefficients for formate abstraction from methyl formate, isopropyl formate and tertbutyl formate against their respective Zagreb indices. The Zagreb index is a topological index calculated by summing the squares of the degrees of each vertices, i.e., the number of atoms each atom is bonded to is squared and the sum is the Zagreb index [144]. The correlations demonstrated in Figure 6.26 with the Zagreb index are also observed with the Wiener index. Correlations plotted in Figure 6.26 could be used in an updated SAR approach.

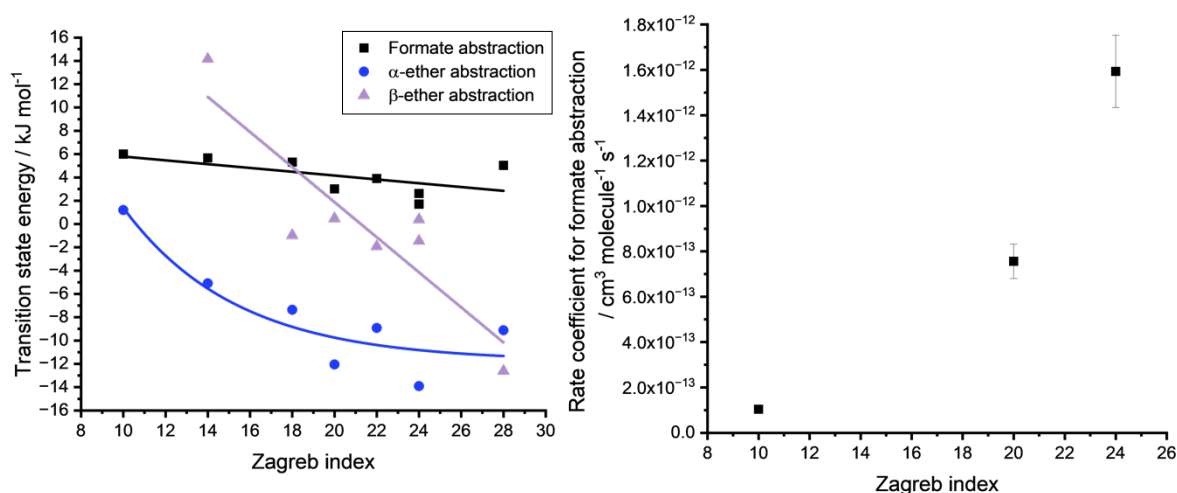


Figure 6.26 – Example correlations between physical quantities and a topological index, the Zagreb index. The left figure presents the transition state energies for hydrogen abstraction from the formate site (black squares), alpha to the ether group (blue circles) and beta to the ether group (purple triangles) calculated at the M062X/6-31+G** level of theory. The right figure shows the experimental rate coefficients for formate abstraction in methyl formate, isopropyl formate and tertbutyl formate.

McGillen et al. [145] have developed a new style of SAR based on the electrotopological state. The electrotopological state describes the electronic character of each atom within a molecule and the distances between atoms. Although the McGillen et al. [145] SAR for alkanes and haloalkanes leads to accurate rate coefficient predictions, and has fewer parameters than the current Jenkin et al. [15] SAR, the benefit of this new SAR over current group additivity may be overstated. Whilst the SAR is based on a fundamental molecular property, multiple empirical parameters, without any physical basis, are incorporated into the SAR. Arguably, group additivity has a similar level of physical basis. The requirement to include these additional parameters, suggests the underlying indices inadequately represent the reaction kinetics of even a simple class of molecule. Therefore, this new topological approach is unlikely to revolutionise gas phase kinetic SARs. However, McGillen et al. [145] are working on adapting this electrotopological state SAR to oxygenated molecules such as ethers. As the community is so accustomed to group additivity approaches, any alternative must be at least as easy to implement or provide drastic improvements in predictions. It may be that different SAR approaches are required for different use cases.

6.8.2. Machine Learning

Whilst machine learning approaches have increased in popularity, to the best of my knowledge, no machine learning model predicts the site-specific kinetics of multifunctional organic compounds. However, several models aim to predict the reaction kinetics of gas-phase organic species. One popular method to construct these models is the use of artificial neural networks (ANNs) trained on chemical descriptors such as topological indices. However, a key disadvantage of ANNs is the large amount of data required to train a reliable model. The total rate coefficients of gas phase organic compounds reacting with OH, Cl, NO₃ and O₃ provide a large body of data to train an ANN. For site-specific rate coefficients, the data are far more limited. The lack of site-specific data is a key barrier to building a reliable machine learning model to predict accurately the site-specific kinetics of organic molecules in the gas phase. The ultimate aim is to predict the site-specific kinetics of molecules across multiple phases (gas, aqueous, particle) under atmospheric conditions.

A machine learning model may provide several advantages in SAR development, particularly if a transfer learning approach is implemented. Unlike traditional group additivity SARs, which optimise substituent factors exclusively on molecules using the substituent factor in its calculation, machine learning SARs can use more input data to inform predictions. For example, the hydrogen bond interactions influencing reactivity in the esters are also observed in ketones. Long-range effects are also observed across oxygenated molecules such as esters, alcohols and ethers. Using a larger variety of molecules to base predictions on, rather than using the alkanes as a constant baseline, may also improve predictions in multifunctional molecules containing a combination of functional groups at varying distances to one another. The larger range of input parameters from topological indices and physical properties, such as BDEs, to overall and site-specific kinetics across a range of molecules would likely increase the flexibility of the SAR. A machine learning SAR could also be user-friendly and easy to implement through a user interface, meaning manual calculations across a large number of parameters are not required which would hinder the SARs adoption.

Although a machine learning SAR may sound promising, any SAR will be limited by the quality of the input data. To develop any SAR that can accurately predict site-specific kinetics will likely require an evaluated dataset of site-specific kinetics across the oxygenates.

6.9. Conclusions

This work has determined the experimental overall and site-specific kinetics of the OH radical with methyl formate, ethyl formate, isopropyl formate, n-butyl formate and tertbutyl formate. Site-specific rate coefficients for formate abstraction demonstrate that formate abstraction is dependent on the adjacent R group. However, the current SAR by Jenkin et al. [15] predicts a constant rate coefficient for formate abstraction, irrespective of the adjacent R group. The Jenkin et al. [15] SAR underpredicts formate reactivity, and the discrepancy between the SAR calculation and experimental value increases with increasing R group. At 298 K the discrepancies are 11% for methyl formate, 25% for isopropyl formate and 37% for tertbutyl formate. This work also determined that the reaction sites within esters are not independent of one another, which is a fundamental assumption in group additivity SARs. Coupled reaction sites were determined for methyl formate as outlined in Chapter 3 and as outlined in Section 6.2 above; reaction sites in other esters are also dependent on adjacent R groups.

By incorporating site-specific kinetics directly into the SAR, the updated SAR presented in this work (EsterSAR2.1) more accurately predicts the rate coefficients for formate abstraction. Including site-specific kinetics in SAR development of other oxygenated molecules will likely lead to SARs that more accurately predict site-specific kinetics. By expanding the temperature range of the SAR up to 600 K, this work was able to include more experimental site-specific kinetics in the SAR development, leading to improvements over an atmospheric temperature range. Current SARs do not include site-specific kinetics for other oxygenated molecules, perhaps due to the limited experimental data available.

Despite the significant improvement in the updated SAR's predictive abilities over the current SAR, this work has highlighted several challenges with group

additivity SARs. The SAR developed in this work does not predict that the reaction site alpha to the ether group dominates, meaning the SAR could not extrapolate the experimental site-specific kinetics accurately to other reaction sites within the molecule. This is likely due to the SAR being based on alkane reactivity, which is significantly altered in esters and other oxygenated molecules. Furthermore, the number of parameters used within the SAR had to be expanded in this work to capture the dependence of the adjacent R group on formate reactivity. This work's approach only accounts for the shape of the R group, rather than the size or electron-donating ability. Correlations between the transition state energies and the Zagreb index could be incorporated into a future SAR, which alters the traditional Arrhenius equation. This work altered the Arrhenius equation for substituent factors and SAR calculated rate coefficients through the incorporation of an empirical parameter n . The parameter n has no theoretical meaning. Including parameters that have physical meaning, for example, if they could describe hydrogen-bonding influences, would likely lead to a more robust SAR capable of accurately predicting overall and site-specific rate coefficients for oxygenated and multifunctional compounds.

Finally, this work proposed alternative SAR approaches, such as implementing topological indices or a machine learning SAR. As group additivity SARs struggle to represent our current understanding of atmospheric chemistry, exploring and developing other approaches is required. Developing SARs that accurately predict the site-specific kinetics of oxygenated and multifunctional compounds is critical to predicting the atmospheric impacts of a molecule. As the oxidation of methyl formate exemplifies, abstraction at different reaction sites can have very different atmospheric impacts.

6.10. Future Works

The lack of site-specific experimental rate coefficients is a key barrier to advancing our understanding of atmospheric chemistry. For molecules whose reaction products are the same regardless of the initial site of attack, there is little benefit in determining site-specific kinetics when the products are known. However, this is not the case for many molecules, as outlined throughout this thesis for the

esters. Studies that focus on experimentally determining the overall kinetics, whilst ignoring site-specific kinetics, do not determine a molecule's atmospheric impact. However, reaction products also need to be known. For the esters, reaction product information often comes from Cl-initiated experiments. Products from Cl-initiated studies have been used in conjunction with OH-initiated site-specific kinetics determined in this work to outline the atmospheric impact of esters. The updated SAR for the esters may be implemented into GEOS-Chem to improve the representation of esters within atmospheric chemical models and more accurately predict concentrations of organic acids. One key barrier to this is understanding the emissions of esters, for which data is limited.

Whilst this work determined the site-specific kinetics for formate abstraction ($k(\text{ROC}(\text{O})\text{-H})$), the site-specific kinetics along the alkyl chain have not been as well characterised. There are still several questions surrounding ester reactivity that could be answered with a few targeted studies:

1. Determination of the site-specific kinetics along the alkyl chain, e.g., in n-propyl formate and further along the chain in n-butyl formate.
2. Comparing the site-specific kinetics along the alkyl chain between analogous formates, acetates, propanoates and butanoates.
3. Determination of OH + n-pentyl formate kinetics to probe whether the long-range effects of the ether group decrease after three carbon atoms.
4. Evaluating the overall and site-specific kinetics of unsaturated esters.

Unsaturated ester kinetics such as methyl methacrylate and allyl acetate were not included in this thesis. However, understanding the competition between OH addition and abstraction and how this is influenced by the ester functionality would significantly advance our understanding of ester reactivity.

Developing a database of evaluated site-specific kinetics for oxygenated molecules and multifunctional compounds would be incredibly beneficial for SAR development. Such a database could be used to train new SAR approaches for example, based on machine learning. A machine learning model developed across a range of oxygenated molecules would be more robust. However, as with any model, it will only be as good as the input data. Expanding the body of literature on

the site-specific kinetics of organic molecules would be advantageous for both further SAR development and our understanding of reactivity.

Chapter 7 Conclusions and future works

Esters are used in a wide range of VCPs and are a proposed sustainable alternative to petrochemical derived VCPs, solvents and chemicals used for energy storage. Whilst there is currently large uncertainty around ester emissions, it is likely they will increase in a net zero world. Understanding ester reactivity is important to model concentrations of carcinogens such as formaldehyde and organic acids such as formic acid, which have important implications for the formation of aerosols and acid rain.

To develop our understanding of ester reactivity, this work began by determining the overall and site-specific kinetics of OH radicals with the smallest ester, methyl formate. The overall rate coefficients were determined in Chapter 3, in excellent agreement with literature studies at 298 K. Overall kinetics determined in this work bridges the gap in the literature between 372 and 876 K. The secondary KIE (k_{OD}/k_{OH}) for methyl formate was observed to be positive, indicating the OH/OD is involved in the transition state. This was confirmed with *ab initio* calculations of the transition state structures and energies by Dr Robin Shannon. Transition state structures for methyl and formate abstraction involve hydrogen bonding interactions. This is particularly true following methyl abstraction which has a ring-like transition state. However, the ring-like structure has an entropic penalty. Consequently, the formate transition state is entropically favoured and found to dominate slightly at room temperature. The overall rate coefficients of deuterated isotopomers of methyl formate decrease with increasing isotopic substitution, as expected according to the KIE. The similar KIE for $\text{CH}_3\text{OC}(\text{O})\text{D}$ and $\text{CD}_3\text{OC}(\text{O})\text{H}$ hints at similar branching ratios for methyl and formate abstraction. Through the overall kinetics of deuterated isotopomers this work also determined the reaction sites in methyl formate are coupled and cannot be viewed as independent of one another.

Chapter 4 used OH and OD yields generated from the internal isomerisation of excited peroxy radicals, $^*\text{OOCH}_2\text{OC}(\text{O})\text{H}$ and $\text{CH}_3\text{OC}(\text{O})\text{OO}^*$ formed following the OH-initiated oxidation of $\text{CH}_3\text{OC}(\text{O})\text{H}$ and $\text{CH}_3\text{OC}(\text{O})\text{D}$ to generate Stern-Volmer

plots. Thermal decomposition of the $\text{CH}_3\text{OC}(\text{O})$ radical formed following formate abstraction is experimentally measured in this work. This provides an update for the MCM which currently predicts $\text{CH}_3\text{OC}(\text{O})$ decomposition at room temperature, neglecting the low NO_x chemistry $\text{CH}_3\text{OC}(\text{O})\text{O}_2$ can partake in. Above 420 K when $\text{CH}_3\text{OC}(\text{O})$ decomposition dominates, Stern-Volmer intercepts are attributed to methyl abstraction, providing experimental site-specific kinetics for the reactions of OH radicals with methyl formate. Furthermore, site-specific kinetics for methyl abstraction are also determined from the isomerisation and decomposition of the thermalised peroxy radical, $\text{OOCH}_2\text{OC}(\text{O})\text{H}$. Excellent agreement between the experimental overall and site-specific kinetics and MESMER predictions, provides confidence in extrapolation of the experimental kinetics down to atmospherically relevant temperatures.

The general methodology used in Chapters 3 and 4 to determine site-specific kinetics has been applied to isopropyl formate in Chapter 5. In isopropyl formate, OH regeneration from the thermalised peroxy radicals occurs at a much lower temperature than in methyl formate. Consequently, formate abstraction was determined at room temperature in good agreement with the study by Pimentel et al. The U-shaped temperature dependence of the overall rate coefficient is attributed to tertiary abstraction which has a negative activation energy, determined via *ab initio* calculations. The flat temperature dependence between 298 and 393 K correlates well with the similar branching ratio for tertiary abstraction determined in this work at 393 K and by Pimentel et al. at 298 K.

The ester kinetics outlined in Chapters 3, 4 and 5 are combined in Chapter 6 alongside further experimental work of the site-specific kinetics of ethyl formate, tertbutyl formate and n-butyl formate. This work clearly demonstrates formate abstraction is dependent on the adjacent R group. Experimental site-specific kinetics are implemented directly into the development of a new ester SAR, leading to significant improvements in predictions of formate reactivity over the current SAR by Jenkin et al. [15]. Despite improvements, this work demonstrates the current group additivity approach is inappropriate for oxygenated molecules whose

reactivity is influenced by hydrogen bonding and exhibits both positive and negative temperature-dependent kinetics.

To fully understand ester reactivity and the influence of R_1 on the reactivity of R_2 ($R_1OC(O)R_2$), a larger body of experimental overall and site-specific kinetics is required. It would be particularly beneficial to investigate longer chain esters which are prevalent in VCPs and likely formed in peroxy radical recombination reactions. Nonetheless, there is still information in the literature which has not been incorporated into the updated SAR in Chapter 6. Utilising the full range of experimental site-specific kinetics of oxygenated molecules in future SAR development will likely provide more accurate predictions of oxygenate reactivity including esters and multifunctional compounds.

Appendix A Equation derivations

A.1. Stern-Volmer Analysis

Stern-Volmer (SV) analysis was initially developed by Otto Stern and Max Volmer to determine the ratio of fluorescence lifetimes and the fluorescence quantum yield in the presence and absence of a fluorescence quencher [146]. An example fluorescent system is shown below (RA.1 – RA.4) where $[F]$ is the ground state of the fluorophore, $[F^*]$ is the fluorophore in the fluorescing state, S_1 , $[Q]$ is the quencher, k_{abs} is the absorption rate coefficient, k_f is the fluorescence rate coefficient, k_{nf} is the rate coefficient from non-fluorescent emission and k_q is the quenching rate coefficient.



$$\frac{d[F^*]}{dt} = k_{abs}[F] - [F^*](k_f + k_{nf} + k_q[Q]) \quad \text{EA.1}$$

Due to continuous irradiation, with $[F]$ always greater than $[F^*]$, a stationary state occurs in which $[F^*]$ is constant. Thus, a steady-state approximation can be used with the loss of $[F^*]$ equal to its production (EA.2). This gives rise to the following equation, EA.3.

$$\frac{d[F^*]}{dt} = 0 \quad \text{EA.2}$$

$$k_{abs}[F] = [F^*](k_f + k_{nf} + k_q[Q]) \quad \text{EA.3}$$

The fluorescence quantum yield, ϕ , is defined by the ratio of emitted to absorbed photons:

$$\phi = \frac{\text{emitted photons } (k_f[F^*])}{\text{absorbed photons } (k_{\text{abs}}[F])} \quad \text{EA.4}$$

Hence, ϕ_Q , the quantum yield with the quencher present is:

$$\phi_Q = \frac{k_f[F^*]}{[F^*](k_f + k_{\text{nf}} + k_q[Q])} = \frac{k_f}{k_f + k_{\text{nf}} + k_q[Q]} \quad \text{EA.5}$$

And without the quencher present, when $[Q] = 0$:

$$\phi_0 = \frac{k_f}{k_f + k_{\text{nf}}} \quad \text{EA.6}$$

This gives rise to the ratio ϕ_0/ϕ_Q - the equation describing the SV plot.

$$\frac{\phi_0}{\phi_Q} = \frac{\frac{k_f}{k_f + k_{\text{nf}}}}{\frac{k_f}{k_f + k_{\text{nf}} + k_q[Q]}} = \frac{k_f + k_{\text{nf}} + k_q[Q]}{k_f + k_{\text{nf}}} = \frac{k_f + k_{\text{nf}}}{k_f + k_{\text{nf}}} + \frac{k_q[Q]}{k_f + k_{\text{nf}}} \quad \text{EA.7}$$

$$\frac{\phi_0}{\phi_Q} = 1 + \frac{1}{k_f + k_{\text{nf}}} k_q[Q] \quad \text{EA.8}$$

SV analysis is commonly used in chemical reactions where the yield of a product, such as OH, is dependent on the extent of quenching. For the reaction of methyl formate with OH the yield of OH is dependent on the competition between collisional stabilisation of RO_2^* and an internal isomerisation and hydrogen abstraction. Using the simplified reaction scheme shown in Figure 3.4, with the yield of OH described as the fraction of OH recycled relative to the amount of OH consumed, the following analytical solution arises.

$$Y_{\text{OH}} = \frac{k_b[\text{RO}_2^*]}{k_a[\text{OH}]} \quad \text{EA.9}$$

$$\frac{d[\text{OH}]}{dt} = -k_a[\text{OH}] + k_b[\text{RO}_2^*] \quad \text{EA.10}$$

$$\frac{d[\text{RO}_2^*]}{dt} = -k_b[\text{RO}_2^*] - k_2[\text{M}][\text{RO}_2^*] + k_a[\text{OH}] \quad \text{EA.11}$$

To obtain the overall solution the differential describing $[RO_2^*]$ needs to be solved, here it is done so using an integrating factor (IF). Following multiplication by the IF the equation can then be integrated with respect to t , time, and finally divided through by the IF.

$$\frac{d[RO_2^*]}{dt} + [RO_2^*](k_b + k_2[M]) = k_a[OH] \quad \text{EA.12}$$

$$IF = \exp^{\int k_b + k_2[M] dt} = \exp^{(k_b + k_2[M])t} \quad \text{EA.13}$$

$$\frac{d(\exp^{(k_b + k_2[M])t} [RO_2^*])}{dt} = \exp^{(k_b + k_2[M])t} k_a[OH] \quad \text{EA.14}$$

$$[RO_2^*] = \frac{1}{k_b + k_2[M]} k_a[OH] \quad \text{EA.15}$$

Substituting this solution into the Y_{OH} :

$$Y_{OH} = \frac{k_b}{k_b + k_2[M]} \quad \text{EA.16}$$

When $[M] = 0$ the Y_{OH} becomes equal to 1. The SV parameter describing the yield in the absence and presence of the quencher thus becomes $1/Y_{OH}$.

$$\frac{Y_0}{Y_Q} = \frac{1}{Y_{OH}} \quad \text{EA.17}$$

$$\frac{1}{Y_{OH}} = \frac{k_b + k_2[M]}{k_b} = 1 + \frac{k_2}{k_b}[M] \quad \text{EA.18}$$

The resulting SV plot is a straight line of $1/Y_{OH}$ against $[M]$, where $[M]$ is the total gas concentration. Yields of OH decrease as a function of $[M]$ due to increasing collisional stabilisation of the excited RO_2^* , k_2 . The SV slope demonstrates the rate at which this collisional stabilisation is occurring whilst the intercept represents the yield of OH at 0 Torr.

A.2. Simple growth and decay derivation

The derivation for the simple growth and decay of OD according to the equations EA.19 – EA.27.

$$\frac{d[\text{OH}]}{dt} = -k_1[\text{OH}] \quad \text{EA.19}$$

$$[\text{OH}] = [\text{OH}]_0 \exp(-k_1 t) \quad \text{EA.20}$$

$$\frac{d[\text{OD}]}{dt} = k_1[\text{OH}] - k_2[\text{OD}] \quad \text{EA.21}$$

$$\frac{d[\text{OD}]}{dt} + k_2[\text{OD}] = k_1[\text{OH}]_0 \exp(-k_1 t) \quad \text{EA.22}$$



Multiplying by the integrating factor, $\exp(k_2 t)$, gives:

$$\exp(k_2 t) d[\text{OD}] = k_1[\text{OH}]_0 \exp((k_2 - k_1)t) dt \quad \text{EA.23}$$

Which integrates to:

$$\exp(k_2 t) [\text{OD}] = \frac{k_1[\text{OH}]_0}{k_2 - k_1} \exp((k_2 - k_1)t) + C \quad \text{EA.24}$$

Now that the integration is done, we find $[\text{OD}]$ as a function of t by dividing through by the integrating factor and solving for C .

$$[\text{OD}] = \frac{k_1[\text{OH}]_0}{k_2 - k_1} \exp(-k_1 t) + C \exp(-k_2 t) \quad \text{EA.25}$$

As $[\text{OD}] = 0$ when $t = 0$,

$$C = \frac{-k_1[\text{OH}]_0}{k_2 - k_1} \quad \text{EA.26}$$

And OD as a function of time is equal to EA.27.

$$[\text{OD}] = \frac{k_1[\text{OH}]_0}{k_2 - k_1} (\exp(-k_1 t) - \exp(-k_2 t)) \quad \text{EA.27}$$

As under this simple scheme, all of the OH is converted into OD , the maximum signal height of OD is equal to the initial concentration of OH , $[\text{OH}]_0$.

A.3. Triexponential equation derived by Dr Mark Blitz according to the scheme in Figure 4.11

$$A = k_{\text{Cl}}$$

$$B = -k_{\text{R}}$$

$$C = k_R$$

$$D = -(k_L + k_D)$$

$$L = -(B + D)$$

$$M = B \times D$$

$$N = [Cl]_0 \times C \times A$$

$$P = 0.5 \times (-L - \sqrt{L^2 - 4M})$$

$$Q = 0.5 \times (-L + \sqrt{L^2 - 4M})$$

$$R = \frac{N}{A^2 - A \times L + M}$$

$$C1 = \frac{Q \times R + A \times R}{P - Q}$$

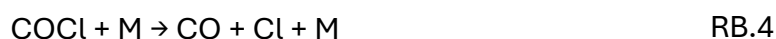
$$C2 = -(C1 + R)$$

$$[OH] = C1 \times \exp(Pt) + C2 \times \exp(Qt) + R \times \exp(-At)$$

Appendix B Supplementary Cl-initiated reactions

B.1 (COCl)₂ as a precursor to Cl

(COCl)₂ was used as the Cl precursor to avoid potential chain branching from the alternative Cl precursor, Cl₂. Cl is produced from (COCl)₂ via reactions RB.1 – RB.4.



Whilst there are no literature studies on the quantum yield of Cl from R1 at 266 nm, Ghosh et al. [147] studied the reaction at 351, 248 and 191 nm. At 351 nm and 248 nm growth in the Cl fluorescence signal following an initial photolytic jump was observed, indicating the secondary production of Cl via formation and subsequent decomposition of thermalised COCl. At 351 nm, they observed a pressure dependence in the total Cl yield, decreasing from 2.17 ± 0.33 at 16 Torr to 1.18 ± 0.17 at 122 Torr. However, no pressure dependence was observed at 193 and 248 nm. Stuhr et al. [148] measured the formation of Cl following the photolysis of (COCl)₂ at 266 and 355 nm. Cl was monitored via the time-resolved formation of HCl which titrated Cl via the reaction of Cl + C₂H₆, which was present in large excess. Cl₂ was also measured directly via PEPICO spectroscopy at the UV of the swiss light source. At 355 nm Stuhr et al. [148] also observed a pressure dependence in the competition between COCl* stabilisation and decomposition. However, at 266 nm no pressure dependence was observed. They determined the rate of COCl decomposition to be $1.79 \times 10^{-14} \text{ cm}^3 \text{ molecule}^{-1} \text{ s}^{-1}$ at 295 K at both 355 and 266 nm with excellent agreement between the two wavelengths. Stuhr et al. [148] also observed the formation of Cl₂⁺ promptly after time zero at 213, 266 and 355 nm which they attributed to direct Cl₂ production from (COCl)₂ photolysis (RB.5).



The direct formation of Cl₂ was first proposed by Huang et al. [149] after observing the direct production of Cl₂ following (COCl)₂ photolysis via cavity ring-down absorption spectroscopy at 248 nm. Whilst Huang et al. [149] observe a direct yield

of 14% at 248 nm, Stuhr et al. observed yields of $(5.0 \pm 1.6)\%$ at 213 nm, $(10.0 \pm 3.3)\%$ at 266 nm and $(5.6 \pm 2.0)\%$ at 355 nm.

Figure B.1 shows Stern-Volmer plots following the typical analysis of OH decay traces via EB.4 and analysis that includes the decomposition of COCl. Individual OH decay analysis accounting for the secondary production of Cl does produce higher OH yields, however, these are within the OH yield errors when no secondary production is accounted for. Without COCl analysis the SV intercept is 1.44 ± 0.21 and with COCl analysis the SV intercept is 1.37 ± 0.24 giving OH yields of 0.69 ± 0.10 and 0.73 ± 0.13 , respectively.

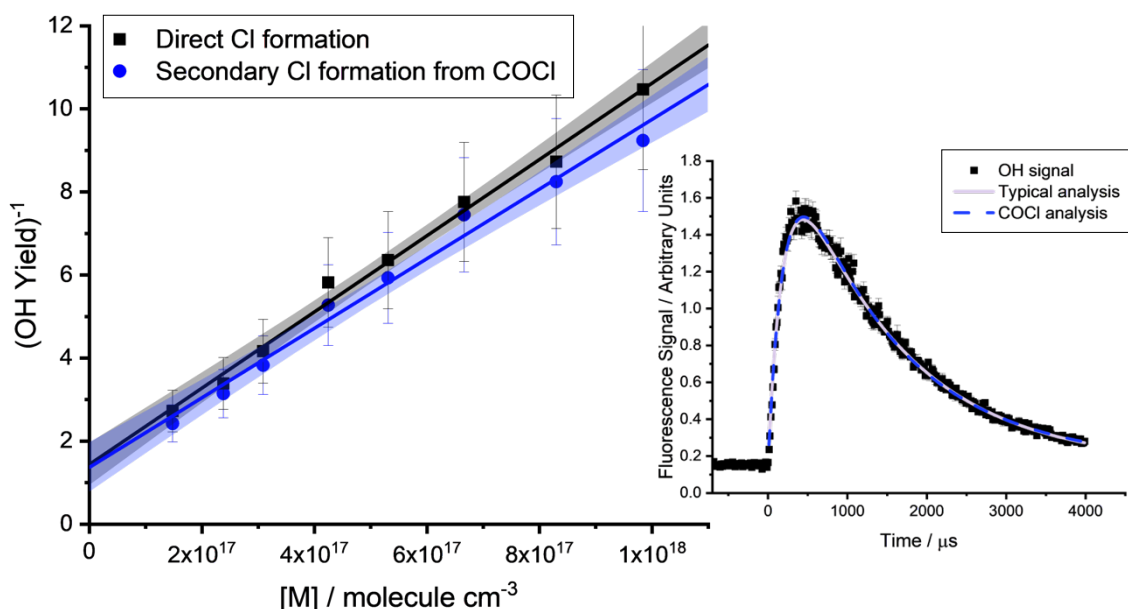


Figure B.1 - Stern-Volmer plots from the Cl-initiated oxidation of methyl formate at 300 K following the analysis of OH traces via two methods; excluding (black) and including (blue) the secondary production of Cl from COCl. The inset shows an example OH trace fit with the two equations.

The pressure-dependent rate for COCl decomposition at 300 K obtained from global analysis is $(1.13 \pm 0.51) \times 10^{-14} \text{ cm}^3 \text{ molecule}^{-1} \text{ s}^{-1}$. Within errors, this agrees with the rate of COCl decomposition determined by Stuhr et al. [148] to be $(1.79 \pm 0.17) \times 10^{-14} \text{ cm}^3 \text{ molecule}^{-1} \text{ s}^{-1}$. However, it is lower than the recommended literature value of $(2.00 \pm 0.40) \times 10^{-14} \text{ cm}^3 \text{ molecule}^{-1} \text{ s}^{-1}$ [150]. The rate of COCl

decomposition determined in this work was only identifiable from one 298 K data set. Despite agreement with the literature, due to difficulties extracting this information from all experimental data and given that these results lie within the experimental errors of analysis excluding COCl decomposition, COCl decomposition has not been accounted for in the following Cl yields. Furthermore, it is likely the fraction of COCl instantaneously decomposing will increase with increasing temperature, reducing the impact of COCl decomposition on the OH and OD yields.

B.2 OH LIF Signal Quenching by Oxygen and Methyl Formate

Bimolecular collisions of electronically excited OH and OD with a quencher such as oxygen or methyl formate remove OH/OD from their electronically excited states leading to a reduction in the $X^2\Pi \rightarrow A^2\Sigma^+$ fluorescence population and consequently the signal of OH/OD. Determining their respective quenching factors is required to account for this removal and obtain accurate experimental yields. For Cl-initiated experiments where the reaction of Cl + tBuOOH is used as a reference, quenching factors of oxygen and methyl formate are required to correct the reference signal obtained in the absence of either molecule. Calibration factors were calculated via EB.1. For oxygen, the OH signal from the photolysis of tBuOOH was used in the absence and presence of up to $\sim 5 \times 10^{16}$ molecule cm^{-3} added oxygen and the quenching factor was determined as the slope of the calibration factors as a function of added oxygen. An example of this is shown in the inset of Figure B.2.

$$\text{Calibration factor} = \frac{\text{OH signal in the absence of oxygen}}{\text{OH signal in the presence of oxygen}} \quad \text{EB.1}$$

Table B.1 – Oxygen quenching factors of OH

Temperature / K	Quenching Factor / $1\text{E}17 \text{ molecule}^{-1} \text{ cm}^3$
300	4.81 ± 0.05
300	4.74 ± 0.07
300	3.53 ± 0.21
300	4.04 ± 0.19
353	4.30 ± 0.19
373	5.00 ± 0.63
393	4.42 ± 0.50
393	3.09 ± 0.11
423	4.88 ± 0.16
448	4.80 ± 0.22

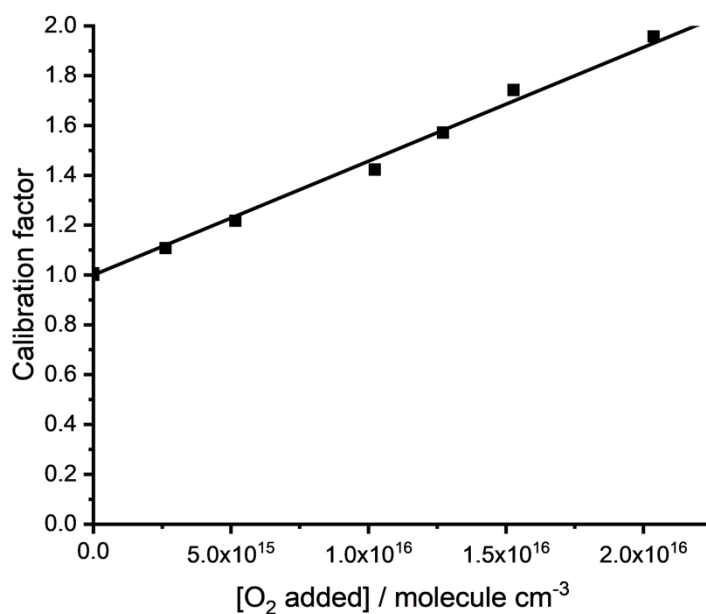


Figure B.2 – An example plot to calculate the quenching factor at 45 Torr and 448 K.

Experiments to determine the oxygen quenching factor were repeated over 298 – 448 K and are shown in Table B.1 and Figure B.3. At low rotational levels, quenching is attributed to anisotropic interactions between OH and the collisional partner. As higher rotational states are accessed with increasing temperatures,

orientational influences are averaged out leading to a decreased likelihood of complex formation, hence a decrease in the collisional cross section and quenching factor [151]. However, as Figure B.3 demonstrates, the experimental quenching rates determined in this work are independent of temperature. The temperature range has been fit with a linear line, with a slope of zero to give an intercept and final quenching factor of $(4.74 \pm 0.07) \times 10^{-17} \text{ cm}^3 \text{ molecule}^{-1}$. EB.2 relates the quenching factor to the rate constant for oxygen quenching, the rate of OH fluorescence and the rate constant for argon quenching. Using a rate coefficient of OH fluorescence of $1.48 \times 10^6 \text{ s}^{-1}$ and rate constant for oxygen quenching of $1.39 \times 10^{-10} \text{ cm}^3 \text{ molecule}^{-1} \text{ s}^{-1}$ both determined by Bailey et al. [152] the experimentally determined

$$\text{Quenching factor} = \frac{k_{\text{qO}_2}[\text{O}_2]}{k_f + k_{\text{qAr}}[\text{Ar}]} \quad \text{EB.2}$$

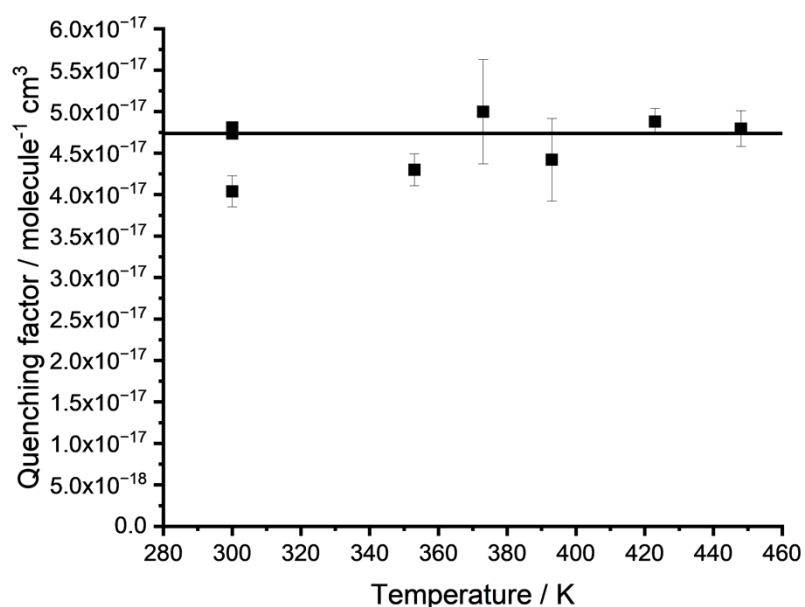


Figure B.3 – Quenching factors of OH by oxygen as a function of temperature.

This is in contrast to the 300 K quenching rate of $(1.17 \pm 0.04) \times 10^{-10} \text{ cm}^3 \text{ molecule}^{-1}$ determined by Kenner et al. [153]. The reason for such large discrepancies between this work and the literature could be due to the integration window. This work did not integrate the whole fluorescence signal potentially leading to an underprediction of the quenching rate in comparison with Kenner et

al. [153]. Additionally, Kenner et al. [153] measured the room temperature quenching rate of OD to be $(0.87 \pm 0.07) \times 10^{-10} \text{ cm}^3$, 25.6% lower than quenching of OH. As demonstrated in the inset of Figure B.4, this work observed similar quenching rates for OH and OD.

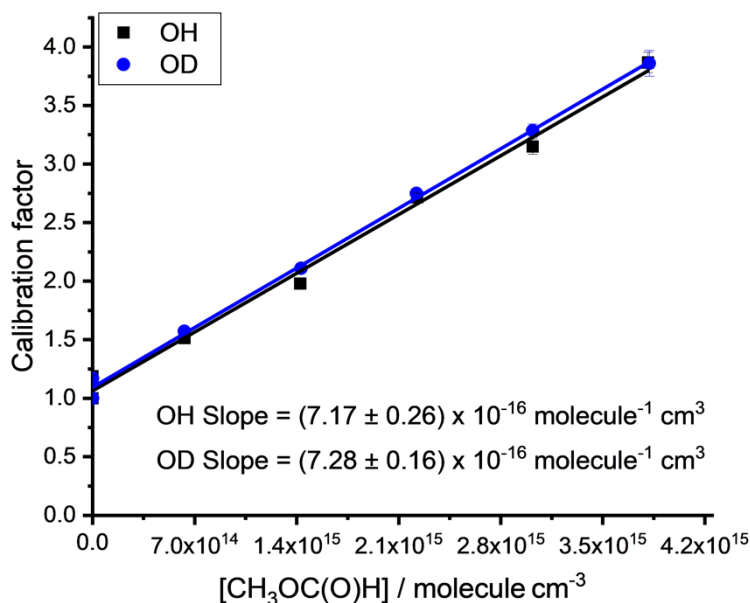


Figure B.4 – An example plot where the quenching factor of OH and OD by $\text{CH}_3\text{OC}(\text{O})\text{H}$ was calculated at 47 Torr and 573 K. There is good agreement between OH and OD indicating a global calibration factor can be used for both LIF signals.

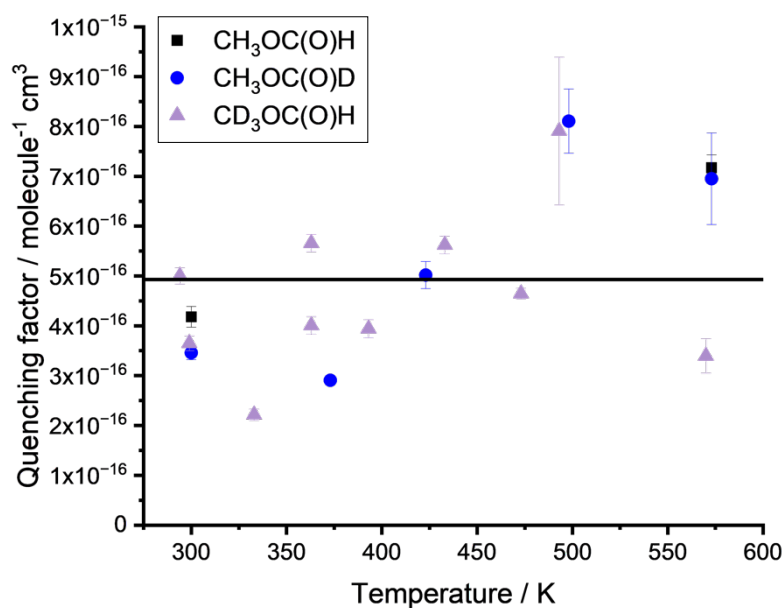
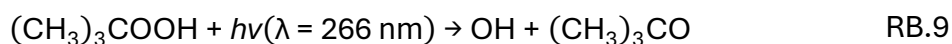
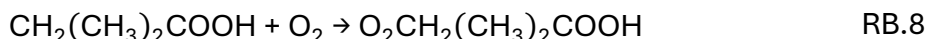
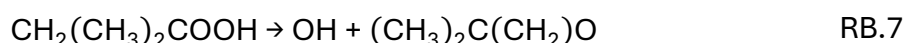


Figure B.5 – Quenching factors of OH by $\text{CH}_3\text{OC}(\text{O})\text{H}$, $\text{CH}_3\text{OC}(\text{O})\text{D}$ and $\text{CD}_3\text{OC}(\text{O})\text{H}$ as a function of temperature.

Experiments to determine the methyl formate quenching factor were conducted over 294 – 573 K. A temperature-independent quenching factor was calculated from the three methyl formate isotopomers, CH₃OC(O)H, CH₃OC(O)D and CD₃OC(O)H, to be $(4.93 \pm 0.43) \times 10^{-16}$ molecule cm⁻³. Figure 4 demonstrates, the quenching factor is the same for both OH and OD. Increased scatter in the methyl formate quenching factors is likely due to the larger timeframe in which experiments were conducted. Over the longer timeframe, it is possible that small undocumented changes in the signal integration window may have occurred, leading to a variation in the total OH signal and hence variation in the rate of OH quenching by methyl formate. The quenching factors of oxygen and methyl formate are used to calculate the yields of OH and OD from the Cl-initiated experiments of methyl formate and its deuterated isotopomers, where the reference signal of tBuOOH is obtained in the absence of oxygen and methyl formate.

B2.3 Branching ratio for the reaction of Cl + (CH₃)₃COOH

Cl-initiated oxidation of tBuOOH proceeds via hydrogen abstraction from a methyl (RB.6a) or the peroxide group (RB.6b). Hydrogen abstraction from the peroxide group does not lead to the production of OH. However, methyl abstraction produces a QOOH species which decomposes to OH (RB.7) rapidly over a 52.3 kJ mol⁻¹ barrier in competition with an addition reaction with oxygen (R8) [154, 155].



If the branching ratio for the reaction of Cl + tBuOOH is known, the production of OH following methyl abstraction can be used as an OH signal reference. An example OH trace following the Cl + tBuOOH reaction is shown in Figure B.6, demonstrating the instantaneous OH production via RB.9 and OH growth via RB.6a and RB.7. The signal height from OH growth is a good reference to quantify yields of OH from the Cl-initiated oxidation of methyl formate isotopomers; OH

production from $\text{Cl} + \text{tBuOOH}$ is pressure-independent, a requirement to determine how OH/OD yields from the isotopomers of methyl formate were changing with pressure. Furthermore, this reference calibrated the chlorine concentration delivered to the cell. Using the pressure-independent photolytic production of OH it was confirmed that the chlorine concentration was found to increase with increasing pressure, likely due to a decrease in contact with the metal pipework as the pressure increased. An example of this is shown in the inset of Figure B.6.

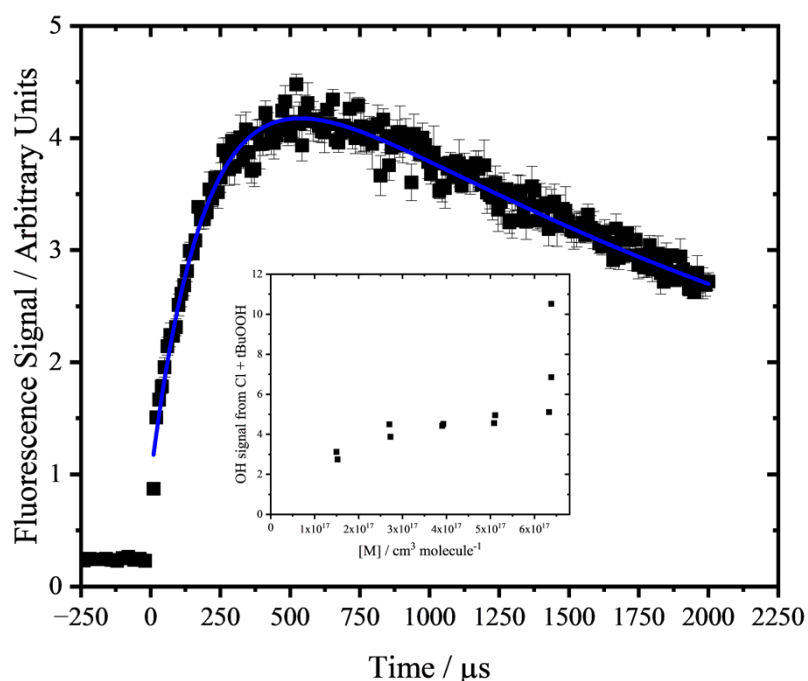
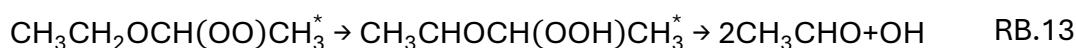
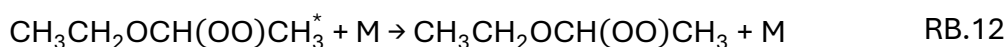
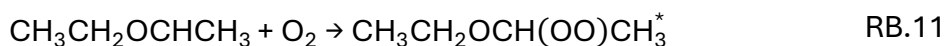
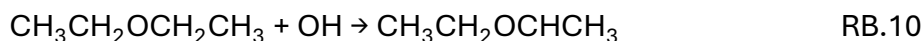


Figure B.6 – Example OH decay in the presence of 9.37×10^{13} molecule cm^{-3} of $(\text{COCl})_2$, 2.36×10^{16} molecule cm^{-3} of tBuOOH and 3.93×10^{17} molecule cm^{-3} of argon.

The branching ratio for methyl abstraction by Cl from tBuOOH (RB.6a), is quantified via another reference, the Cl-initiated oxidation of diethyl ether (R10). OH is produced with a 100% yield at zero pressure, via RB.10 – RB.13 [156].



The yield of OH from diethyl ether is determined via the change in reaction rate in the absence and presence of oxygen, as outlined above, to give a reference for the experimental pressure. The branching ratio for the reaction of Cl with tBuOOH is then determined via EB.3.

$$\text{Cl} + \text{tBuOOH ratio} = \text{DEE OH yield at [M]} \times \frac{\text{OH signal from Cl+tBuOOH}}{\text{OH signal from Cl+DEE}} \quad \text{EB.3}$$

Table B.2 – Branching ratios for the reaction of Cl with (CH₃)₃COOH. At 294 K the average is 0.18 ± 0.03 and at 423 K 0.32 ± 0.06, errors are at the 1 σ level.

Temperature / K	Branching ratio
294	0.18 ± 0.03
294	0.15 ± 0.03
294	0.21 ± 0.04
423	0.40 ± 0.09
423	0.43 ± 0.01
423	0.27 ± 0.01
423	0.31 ± 0.01
423	0.29 ± 0.02
423	0.32 ± 0.02

Branching ratio results at 294 and 423 K are shown in Figure B.7. The room temperature branching ratio determined in this work for hydrogen abstraction by Cl at the methyl site of tBuOOH ((CH₃)₃COOH) is 0.18 ± 0.03 in excellent agreement with 0.15 ± 0.2 determined by Zador et al. [155]. This is congruous with the bond dissociation enthalpies; the O-H bond (85 ± 2 kcal mol⁻¹) is weaker than the C-H bond (~ 101 kcal mol⁻¹) suggesting abstraction from this site will dominate. Whilst there is excellent agreement with the literature, yields determined in this work were not conducted at the high-pressure limit for QOOH thermal decomposition, and at 423 K, 2.83 × 10¹⁵ molecule cm⁻³ of oxygen was present. Using the rates outlined in Zador et al. [155] competition from QOOH + O₂ (R20) has a rate of 1700 s⁻¹ compared to a rate of 22000 s⁻¹ for QOOH decomposition to OH (the reaction of interest) at 8.9 Torr, the 423 K experimental pressure. Therefore, the fraction of QOOH going to OH

with 2.83×10^{15} molecule cm^{-3} of oxygen present is $22000/23700 = 0.928$. If no oxygen was present, the amount of QOOH decomposing to OH would be larger than observed by $1/0.928 = 1.077$. So, the yield of OH in the absence of any oxygen is equal to the yield of OH observed in the presence of oxygen multiplied by 1.077. This increases the 18% yield observed to 19.4% (18×1.077), remaining within the statistical uncertainties.

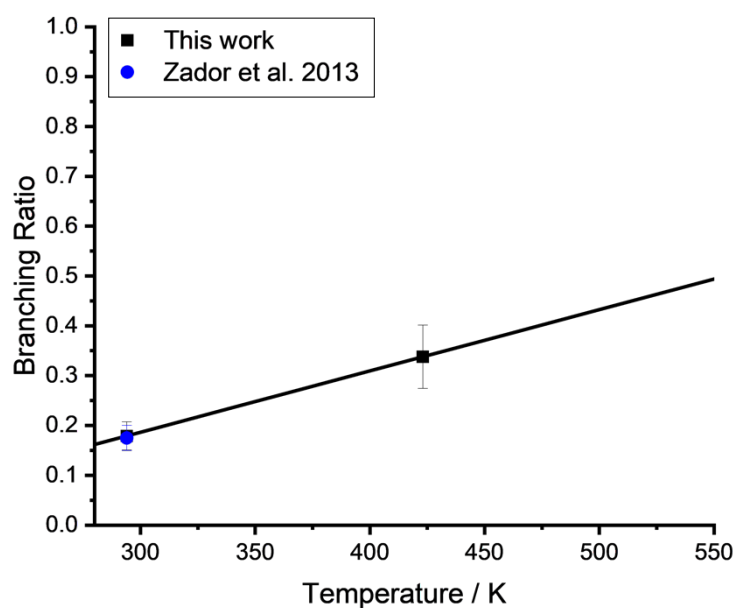


Figure B.7 – Temperature dependent branching ratios for methyl abstraction from the Cl-initiated oxidation of tBuOOH.

Appendix C Chapter 4 supplementary Information

C1 $k(\text{R}+\text{O}_2)$ bimolecular plot at 398 K

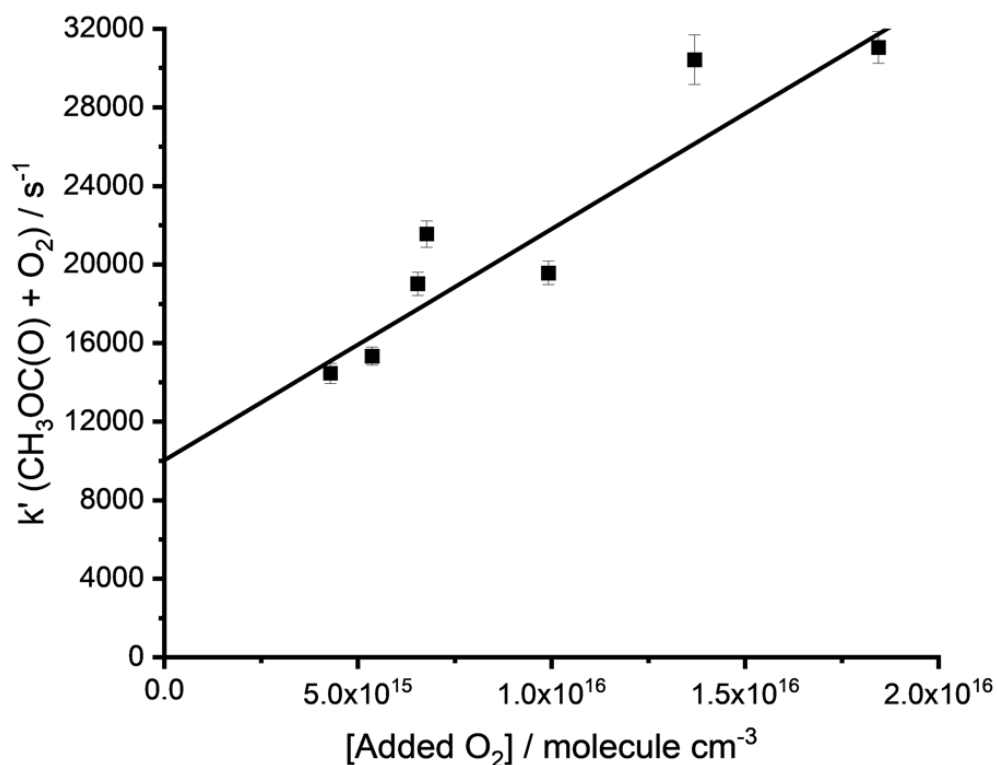


Figure C.1 – Bimolecular plot for $k(\text{CH}_3\text{OC}(\text{O}) + \text{O}_2)$ at 398 K. Individual points on the bimolecular plot are determined from individual analysis of OH decays, whose data are shown in Figure C2. The intercept is $10,031 \pm 1786 \text{ s}^{-1}$, approximately equivalent to the rate of $\text{CH}_3\text{OC}(\text{O})$ decomposition. The slope is $(1.18 \pm 0.21) \times 10^{-12} \text{ cm}^3 \text{ molecule}^{-1} \text{ s}^{-1}$, the bimolecular rate coefficient for $k(\text{CH}_3\text{OC}(\text{O}) + \text{O}_2)$ at 398 K. Global fits are shown in Figure C.2.

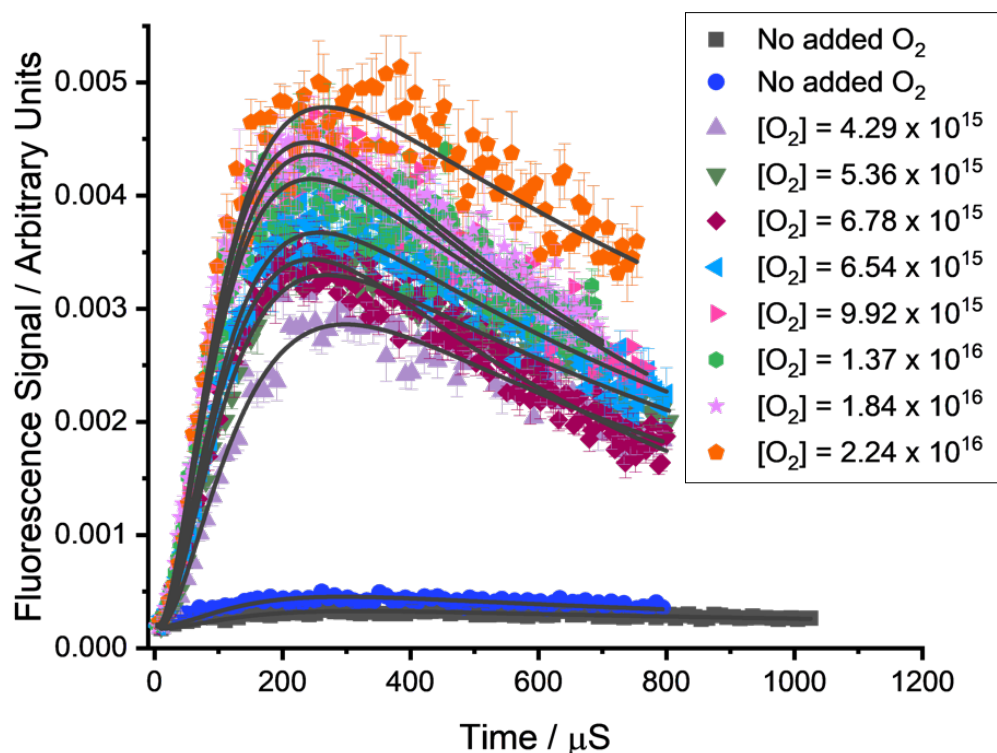


Figure C.2 – Each trace of OH following the reaction of Cl + CH₃OC(O)D has been fit globally at 398 K to determine the bimolecular rate coefficient for $k(\text{CH}_3\text{OC(O)} + \text{O}_2)$, equal to $(1.18 \pm 0.29) \times 10^{-12} \text{ cm}^3 \text{ molecule}^{-1} \text{ s}^{-1}$, in excellent agreement with the individual analysis presented in Figure C.1.

C2 OD trace analysis following the OH and Cl-initiated oxidation of CH₃OC(O)D

OD traces were analysed according to the simple scheme outlined above in Appendix B. However, more complex schemes were tested to ensure $k(\text{R} + \text{O}_2)$ and OD regeneration from the thermalised RO₂, OCH₂OC(O)D, did not interfere with the OD decay. Figure C.3 illustrates analogous OH and OD decays collected under the same experimental conditions and demonstrates excellent agreement between the analytical solution outlined in Appendix B and a MATLAB-derived numerically integrated fit according to the same scheme.

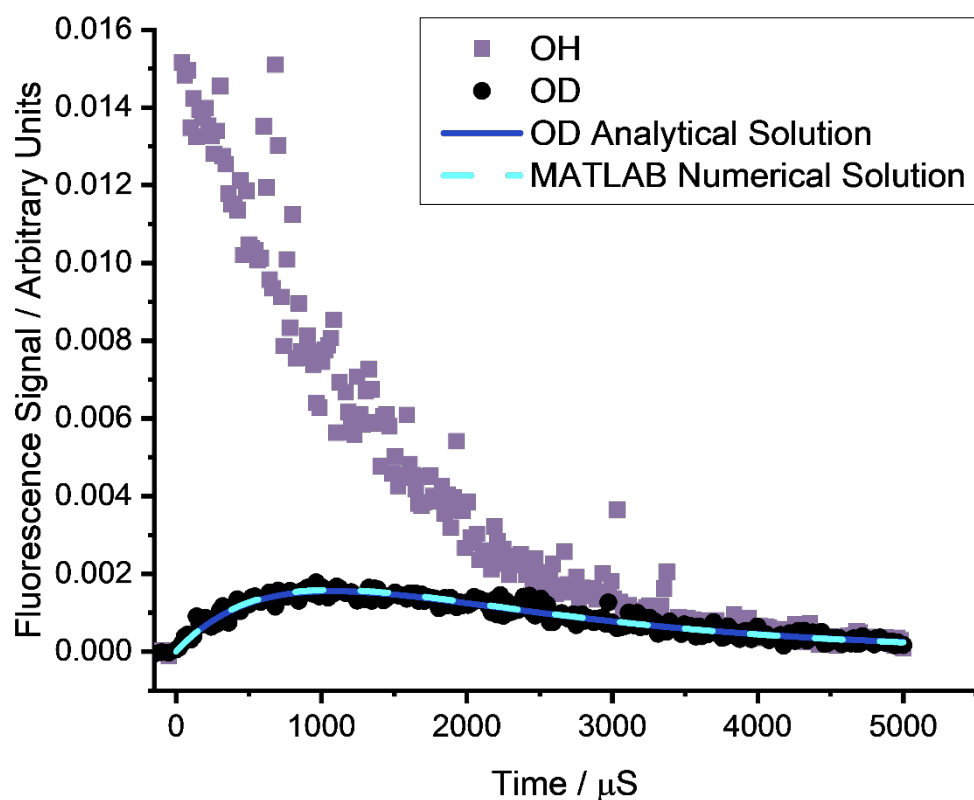


Figure C.3 – OH and OD decays measured at 298 K. The solid blue line through the OD decay is an analytically derived scheme for EC.1 – EC.2. The cyan dashed line is the MATLAB numerically integrated equivalent.

The MATLAB numerical integration OD fit shown in Figure C.3 accounts for a simple growth (EC.1) and decay (EC.2).



More complex schemes tested included accounting for the regeneration of OD via the formation of an excited peroxy radical (RO_2^*). EC.3 – EC.6 illustrate the scheme and Figure C.4 presents the fit with the pink dotted line.



The other scheme tested was EC.3 – EC.5 and EC.6, testing the cycling of OD reacting with $\text{CH}_3\text{OC}(\text{O})\text{D}$ to regenerate RO_2^* which can subsequently regenerate OD again via EC.4.

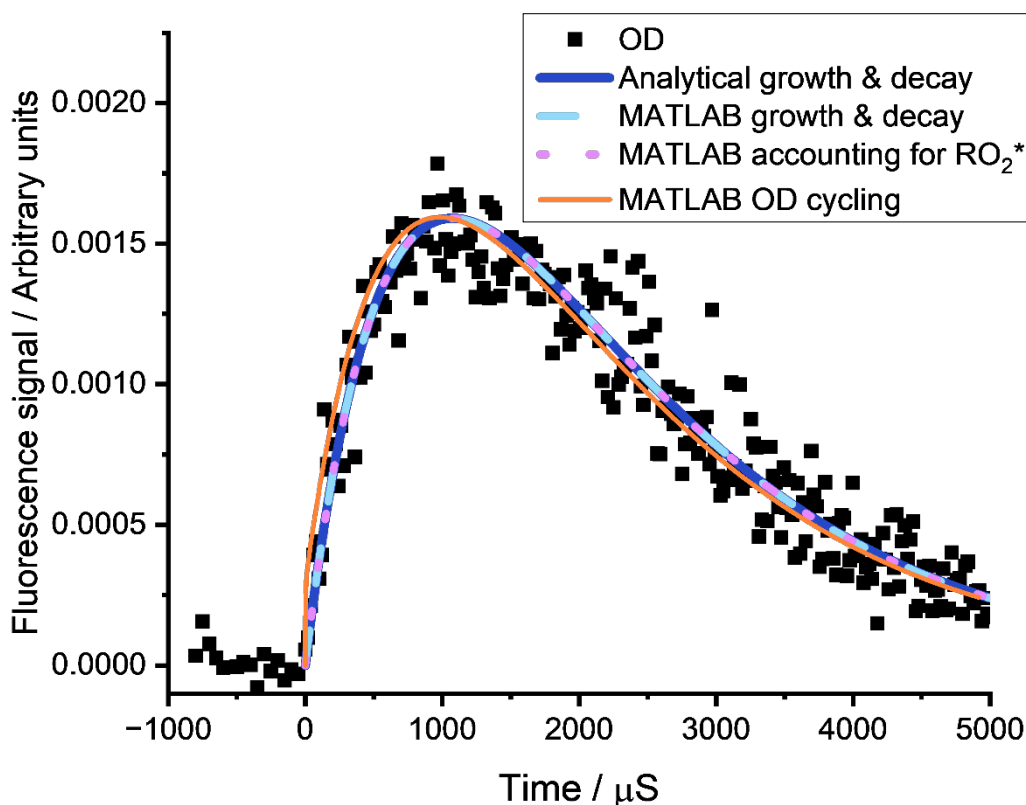


Figure C.4 – The analytical scheme is shown with the blue solid line, the MATLAB equivalent scheme is shown in the cyan dashed line, the MATLAB scheme accounting for production of the excited peroxy radical is shown in the pink dotted line and the MATLAB scheme accounting for OD to regenerate RO_2^* is shown in solid orange.

C3 OH and OD yields following the Cl-initiated oxidation of $\text{CH}_3\text{OC}(\text{O})\text{D}$

Following Cl-initiated experiments, both OH and OD yields, were determined by comparing their respective signal heights once corrected for quenching by oxygen and methyl formate (Appendix B) and referenced against the signal height of OH from tBuOOH, corrected for the Cl + tBuOOH branching ratio (Appendix B). OH and OD yields are presented in Figure C.5.

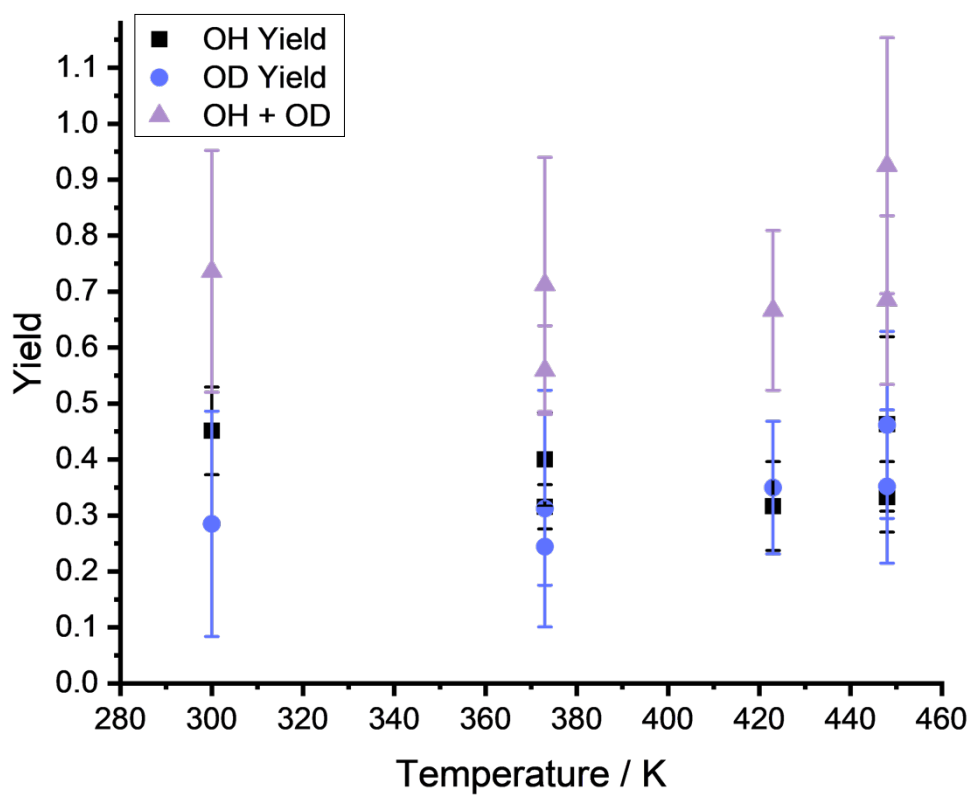


Figure C.5 – OH and OD yields following the Cl-initiated oxidation of CH₃OC(O)D. The yield sum is less than 1, which is likely due to a systematic underrepresentation of OD yields.

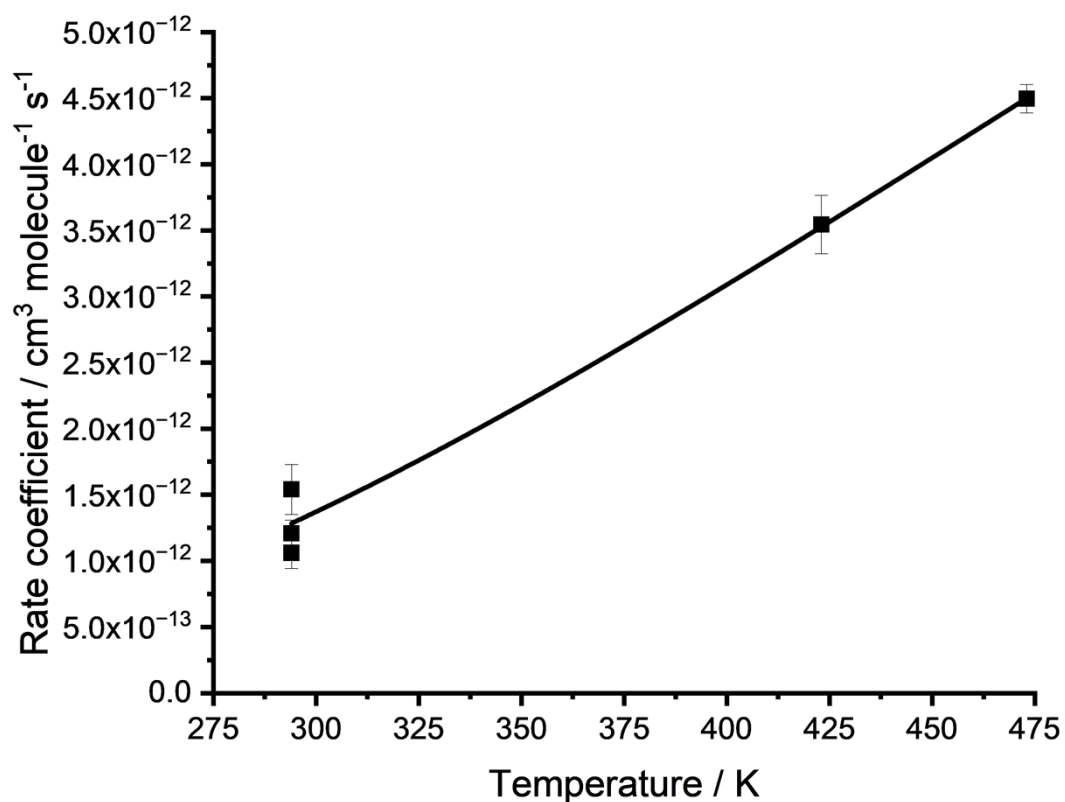


Figure C.6 - Limited experiments determined the overall kinetics of Cl + CH₃OC(O)D, at 294, 423 and 473 K. The fitted line is an Arrhenius temperature-dependent fit:

$$k(\text{Cl} + \text{CH}_3\text{OC}(\text{O})\text{D}) = \left((3.53 \pm 0.51) \times 10^{-11} \right) \times \exp \left(\frac{8098 \pm 522}{RT} \right)$$

C4 MESMER fits to the OH and OD yields from the OH-initiated oxidation of CH₃OC(O)H and CH₃OC(O)D

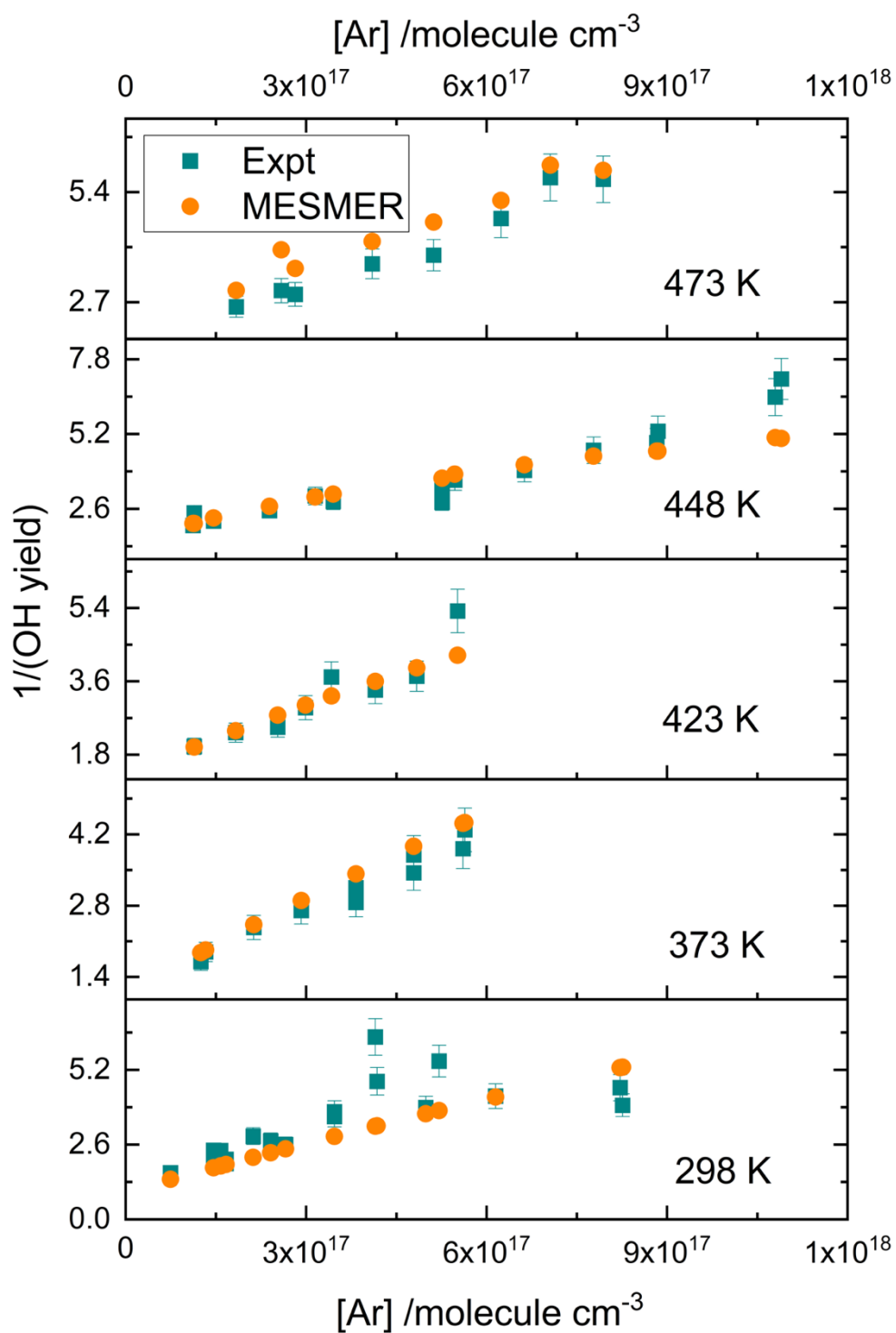


Figure C.7 – MESMER predicted OH yields are shown in orange circles alongside the experimental OH yields (cyan squares) presented in Chapter 4.

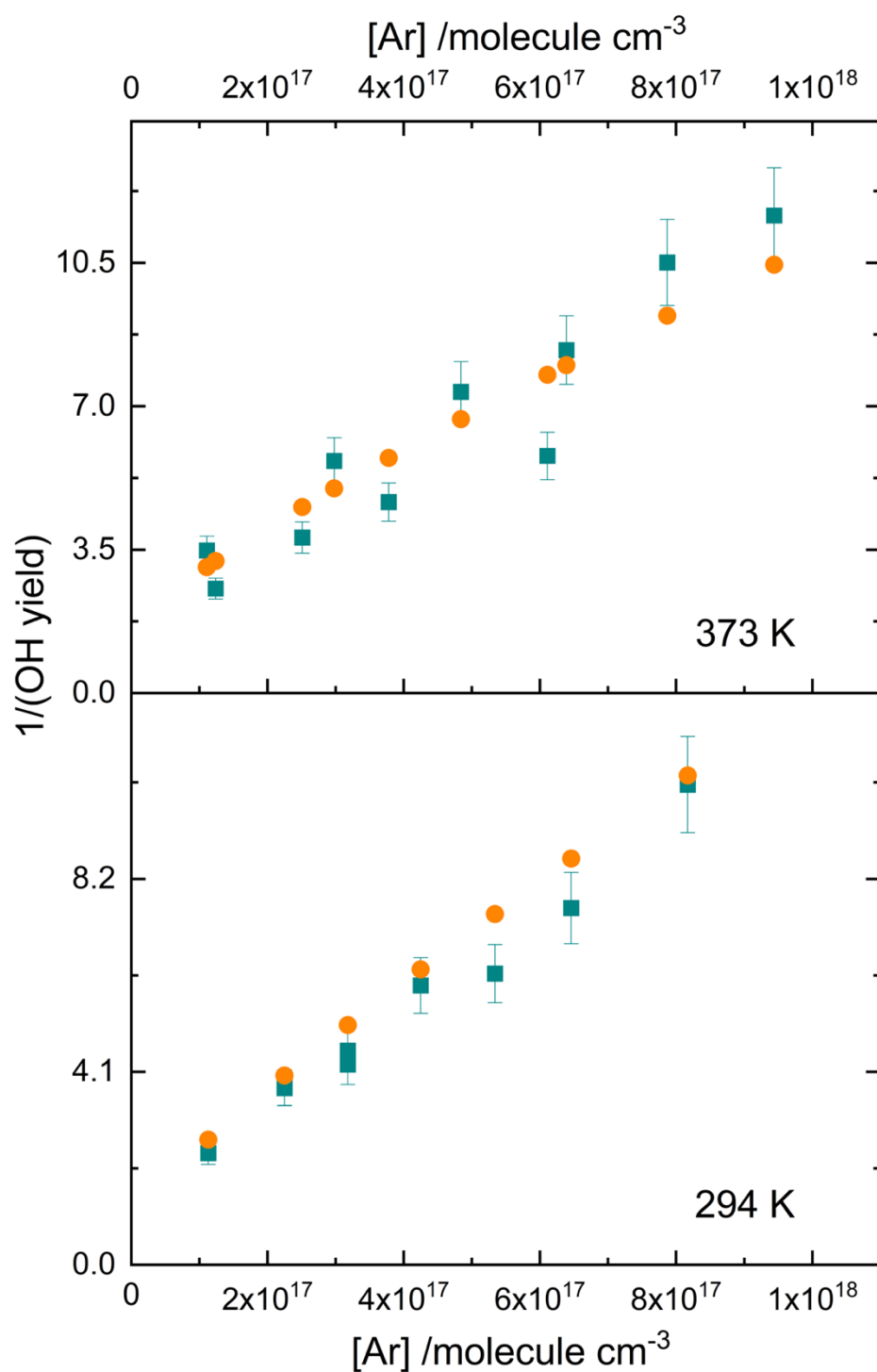


Figure C.8 – OH yields following the OH-initiated oxidation of $\text{CH}_3\text{OC}(\text{O})\text{D}$, representing the competition between the internal isomerisation and collisional stabilisation of the $\text{CH}_3\text{OC}(\text{O})\text{OO}^*$ peroxy radical formed following formate abstraction. MESMER predicted OH yields are shown in orange circles alongside the experimental OH yields (cyan squares) presented in Chapter 4.

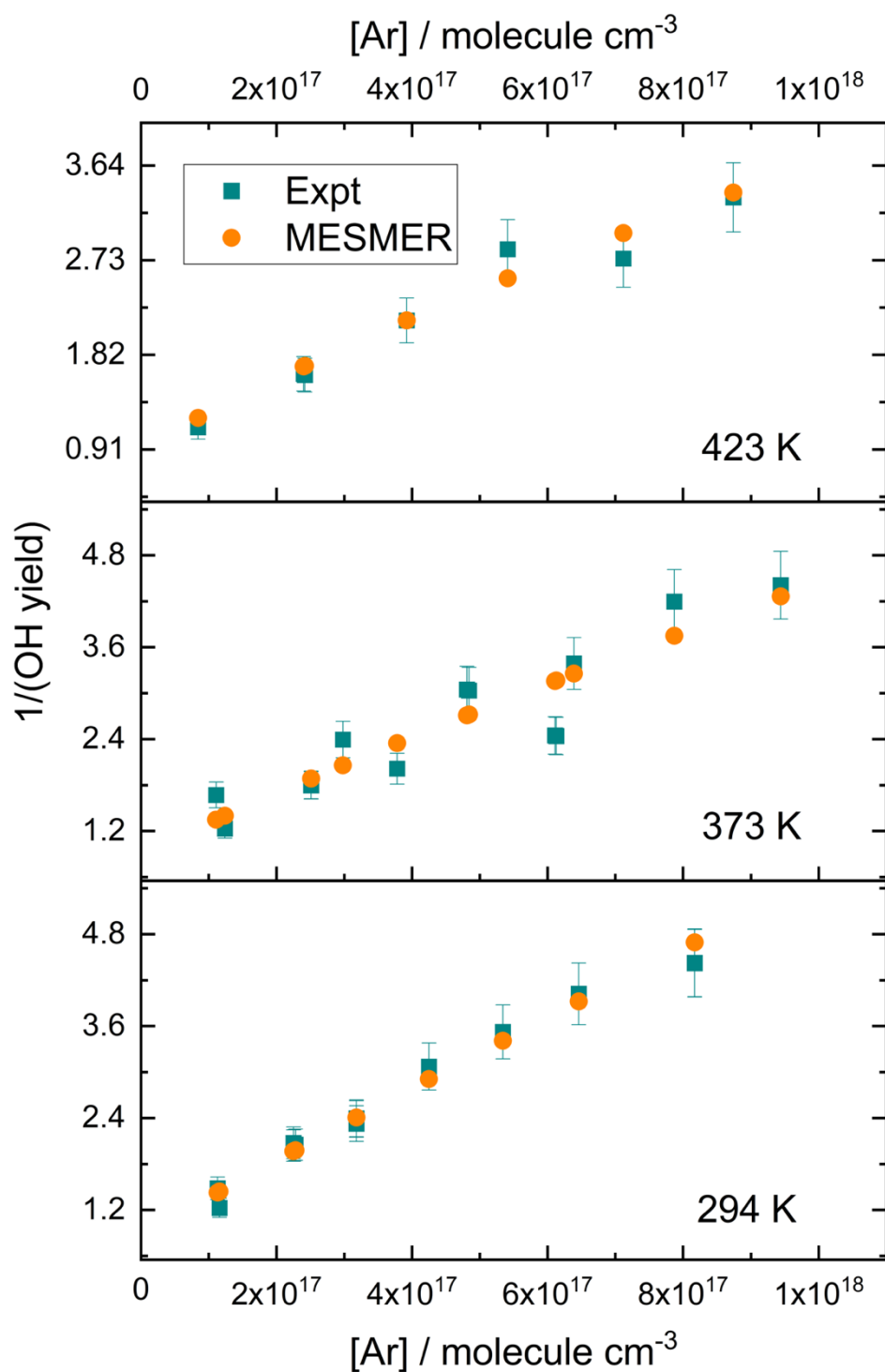
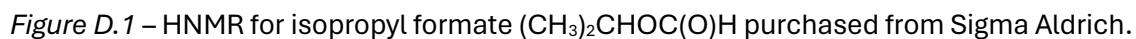


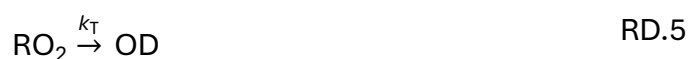
Figure C.9 – OD yields following the OH-initiated oxidation of $\text{CH}_3\text{OC}(\text{O})\text{D}$, representing the competition between the internal isomerisation and collisional stabilisation of the $\text{CH}_3\text{OC}(\text{O})\text{OO}^*$ peroxy radical formed following methyl abstraction. MESMER predicted OD yields are shown in orange circles alongside the experimental OH yields (cyan squares) presented in Chapter 4. The y-axis is labelled incorrectly and should say $1/(\text{OD yield})$.

D1 NMR Data for purchased and synthesised (CH₃)₂CHOC(O)H and synthesised (CH₃)₂CHOC(O)D – with thanks to Alex Heyam for running the NMRs



D2 Analysis of OD traces following the reactions of OH/OD + (CH₃)₂CHOC(O)D at 433 K and above

At 392 K, OD decays become biexponential. OD is regenerated following the internal isomerisation of a peroxy radical ((CH₃)₂C(OO)OC(O)D) that abstracts from the deuterated site to form QOOH (CH₃)₂C(OOD)OC(O)), followed by decomposition to OD. Both the OH and OD initiated reactions of (CH₃)₂CHOC(O)D lead to the production of OD via the isomerisation of (CH₃)₂C(OO)OC(O)D. The mechanism for OD production can be simplified and represented by reactions RD.1 – RD.5.



At 433 K the kinetics of OH/OD + (CH₃)₂CHOC(O)D were determined at 127 Torr with concentrations of (CH₃)₂CHOC(O)D varied between 1.90×10^{14} – 1.48×10^{15} molecules cm⁻³. The OD trace at 1.48×10^{15} molecules cm⁻³ is shown in Figure D.4 and appears prolifically biexponential. A biexponential fit is shown in Figure D.4 and the yield of OD regenerated from this fit is calculated to be 0.89 ± 0.16 . However, the trace in Figure D.5 at 1.90×10^{14} , where OD + (CH₃)₂CHOC(O)D is occurring on a slower time scale highlights complexity in the OD trace that a simple biexponential fit does not capture.

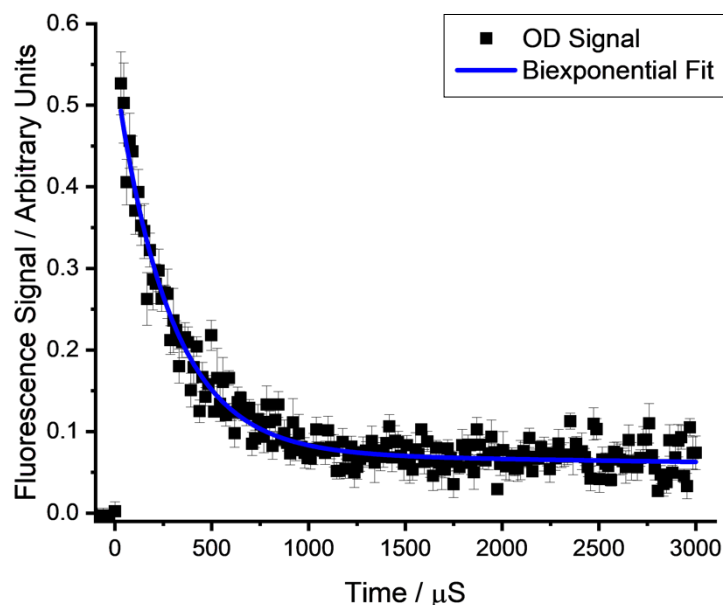


Figure D.4 - OD decay at 433 K, 127 Torr and $(\text{CH}_3)_2\text{CHOC}(\text{O})\text{D} = 1.48 \times 10^{15} \text{ molecules cm}^{-3}$.

The experiments at 433 K begin with a starting ratio of OH/OD of 4.18/0.89 calculated from comparative traces of OH and OD in the absence of isopropyl formate. The OH and OD initiated oxidation of isopropyl formate is occurring simultaneously within the reaction cell and both reactions lead to the production of OD. As the initial starting concentration of OH is much larger than OD, this is leading to the production of more OD than is initially delivered at time zero ($[\text{OD}]_t > [\text{OD}]_0$). Fitting the OD traces in MATLAB according to the scheme outlined in RD.1 – RD.5 produces a much better fit than a biexponential fit, as demonstrated in Figure D.5. In the MATLAB fitting, the initial concentration of OH and the rate of k_{OH} is fixed at the values determined by fitting the analogous OH decay in Origin with a single exponential. The production of OD from the OH and OD initiated reactions is assumed to be equal. However, there may be subtle differences in the branching ratios of the two reactions. Incorporating separate recycling parameters would double the number of parameters in the MATLAB fitting, which may increase the error / reduce the meaning of the results.

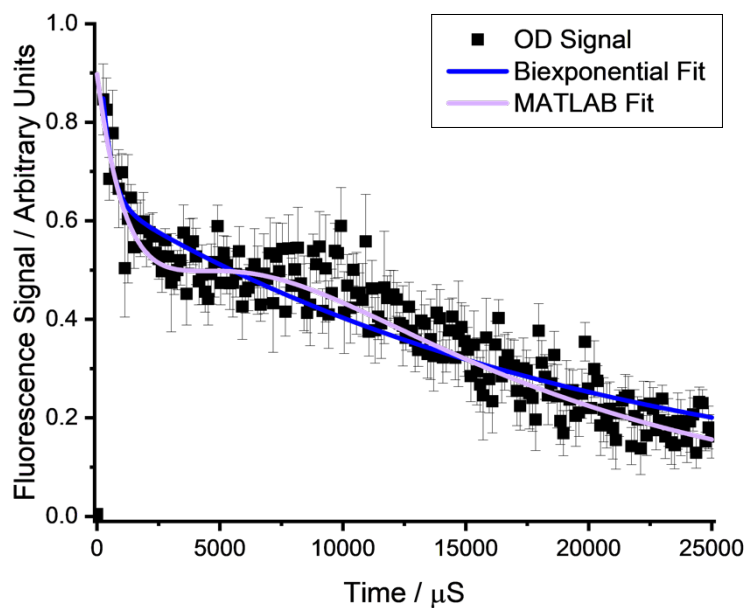


Figure D.5 - OD decay at 433 K, 127 Torr and $(\text{CH}_3)_2\text{CHOC}(\text{O})\text{D} = 1.90 \times 10^{14} \text{ molecules cm}^{-3}$.

Figure D.6 shows the bimolecular plot for the reactions of OH and OD with $(\text{CH}_3)_2\text{CHOC}(\text{O})\text{D}$ at 433 K. OH pseudo-first order rates are determined from single exponential fits within Origin, whilst OD pseudo-first order rates are determined from MATLAB fitting, as outlined above. Whilst the Origin fitting produces errors at a single standard deviation, MATLAB fitting does not. Unweighted fits produce $k_{\text{OH}} = (1.85 \pm 0.07) \times 10^{-12} \text{ cm}^3 \text{ molecule}^{-1} \text{ s}^{-1}$ and $k_{\text{OD}} = (2.07 \pm 0.09) \times 10^{-12} \text{ cm}^3 \text{ molecule}^{-1} \text{ s}^{-1}$.

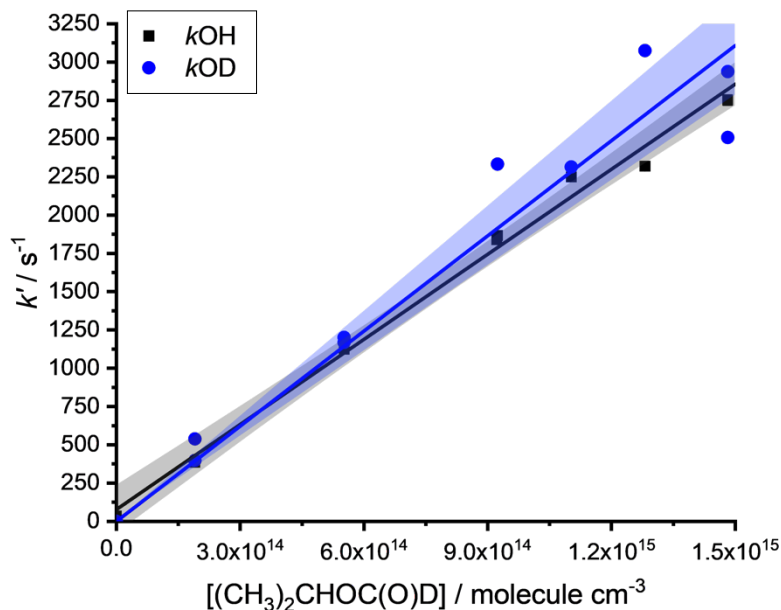


Figure D.6 – Bimolecular plot for the reactions of OH (black squares) and OD (blue circles) with $(CH_3)_2CHOC(O)D$ at 433 K and 127 Torr. Shading represents the 95% confidence limits.

Similar to experiments at 433 K, the abnormal behaviour of the OD traces at 473 K is most notable at low concentrations of $(CH_3)_2CHOC(O)D$. At low concentrations of $(CH_3)_2CHOC(O)D$, the rate of OD regeneration becomes competitive with the initial $OD + (CH_3)_2CHOC(O)D$ reaction and can therefore be seen visually as both processes are occurring on a similar timescale. At higher concentrations of $(CH_3)_2CHOC(O)D$, when $OD + (CH_3)_2CHOC(O)D$ is much faster than OD regeneration, OD traces appear more “normal” and could be mistaken for simple biexponentials. This effect highlights the importance of determining bimolecular rate coefficients over a substantial range of reactant concentrations. If experiments had not been conducted at low concentrations of isopropyl formate, the kinetic traces may have been mistaken for biexponentials leading to inaccurate determinations of the rate coefficient and yields of OD regenerated. At 473 K, the regeneration of OD is occurring on a faster timescale, such that it is being produced faster than it can be consumed. This leads to a “growth” in the OD time profile following an initial decay. An example is shown in Figure D.7.

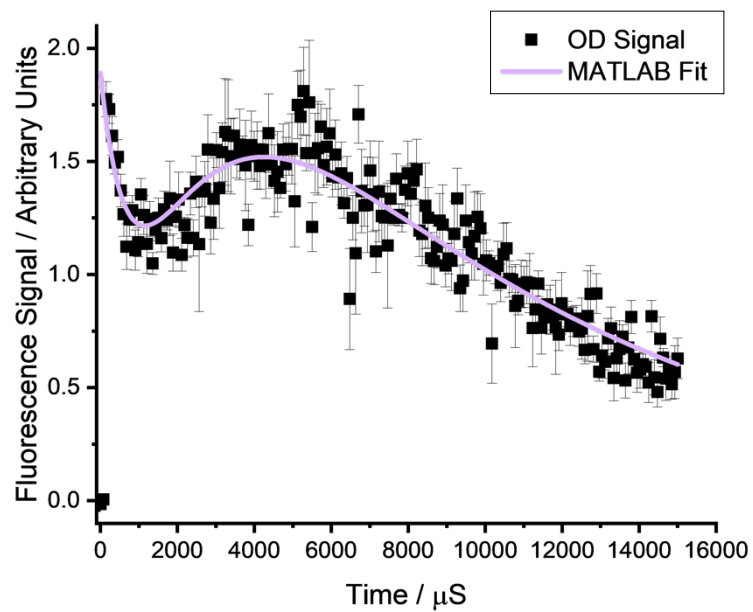


Figure D.7 - OD decay at 473 K, 120 Torr and $(\text{CH}_3)_2\text{CHOC}(\text{O})\text{D} = 3.84 \times 10^{14} \text{ molecules cm}^{-3}$.

Appendix E The overall and site-specific kinetics of ethyl formate, tertbutyl formate and n-butyl formate

E1 Ethyl formate

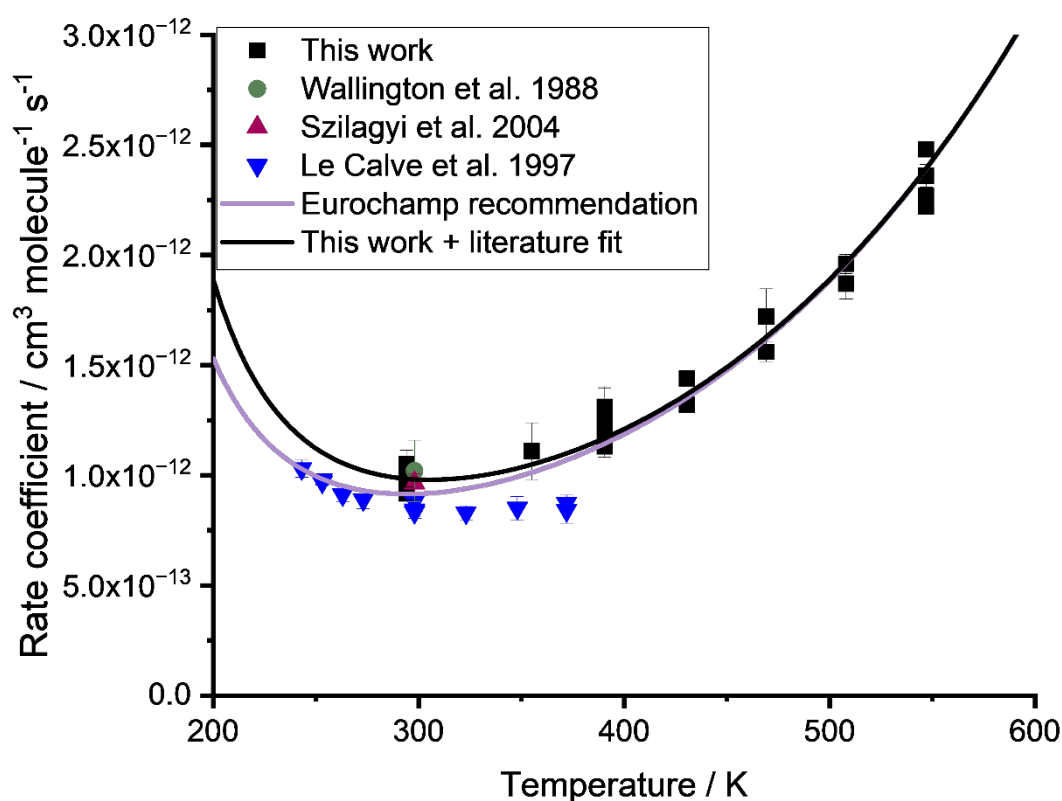


Figure E.1 – The overall kinetics of OH + ethyl formate, determined by Dr Lavinia Onel (black squares), alongside literature studies and the recommendation by Eurochamp (purple solid line). The black solid line is a non-Arrhenius temperature-dependent fit to the data shown in the Figure and is used in SAR development in Chapter 6.

The site-specific rate coefficients were also determined via studies of OH + ethyl formate and its deuterated isotopomer $\text{CH}_3\text{CH}_2\text{OC}(\text{O})\text{D}$. As discussed in Chapters 4 and 5 for methyl formate and isopropyl formate, the reaction of OH + ethyl formate also regenerates OH from the internal isomerisation and subsequent decomposition of RO_2 radicals. As with the methyl and isopropyl systems, OH can come from the excited RO_2^* or the thermalised RO_2 . Above 390 K, $\text{CH}_3\text{CH}_2\text{OC}(\text{O})$ decomposes. Consequently, the Stern-Volmer intercepts can be attributed to

abstraction from the CH₃ and/or the CH₂ reaction site. Branching ratios for formate abstraction are presented in Figure 6.14 from both the Stern-Volmer intercepts and the thermalised RO₂ radical(s).

E2 tertButyl formate

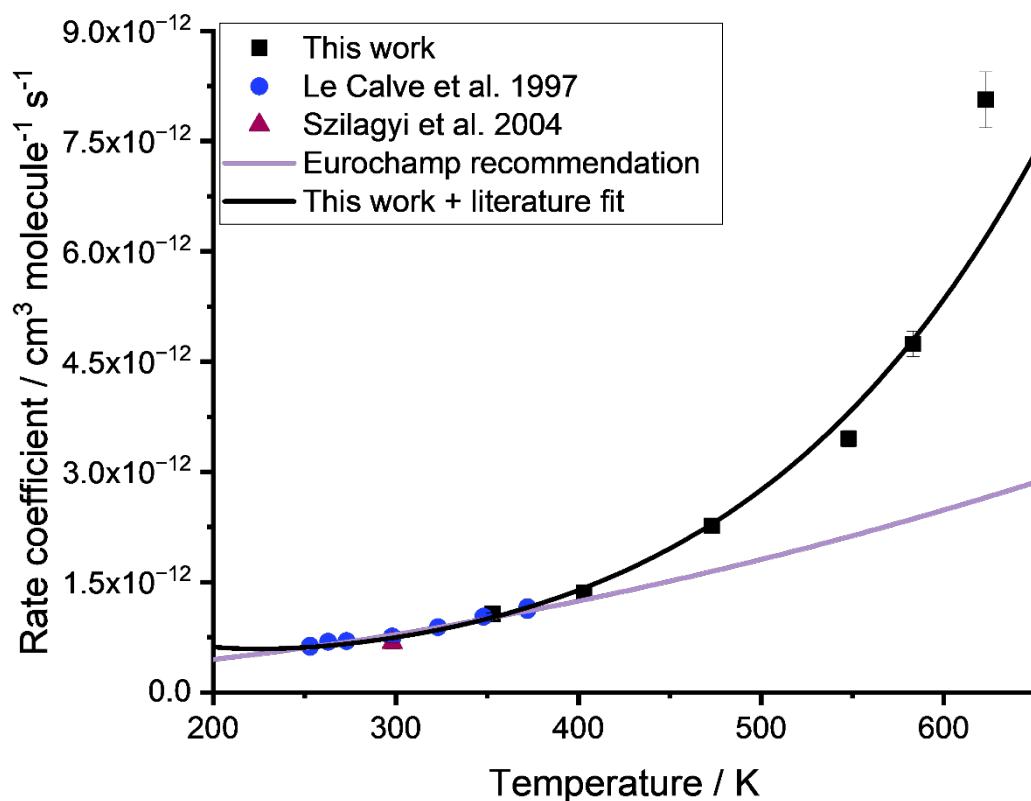


Figure E.2 – The overall kinetics of tertbutyl formate determined in this work (in collaboration with Dr Lavinia Onel and master's student Owen Dudman). The temperature-dependence has been updated to a non-Arrhenius equation (solid black line) fitting the data shown in the Figure and is used in SAR development in Chapter 6.

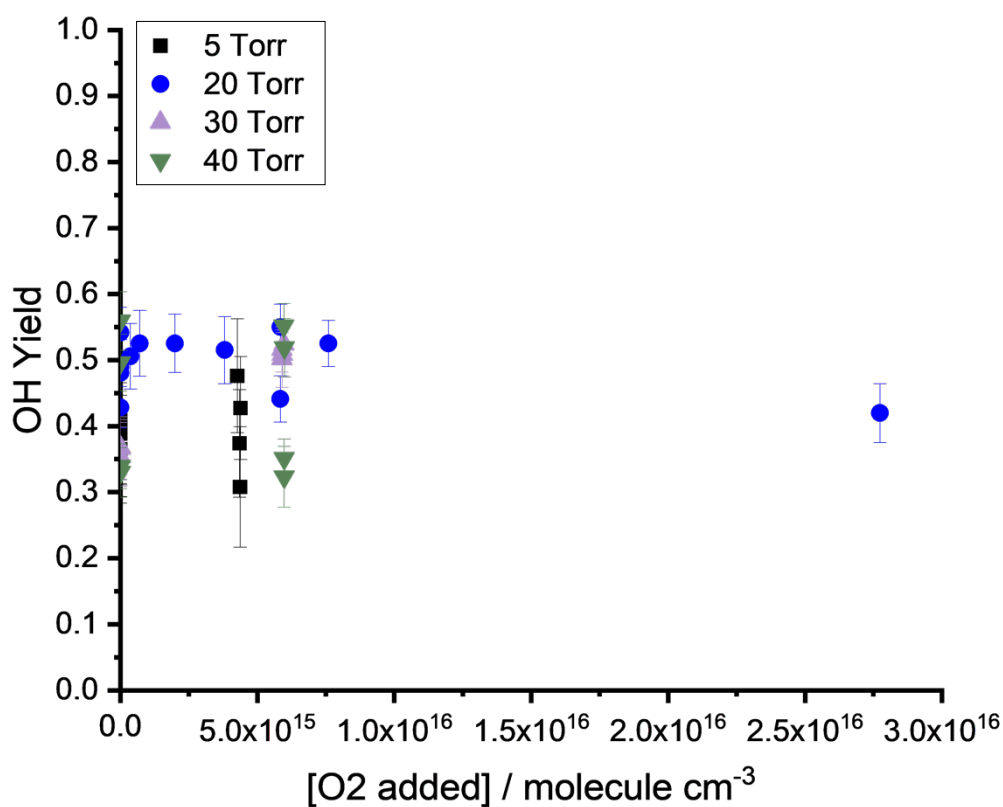


Figure E.3 – OH yields following the OH-initiated oxidation of tertbutyl formate determined as a function of added oxygen at 453 K and 5, (black squares), 20 (blue circles), 30 (purple triangles) and 40 (green triangles) Torr. OH yields are independent of added oxygen, indicating $(\text{CH}_3)_3\text{COC}(\text{O})$ thermally decomposes at this temperature and cannot be captured by reaction with oxygen.

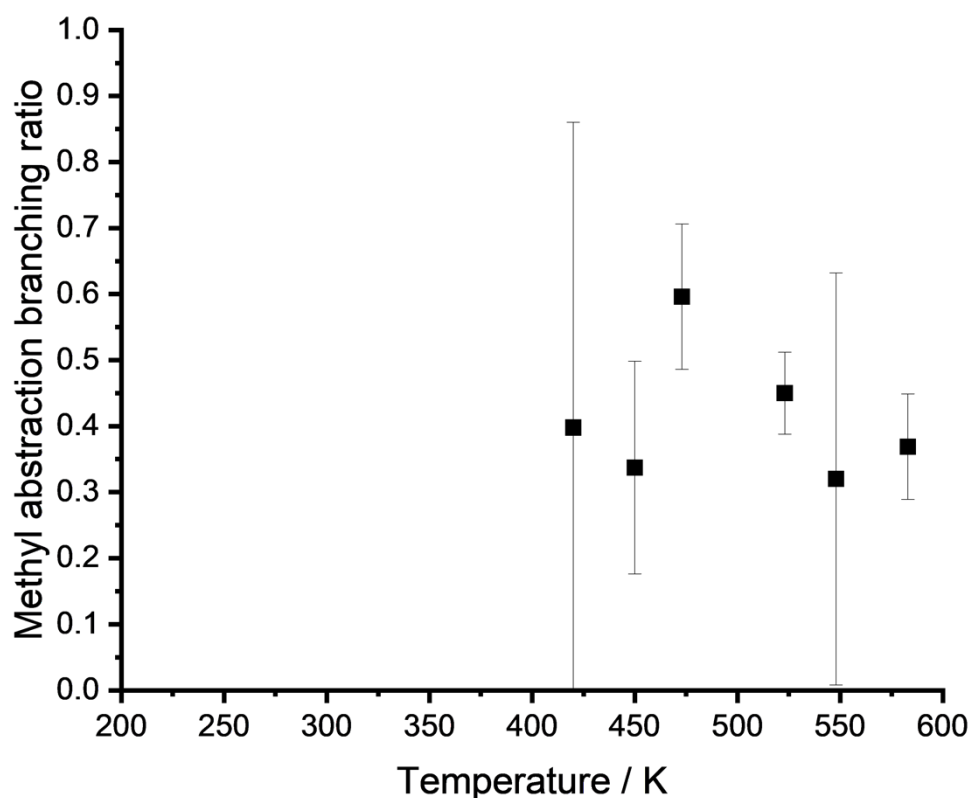


Figure E.4 – Branching ratios for methyl abstraction following OH + tertbutyl formate. As there are only two reaction sites in tertbutyl formate, when $(\text{CH}_3)_3\text{COC}(\text{O})$ thermally decomposes, OH yields can be attributed to methyl abstraction. At 420 and 450 K, branching ratios are determined from the Stern-Volmer intercept. Other branching ratios come from the thermalised RO_2 above 120 Torr.

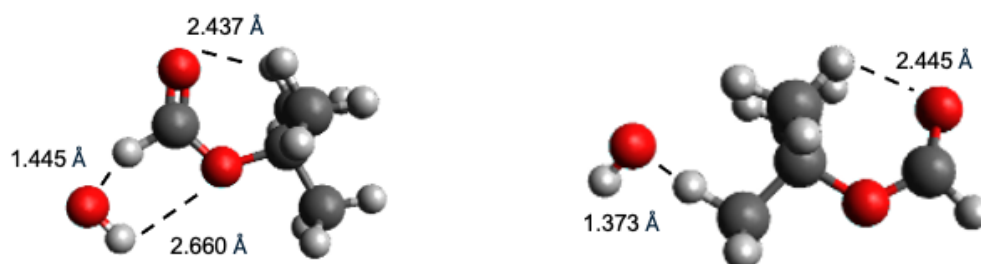


Figure E.5 – Transition state structures for OH + tertbutyl formate have been determined at the M062X/6-31+G** level of theory. The left figure shows the transition state for formate abstraction which has a transition state energy of 1.7 kJ mol^{-1} . The transition state for methyl abstraction has two conformers with energies 8.9 kJ mol^{-1} and -1.5 kJ mol^{-1} . The higher energy conformer is shown on the right hand side in this Figure. Hydrogen bond interactions are illustrated via dashed lines.

E3 n-Butyl formate

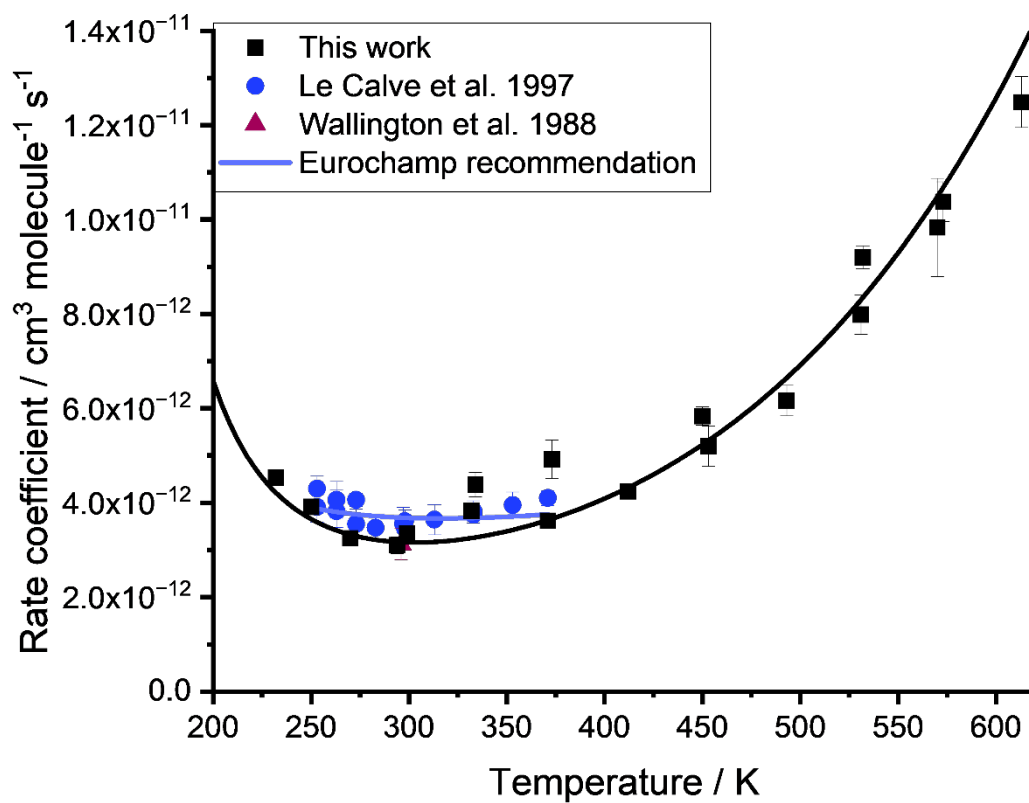


Figure E.6 – This work determined the temperature dependence of OH + n-butyl formate between 232 and 605 K. Shown here in black squares alongside literature values and the Eurochamp recommendation, used in SAR development in Chapter 6.

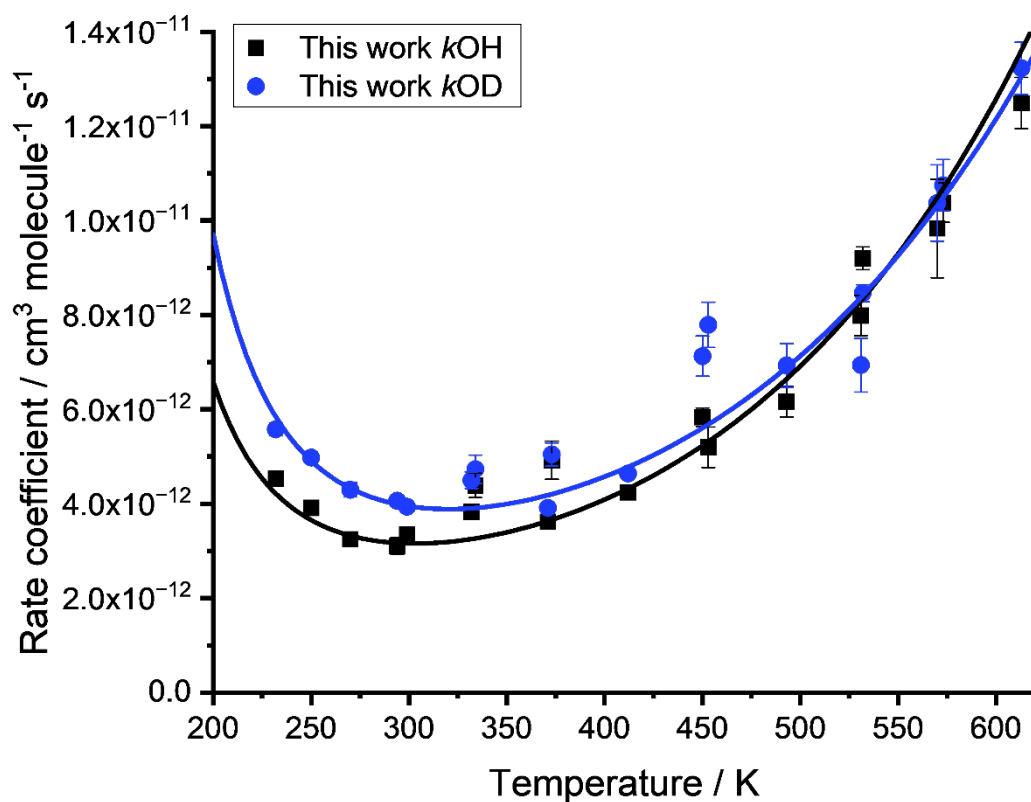


Figure E.7 – OH and OD-initiated reactions of n-butyl formate determined in this work between 232 and 605 K. Solid lines represent non-Arrhenius temperature-dependent fits.

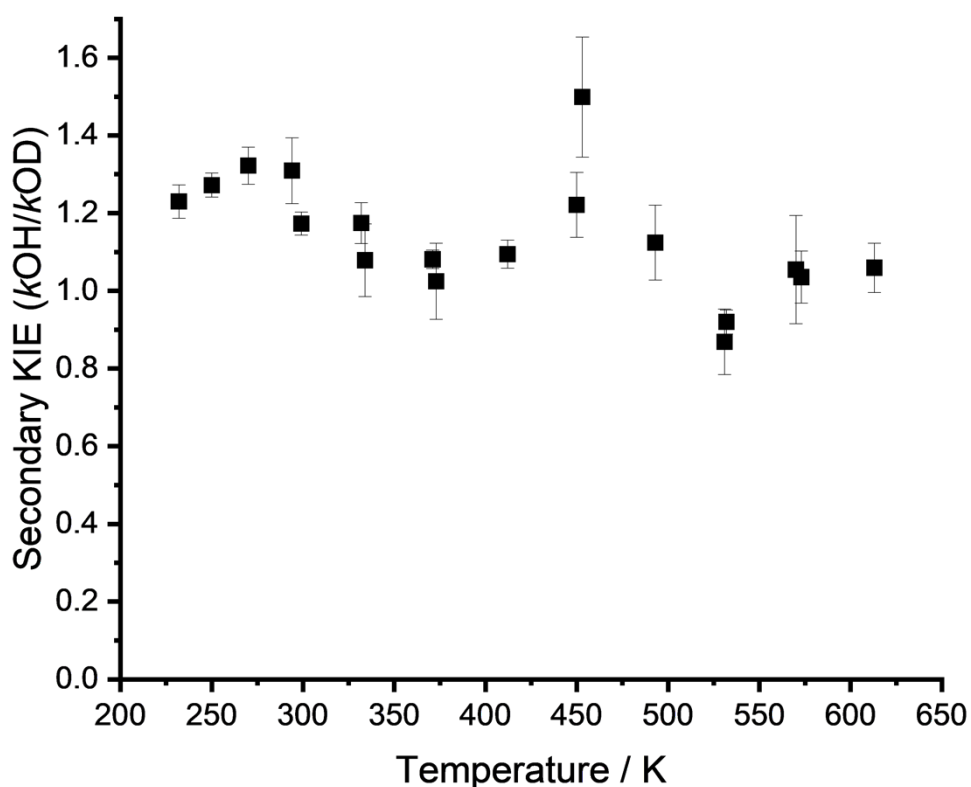


Figure E.8 – The positive secondary KIE ($k_{\text{OH}}/k_{\text{OD}}$) indicates OH/OD is partaking in the transition state.

Above 493 K, OH decays following the OH-initiated oxidation of n-butyl formate became biexponential. Biexponential behaviour is attributed to the thermal isomerisation of the peroxy radical $\text{CH}_3\text{CH}_2\text{CH}_2\text{CH}(\text{OO})\text{OC}(\text{O})\text{H}$. Therefore, OH yields are equivalent to the branching ratios for abstraction from the reaction site adjacent to the ether group, presented in Figure 6.23. Isomerisation of the $\text{CH}_3\text{CH}_2\text{CH}_2\text{CH}(\text{OO})\text{OC}(\text{O})\text{H}$ radical was found to have an energy barrier of 76.3 kJ mol^{-1} and is shown in Figure E.9. The next lowest energy barrier was 95.3 kJ mol^{-1} , for isomerisation of the $\text{CH}_3\text{CH}_2\text{CH}(\text{OO})\text{CH}_2\text{OC}(\text{O})\text{H}$ peroxy radical, forming a seven-membered ring and abstracting the formate hydrogen.

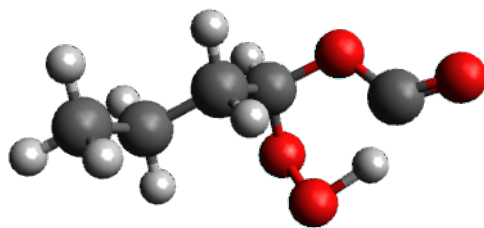


Figure E.9 – Transition state for the internal isomerisation of $\text{CH}_3\text{CH}_2\text{CH}_2\text{CH}(\text{OO})\text{OC}(\text{O})\text{H}$, obtained at the M062X/6-31+G** level of theory.

This work mapped out the potential energy surface for OH + n-butyl formate. Table E.1 shows the lowest energy transition state structures found for OH + n-butyl formate from each reactive site. The reaction site alpha to the ether group has the lowest transition state energy and the strongest hydrogen bonded transition state. The upturn in the overall rate coefficient below 300 K is likely due to abstraction from the alpha site dominating, this is supported by the secondary KIE increasing with decreasing temperature.

Table E.1 - Transition state structures for the reaction of OH with n-butyl formate, following abstraction from each reactive site labelled $\text{C}_1 - \text{C}_5$, beginning at the formate site. Only the lowest energy conformers are found.

Transition state	Transition state energy / kJ mol^{-1}
	3.9

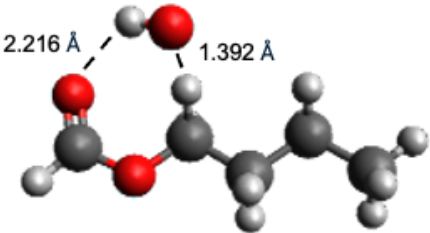
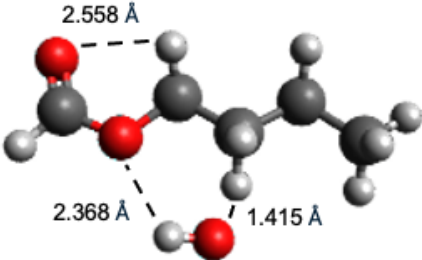
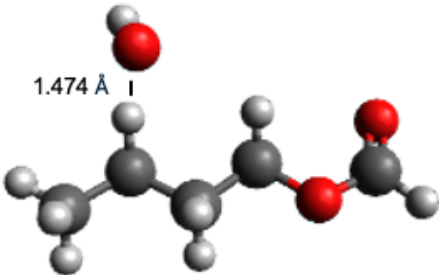
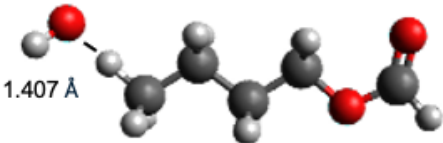
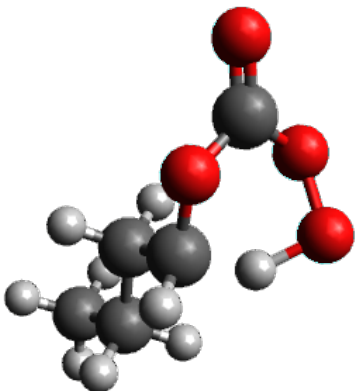
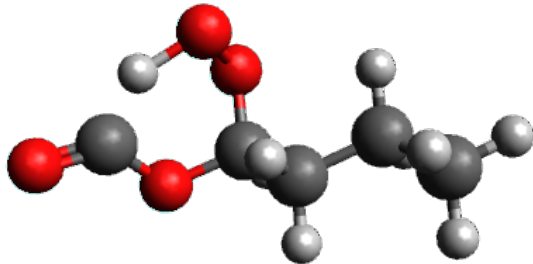
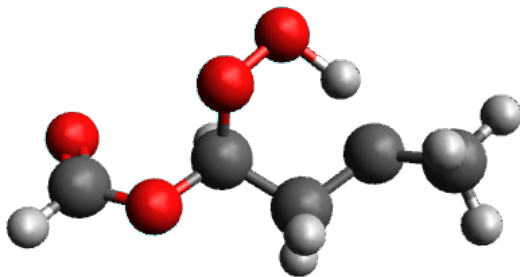
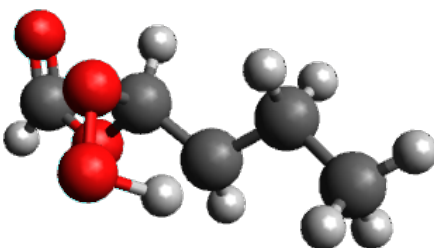
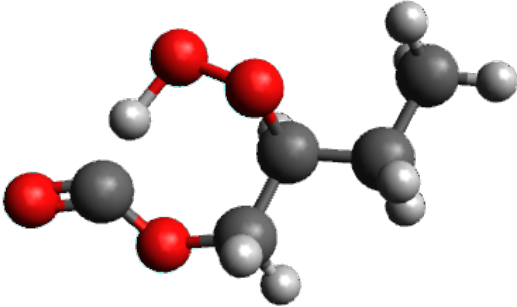
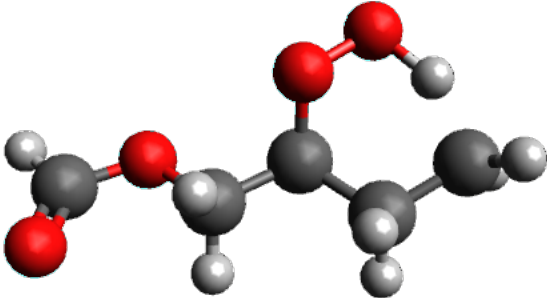
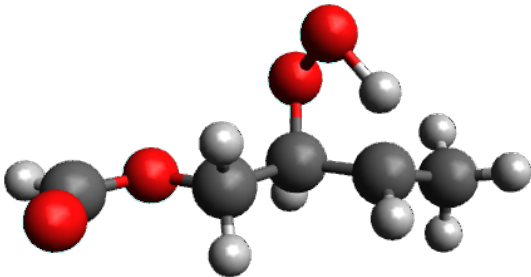
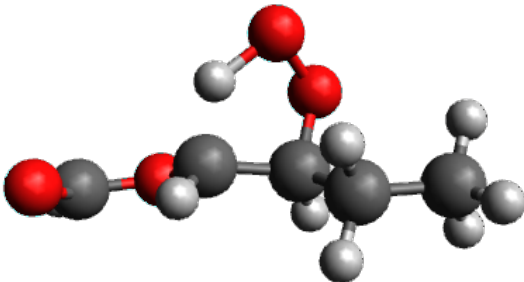
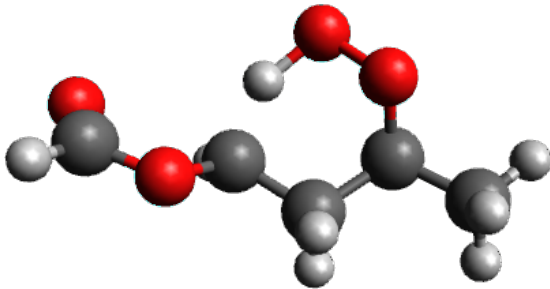
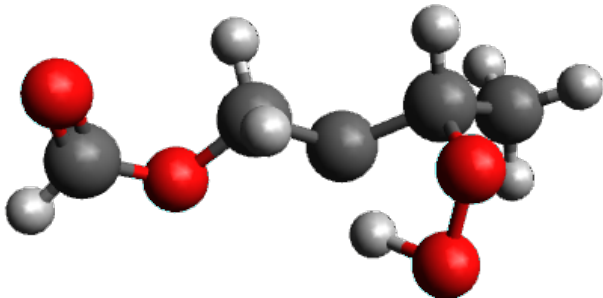
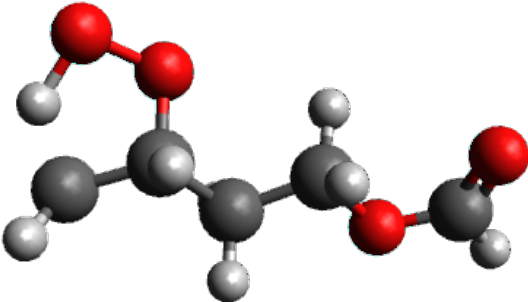
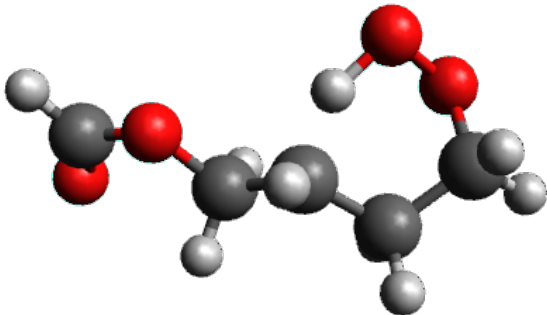
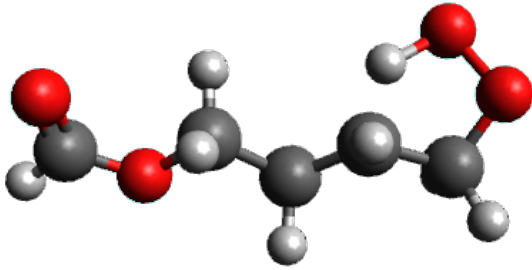
	<p>-8.9</p>
	<p>-1.9</p>
	<p>0.9</p>
	<p>9.5</p>

Table E.2 – Transition state structures for the internal isomerisation of RO₂ radicals to QOOH, following abstraction at each reaction site.

Abstraction Site	Transition State	<i>ab initio</i> Barrier / kJ mol ⁻¹
Formate abstraction (C ₁)		99.3
CH ₂ alpha-ether abstraction (C ₂)		76.3
CH ₂ alpha-ether abstraction (C ₂)		98.4
CH ₂ alpha-ether abstraction (C ₂)		132.7

CH ₂ abstraction (C ₃)		95.3
CH ₂ abstraction (C ₃)		107.5
CH ₂ abstraction (C ₃)		146.9
CH ₂ abstraction (C ₃)		147.9

CH ₂ abstraction (C ₄)		99.6
CH ₂ abstraction (C ₄)		153.0
CH ₂ abstraction (C ₄)		160.2
CH ₃ abstraction (C ₅)		100.9

<p>CH₃ abstraction (C₅)</p>		<p>148.5</p>
---	--	--------------

References

1. Eastman Chemical Company, *Texanol ester alcohol*. 2025 [cited 2025 25th April].
2. Good, D.A. and J.S. Francisco, *Tropospheric oxidation mechanism of dimethyl ether and methyl formate*. The Journal of Physical Chemistry A, 2000. **104**(6): p. 1171-1185.
3. Liu, T., et al., *Atmospheric oxidation capacity and ozone pollution mechanism in a coastal city of southeastern China: analysis of a typical photochemical episode by an observation-based model*. Atmospheric Chemistry and Physics, 2022. **22**(3): p. 2173-2190.
4. Orlando, J.J. and G.S. Tyndall, *The Atmospheric Oxidation of Ethyl Formate and Ethyl Acetate over a Range of Temperatures and Oxygen Partial Pressures*. International Journal of Chemical Kinetics, 2010. **42**(7): p. 397-413.
5. Crounse, J.D., et al., *Autoxidation of Organic Compounds in the Atmosphere*. Journal of Physical Chemistry Letters, 2013. **4**(20): p. 3513-3520.
6. von Schneidemesser, E., et al., *Chemistry and the Linkages between Air Quality and Climate Change*. Chemical Reviews, 2015. **115**(10): p. 3856-3897.
7. McGillen, M.R., et al., *Database for the kinetics of the gas-phase atmospheric reactions of organic compounds*. Earth System Science Data, 2020. **12**: p. 1203 - 1216.
8. Le Calvé, S., G. Le Bras, and A. Mellouki, *Temperature Dependence for the Rate Coefficients of the Reactions of the OH Radical with a Series of Formates*. The Journal of Physical Chemistry A, 1997. **101**: p. 5489-5493.
9. Lam, K.Y., D.F. Davidson, and R.K. Hanson, *High-Temperature Measurements of the Reactions of OH with Small Methyl Esters: Methyl Formate, Methyl Acetate, Methyl Propanoate, and Methyl Butanoate*. The Journal of Physical Chemistry A, 2012. **116**(50): p. 12229-12241.
10. Jiménez, E., et al., *First evidence of the dramatic enhancement of the reactivity of methyl formate (HC(O)OCH_3) with OH at temperatures of the interstellar medium: a gas-phase kinetic study between 22 K and 64 K*. Physical Chemistry Chemical Physics, 2016. **18**(3): p. 2183-2191.
11. Wallington, T.J., et al., *Atmospheric Oxidation Mechanism of Methyl Formate*. The Journal of Physical Chemistry A, 2001. **105**(21): p. 5146-5154.
12. Good, D.A., et al., *An Experimental and Computational Study of the Kinetics and Mechanism of the Reaction of Methyl Formate with Cl Atoms*. The Journal of Physical Chemistry A, 2000. **104**(7): p. 1505-1511.
13. Robertson, N.C.K., et al., *Temperature-Dependent, Site-Specific Rate Coefficients for the Reaction of OH (OD) with Methyl Formate Isotopologues via Experimental and Theoretical Studies*. The Journal of Physical Chemistry A, 2024. **128**(25): p. 5028-5040.
14. Luque, J. and D.R. Crosely, *LIFBASE: Database and Spectral Simulation Program*. 1995, SRI International.
15. Jenkin, M.E., et al., *Estimation of rate coefficients and branching ratios for gas-phase reactions of OH with aliphatic organic compounds for use in automated mechanism construction*. Atmospheric Chemistry and Physics, 2018. **18**(13): p. 9297-9328.

16. McGillen, M.R., et al., *Database for the kinetics of the gas-phase atmospheric reactions of organic compounds*. Earth System Science Data, 2020. **12**(2): p. 1203-1216.
17. Pimentel, A.S., et al., *Atmospheric chemistry of isopropyl formate and tert-butyl formate*. International Journal of Chemical Kinetics, 2010. **42**(8): p. 479-498.
18. Ashenhurst, J. *Fischer Esterification – Carboxylic Acid to Ester Under Acidic Conditions*. 2025 [cited 2025 5th March].
19. Wallington, T.J., et al., *The gas phase reactions of hydroxyl radicals with a series of esters over the temperature range 240–440 K*. International Journal of Chemical Kinetics, 1988. **20**(2): p. 177-186.
20. Zaras, A.M., et al., *A Chemical Kinetic Investigation on Butyl Formate Oxidation: Ab Initio Calculations and Experiments in a Jet-Stirred Reactor*. Energy & Fuels, 2017. **31**(6): p. 6194-6205.
21. Kwok, E.S.C. and R. Atkinson, *Estimation of hydroxyl radical reaction rate constants for gas-phase organic compounds using a structure-reactivity relationship: an update*. Atmospheric Environment, 1995. **29**(14): p. 1685-1695.
22. Yang, J., et al., *A revised reaction kinetic mechanism for the oxidation of methyl formate*. Combustion and Flame, 2024. **261**.
23. Calvert, J.G., et al., *The Mechanisms of Reactions Influencing Atmospheric Ozone*. 2015, New York: Oxford University Press.
24. Ortiz, J.D. and R. Jackson, *Understanding Eunice Foote's 1856 experiments: heat absorption by atmospheric gases*. Notes and Records: the Royal Society Journal of the History of Science, 2022. **76**(1): p. 67-84.
25. Friedlingstein, P., et al., *Global Carbon Budget 2024*. Earth System Science Data, 2025. **17**(3): p. 965-1039.
26. Kwon, E.E., et al., *Sustainable production of alkyl esters via thermal process in the presence of carbon black*. Environmental Research, 2020. **183**: p. 109199.
27. Saetiao, P., et al., *Enhancing Sustainable Production of Fatty Acid Methyl Ester from Palm Oil Using Bio-Based Heterogeneous Catalyst: Process Simulation and Techno-Economic Analysis*. ACS Omega, 2023. **8**(33): p. 30598-30611.
28. Layton, D.S. and C.T. Trinh, *Microbial synthesis of a branched-chain ester platform from organic waste carboxylates*. Metabolic Engineering Communications, 2016. **3**: p. 245-251.
29. Lee, J.-W. and C.T. Trinh, *Towards renewable flavors, fragrances, and beyond*. Current Opinion in Biotechnology, 2020. **61**: p. 168-180.
30. Kim, G.B., H.R. Kim, and S.Y. Lee, *Comprehensive evaluation of the capacities of microbial cell factories*. Nature Communications, 2025. **16**(1): p. 2869.
31. Teng, Y., T. Jiang, and Y. Yan, *The expanded CRISPR toolbox for constructing microbial cell factories*. Trends in Biotechnology, 2024. **42**(1): p. 104-118.
32. Air Quality Expert Group, *Non-methane Volatile Organic Compounds in the UK*, Department for Environment, Food and Rural Affairs, Scottish Government, Welsh Government and Department of Agriculture, Environment and Rural Affairs in Northern Ireland, Editor. 2020: <https://uk->

air.defra.gov.uk/assets/documents/reports/cat09/2006240803_Non_Methane_Volatile_Organic_Compounds_in_the_UK.pdf.

33. Borbon, A., et al., *Emission ratios of anthropogenic volatile organic compounds in northern mid-latitude megacities: Observations versus emission inventories in Los Angeles and Paris*. Journal of Geophysical Research-Atmospheres, 2013. **118**(4): p. 2041-2057.
34. Elliott, M., et al., *UK Informative Inventory Report (1990 to 2022)*. 2024.
35. McDonald, B.C., et al., *Volatile chemical products emerging as largest petrochemical source of urban organic emissions*. Science, 2018. **359**(6377): p. 760-764.
36. Sang, R., et al., *Methyl formate as a hydrogen energy carrier*. Nature Catalysis, 2023. **6**(6): p. 543-550.
37. Huang, G., et al., *Speciation of anthropogenic emissions of non-methane volatile organic compounds: a global gridded data set for 1970–2012*. Atmospheric Chemistry Physics, 2017. **17**(12): p. 7683-7701.
38. Japar, S.M., et al., *Ozone-Forming Potential of a Series of Oxygenated Organic Compounds*. Environmental Science & Technology, 1991. **25**: p. 415-420.
39. Yu, H., et al., *Atmospheric Photo-Oxidation of 2-Ethoxyethanol: Autoxidation Chemistry of Glycol Ethers*. The Journal of Physical Chemistry A, 2023. **127**(45): p. 9564-9579.
40. Peräkylä, O., et al., *Large Gas-Phase Source of Esters and Other Accretion Products in the Atmosphere*. Journal of the American Chemical Society, 2023. **145**(14): p. 7780-7790.
41. Franzon, L., et al., *Ether and ester formation from peroxy radical recombination: a qualitative reaction channel analysis*. Atmospheric Chemistry Physics, 2024. **24**(20): p. 11679-11699.
42. Li, M., et al., *Tropospheric OH and stratospheric OH and Cl concentrations determined from CH₄, CH₃Cl, and SF₆ measurements*. npj Climate and Atmospheric Science, 2018. **1**: p. article no: 29.
43. Heard, D.E. and M. Pilling, J., *Measurement of OH and HO₂ in the Troposphere*. Chemical Reviews, 2003. **103**(12): p. 5163-5198.
44. Nicely, J.M., et al., *Changes in Global Tropospheric OH Expected as a Result of Climate Change Over the Last Several Decades*. Journal of Geophysical Research-Atmospheres, 2018. **132**(18): p. 10,774-10,795.
45. Atkinson, R., *Rate constants for the atmospheric reactions of alkoxy radicals: An updated estimation method*. Atmospheric Environment, 2007. **41**(38): p. 8468-8485.
46. Barber, V.P. and J.H. Kroll, *Chemistry of Functionalized Reactive Organic Intermediates in the Earth's Atmosphere: Impact, Challenges, and Progress*. The Journal of Physical Chemistry A, 2021. **125**(48): p. 10264-10279.
47. Tyndall, G.S., A.S. Pimentel, and J.J. Orlando, *Temperature dependence of the alpha-ester rearrangement reaction*. The Journal of Physical Chemistry A, 2004. **108**(33): p. 6850-6856.
48. Newland, M.J., et al., *Low-NO atmospheric oxidation pathways in a polluted megacity*. Atmospheric Chemistry and Physics, 2021. **21**: p. 1613-1625.
49. Fittschen, C., L.K. Whalley, and D.E. Heard, *The Reaction of CH₃O₂ Radicals with OH Radicals: A Neglected Sink for CH₃O₂ in the Remote Atmosphere*. Environmental Science & Technology, 2014. **48**(14): p. 7700-7701.

50. Jenkin, M.E., et al., *Estimation of rate coefficients and branching ratios for reactions of organic peroxy radicals for use in automated mechanism construction*. Atmospheric Chemistry and Physics, 2019. **19**: p. 7691-7717.
51. Iyer, S., et al., *Computational Investigation of $RO_2 + HO_2$ and $RO_2 + RO_2$ Reactions of Monoterpene Derived First-Generation Peroxy Radicals Leading to Radical Recycling*. J. Phys. Chem. A, 2018. **122**(49): p. 9542-9552.
52. Winiberg, F.A.F., et al., *Direct measurements of OH and other product yields from the $HO_2 + CH_3C(O)O_2$ reaction*. Atmospheric Chemistry and Physics, 2016. **16**: p. 4023-4042.
53. Wang, Z., et al., *Efficient alkane oxidation under combustion engine and atmospheric conditions*. Communications Chemistry, 2021. **4**: Article no: 18.
54. Bianchi, F., et al., *Highly Oxygenated Organic Molecules (HOM) from Gas-Phase Autoxidation Involving Peroxy Radicals: A Key Contributor to Atmospheric Aerosol*. Chemical Reviews, 2019. **119**(6): p. 3472-3509.
55. Kroll, J.H. and J.H. Seinfeld, *Chemistry of secondary organic aerosol: Formation and evolution of low-volatility organics in the atmosphere*. Atmospheric Environment, 2008. **42**(16): p. 3593-3624.
56. Li, W., et al., *Potential of select intermediate-volatility organic compounds and consumer products for secondary organic aerosol and ozone formation under relevant urban conditions*. Atmospheric Environment, 2018. **178**: p. 109-117.
57. Sasidharan, S., et al., *Secondary Organic Aerosol Formation from Volatile Chemical Product Emissions: Model Parameters and Contributions to Anthropogenic Aerosol*. Environmental Science & Technology, 2023. **57**(32): p. 11891-11902.
58. Sander, R., *Compilation of Henry's law constants (version 5.0.0) for water as solvent*. Atmospheric Chemistry Physics, 2023. **23**(19): p. 10901-12440.
59. Calvert, J.G., et al., *The Mechanisms of Atmospheric Oxidation of the Oxygenates*. 2011, New York: Oxford University Press.
60. Longnecker, E., et al. *A Quantitative Study of Surface Films Formed in a University Classroom*. Atmospheric Chemical Mechanisms. 2024. UC Davis.
61. Penner, J.E., 5: *Aerosols, their Direct and Indirect Effects*, in *TAR Climate Change 2001: The Scientific Basis*, A.P.M. Baede, Editor. 2001, Intergovernmental Panel on Climate Change.
62. Tan, F., et al., *Hygroscopic behavior and aerosol chemistry of atmospheric particles containing organic acids and inorganic salts*. npj Climate and Atmospheric Science, 2024. **7**(1): p. 203.
63. Finlayson-Pitts, B.J., *Introductory lecture: atmospheric chemistry in the Anthropocene*. Faraday Discussions, 2017. **200**: p. 11-58.
64. Lelieveld, J., et al., *Loss of life expectancy from air pollution compared to other risk factors: a worldwide perspective*. Cardiovascular Research, 2020. **116**(11): p. 1910-1917.
65. Mebrahtu, T.F., et al., *Impact of an urban city-wide Bradford clean air plan on health service use and nitrogen dioxide 24 months after implementation: An interrupted time series analysis*. Environmental Research, 2025. **270**: p. 120988.
66. Aumont, B., et al. *Generator for Explicit Chemistry and Kinetics of Organics in the Atmosphere (GECKO-A)*. 2025.

67. Vereecken, L., et al., *Perspective on Mechanism Development and Structure-Activity Relationships for Gas-Phase Atmospheric Chemistry*. International Journal of Chemical Kinetics, 2018. **50**(6): p. 435-469.
68. Bonchev, D., *Chemical Graph Theory: Introduction and Fundamentals*. 1991: Taylor & Francis.
69. Atkinson, R., *Kinetics and mechanisms of the gas-phase reactions of the hydroxyl radical with organic compounds under atmospheric conditions*. Chemical Reviews, 1986. **86**(1): p. 69-201.
70. Atkinson, R., *A Structure-Activity Relationship for the Estimation of Rate Constants for the Gas-Phase Reactions of OH Radicals with Organic Compounds*. International Journal of Chemical Kinetics, 1987. **19**: p. 799-828.
71. Brasseur, G.P. and D.J. Jacob, *Modeling of Atmospheric Chemistry*. Vol. 1. 2017, United Kingdom: Cambridge University Press.
72. Sinha, V., et al., *OH Reactivity Measurements within a Boreal Forest: Evidence for Unknown Reactive Emissions*. Environmental Science & Technology, 2010. **44**(17): p. 6614-6620.
73. Medeiros, D.J., et al., *Direct Measurements of Isoprene Autoxidation: Pinpointing Atmospheric Oxidation in Tropical Forests*. American Chemical Society, 2022.
74. Saunders, S.M., et al., *Protocol for the development of the Master Chemical Mechanism, MCM v3 (Part A): tropospheric degradation of non-aromatic volatile organic compounds*. Atmospheric Chemistry and Physics, 2003. **3**: p. 161-180.
75. Bey, I., et al., *Global modeling of tropospheric chemistry with assimilated meteorology: Model description and evaluation*. Journal of Geophysical Research: Atmospheres, 2001. **106**(D19): p. 23073-23095.
76. Bates, K.H., et al., *Impacts of updated reaction kinetics on the global GEOS-Chem simulation of atmospheric chemistry*. Geoscientific Model Development, 2024. **17**(4): p. 1511-1524.
77. Arrhenius, S., *Über die Reaktionsgeschwindigkeit bei der Inversion von Rohrzucker durch Säuren*. Zeitschrift für Physikalische Chemie, 1889. **4U**(1): p. 226-248.
78. Klippenstein, S.J., *Spiers Memorial Lecture: Theory of unimolecular reactions*. Faraday Discussions, 2022. **238**(0): p. 11-67.
79. Glowacki, D.R., et al., *MESMER: An Open-Source Master Equation Solver for Multi-Energy Well Reactions*. The Journal of Physical Chemistry A, 2012. **116**(38): p. 9545-9560.
80. Atkins, P., J. de Paula, and R. Friedman, *Physical Chemistry: Quanta, Matter, and Change*. 2014: OUP Oxford.
81. M. J. Frisch, et al., *Gaussian 09. Revision A.02*. 2009, Gaussian, Inc.: Wallingford CT.
82. Zhao, Y. and D.G. Truhlar, *The M06 suite of density functionals for main group thermochemistry, thermochemical kinetics, noncovalent interactions, excited states, and transition elements: two new functionals and systematic testing of four M06-class functionals and 12 other functionals*. Theoretical Chemistry Accounts, 2008. **120**(1): p. 215-241.
83. Tully, F.P., et al., *Hydrogen-atom abstraction from alkanes by hydroxyl. 2. Ethane*. The Journal of Physical Chemistry, 1986. **90**(4): p. 691-698.

84. Droege, A.T. and F.P. Tully, *Hydrogen-atom abstraction from alkanes by hydroxyl. 3. Propane*. The Journal of Physical Chemistry, 1986. **90**(9): p. 1949-1954.
85. Voráč, J., P. Dvořák, and M. Mrkvičková, *Laser-Induced Fluorescence of Hydroxyl (OH) Radical in Cold Atmospheric Discharges*, in *Photon Counting - Fundamentals and Applications*, N. Britun and A. Nikiforov, Editors. 2017, IntechOpen: Rijeka.
86. ET Enterprises Ltd 9813B series data sheet. 2016.
87. Spring, K.R., J.C. Long, and M.W. Davidson. *Channel Photomultipliers*. 2025 [cited 2025 26th April].
88. Tully, F.P. and A.R. Ravishankara, *Flash photolysis-resonance fluorescence kinetic study of the reactions $\text{OH} + \text{H}_2 \rightarrow \text{H}_2\text{O} + \text{H}$ and $\text{OH} + \text{CH}_4 \rightarrow \text{H}_2\text{O} + \text{CH}_3$ from 298 to 1020 K*. The Journal of Physical Chemistry, 1980. **84**(23): p. 3126-3130.
89. Neill, J.L., et al., *Laboratory and Tentative Interstellar Detection of Trans-Methyl Formate Using the Publicly Available Green Bank Telescope Primos Survey*. The Astrophysical Journal, 2012. **755**(2): p. 153.
90. Putrasari, Y. and O. Lim, *Dimethyl Ether as the Next Generation Fuel to Control Nitrogen Oxides and Particulate Matter Emissions from Internal Combustion Engines: A Review*. ACS Omega, 2022. **7**(1): p. 32-37.
91. Millet, D.B., et al., *A large and ubiquitous source of atmospheric formic acid*. Atmospheric Chemistry and Physics, 2015. **15**(11): p. 6283-6304.
92. Good, D.A., et al., *Kinetics and reaction mechanism of hydroxyl radical reaction with methyl formate*. The Journal of Physical Chemistry A, 1999. **103**(50): p. 10893-10898.
93. Palazzetti, F. and P.-Y. Tsai, *Photodissociation Dynamics of CO-Forming Channels on the Ground-State Surface of Methyl Formate at 248 nm: Direct Dynamics Study and Assessment of Generalized Multicenter Impulsive Models*. The Journal of Physical Chemistry A, 2021. **125**(5): p. 1198-1220.
94. Li, X., et al., *Benchmark Calculations for Bond Dissociation Enthalpies of Unsaturated Methyl Esters and the Bond Dissociation Enthalpies of Methyl Linolenate*. The Journal of Physical Chemistry A, 2016. **120**(23): p. 4025-4036.
95. Luo, Y.-R., *Comprehensive Handbook of Chemical Bond Energies*. 1st Edition ed. 2007, Boca Raton: CRC Press.
96. Szilágyi, I., et al., *Direct Kinetic Study of Reactions of Hydroxyl Radicals with Alkyl Formates*. Zeitschrift für Physikalische Chemie, 2009. **218**(4): p. 479-492.
97. Keller-Rudek, H., et al., *The MPI-Mainz UV/VIS Spectral Atlas of Gaseous Molecules of Atmospheric Interest*. Earth System Science Data, 2013. **5**(2): p. 365-373.
98. Werner, H.-J., et al., *Molpro: a general-purpose quantum chemistry program package*. WIREs Computational Molecular Science, 2012. **2**(2): p. 242-253.
99. Klippenstein, S.J., L.B. Harding, and B. Ruscic, *Ab Initio Computations and Active Thermochemical Tables Hand in Hand: Heats of Formation of Core Combustion Species*. The Journal of Physical Chemistry A, 2017. **121**(35): p. 6580-6602.
100. Bloino, J., M. Biczysko, and V. Barone, *General Perturbative Approach for Spectroscopy, Thermodynamics, and Kinetics: Methodological Background*

- and Benchmark Studies. *Journal of Chemical Theory and Computation*, 2012. **8**(3): p. 1015-1036.
101. Kállay, M., et al., *The MRCC program system: Accurate quantum chemistry from water to proteins*. *The Journal of Chemical Physics*, 2020. **152**(7).
 102. Cowan, R.D. and D.C. Griffin, *Approximate relativistic corrections to atomic radial wave functions**. *Journal of the Optical Society of America*, 1976. **66**(10): p. 1010-1014.
 103. Shannon, R.J., et al., *ChemDyME: Kinetically Steered, Automated Mechanism Generation through Combined Molecular Dynamics and Master Equation Calculations*. *Journal of Chemical Theory and Computation*, 2021. **17**(8): p. 4901-4912.
 104. Skodje, R.T. and D.G. Truhlar, *Parabolic tunneling calculations*. *The Journal of Physical Chemistry*, 1981. **85**(6): p. 624-628.
 105. Sharma, S., S. Raman, and W.H. Green, *Intramolecular Hydrogen Migration in Alkylperoxy and Hydroperoxyalkylperoxy Radicals: Accurate Treatment of Hindered Rotors*. *The Journal of Physical Chemistry A*, 2010. **114**(18): p. 5689-5701.
 106. Gang, J., M.J. Pilling, and S.H. Robertson, *Partition functions and densities of states for butane and pentane*. *Journal of the Chemical Society, Faraday Transactions*, 1996. **92**(19): p. 3509-3518.
 107. Yu, T., J. Zheng, and D.G. Truhlar, *Multi-structural variational transition state theory. Kinetics of the 1,4-hydrogen shift isomerization of the pentyl radical with torsional anharmonicity*. *Chemical Science*, 2011. **2**(11): p. 2199-2213.
 108. Wu, J., et al., *Pressure-dependent kinetics of methyl formate reactions with OH at combustion, atmospheric and interstellar temperatures*. *Physical Chemistry Chemical Physics*, 2018. **20**(41): p. 26190-26199.
 109. Hess, W.P. and F.P. Tully, *Hydrogen-atom abstraction from methanol by hydroxyl radical*. *The Journal of Physical Chemistry*, 1989. **93**(5): p. 1944-1947.
 110. Carr, S.A., M.A. Blitz, and P.W. Seakins, *Site-Specific Rate Coefficients for Reaction of OH with Ethanol from 298 to 900 K*. *Journal of Physical Chemistry A*, 2011. **115**(15): p. 3335-3345.
 111. Feilberg, K.L., M.S. Johnson, and C.J. Nielsen, *Relative Reaction Rates of HCHO, HCDO, DCDO, H¹³CHO, and HCH¹⁸O with OH, Cl, Br, and NO₃ Radicals*. *The Journal of Physical Chemistry A*, 2004. **108**(36): p. 7393-7398.
 112. D'Anna, B., et al., *Experimental and theoretical studies of gas phase NO₃ and OH radical reactions with formaldehyde, acetaldehyde and their isotopomers*. *Physical Chemistry Chemical Physics*, 2003. **5**(9): p. 1790-1805.
 113. Carr, S.A., et al., *Experimental and Theoretical Study of the Kinetics and Mechanism of the Reaction of OH Radicals with Dimethyl Ether*. *The Journal of Physical Chemistry A*, 2013. **117**(44): p. 11142-11154.
 114. Harry, C., J. Arey, and R. Atkinson, *Rate constants for the reactions of OH radicals and Cl atoms with di-n-propyl ether and di-n-butyl ether and their deuterated analogs*. *International Journal of Chemical Kinetics*, 1999. **31**(6): p. 425-431.
 115. Szabó, E., et al., *Kinetics of the OH-radical initiated reactions of acetic acid and its deuterated isomers*. *Reaction Kinetics and Catalysis Letters*, 2009. **96**(2): p. 299-309.

116. Bansch, C. and M. Olzmann, *Reaction of dimethoxymethane with hydroxyl radicals: An experimental kinetic study at temperatures above 296 K and pressures of 2, 5, and 10 bar*. Chemical Physics Letters, 2019. **720**: p. 19-24.
117. Potter, D.G., M.A. Blitz, and P.W. Seakins, *A generic method for determining $R + O_2$ rate parameters via OH regeneration*. Chemical Physics Letters, 2019. **730**: p. 213-219.
118. Romero, M.T.B., et al., *OH formation from the $C_2H_5CO + O_2$ reaction: An experimental marker for the propionyl radical*. Chemical Physics Letters, 2005. **408**(4): p. 232-236.
119. Minwegen, H., et al., *Experimental and theoretical investigations of methyl formate oxidation including hot beta-scission*. Proceedings of the Combustion Institute, 2019. **37**(1): p. 307-314.
120. Dontgen, M., L.C. Kroger, and K. Leonhard, *Hot beta-scission of radicals formed via hydrogen abstraction*. Proceedings of the Combustion Institute, 2017. **36**(1): p. 135-142.
121. Rickard, A. *The Master Chemical Mechanism: CH_3OCHO* . 2022 [cited 2022 4 July]; Available from: <http://mcm.york.ac.uk/browse.htm?species=CH3OCHO>.
122. The Good Scents Company *isopropyl formate*. 2021 [cited 2025 9th March].
123. Stemmler, K., W. Mengon, and J.A. Kerr, *Hydroxyl-radical-initiated oxidation of isobutyl isopropyl ether under laboratory conditions related to the troposphere Product studies and proposed mechanism*. Journal of the Chemical Society, Faraday Transactions, 1997. **93**(16): p. 2865-2875.
124. Szilágyi, I., et al., *Direct kinetic study of reactions of hydroxyl radicals with alkyl formates*. Zeitschrift Fur Physikalische Chemie-International Journal of Research in Physical Chemistry & Chemical Physics, 2004. **218**(4): p. 479-492.
125. Zhang, Y.J., et al., *Reactions of OH and Cl with isopropyl formate, isobutyl formate, n-propyl isobutyrate and isopropyl isobutyrate*. Chemical Physics Letters, 2014. **602**: p. 68-74.
126. Atkinson, R., *Gas-phase Tropospheric Chemistry of Organic Compounds*. Journal of Physical and Chemical Reference Data, 1994.
127. Atkinson, R., et al., *Evaluated kinetic and photochemical data for atmospheric chemistry: Volume II; gas phase reactions of organic species*. Atmospheric Chemistry Physics, 2006. **6**(11): p. 3625-4055.
128. Calvert, J.G., et al., *Mechanisms of Atmospheric Oxidation of the Alkanes*. 2008: Oxford University Press.
129. National Institute of Standards and Technology *Formic acid, 1-methylethyl ester*. 2025 [cited 2025 5th March].
130. Thévenet, R., A. Mellouki, and G. Le Bras, *Kinetics of OH and Cl reactions with a series of aldehydes*. International Journal of Chemical Kinetics, 2000. **32**(11): p. 676-685.
131. Mellouki, A., S. Teton, and G. Lebras, *Kinetics of OH radical reactions with a series of ethers*. International Journal of Chemical Kinetics, 1995. **27**(8): p. 791-805.
132. Shi, C., et al., *Geometric isotope effect of deuteration in a hydrogen-bonded host-guest crystal*. Nature Communications, 2018. **9**(1): p. 481.
133. Nelson, L., et al., *Absolute and relative rate constants for the reactions of hydroxyl radicals and chlorine atoms with a series of aliphatic alcohols and*

- ethers at 298 K. *International Journal of Chemical Kinetics*, 1990. **22**(11): p. 1111-1126.
134. Mellouki, A., S. Teton, and G. Le Bras, *Kinetics of OH radical reactions with a series of ethers*. *International Journal of Chemical Kinetics*, 1995. **27**(8): p. 791-805.
 135. Atkinson, R., et al., *Rate constants for the gas-phase reaction of OH radicals with a series of ketones at 299 ± 2 K*. *International Journal of Chemical Kinetics*, 1982. **14**(8): p. 839-847.
 136. Le Calvé, S., et al., *Kinetic Studies of OH Reactions with a Series of Ketones*. *The Journal of Physical Chemistry A*, 1998. **102**(24): p. 4579-4584.
 137. Mellouki, A., G. Le Bras, and H. Sidebottom, *Kinetics and Mechanisms of the Oxidation of Oxygenated Organic Compounds in the Gas Phase*. *Chemical Reviews*, 2003. **103**(12): p. 5077-5096.
 138. Smith, I.W.M. and A.R. Ravishankara, *Role of Hydrogen-Bonded Intermediates in the Bimolecular Reactions of the Hydroxyl Radical*. *The Journal of Physical Chemistry A*, 2002. **106**(19): p. 4798-4807.
 139. Wallington, T.J., et al., *Atmospheric Oxidation Mechanism of Methyl Pivalate, $(CH_3)_3CC(O)OCH_3$* . *The Journal of Physical Chemistry A*, 2001. **105**(30): p. 7225-7235.
 140. Mapelli, C., et al., *Atmospheric oxidation of new “green” solvents – Part 2: methyl pivalate and pinacolone*. *Atmospheric Chemistry Physics*, 2023. **23**(13): p. 7767-7779.
 141. Andersen, V.F., et al., *Atmospheric Chemistry of Ethyl Propionate*. *The Journal of Physical Chemistry A*, 2012. **116**(21): p. 5164-5179.
 142. (IARC), International Agency for Research on Cancer *List of Classifications*. 2025 [cited 2025 11th April].
 143. Zhang, Y.J., et al., *Reactions of OH and Cl with isopropyl formate, isobutyl formate, n-propyl isobutyrate and isopropyl isobutyrate*. *Chemical Physics Letters*, 2014. **602**: p. 68-74.
 144. Das, K.C., K. Xu, and J. Nam, *Zagreb indices of graphs*. *Frontiers of Mathematics in China*, 2015. **10**(3): p. 567-582.
 145. McGillen, M.R., et al., *The use of the electrotopological state as a basis for predicting hydrogen abstraction rate coefficients: a proof of principle for the reactions of alkanes and haloalkanes with OH*. *Environmental Science: Atmospheres*, 2024. **4**(1): p. 18-34.
 146. Gehlen, M.H., *The centenary of the Stern-Volmer equation of fluorescence quenching: From the single line plot to the SV quenching map*. *Journal of Photochemistry and Photobiology C: Photochemistry Reviews*, 2020. **42**: p. Article no: 100338.
 147. Ghosh, B., D.K. Papanastasiou, and J.B. Burkholder, *Oxalyl chloride, $ClC(O)C(O)Cl$: UV/vis spectrum and Cl atom photolysis quantum yields at 193, 248, and 351 nm*. *Journal of Chemical Physics*, 2012. **137**(16).
 148. Stuhr, M., et al., *UV photolysis of oxalyl chloride: $ClCO$ radical decomposition and direct Cl_2 formation pathways*. *International Journal of Chemical Kinetics*, 2024. **56**: p. 482-498.
 149. Huang, T.-K., et al., *Cl_2 Elimination in 248 nm Photolysis of $(COCl)_2$ Probed with Cavity Ring-Down Absorption Spectroscopy*. *The Journal of Physical Chemistry A*, 2017. **121**(15): p. 2888-2895.

150. Atkinson, R., et al., *Evaluated kinetic and photochemical data for atmospheric chemistry: Volume III; gas phase reactions of inorganic halogens*. Atmospheric Chemistry Physics, 2007. **7**(4): p. 981-1191.
151. Lehman, J.H. and M.I. Lester, *Dynamical Outcomes of Quenching: Reflections on a Conical Intersection*. Annual Review of Physical Chemistry, Vol 65, 2014. **65**: p. 537-555.
152. Bailey, A., et al., *Collisional quenching of OH ($A^2\Sigma^+$, $v'=0$) by N_2 , O_2 and CO_2 between 204 and 294 K. Implications for atmospheric measurements of OH by laser-induced fluorescence* Journal of the Chemical Society-Faraday Transactions, 1997. **93**(16): p. 2915-2920.
153. Kenner, R.D., F.P. Capetanakis, and F. Stuhl, *Kinetic isotope effects in the electronic quenching of OD/OH ($A^2\Sigma^+$, $v'=0$) at 296 \pm 4 K*. Journal of Physical Chemistry, 1990. **94**(6): p. 2441-2446.
154. Whelan, C.A., et al., *Temperature and Pressure Dependent Kinetics of QOOH Decomposition and Reaction with O_2 : Experimental and Theoretical Investigations of QOOH Radicals Derived from Cl (CH_3)₃COOH*. Journal of Physical Chemistry A, 2019. **123**: p. 10254 - 10262.
155. Zador, J., et al., *Directly measuring reaction kinetics of QOOH - a crucial but elusive intermediate in hydrocarbon autoignition*. Physical Chemistry Chemical Physics, 2013. **15**(48): p. 21103-21103.
156. Potter, G.D., *Kinetic studies of ether low temperature combustion mechanisms using laser photolysis and modelling*, School of Chemistry. 2019, University of Leeds.